The Dissertation Committee for Preethi Mathew Certifies that this is the approved version of the following dissertation:

CATHODE CATALYSTS FOR LOW-TEMPERATURE FUEL CELLS: ANALYSIS OF SURFACE PHENOMENA

Committee:

Arumugam Manthiram, Supervisor

John B Goodenough, Co-Supervisor

Allen J Bard

Charles B Mullins

Guihua Yu

CATHODE CATALYSTS FOR LOW-TEMPERATURE FUEL CELLS: ANALYSIS OF SURFACE PHENOMENA

by

Preethi Mathew, B.Tech., M.Tech.

Dissertation

Presented to the Faculty of the Graduate School of

The University of Texas at Austin

in Partial Fulfillment

of the Requirements

for the Degree of

Doctor of Philosophy

The University of Texas at Austin

December 2013

Dedication

To my beloved Lord (Papa)

and

To my beloved parents

Acknowledgement

I wish to place on record my profound gratitude to my dissertation advisors, Professors John B. Goodenough and Arumugam Manthiram for their invaluable guidance, constant encouragement and inspiring discussions as well as the opportunity to continue my Doctoral degree. I am forever indebted to both of them for the freedom given to pursue my research interests. I express my gratefulness to Professors Allen J. Bard, Charles B. Mullins and Guihua Yu for serving on my dissertation committee and for their helpful suggestions and ideas. I also wish to thank Dr. Jeremy P. Meyers for his guidance and support.

My sincere thanks are due to Dr. Thomas Cochell and Dr. Wei Li for stimulated discussions and their assistance on a variety of topics. I wish to thank Dr. Nathan Miller, Dr. Wei Li, Dr. Hugo Celio, Craig Milroy, and Zachary Moorhead-Rosenberg for ICP-MS, TEM, UVPES, XPS, and magnetic measurements, respectively. I thank Dr. Xiaole Chen and CEC for assistance with QCM-D measurements. I also thank past and current members of my research groups for their assistance and support. I wish to thank the staff of the Texas Materials Institute and the Materials Science and Engineering Graduate program for their support. Financial support by Norman Hackerman Advanced Research Program, Argonne National Laboratories–DOE project, Office of Naval Research (MURI), and Robert A. Welch Foundation is gratefully acknowledged.

I humbly thank my parents and my siblings for their unconditional love and support over the years. I also thank my friends for their encouragement during this journey. I thank my Lord and Savior Jesus Christ for loving me just as I am, restoring me, and meeting all my needs according to His riches in glory.

CATHODE CATALYSTS FOR LOW-TEMPERATURE FUEL CELLS: ANALYSIS OF SURFACE PHENOMENA

Preethi Mathew, Ph.D.

The University of Texas at Austin, 2013

Supervisors: Arumugam Manthiram, John B Goodenough

The electrochemical oxygen reduction reaction (ORR) steps on a noble metal catalyst in an acidic aqueous electrolyte depend on the nature of the catalytic surface with which the O_2 molecule interacts. It has been assumed that the O_2 molecules interact directly with a bare noble-metal surface. By studying the nature of chemisorbed species on the surface of a metal catalyst as a function of the voltage on the anodic and cathodic sweeps, it is shown here that the O_2 reacts with a surface covered with oxide species extracted from the aqueous electrolyte and not from the O_2 molecules; the ORR is more active when the surface species are OH rather than O. Moreover, the strength of the chemical bond of the adsorbed species was shown to depend on the relative strengths of the metal-metal versus metal-oxide bonds. The Pt-Pt bonds are stronger than the Pd-Pd bonds, and the relative Pd-O bonds are stronger than the relative Pt-O bonds. As a result, the chemisorbed O species is stable to lower anodic potentials on Pd. CO oxidation to CO_2 occurs at a higher potential on Pd than on Pt, which is why Pd (not Pt) is tolerant to methanol. Experiments with alloys show the following: (1) methanol tolerance decreases with the increase of Pt in the Pd-Pt alloys with Pd_3Pt/C showing an initial tolerance that decreases with cycling; (2) OH is formed on Pt_3Co/C and core-shell Pt-Cu/C, which results in a higher activity and durability for the ORR on these catalysts; (3) a 300 ^oC

anneal is needed to stabilize the Pd_3Au/C catalyst that forms an O adsorbate; and (4) OH is formed on Pd_3Co/C and Pd_3CoNi/C. These studies provide a perspective on possible pathways of the ORR on oxide-coated noble-metal alloy catalysts.

Table of Contents

List of Tables

List of Figures

1. Introduction

A fuel cell is an electrochemical device that converts the chemical energy of a fuel into useful energy through reactions involving an oxidizing agent generating water as the by-product. Fuel cells hold the promise of green power when compared with other energy conversion devices. The fuel cells are primarily classified by the kind of ion-conducting electrolytes used, which in turn determines the kind of chemical reactions that occur in the fuel cell, the operating range of temperature, the type of fuel and the catalysts used. This classification guides the applications of the fuel cells. The major types of fuel cells are: the polymer electrolyte (or proton exchange) membrane fuel cell (PEFC), the direct methanol fuel cell (DMFC), the alkaline fuel cell (AFC), phosphoric acid fuel cell (PAFC), molten carbonate fuel cell (MCFC) and solid oxide fuel cell (SOFC). The features of the different types of fuel cells [1] are summarized in Figure 1.1.

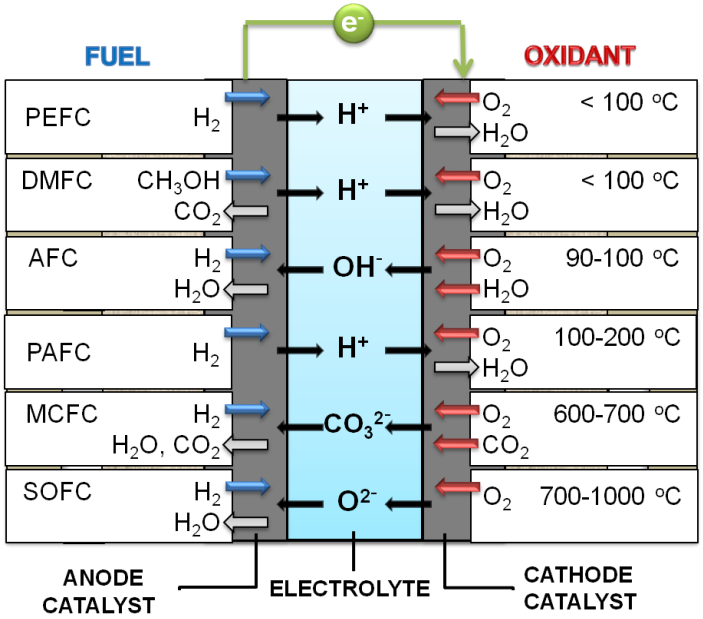

Figure 1.1: Features of the different types of fuel cells.

The types of fuel cells studied in this work are PEFCs and DMFCs, which are also called low-temperature fuel cells. Both the fuel cells use a polymer electrolyte membrane for ionic conduction.

1.1. POLYMER ELECTROLYTE FUEL CELLS (PEFCS)

A PEFC consists of anode and cathode catalysts of suitable material and a proton conducting membrane. It is a promising technology for automotive applications owing to its low emissions, low operating temperature, high power density, and short start-up time [2]. Figure 1.1 shows the schematic of a single cell PEFC. The thermodynamic cell potential for the overall cell reaction of the PEFC (Equation (1.1)) is 1.229 V vs RHE.

$$2H_2 + O_2 \leftrightarrow 2H_2O \tag{1.1}$$

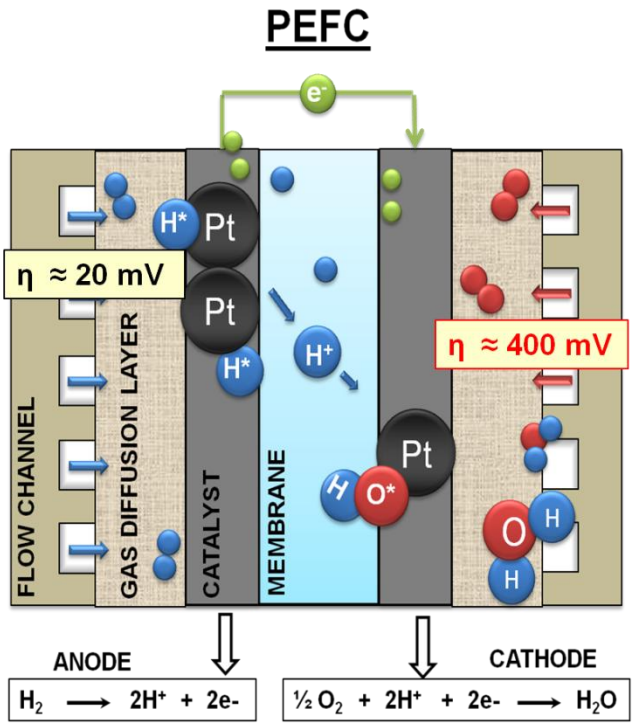

Figure 1.2: Schematic diagram of a typical PEFC showing the cross-sectional view, the approximate overpotential losses for a cell operating at 1 A cm^{-2} [3], and the reactions at the anode and the cathode.

Hydrogen is oxidized at the anode to form protons and electrons. The protons are transferred to the cathode via the proton-conducting aqueous electrolyte and Nafion membrane. Oxygen reacts with the protons and electrons from the external circuit to form water.

PEFCs are at present in the forefront of all types of fuel cells because of the multitude of research and development carried out in the field since its application in NASA's Gemini space flights as an auxiliary power source. This application was later stimulated into a worldwide renaissance for the transport application under the New Generation of Vehicles program, which was sponsored by the US government [3]. Presently, the US Department of Energy's (DOE) Office is developing and demonstrating the use of fuel cell power for transportation, stationary, and portable applications. The program is focused on PEFCs for vehicles and targets at least 5000 hours as a test for the durability with cycling [4].

The challenges in the commercialization of the PEFCs are performance, durability, and cost. Some of the scientific challenges to be solved for further advances in the technology of the fuel cells are the development of electrode catalysts with tolerance to carbon monoxide (DMFCs), finding cathode catalysts to reduce the performance losses, and finding a cost effective proton conducting membrane that is a vital component of the PEFC.

Platinum (Pt) has been used as the catalyst since the first prototypes of the PEFCs [5]. For a typical PEFC operating at current densities of 1 A cm^{-2}, the overpotential at the hydrogen electrode is about 20 mV and that at the oxygen electrode is approximately 400 mV. The part of the overpotential loss at the oxygen electrode at open circuit conditions contributes to lowering of the reversible potential of the PEFC, which is due to the low exchange current density (i_o) for the oxygen reduction reaction (ORR) (*c.a.* 10^{-9} A cm^{-2}

against 10^{-3} A cm^{-2} for the hydrogen oxidation reaction). The low i_o at the cathode causes competing anodic reactions such as oxide formation and oxidation of organic impurities, which results in a mixed potential of 1.00 V at the cathode catalyst [3]. The sluggish cathode reaction kinetics (Figure 1.2) for the ORR, which limits the efficiency and power density, constitutes the significant performance barrier and high cost. A typical polarization curve of a PEFC is shown in Figure 1.3. Also, in the PEFCs, the ORR occurs in the potential range wherein the surface of the catalyst is oxidized (Figure 1.3).

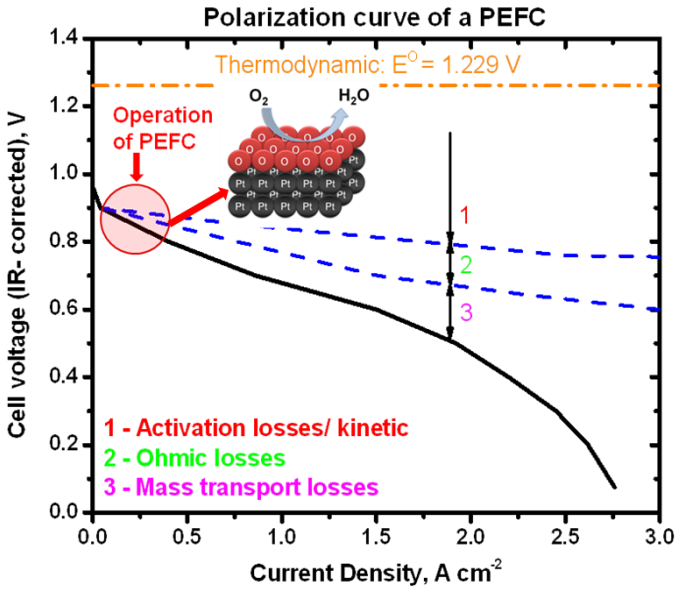

Figure 1.3: Polarization curve of single cell PEFC showing different polarization losses, and the region of operation of a typical PEFC which overlaps with the surface oxidation of the catalysts.

Researchers are seeking to improve the catalyst performance and reduce the cost of the precious metals in the fuel cells by lowering the Pt loading, reducing the size of the catalyst particles, thereby increasing the active area and the ORR activity, supporting Pt on inexpensive and electronically conductive supports such as carbon (C), and employing

new catalyst (non-Pt) materials. Bockris and coworkers [6] have shown that the ORR rates could be greatly enhanced by the use of alloy catalysts; it has also been reported from *ab-initio* studies [7] that while Pt is the best elemental catalyst for the ORR, alloying of Pt could improve the fuel-cell performance. Alloying of Pt with inexpensive metals reduces the amount of Pt per gram of the catalyst and lowers the cost.

Degradation behavior of the membrane-electrode-assembly (MEA) in a PEFC stack has been extensively studied under various operating conditions of the PEFC. Experiments using electron probe microanalyzer and X-ray fluorescence [8] have shown decay in the performance of the stack due to catalyst degradation and the presence of Pt in the membrane of the used PEFC [9]. The Pt catalyst gradually degrades upon potential cycling resulting in a lack of durability for reliable applications. The durability issues are due to various degradation mechanisms [10] as shown in Figure 1.4. The catalyst degradation is associated with a loss in the active area of the catalyst.

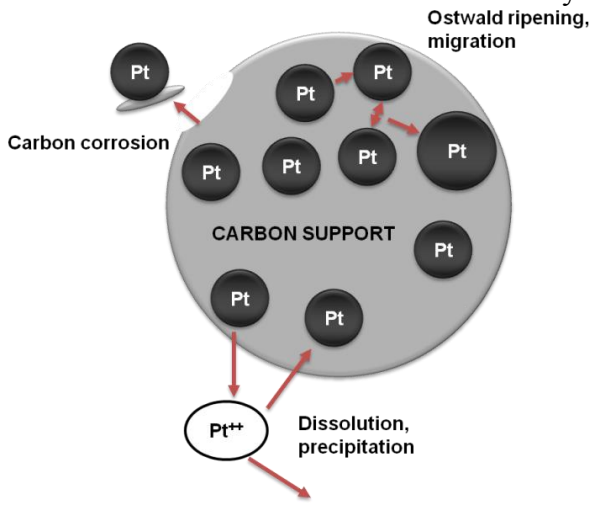

Figure 1.4: Different degradation mechanisms of the carbon-supported Pt cathode catalyst in a fuel cell.

1.2. DIRECT METHANOL FUEL CELLS (DMFCS)

DMFCs, which are a subset of PEFCs, operate on liquid methanol fuel instead of H_2 gas, which is an attractive fuel due to its high energy density. Figure 1.5 shows the schematic of a typical DMFC. The overall cell reaction of the DMFC is given by Equation (1.2) and the thermodynamic cell potential is 1.209 V vs RHE.

$$2CH_3OH + 3O_2 \rightarrow 2CO_2 + 4H_2O \quad (1.2)$$

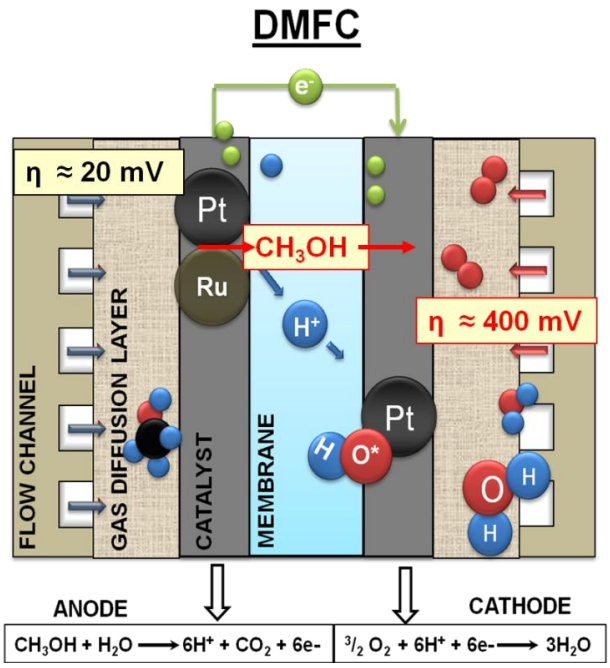

Figure 1.5: Schematic diagram of a typical DMFC showing the cross-sectional view, the approximate overpotential losses for a cell operating at 1 A cm^{-2} [3], the methanol crossover from anode to cathode, and the reactions at the anode and the cathode.

The working of a DMFC is similar to the PEFC except that methanol (CH_3OH) is oxidized at the anode to form protons, carbon dioxide, and electrons. The major limitation of the DMFCs, in addition to the sluggish ORR kinetics, is catalyst degradation, cost, and methanol crossover. Methanol from the anode is transported along

with protons and water through the polymer membrane to the cathode, thereby poisoning the cathode catalyst and decreasing the performance of a DMFC.

1.3. CATHODE CATALYSTS

An ideal cathode catalyst should facilitate fast reaction kinetics for the ORR with no overpotential losses. However, a typical fuel cell cathode catalyst exhibits sluggish ORR kinetics and high overpotential losses. The electrochemical reaction at the cathode catalyst, which is more complex than that at the anode, involves a four electron transfer reaction with multiple elementary steps involving the formation of chemisorbed intermediates. The overall cell potential and cell performance of a fuel cell are determined by the thermodynamics and reaction kinetics of the ORR at the cathode catalyst as discussed in Sections 1.1 and 1.2. The reaction rate of a heterogeneous catalytic reaction is determined by the metal-adsorbate bond strength, which is explained by the Sabatier principle [11, 12]. The surface of the catalyst is blocked when the intermediate binds too strongly with the metal catalyst and the reaction is limited by the dissociation of the intermediates/products. If the interaction is too weak, the intermediate will fail to chemisorb.

The targets for the practical application of room-temperature fuel cells include the reduction of the overpotential losses for the ORR, material cost, and catalyst degradation. Figure 1.6 shows the DOE target of a PEFC, the cathode catalysts, and the cost break-down of the individual components in a PEFC.

Figure 1.7 shows the possible reaction mechanisms of the ORR on a Pt catalyst reported in the literature [7, 14]. The four-electron pathway of reduction of oxygen to form water, shown by the red arrows, is the preferred reaction. The two-electron pathway involves the formation of hydrogen peroxide and results in the incomplete reduction of

oxygen. The formation of hydrogen peroxide formation competes with the ORR leading to a reduction in the cell potential.

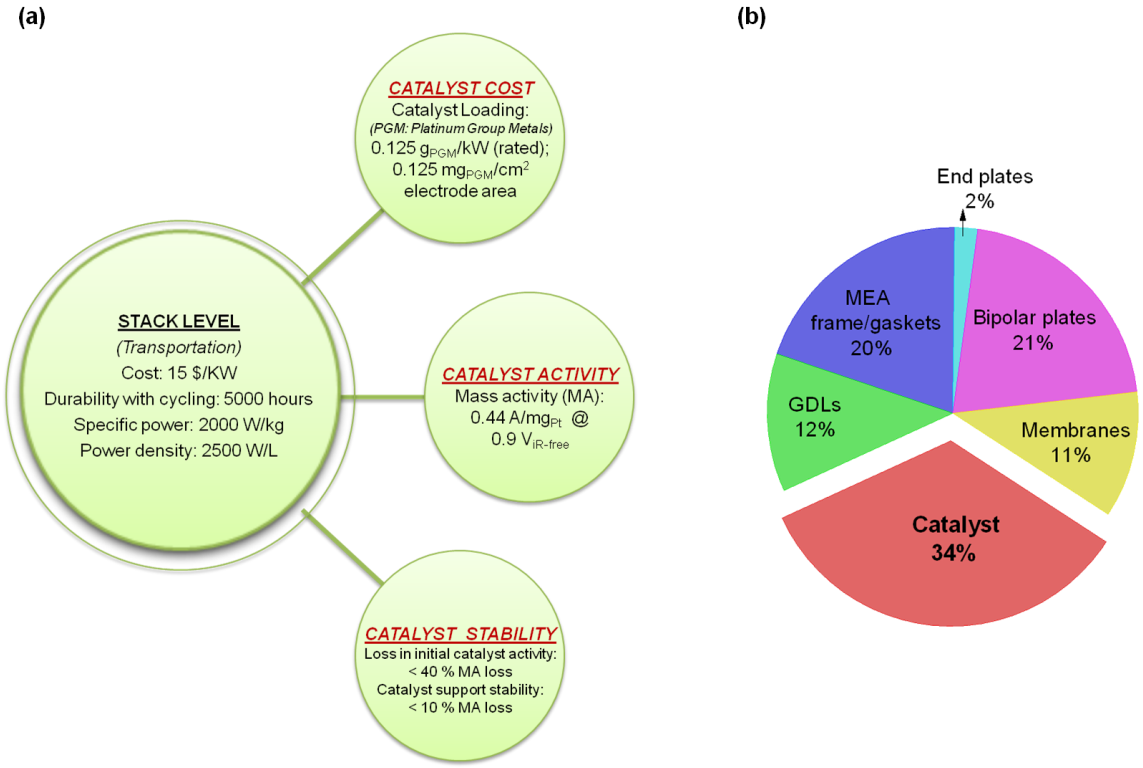

Figure 1.6: (a) Research goals (DOE target) of a PEFC and cathode catalyst (data taken from reference 4) and (b) the costs of the individual components in a fuel cell (data taken from reference 13).

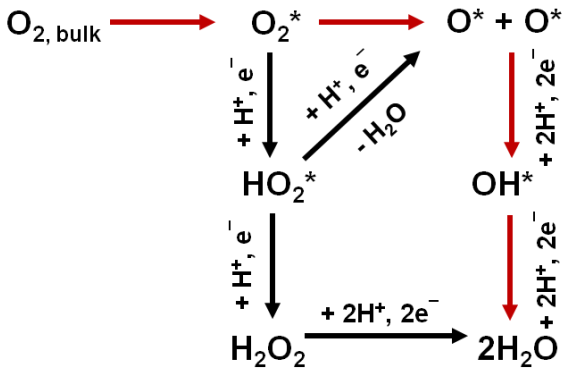

Figure 1.7: Suggested reaction mechanisms of the ORR on a Pt catalyst (* indicates an active surface site).

Considerable work has been carried out to improve the performance and the ORR activity of the catalysts. The recent developments include the use of Pt monolayer catalysts [15, 16], Pt-skin catalysts [17, 18], core-shell catalysts [19, 20], and Pt binary- and ternary-alloy catalysts [21]. Studies have been pursued to describe the influence of the variations in the electronic structure on the catalytic activity and durability. The work functions of selected transition metals are shown in Figure 1.8. Alloying metals with different atomic sizes and work functions modify the resultant properties of the alloy, which influence the catalytic property.

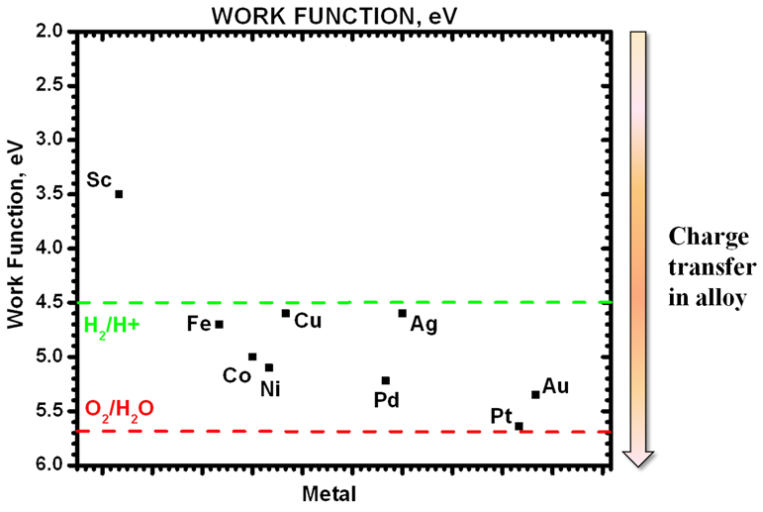

Figure 1.8: Work function of selected transition metals [22] and the redox levels of H^+/H_2 and H_2O/O_2 couples [23].

1.4. DESCRIPTION OF THE RESEARCH PROBLEM

In a typical use of the fuel cell, start-up and shut-down cycles, or starvation of hydrogen fuel during normal operation of the cell could result in a reversal of current flow and can raise the potential of the cathode interface to about 1.5 V vs RHE. It has been reported that these extreme operating conditions accelerate the degradation of the

fuel cell performance by increased carbon corrosion, accelerated Pt dissolution, and dissolution of the surface oxide [24]. It was reported in Section 1.1 that a mixed potential exists on the catalyst during the operation of a fuel cell resulting in the formation of surface oxides. It has also been reported that the presence of oxygen even in the lower potential regions form surface oxide up to a few layers, roughens the surface and results in the electrochemical dissolution of the surface oxides [25]. Moreover, it is reported that the oxide alters the behavior of the catalyst and affects the mechanism and kinetics of the ORR on the surface by imposing a barrier to charge transfer across the surface-oxide film [26, 27].

It has also been reported that most of the electrochemical reactions on noble metals proceed via the formation of adsorbed (chemisorbed) intermediates [28] and that the formation of an oxide film occurs at positive potentials. The electrochemical measurements on polycrystalline Pt have revealed the presence of multiple oxides on the Pt surface at different potentials [29-32]. Most electrochemical investigations suggest surface oxides such as Pt-O (PtO) and PtO_2 as stable, but the possibility of the presence of unstable adsorbates during the span of potential cycling that convert to stable phases and their origin has yet to be explored.

A typical current-potential voltammogram of Pt shows multiple peaks for the anodic formation of surface oxide and a single cathodic reduction peak of the oxide. This behavior has not been satisfactorily explained. There are two types of adsorbates; those that are weakly bound (physisorbed) and those that are strongly bound (chemisorbed). All adsorbates referred to in this dissertation are chemisorbed unless specifically mentioned as physisorbed.

The origin of adsorbed surface oxides on carbon-supported catalysts and their role in the ORR have yet to be explored experimentally. In particular, recent developments in

the improvement of the ORR activity and stability/durability on alloys of Pd and on alloys of Pt are not clearly understood. Moreover, since Pd is tolerant to methanol and Pt is not, there is a need to explore how and why the tolerance changes with the composition of the Pd-Pt alloys. Figure 1.9 shows the summary of the research problem.

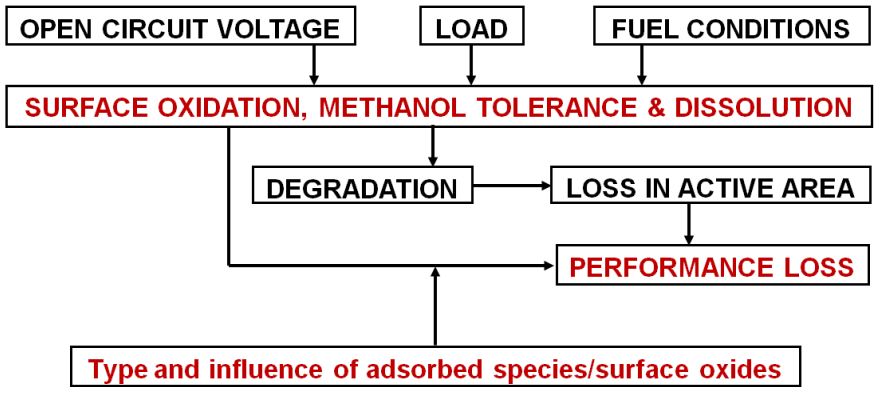

Figure 1.9: Summary of the research problem.

1.5. SCOPE AND OBJECTIVES

A PEFC converts the chemical energy of the hydrogen (H_2) - oxygen (O_2) reaction to electrical energy. The reactions are represented by,

At anode: $H_2 \leftrightarrow 2H^+ + 2e^-$; $E^o = 0.000$ V vs RHE (1.3a)

At cathode: $\frac{1}{2}O_2 + 2H^+ + 2e^- \leftrightarrow H_2O$; $E^o = 1.229$ V vs RHE (1.3b)

Overall reaction: $H_2 + \frac{1}{2}O_2 \leftrightarrow H_2O$; $E^o = 1.229$ V vs RHE (1.3c)

A DMFC converts the chemical energy of methanol (CH_3OH) and oxygen (O_2) to electrical energy via the formation of water and carbon dioxide. The reactions are represented by,

At anode: $CH_3OH + H_2O \leftrightarrow CO_2 + 6H^+ + 6e^-$; $E^o = -0.020$ V vs RHE (1.4a)

At cathode: $\frac{3}{2}O_2 + 6H^+ + 6e^- \leftrightarrow 3H_2O$; $E^o = 1.229$ V vs RHE (1.4b)

Overall reaction: $CH_3OH + \frac{3}{2}O_2 \leftrightarrow CO_2 + 2H_2O$; $E^o = 1.209$ V vs RHE (1.4c)

However, the actual cell potentials of both the PEFC and DMFC are lower than their respective thermodynamic potentials due to various polarization losses.

The ORR involves the reduction of an O_2 molecule. A question to be answered is whether the stable oxide intermediates on a Pt surface are the result of the reaction with the water of the electrolyte. If the latter is the case, do these surface oxides hinder the ORR kinetics or are they necessary precursors to the reduction of O_2? The latter question is not addressed, but which oxide adsorbate is associated with the ORR activity and where this adsorbate is stabilized needs to be explored. Fig 1.10 shows a schematic of the three-phase boundary of carbon-supported catalysts, electrolyte, and O_2 gas at which the ORR occurs on a Pt/C catalyst.

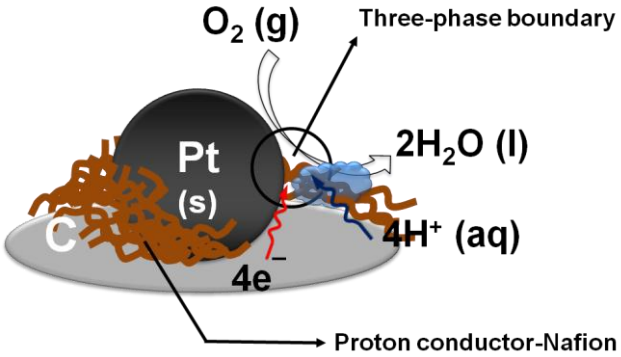

Figure 1.10: Schematic of a three-phase boundary on the cathode catalyst.

The strategy of this study is to analyze the surface of the cathode catalyst by evaluating the adsorbed species on the catalyst during surface oxidation in an aqueous electrolyte and to identify the stable species on the catalyst surface as a function of voltage. The analyses are carried out for the cathode catalyst with a three-electrode cell configuration. In order to reduce the lead time in the fuel cell stack testing and to obtain easily verifiable and reproducible benchmarks for the components, studies were carried out to characterize the catalysts independently to determine properties like

electrochemical surface area (ECSA), catalytic activity, and durability. *Ex situ* characterization of the catalysts as thin-films on rotating disk electrodes (RDE) or glassy carbon electrodes (GC) in liquid electrolytes are used to compare the different catalysts. The surface phenomena occurring on a catalyst are related to the changes across the electrode-electrolyte interface as shown in Figure 1.11. Electrochemical quartz crystal nanogravimtery (EQCN) is a technique to characterize the structure and composition of the interface, which allows the combination of measurements of electrochemical process and simultaneous mass changes. Studies using ECQN have revealed detailed mechanistic information about surface adsorption-desorption, nucleation, and growth of thin film, mass loss, and multilayer deposition [33].

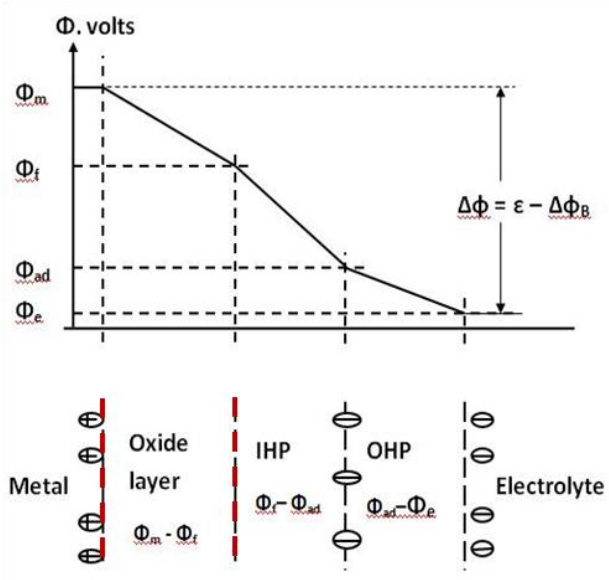

Figure 1.11: Schematic of the double-layer model of an electrode-electrolyte interface [34].

The objectives of the present study are:

- To analyze the nature and type of surface oxides (or adsorbed intermediates) formed on different catalyst surfaces as a function of the applied voltage and

to develop an understanding of the relation between the surface oxides, the catalytic activity, and durability. This study evaluates the species-specific oxides on the catalyst with an *in situ* technique used to measure the interfacial mass-changes at the electrode-electrolyte interface. The knowledge of the mechanism of surface oxidation on the catalysts and the role of these oxides in catalyst dissolution help to understand the generation of soluble species in the electrolyte of a fuel cell.

- To study the influence of non-adsorbing and adsorbing molecules on the surface oxidation. The non-adsorbing electrolyte (perchloric acid) mimics the non-adsorbing characteristics of the polymer electrolyte, and the adsorbing electrolyte (sulfuric acid) mimics the characteristics of the hydrophilic sulfonic acid functional groups of the polymer electrolyte
- To study the interfacial phenomena and to elucidate the actual mechanisms of oxide chemisorption on carbon-supported catalyst nanoparticles. Carbon-supported cathode catalyst nanoparticles are used in a fuel cell. These catalysts have high surface area and roughness, and the surface phenomena on the nanoparticles are different from that on a bulk polycrystalline material.
- To understand the effect of alloying metals with different elemental properties, *viz*., work functions, atomic sizes, and segregation energies, on the electronic modifications, the lattice structure and the metal-metal interaction in the alloys. This study determines the influence of the alloy properties on the type and amount of chemisorbed species during the surface oxidation.
- To synthesize different alloys with a combination of noble and base metals and to study the influence of the ligand effect (electronic modifications) and

alloy geometry, *viz*., compression vs expansion of the lattice, on the metal-metal interactions and the metal-adsorbate interactions.

- To analyze and compare the metal-metal bonding vs the metal-adsorbate bonding in order to understand the role of carbon monoxide (methanol oxidation intermediate), the strength of metal-oxide bonds, and the role of these oxides on the origin of methanol tolerance.

1.6. METHODOLOGY

A summary of the methodology followed in this work is given in Figure 1.12. In this work, we present the results on the surface phenomena of the different catalysts. The carbon-supported Pt-based catalysts were commercially purchased from suppliers of fuel cell grade catalysts. The carbon-supported Pd-based catalysts for this study were synthesized in-house by the easily scalable polyol reduction method. The structural and chemical characterizations of all the catalysts were carried out by Energy Dispersive X-ray Spectroscopy (EDS), Thermogravimetric Analysis (TGA), X-ray Diffraction (XRD), X-ray Photoelectron Spectroscopy (XPS), and Transmission Electron Microscopy (TEM). The electrochemical characterization of the catalysts was carried out by Cyclic Voltammetry (CV) and Electrochemical Quartz Crystal Nanogravimetry (EQCN). The performance of the catalysts was determined with Rotating Disk Electrode (RDE) and Rotating Ring Disk Electrode (RRDE) measurements. The methanol tolerance of the catalysts was determined by CO-stripping voltammetry. The durability of the catalysts was studied by accelerated degradation tests, EQCN, and Inductively Coupled Plasma–Mass Spectroscopy (ICP-MS).

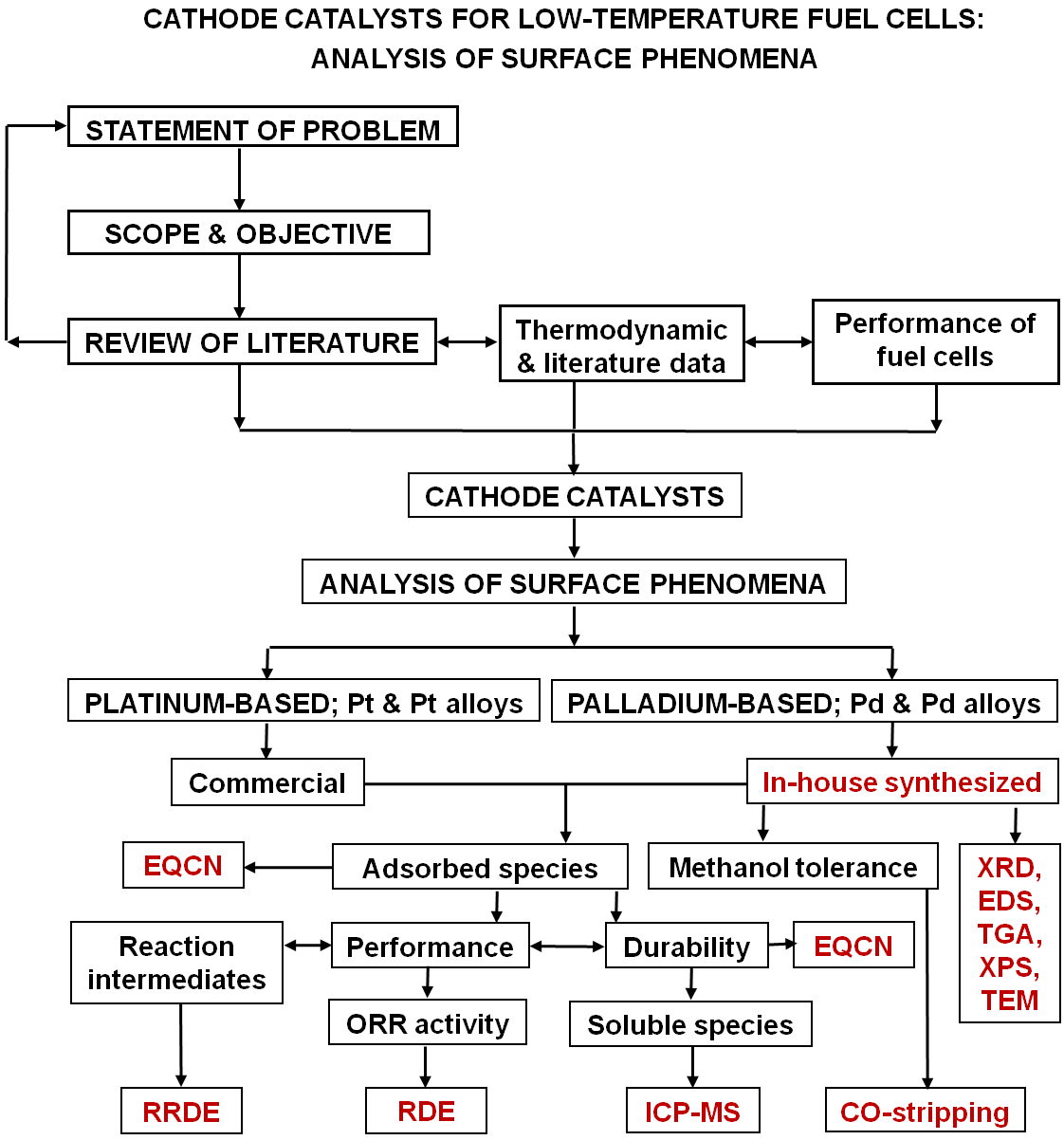

Figure 1.12: Summary of methodology.

2. Experimental techniques

ACS grade chemicals and reagents were used as received for the studies. This chapter details the various techniques used throughout the dissertation. Novel techniques and/or important variations will be discussed in the respective chapters. Carbon-supported catalysts with 40 % metal loading (weight basis) were used for the studies. The list of consumables, compressed gases, and equipments used are given in appendix A.

2.1. SYNTHESIS OF CARBON-SUPPORTED PALLADIUM-BASED CATALYSTS

The carbon-supported Pd-based catalysts were synthesized by the polyol method. The polyol method consists of reduction of the metal precursor compounds with liquid polyol, which acts as a reducing and dispersing medium. Ethylene glycol (EG) in alkaline medium was used for the polyol redox process. The voltammograms for the oxidation of EG and reduction of the Pd precursor salt in EG at a glassy carbon electrode (GC) in potassium nitrate (0.4 M KNO_3) as the supporting electrolyte are shown in Figure 2.1 (a and b). It is seen that the Pd is reduced before the EG, which makes the spontaneous reduction of the metal precursor salt unfavorable at room temperature. Addition of sodium hydroxide (NaOH) lowers the oxidation potential of EG, and increasing the concentration of NaOH enables complete oxidation of EG. Also, increasing the temperature oxidizes EG at lower potentials. Water was added to the dispersion, if required, as the azeotropic behavior of the polyol-water systems lowers the boiling point of EG and helps to complete the oxidation of EG. The metal precursor salt that can be reduced under these conditions acts as a seed for the reduction of the salts that are difficult to be reduced by this process, as shown in Figure 2.1 (d). The characteristics of the catalyst material can be modified by adjusting the parameters such as the polyol

medium, reaction temperature and time, pH of the solution, and nature of the precursor salt.

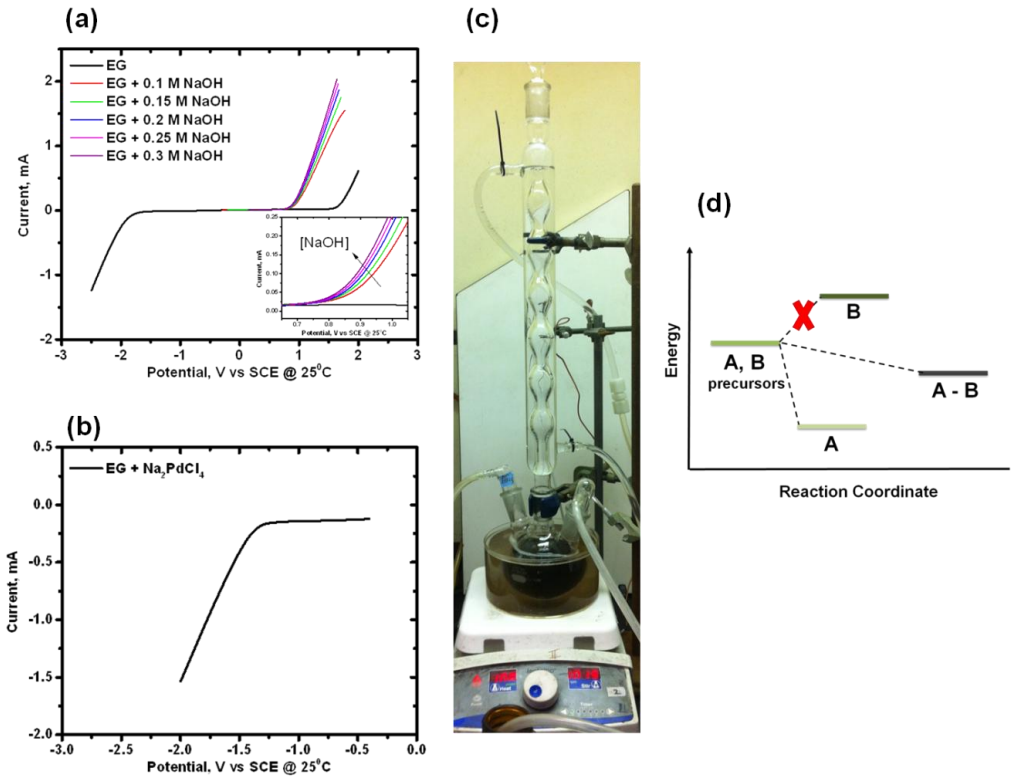

Figure 2.1: (a) Voltammogram of the oxidation of ethylene glycol with different concentrations of NaOH (inset: the enlarged view showing the trend of reduction potentials with increasing concentrations of NaOH), (b) voltammogram of Pd salt in ethylene glycol in 0.4 M KNO_3 solution on a glassy carbon electrode at 500 rpm (V vs SCE) at 25 ^{o}C and 50 mV s^{-1}, (c) synthesis of a catalyst under reflux conditions, and (d) reaction coordinate diagram.

The general method of synthesis involves dispersing the carbon support and the metal precursor salts in EG, heating the suspension to a given temperature in an oil bath and under an inert atmosphere (Argon or Nitrogen) with continuous stirring for a specified duration. The supported metal catalyst is then recovered, and the byproducts of the redox process are removed by washing and filtration or centrifugation. The dry

catalyst powder is further heat-treated in an alumina crucible in a tube furnace to the required temperature and time under a reducing atmosphere (10 % Hydrogen/90% Argon gas mixture).

The synthesis conditions and the procedures to obtain specific catalysts are described in the respective chapters. A typical setup is shown in Figure 2.1 (c).

2.2. STRUCTURAL AND CHEMICAL CHARACTERIZATION

2.2.1. X-Ray diffraction (XRD) measurement

The X-ray powder diffraction of the catalysts was carried out with a Philips Model-APD 3520 X-Ray diffractometer with Cu Kα radiation that uses a Philips PW-1830 generator. It is based on a Bragg-Brentano 2-theta/theta setup. In this arrangement the sample moves by an angle theta (θ) and the detector moves at an angle 2-theta (2θ). XRD is based on the scattering of X-rays by the periodic array of atoms in the catalyst material and the crystal structure is determined by Bragg's law. The tube was operated at a voltage of 40 kV and a current of 25 mA. Diffraction patterns were recorded with a fixed slit in the 2θ range of 30^o to 90^o with a stepwise scan rate of 0.03^o with a dwell time of 23 s at each step. The sample in a fine powder form is spread onto a glass slide with a non-volatile inert liquid such as amyl acetate to form a flat film and is allowed to dry. The glass slide with the dry film is inserted into the sample holder in the diffractometer with the clean part of the slide held under the clamp in the holder. All XRD profiles were analyzed with the JADE Plus software package, version 9.0.2. The patterns are fit with the pseudovoigt fit profile to include size broadening effects and the values were recorded for an R^2 (least square fitting residual) value lower than 10 % and a very low value of ESD (estimated standard deviation). From the Williamson-Hall analysis, the microstrain in the catalyst samples involving local lattice distortions was calculated. The

contribution from instrumental broadening was calculated from the diffraction pattern of the external standard (NIST alumina sample, PDF no. 00-046-1212) and was subtracted from diffraction patterns of the catalyst samples. The fraction of the solute (x_B) in the lattice was calculated by the relationship given below [35]:

$$x = \left[\frac{a_{alloy} - a_{A/C}}{a_{vegard,alloy} - a_{A/C}} \right] . x_B \qquad (2.1)$$

where a_{alloy} is the lattice parameter obtained from XRD, $a_{A/C}$ is the lattice parameter of the carbon-supported host metal (A/C), $a_{végard,alloy}$ is the lattice parameter calculated with Végard's law for a solid solution of the carbon-supported alloy (AB/C), and x_B is the nominal atomic fraction of the solute B in the alloy catalyst.

The schematic of XRD and the diffractometer setup are shown in Figure 2.2.

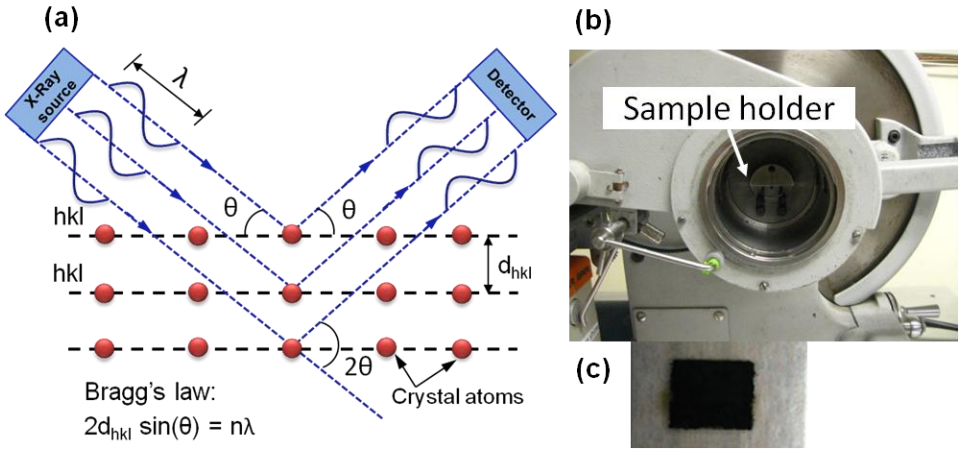

Figure 2.2: (a) Schematic diagram of XRD of a crystalline material, (b) X-ray diffractometer, and (c) sample on a glass slide.

2.2.2. Energy dispersive X-Ray spectroscopy (EDS) measurement

The bulk metal compositions of the catalyst materials were determined with a SEM-EDS (JEOL-JSM5610 scanning electron microscope) having an Oxford instruments energy-dispersive x-ray spectroscopy EDS attachment. In EDS, a high-

energy electron beam incident on the sample generates an electron-hole pair in the inner shell of an atom in the sample. The electron hole is filled by the transition of the outer

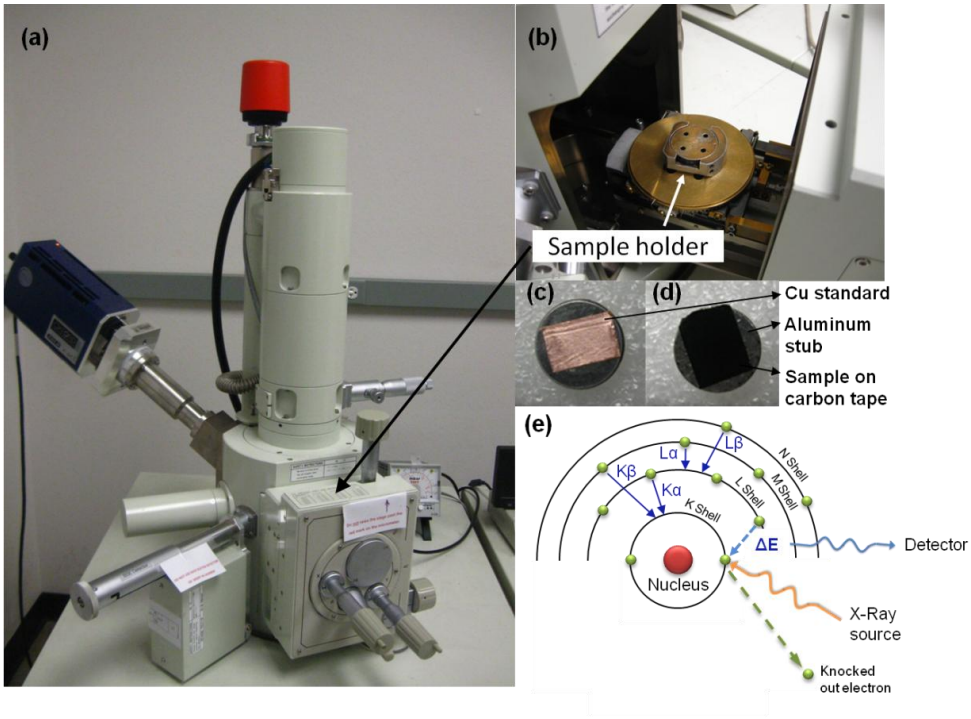

Figure 2.3: (a) SEM-EDS setup, (b) sample holder, (c) and (d) copper (Cu) standard, and sample (catalyst), respectively, and (e) schematic diagram illustrating the principle of Energy-dispersive X-ray spectroscopy (EDS).

shell electrons to the inner shell. This transition emits X-rays characteristic to a particular element in the sample. EDS was operated at an accelerating voltage of 20 kV, emission current of 80 μA, beam current of 20 μA, and a working distance of 20 mm. The device was calibrated with a pure copper (Cu) standard for a dead time of 40% before analyzing the unknown sample. The sample to be analyzed is spread onto a carbon tape attached to an aluminum stub. A flat sample is required. EDS scans for each sample were analyzed and averaged over a large range of different measurement sites on the sample. The EDS

setup and the schematic of EDS are shown in Figure 2.3. The alloy density (ρ_{alloy}) in g cm^{-3} was calculated to a good approximation by

$$\rho_{alloy} = \left[\frac{100}{\frac{w_A}{\rho_A} + \frac{w_B}{\rho_B}} \right] \tag{2.2}$$

where ρ_A and ρ_B are the density of the pure metals A and B respectively; w_A and w_B are the weight % of A and B in the alloy, respectively.

2.2.3. Thermogravimetric analysis (TGA)

The metal loading in the carbon-supported catalysts was analyzed by thermogravimetric analysis with a Perkin Elmer TGA analyzer, model 7. TGA involves the study of change in mass of the sample as a function of temperature. The catalyst sample was taken in a Pt crucible and TGA was carried out by heating the sample from room temperature to 600 ^{o}C in air with a heating rate of 2 or 5 ^{o}C min^{-1} and a cooling rate of 5 or 20 ^{o}C min^{-1}. At 600 ^{o}C, carbon is oxidized to carbon dioxide in air. The remains of the noble metals and the oxides of the less noble metal are characterized by XRD to identify the different phases of the metals. The weight loss from TGA and the identification of the metals in the remains of TGA are used to calculate the accurate metal loading of the carbon-supported catalysts. The setup and the sample TGA curve are shown in Figure 2.4.

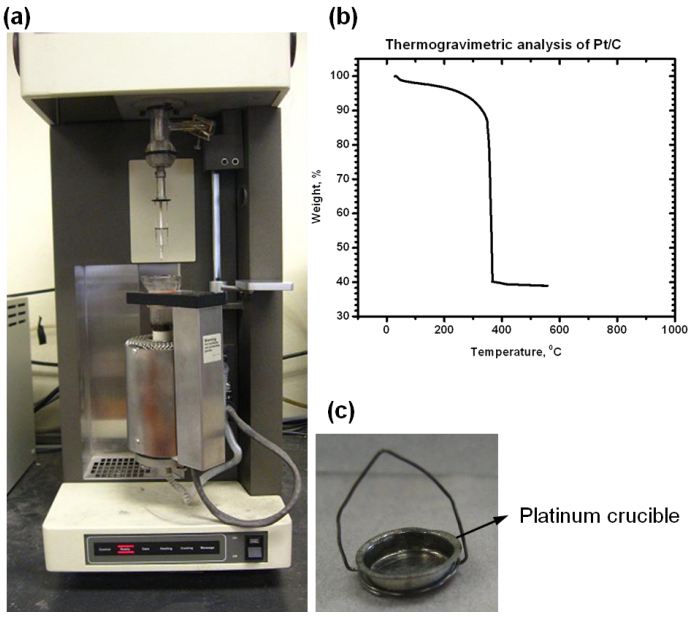

Figure 2.4: (a) Thermogravimetric analyzer (Perkin Elmer TGA 7), (b) a typical thermogravimetric profile (e.g., 40 wt.% Pt/Vulcan XC 72R), and (c) platinum (Pt) crucible.

2.2.4. Transmission electron microscopy (TEM) measurement

The morphology and the particle size distribution of the catalyst materials were determined with a JEOL 2010F TEM operating at 200 keV by using a 400 square mesh (400 lines $inch^{-1}$) Ni/Cu grids with a carbon film on one side. In TEM, a high-energy electron beam is transmitted through an ultra-thin sample to produce high-resolution images. The catalyst sample was wetted with water and dispersed in isopropyl alcohol to form a dilute homogeneous suspension. The ink was drop cast onto the grid and allowed to dry. The film was cast onto the carbon film side of the grid for nanoparticle suspensions. The analysis of the TEM image to determine the particle size distribution was carried out with the ImageJ software (NIH) and the standard deviation of more than 70 particles is measured. The TEM setup and the details are shown in Figure 2.5.

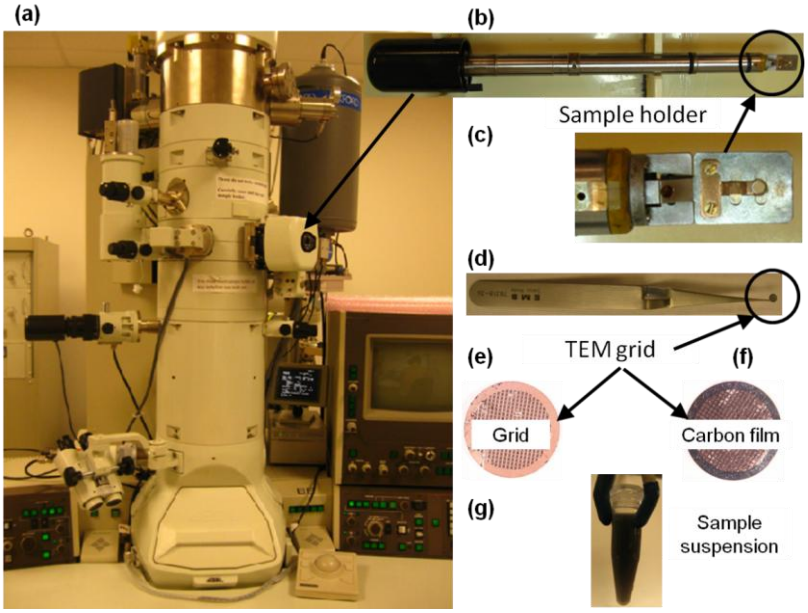

Figure 2.5: (a) Transmission electron microscope (TEM) setup, (b) and (c) sample holder, (d) – (f) TEM grid, and (g) sample suspension.

2.2.5. Inductively coupled plasma (ICP) spectroscopy measurement

The composition of the catalysts was also determined with ICP (Agilent 7500 ce Quadrupole ICP-MS & Varian 715-ES ICP-OES) measurements. ICP-MS & ICP-OES are techniques used for detection of trace amount of metals. In this measurement, inductively coupled plasma is used to produce excited atoms and ions that emit electromagnetic radiation at wavelengths characteristic of a particular element. In ICP-MS, the spectra are analyzed based on their mass-to-charge ratio and in ICP-OES the intensity of emission spectra is measured. The detection limit of ICP-MS is parts-per-trillion (ppt) and that of ICP-OES is parts-per-billion (ppb). Dilute solutions of samples digested in an acid matrix were analyzed. Measurements were made against calibration standards of each element and a blank solution of the acid matrix.

2.2.6. X-ray photoelectron spectroscopy (XPS) measurement

The near-surface composition (~ 10 nm penetration depth) and the chemical states of different metals on the surface of the catalysts were determined with XPS (Kratos Analytical Spectrometer) measurements with monochromatic Al Kα radiation. All XPS spectra were analyzed with the CasaXPS, Casa Software. All spectra were fitted with Gaussian-Lorentzian functions and a Shirley-type background. The spectra were recorded with no charge compensation since survey scans carried out with and without charge compensation showed no shift in the energy scale. The core-level binding energy (BE) change of the alloy compared to the BE of pure metals can be used to understand the degree of alloying. Constraints are essential for accurate representation of the data. Constraints were introduced for peak position, peak intensity ratio, and full width at half-maximum (FWHM) of the doublet pairs in the spectra. The chemical state of the material is obtained from the peak position of the binding energy, which requires accurate calibration of the energy scale. The C 1s peak in the XPS spectra of the carbon-supported catalysts was used as the internal standard to calibrate the energy scale of the respective catalyst. The measured peak position was calibrated against the true value of the peak at 284.5 eV [36]. The peak positions of the doublet pair were constrained by the known values of the elemental binding energies. The elemental quantification was obtained from the peak intensities (peak area). The peak with the largest peak area and no interferences was chosen for the elemental quantification. The model to fit the spectra should be properly correlated for accuracy of the peak area calculation. The relative sensitivity factors (R.S.F) was adjusted accordingly if only one peak of the doublet pair was considered for elemental quantification The relative intensities of the doublet pair peaks are linked by the quantum numbers and appear in the ratio $2j_1+1:2j_2+1$, where j ($j = 1 \pm ½$) is the quantum number due to spin-orbit coupling in the final state of the material. The

relative intensities for the d-orbital doublet peaks were constrained in the ratio 2:3 whereas that of the f-orbital doublet peaks was constrained in the ratio 3:4.

2.3. ELECTROCHEMICAL CHARACTERIZATION

The electrochemical characterization was predominantly carried out with the cyclic voltammetry (CV) technique, shown in Figure 2.6, unless otherwise specified. All the electrochemical measurements were carried out in a three-electrode configuration. Pt wire and a Hydrogen electrode (HydroFlex, Gaskatel GmbH Inc.) were used as the counter (CE) and reference electrodes (RE), respectively. The working electrode (WE) varied depending upon the type of experiment and is specified in the appropriate sections. A 0.5 M H_2SO_4 or a 0.1 M $HClO_4$ solution, as required for the measurements, was used as the electrolyte. The solution was deaerated for 20-30 minutes prior to the start of the experiment, and a continuous purging of the electrolyte was carried out with a stream of inert gas (ultrapure dry nitrogen (N_2) or Argon (Ar)) during the experiment. Use of other gases for the particular measurements is specified in the respective sections. The working electrode was immersed in the electrolyte under potential hold (0.05 V for Pt-based electrodes, 0.4 V for Pd-electrodes) and was cycled several times between E_L and E_H (E_L: 0.05 V and E_H: 1.2 V for Pt-based electrodes, E_L: 0.4 V and E_H: 1.24 V for Pd-based electrodes) in order to produce a clean electrode surface. The electrode surface was considered clean when the cyclic voltammogram becomes invariant with time. The conditioning protocol is varied with the catalyst material. All studies were carried out at room temperature. All potential values are reported against the reversible hydrogen electrode (RHE).

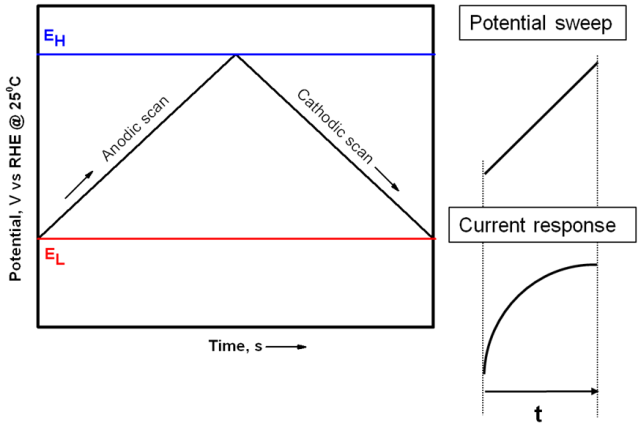

Figure 2.6: Cyclic potential sweep and resulting current response for a potential sweep in cyclic voltammetry (CV).

2.3.1. Preparation of catalyst ink and thin-film electrode

The catalyst inks were prepared by mixing a known amount of the catalyst powder in 5 wt. % Nafion solution and 2-propanol-water mixture. The ink mixture for carbon-supported catalyst was ultrasonicated at room temperature in a bath sonicator to obtain a homogeneous dispersion. The ink mixture for unsupported Pt black catalyst was sonicated with a wand sonicator. Care is taken to avoid the heating of the ink mixture during sonication by adding ice cubes to the bath sonicator or controlling the duration of wand immersion in the ink mixture. 8 - 12 µL of the homogeneous dispersed ink was drop-cast onto a clean and dry glassy-carbon electrode, and the film was dried in air. For *in situ* mass-change studies, 60 µL (sensor geometric area: 1.37 cm^2), and 8 µL (sensor geometric area: 0.196 cm^2) of the ink were drop-cast onto the gold-coated quartz crystal sensors. The method of ink preparation was the same for all the catalyst materials being studied. The Nafion content in the dry catalyst film was maintained at 20–22 wt.%, similar to the content in the membrane electrode assembly used for single-cell testing.

The glassy-carbon electrode, which was used as the substrate for the working electrode, was polished to a mirror finish with a 0.05 µm alumina suspension (Buehler)

on a Microcloth, washed, and rinsed thoroughly in ultrapure water prior to the electrochemical measurements and film casting. An electrode with a rough surface is first polished with 1 μm and 0.3 μm alumina suspensions sequentially on a Nylon polishing pad before polishing with the 0.05 μm alumina suspension.

2.3.2. Rotating (ring) disk electrode (R(R)DE) setup

The electrochemical measurements were conducted in a three-compartment cell with the RDE/RRDE electrode setup (Figure 2.7) and a potentiostat and rotation control (modulated speed rotator, PINE instruments Inc.). Glassy-carbon disk electrodes (PINE instruments Inc., RDE: 5 mm disk diameter; thin gap RRDE: 5.61 mm disk diameter, 7.92 mm ring (Pt) outer-diameter, 320 μm ring-disk gap, 37% collection efficiency) were used as the substrates for the working electrode.

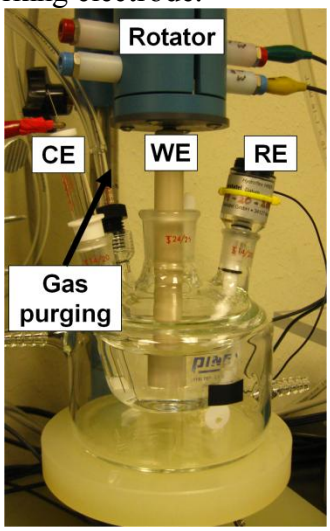

Figure 2.7: R(R)DE setup.

The R(R)DE measurement technique involves forced convection of the reactants and the products, which maintains the concentration of all species close to the electrode surface uniform and equal to the bulk values. Hence, the system reaches steady state

quickly, enabling high precision measurements. In the R(R)DE system, the rotating electrode drags the solution at the surface along with it. With the electrode surface as the frame of reference, the solution that is dragged with the rotating electrode appears nearly stagnant and is called the hydrodynamic boundary layer, δ_H. This layer is assumed to be a laminar boundary layer (or infinite lamina) for the solution of the fluid flow equations (Levich equations) for the R(R)DE system [37]. The infinite lamina offers a uniformly accessible surface. For accurate measurements under infinite lamina, all boundary surfaces are effectively at an infinite distance from the electrode. The boundaries include liquid/air boundary, walls of the electrochemical cell, counter and reference electrodes, and gas feed. The hydrodynamic measurements also require that there be no flow edge or gravitational effects, *i.e.*, the flow in the upper half of the system shall not interfere with the flow in lower half. These effects were minimized in this work by maintaining the distance from the tip of the rotating electrode to the base of the cell, y, at 10 mm, and by using a solution volume of 100 mL. It is also important to maintain a thin film of the catalyst on the GC electrode to minimize the mass transfer and kinetic effects within the film. The kinetics of the reactions on the R(R)DE electrodes are dependent on the hydrodynamic and the diffusion layers, which are a function of the rotation speed of the electrode. The details are given in Figure 2.8.

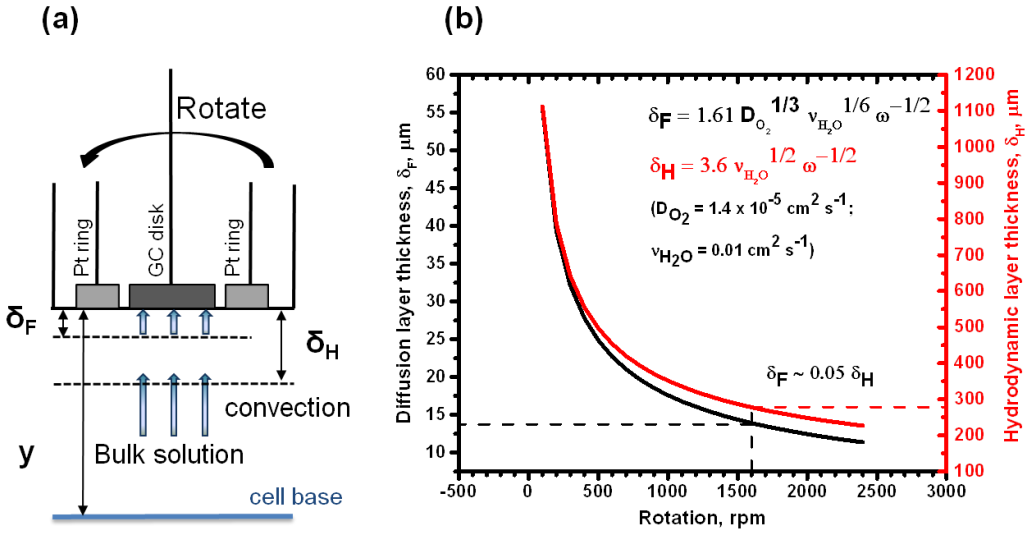

(c)

Type of system	*Transients to reach I_{ss} (1%) @ 1600 rpm*
RDE	108 ms
RRDE	24.85 ms *(r_2/r_1 = 1.114; gap: 320 μm)*

Figure 2.8: (a) Schematic of the flow conditions in a R(R)DE system, (b) diffusion layer and hydrodynamic layer as a function of rotation speed in 0.5 M H_2SO_4 (values of the constants are taken from reference 38), and (c) steady state responses in the R(R)DE system.

2.3.3. Electrochemical quartz crystal nanobalance (EQCN) measurement setup

The *in situ* mass measurements were performed with a quartz crystal analyzer (Maxtek RQCM, INFICON Inc.) and a potentiostat (CHI760C, CH Instruments Inc.) interfaced through a personal computer with the RQCM software. The mass resolution of the equipment is less than 0.4 ng cm^{-2}. The analyzer has a phase-lock oscillator (PLO) circuit that provides high measurement stability over a wide frequency range. A flow cell (Figure 2.9 (a)) or a batch cell (Figure 2.9 (b)) was used for the measurements as required for the specific experiment. In the flow cell (ALS Inc.), the cell of chamber volume ~ <

0.1 mL was connected to the electrolyte reservoir through a gear pump that controls the flow of the electrolyte into the chamber at a pre-determined rate, in this case at ~ 50 μL/s, giving a residence time of 2 s. It is important that there be no pulsations in the flow of the electrolyte through the chamber for accurate mass measurements. An EQCN sensor with a geometric area of 0.196 ± 0.003 cm^2 and a resonant fundamental frequency of 7.995 MHz in air was used as the substrate for the working electrode in the flow cell. The batch cell consists of a CHK-100 Kynar crystal holder (INFICON Inc.) that is immersed into the electrolyte solution (volume: ~ 150 mL). A 5 MHz sensor with an exposed geometric area (front) of 1.37 cm^2 and thickness of 333 μm was used as the working electrode. The details of the EQCN measurement technique are shown in Figure 2.9.

The EQCN sensor consists of a thin quartz crystal sandwiched between two metal electrodes. A sensor coated with gold (Au) on titanium (Ti) underlayer on either side of the quartz crystal was used for electrochemical measurements. An alternating electric field was applied between the metals across the crystal that causes the crystal to vibrate at its resonant frequency (converse piezoelectric effect). Any mass attached to the exposed area of the EQCN sensor changes the vibration frequency of the sensor, and this change is measured. A typical CV and EQCN response of a Pt electrode is shown in Figure 2.10. A standard AT-cut gold-coated quartz crystal oscillator is used for the measurements as it has negligible temperature coefficient at the desired operating temperature. Optically polished sensors (mirror finish) were used for the measurements as high surface roughness can cause large apparent mass loadings resulting in inaccurate results. Any error in the frequency measurements, which is a function of the oscillator and the crystal, is minimized by electrode capacitance cancellation. The capacitance cancellation adjustment was performed with the crystal in the actual solution used for electrochemical measurements. Over or under compensation of capacitance can introduce errors during

the electrochemical measurements. Capacitance cancellation is essential for accurate mass measurements of soft films. For accurate measurements of the EQCN response of the catalyst particles, it is essential to understand the factors affecting the data and the limitations on the use of catalyst nanoparticles for the experiments.

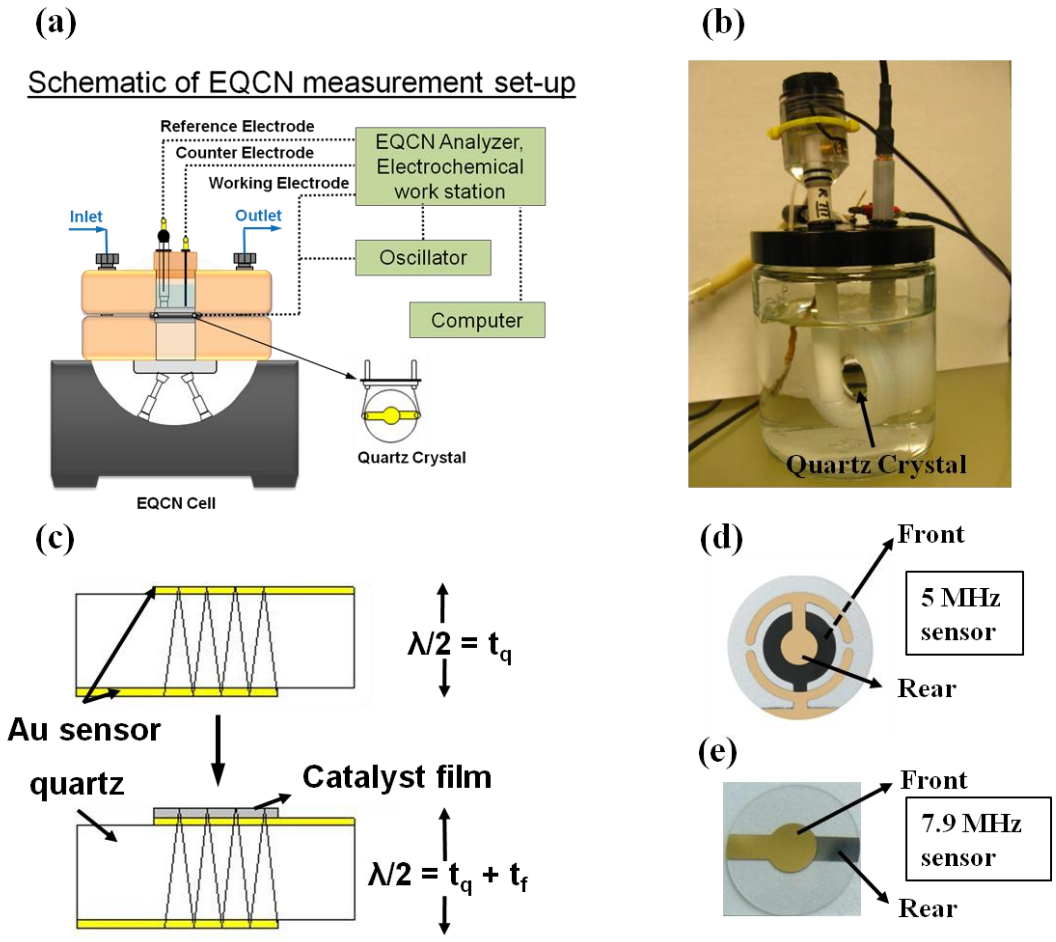

Figure 2.9: (a) EQCN flow cell, (b) EQCN batch cell, (c) working principle of EQCN sensor, and (d) and (e) EQCN sensors.

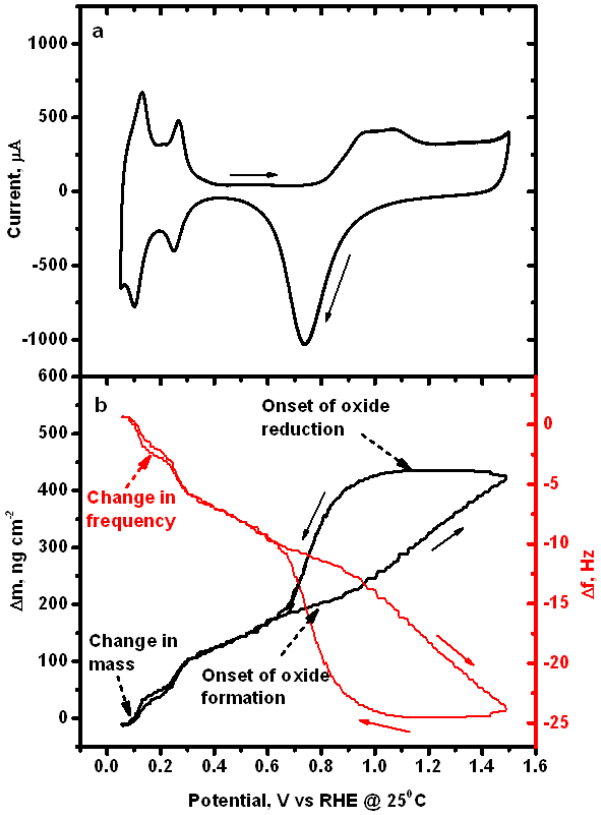

Figure 2.10: (a) CV and (b) associated EQCN mass and frequency response of a Pt quartz crystal electrode in 0.5 M H_2SO_4 at 50 mV s^{-1} and 25 ^oC.

2.3.3.1. Factors affecting EQCN response

A catalyst-loaded EQCN sensor is shown in Figure 2.11a. Some of the factors affecting the EQCN response are the weight of water molecules along with the adsorbate species on the catalyst surfaces, swelling of the ionomer in the presence of the electrolyte, mass change associated with electrosorption, mass change due to electrochemical dissolution, mass changes due to specific adsorption of ions and adsorption of water molecules, changes in properties of solution in the interphase, stress in the metal lattice during adsorption/absorption and oxide formation, and changes in roughness factor. As the viscous loading effect of the electrolyte is negligible for a rigid film on the EQCN sensor and as only the relative values of the change in frequency are measured, the mass-

response data used in the study is not affected by these factors. Any changes observed are reported in the respective chapters. In this work, the film drop-cast onto the gold-coated quartz crystal electrode was close to a rigid film and data from consistent results are reported. Moreover, owing to competitive water electrolysis on the electrode surface, the formation of bubbles is a source of interference. The presence of a bubble would cause a decrease in the mass as the liquid is displaced. In this work, these effects are minimized by the use of a large exposed area and solution volume (batch cell) or a flowing electrolyte that assists in bubble detachment (flow cell); this minimization is generally corroborated by the uniform results obtained in both CV and EQCN data.

2.3.3.2. Establishing the use of EQCN measurement with catalyst loaded sensor

The different forces acting on the loaded sensor are shown in Figure 2.11b. The catalyst film of nanoparticles with Nafion as the binder can form a soft film on the sensor. Liquid can be trapped inside the porous matrix. Also, the liquid layer adjacent to the sensor can dampen the sensor oscillation. The soft film dampens the sensor's oscillations. The damping (energy dissipation) reveals the nature of the film and the liquid adjacent to the sensor. The Maxwell model and Voigt model (Figure 2.11c) were used, respectively, to measure the frequency and the dissipation change for the sensor with the electrolyte and with a soft film (viscoelastic film) with a Q-sense E1, QCM-D electrochemistry module. The change in frequency and the dissipation energy at different harmonics (Figure 2.11d) of sensor oscillations were measured for both the bare Au sensor and a sensor loaded with unsupported Pt (Pt black) in 0.5 M H_2SO_4. Models were used to fit the data. From the measurements, it was seen that the viscosity of the electrolyte film (η_f) adjacent to the sensor was comparable to the viscosity of the bulk electrolyte ($\eta_f \leq \eta$). The thin-film effect was negligible. The effect of swelling and liquid

in the pores were negligible as calculated from the thickness of the catalyst film in the solution.

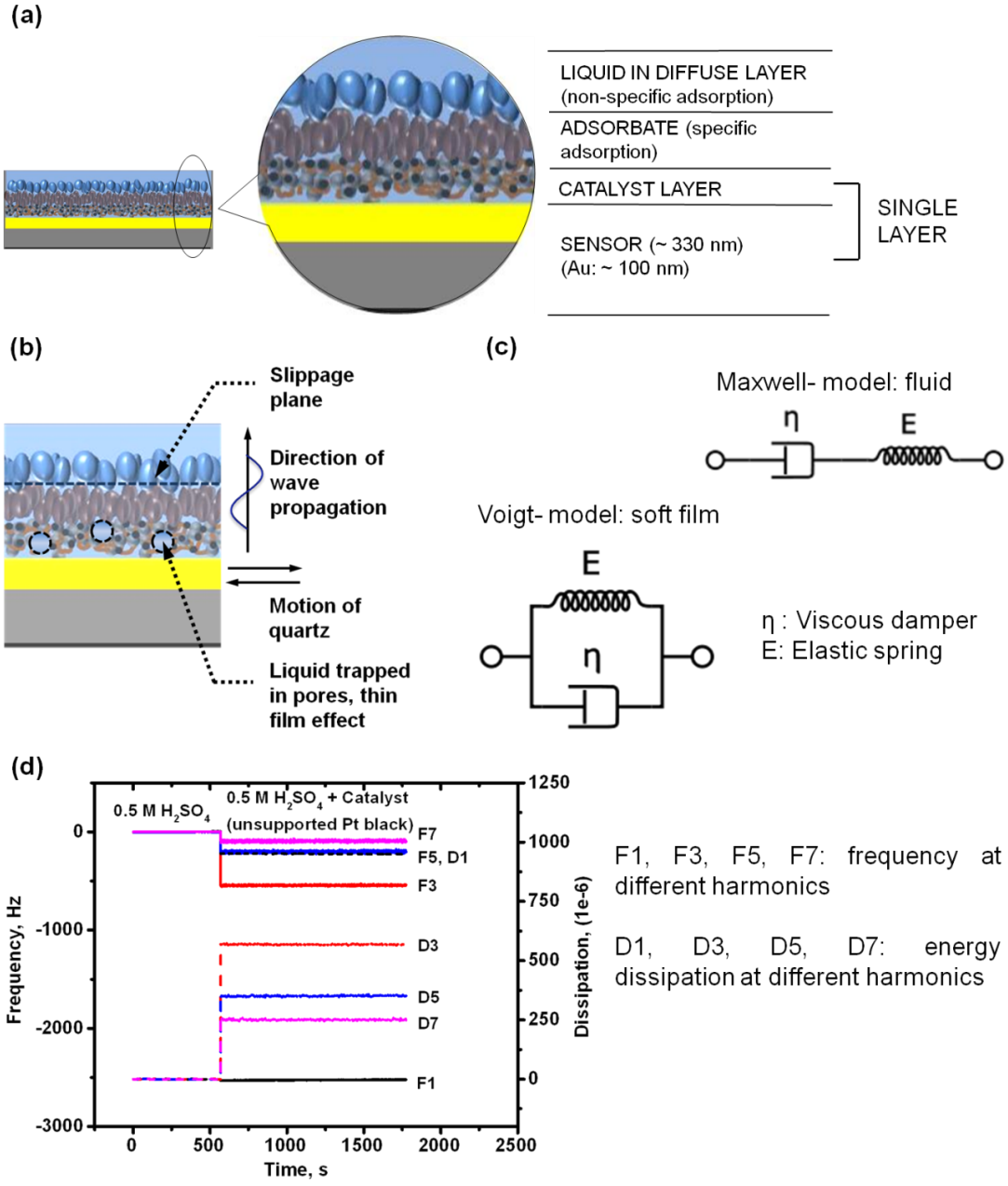

Figure 2.11: (a) Catalyst-loaded EQCN sensor, (b) the different forces acting on the loaded sensor, (c) model used for measuring the fluid properties adjacent to the sensor, and (d) combined frequency (F) and energy dissipation (D) of the bare Au sensor and sensor loaded with unsupported Pt in 0.5 M H_2SO_4.

2.3.4. Interfacial mass change

The change in the interfacial mass (Δm) was calculated from the change of the vibrational frequency (Δf) of the resonator by using the Sauerbrey equation for a rigid model ($\Delta f = -C_f.\Delta m$) [33] and the theoretical value of the calibration constant ($\Delta f = -C_f.\Delta m$), Equation (2.3) as

$$\Delta f = -\frac{2 f_o^2 \Delta m}{nA\sqrt{\mu_q \rho_q}} \tag{2.3}$$

where f_o is the resonant frequency of the quartz resonator, n is the number of harmonics (here, n = 1), A is the piezoelectrically active area, μ_q is the effective piezoelectrically stiffened shear modulus ($\mu_q = 2.947 \times 10^{11}$ g cm^{-1} s^{-2}), and ρ_q is the density of quartz (ρ_q = 2.648 g cm^{-3}).

The amount of the adsorbed intermediate (M) in the oxide region is obtained from the change in mass (Δm) and the faradaic charge (Δq) by using the combination of Faraday's Law and the mass change, Equation (2.4) as

$$M = \frac{\delta \Delta m.n.F}{\Delta q} \tag{2.4}$$

where $\delta\Delta m$ is the interfacial mass change between the potential limits under consideration (the potential limits considered in this work are between the onset of surface oxidation and upper potential, E_H), n is the number of electrons involved in the Faradaic reaction, F is the Faraday constant, Δq is the charge associated with the mass change. The different possible surface oxygenated species (adsorbed) are given in the appendix, Table A.4.

As different carbon-supported catalysts were compared to ascertain their relative performance, the theoretical value of the calibration constant is considered in the calculations. It has been reported that the theoretical value is similar to the measured

value in most cases [39]. The mass changes reported are based on the geometric area (ng (or μg) cm^{-2}_{geo}) of the sensor unless otherwise mentioned.

2.3.5. Measurement of electrochemical active surface area (ECSA) by H_{UPD} method

The maximum electrochemical surface area of Pt ($ECSA_{Pt}$, cm^2) was calculated from the hydrogen adsorption/desorption (H_{ads}/H_{desorp}) charge (H_{UPD}) by assuming the charge for a monolayer of hydrogen (H) coverage to be 210 μC cm^{-2}. The charge for the monolayer was calculated by assuming an equal distribution of the three low-index planes on Pt [40]. It is also assumed that only a monolayer of hydrogen is adsorbed on the Pt surface in a 1:1 ratio [41] and that a constant double-layer charge/discharge extends into the H_{UPD} region. The surface area measurements were carried out based on H_{ads} and H_{desorp}; no significant difference was observed in the values. In this work, the $ECSA_{Pt}$

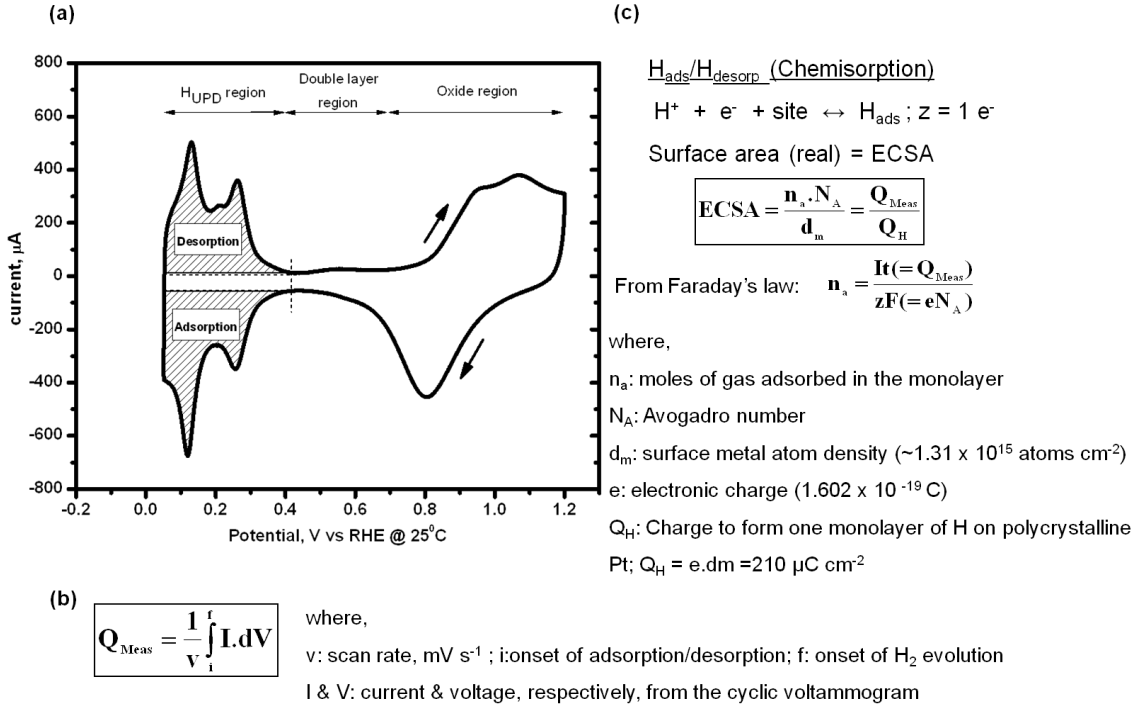

Figure 2.12: (a) CV of unsupported Pt black in 0.5 M H_2SO_4 at 50 mV s^{-1}, (b) determination of charge, and (c) determination of the real surface area of the catalyst.

from H_{desorp} is considered. The double-layer charge is subtracted from the total charge for desorption of the monolayer of hydrogen to obtain the actual $ECSA_{Pt}$. The details are shown in Figure 2.12.

2.3.6. Carbon monoxide (CO) stripping voltammetry

CO stripping voltammetry is a technique used to characterize a fuel-cell catalyst. The onset of CO desorption, peak potential, and shape of the CO desorption voltammogram are a function of the surface of the catalyst. In this method, CO is adsorbed onto the electrode surface in a CO-saturated electrolyte under a potential hold for a specified duration. During this process, only a monolayer is adsorbed on the catalyst surface. The electrolyte is then purged with inert gas (N_2 or Ar) to ensure complete removal of CO from the solution. The catalyst surface adsorbed with CO is subjected to CV to remove completely the adsorbed CO from the surface, and the absence of the CO stripping peak in the subsequent CV cycles confirms the complete desorption of the CO. The CO stripping area corresponds to the ECSA (cm^2) of the catalyst. It has been reported that CO adsorption under a lower hold potential favors end-on adsorption [42] for which the charge for a monolayer coverage is assumed to be 420 $\mu C\ cm^{-2}$. The details are given in Figure 2.13. Experiments were carried out to determine the optimum adsorption time, potential hold, and upper potential for the catalysts. The optimum values for Pt-based and Pd-based catalysts are given in Figures 2.14 and 2.15, respectively. The peak potential of CO stripping voltammetry is a measure of the binding strength of CO to the catalyst surface and an indicator of the performance of the catalyst in the presence of methanol.

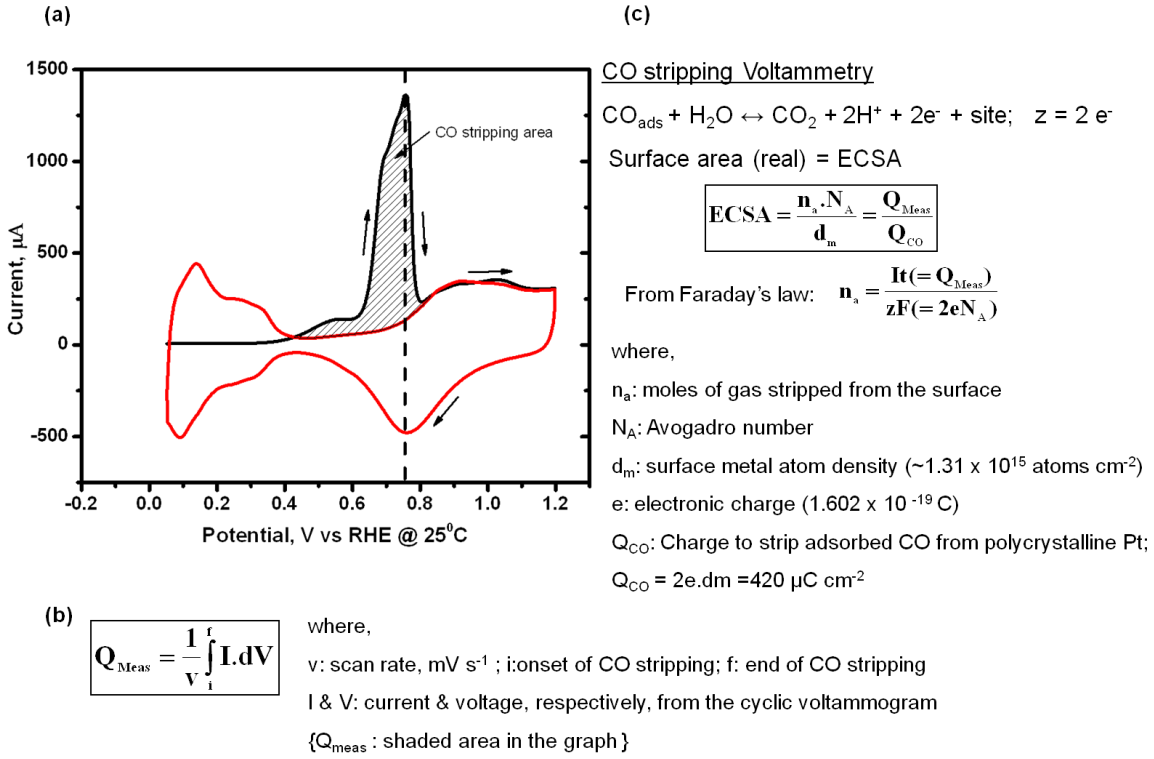

Figure 2.13: (a) CV of unsupported Pt black (black and red lines represent, respectively, with and without CO adsorbed layer) in 0.1 M $HClO_4$ at 50 mV s^{-1}, (b) determination of charge, and (c) determination of the real surface area of the catalyst.

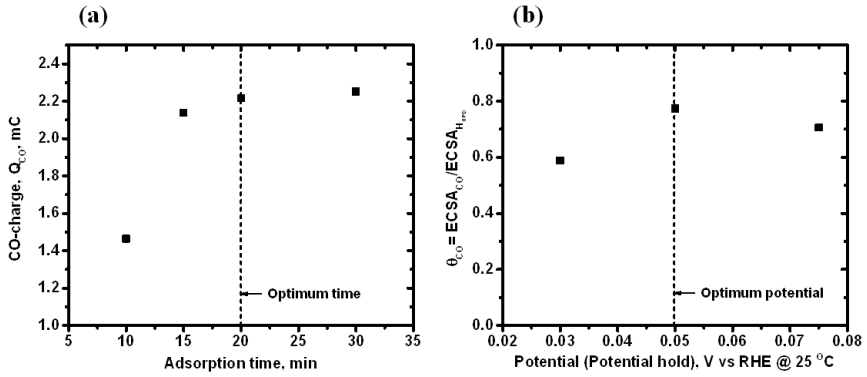

Figure 2.14: (a) Optimum time for CO adsorption at 0.05 V vs RHE at 25 °C and (b) optimum potential hold at 20 minutes of CO adsorption in 0.1 M $HClO_4$ at 50 mV s^{-1} (unsupported Pt black).

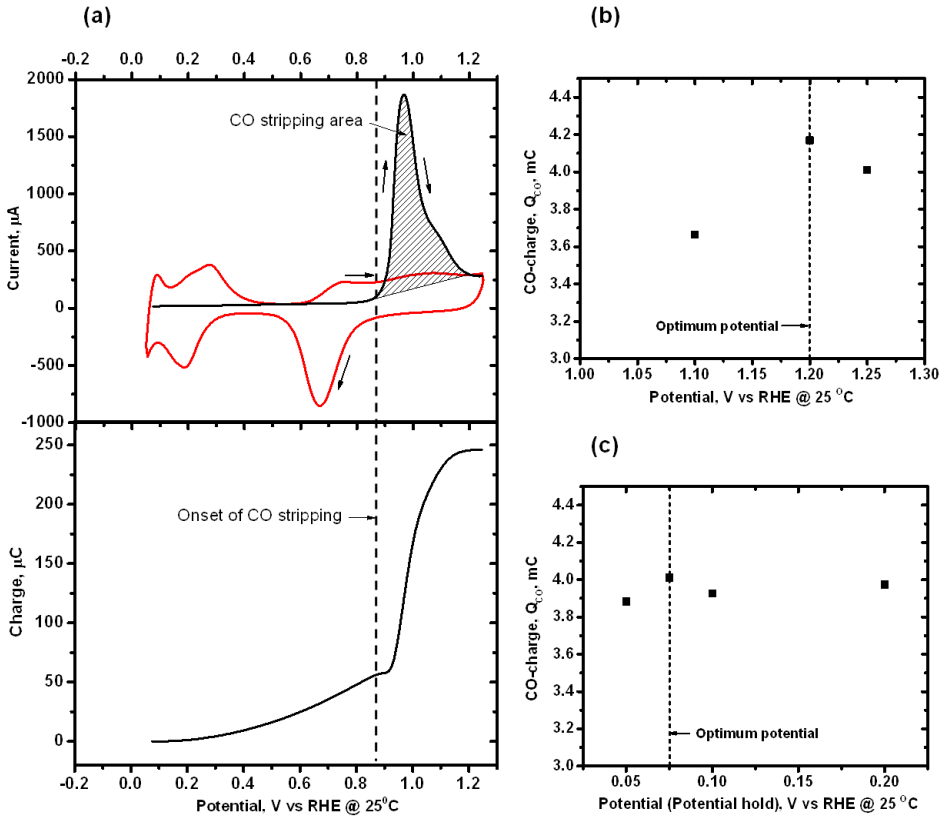

Figure 2.15: (a) CV of 40 wt.% Pd/C (black and red lines represent, respectively, with and without CO adsorbed layer), (b) optimum upper potential for complete CO desorption at a potential hold of 0.075 V vs RHE at 25 ^{o}C, and (c) optimum potential hold at 20 minutes of CO adsorption in 0.1 M $HClO_4$ at 50 mV s^{-1} (40 wt.% Pd/C).

2.3.7. Activity measurement for oxygen reduction reaction (ORR)

ORR activity measurements were conducted by linear sweep voltammetry (LSV) and the RDE setup. All LSV experiments were carried out at a scan rate of 10 or 20 mV s^{-1} and a rotating speed of 1600 rpm in oxygen (O_2) saturated solution. The scan details are given in the respective chapters. Background correction of the disk current was carried out by scanning the electrode with the ORR scan program in a N_2 or Ar -saturated solution. The details are shown in Figure 2.16. The quality of the catalyst film on the

electrode strongly influences the ORR curve. For a good coating, the experimentally determined limiting current is similar to the theoretical value given by Equation (2.5),

$$j_{lim} = 0.62nD^{2/3}\omega^{1/2}\nu^{-1/6}C_{O_2}^{b} \quad (2.5)$$

where j_{lim} is the limiting current density, n is the number of electrons involved in the ORR reaction, D is the diffusivity of oxygen in the specific electrolyte (for 0.5 M H_2SO_4: D = 1.4 x 10^{-5} cm^2 s^{-1}, [38]), ω is the rotation speed, υ is the kinematic viscosity of the electrolyte (for 0.5 M H_2SO_4 : υ = 0.01 cm^2 s^{-1}, [38]), and is the concentration of oxygen in the electrolyte (for 0.5 M H_2SO_4 : = 1.1 x 10^{-6} mol cm^{-3}, [38]). By assuming a negligible film effect on the ORR kinetics, the kinetic current normalized with geometric area in cm^2 is given by Equation (2.6) as

$$\frac{1}{j} = \frac{1}{j_k} + \frac{1}{j_{lim}} \quad (2.6)$$

where j is the measured current density, j_k is the kinetic-limited current density, and j_{lim} is the diffusion-limited current density. The measured current is dependent upon the loading of the catalyst. For a low catalyst loading, the distance between the adjacent catalyst agglomerates increases, which decreases the true surface area of the catalyst resulting in a decrease in the limiting current. An optimum catalyst loading is essential to obtain the required ORR current with insignificant O_2 diffusion effects through the film. Experiments were carried out with different catalyst loadings to obtain the optimum value for the various catalysts studied. In this work, the optimum catalyst loading has been used for the R(R)DE measurements. Typical data for the optimum loading is shown in Figure 2.17. ORR activity is reported as a normalized value. Normalization is based either on the catalyst loading (mass activity) or electrochemical surface area (specific activity).

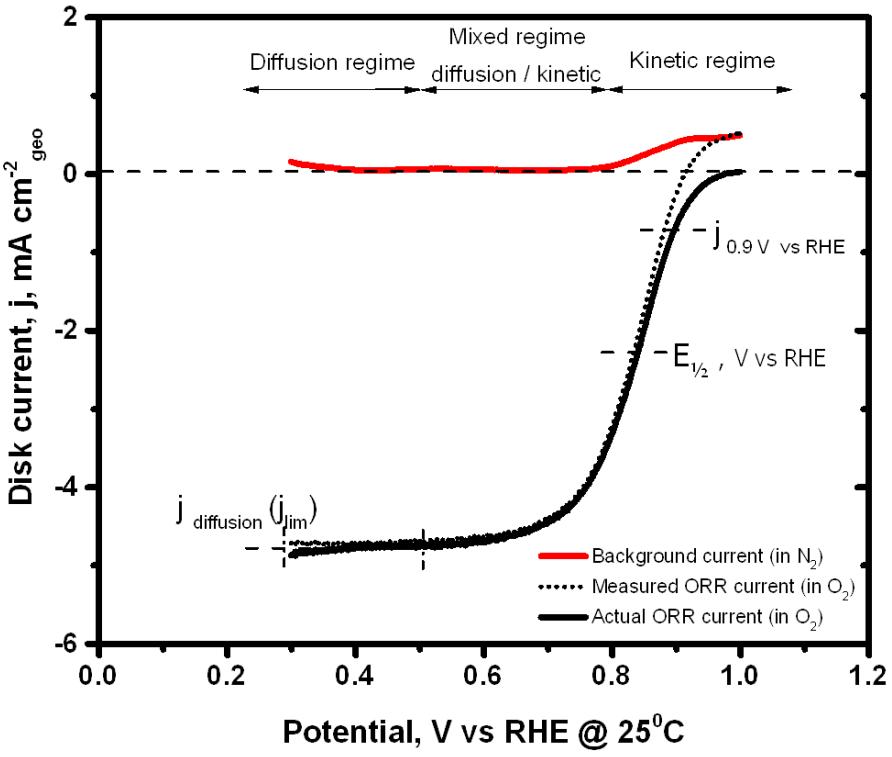

Figure 2.16: Analysis of LSV (LSV of unsupported Pt black from 0.3 to 1.0 V vs RHE at 25 °C and 10 mV s^{-1} at 1600 rpm in O_2-saturated 0.5 M H_2SO_4).

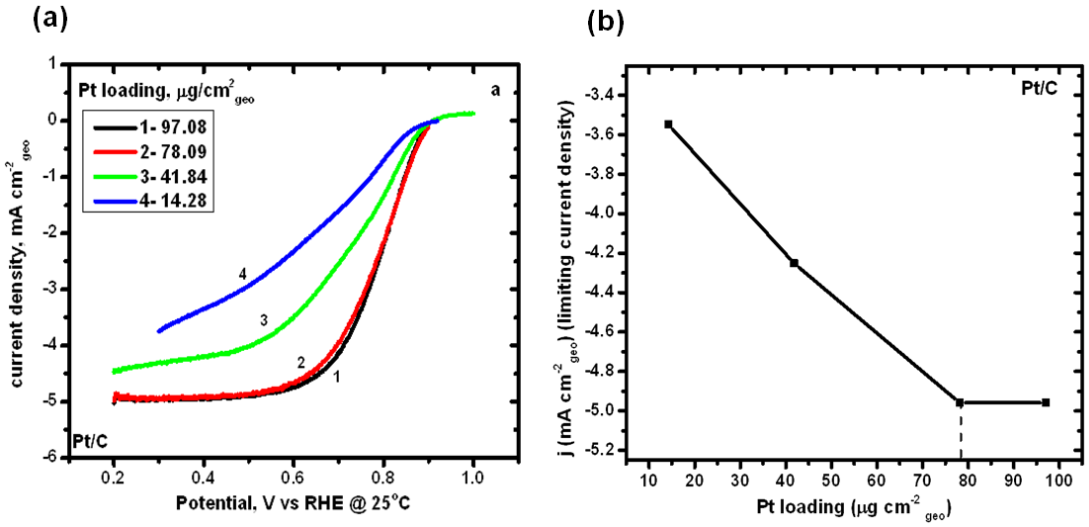

Figure 2.17: (a) ORR polarization curves for different catalyst loadings (e.g., 40 wt.% Pt/C from 0.2 to 1.0 V vs RHE at 25 °C and 20 mV s^{-1} at 1600 rpm in O_2-saturated 0.5 M H_2SO_4), and (b) specific activity as a function of Pt loading.

2.3.8. Determination of hydrogen peroxide (H_2O_2) intermediates

Experiments were carried out to estimate the amount of H_2O_2 intermediates and to compare them with the amount of surface oxide. The efficiency for the collection-generation experiments for each of the catalysts coated onto the glassy carbon electrode substrate was evaluated. The generation-collection (RRDE) experiments were carried out with the RRDE electrode with a Pt ring. The empirical collection efficiency of the electrode was measured in 1 mM $K_3Fe(CN)_6$ in 0.1M $NaNO_3$. The disk was scanned from 0.8 to 0.02 V at 10 mV s^{-1} while the ring was held at a constant potential of 0.8 V. The details are shown in Figures 2.18 and 2.19. The diffusion-limiting disk and ring currents are considered, both being read at the same potential. The experimental determination of the efficiency (N) takes into account the effect of catalyst thickness, catalyst loading, and active-site density; this experiment gives an accurate measure of the selectivity of the ORR on the catalyst being studied. The selectivity and the amount of H_2O_2 are adjusted with the experimental value of N for each catalyst. Once the experimental value of N has been determined, it can be treated as a property of that particular RRDE even if the RRDE is used to study a different half-reaction in a different solution. In the RRDE experiments, O_2 is reduced to H_2O and H_2O_2 at the disk and H_2O_2 is collected at the ring. The reduction of O_2 at the disk can occur through different steps as given by Equations (2.7)-(2.9):

$$O_2 + 4H^+ + 4e^- \leftrightarrow 2H_2O\,; \quad E^O = 1.229\ V_{RHE} \tag{2.7}$$

$$O_2 + 2H^+ + 2e^- \leftrightarrow H_2O_2\,; \quad E^O = 0.695\ V_{RHE} \tag{2.8}$$

$$H_2O_2 + 2H^+ + 2e^- \leftrightarrow 2H_2O; \quad E^O = 1.763\ V_{RHE} \tag{2.9}$$

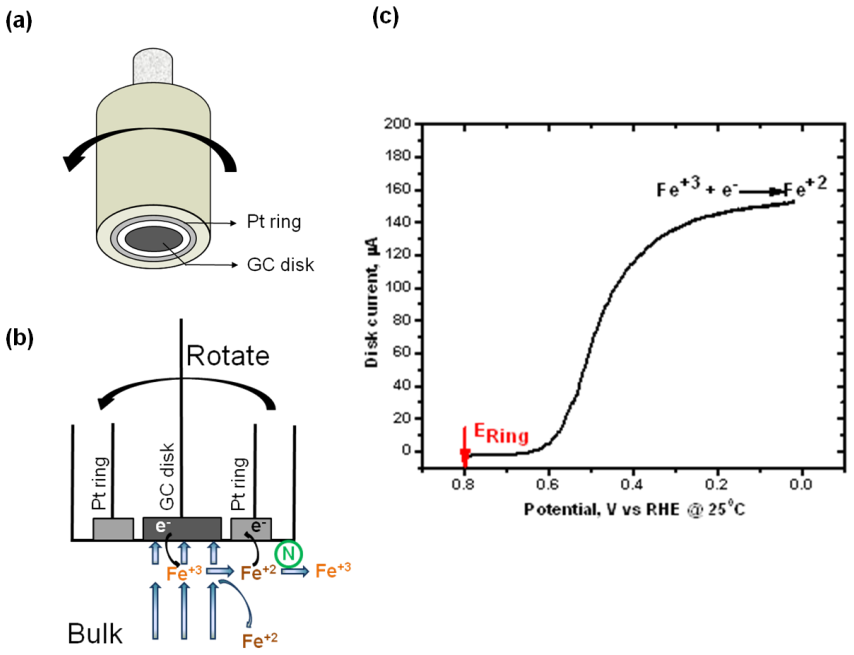

Figure 2.18: (a) RRDE electrode, (b) schematic of generation-collection of the redox species, and (c) potential scan of the redox couple (Fe^{+3}/Fe^{+2}) in 1 mM $K_3Fe(CN)_6$ - 0.1 M $NaNO_3$ solution with disk electrode scanned from 0.8 to 0.02 V vs RHE at 25 ^{o}C and 10 mV s^{-1}, and ring electrode held at 0.8 V vs RHE.

The cathodic limiting current at the disk is a measure of the amount of H_2O_2 generated at the disk, and the anodic limiting current is the amount of H_2O_2 collected at the ring. The amount of H_2O_2 is calculated with Equation (2.10). The disk is scanned at 10 mV s^{-1} while the ring is held at the potential at which the oxidation of H_2O_2 is diffusion-limited. The potential details are given in the specific chapters. The selectivity of the catalyst is given by Equation (2.11).

$$x_{H_2O_2} = \frac{\frac{2I_{Ring}}{N}}{I_{Disk} + \frac{I_{Ring}}{N}} \tag{2.10}$$

$$N_e = \frac{4I_{Disk}}{I_{Disk} + \frac{I_{Ring}}{N}} \tag{2.11}$$

Background corrections of the measured currents were carried out as mentioned in Section 2.3.7.

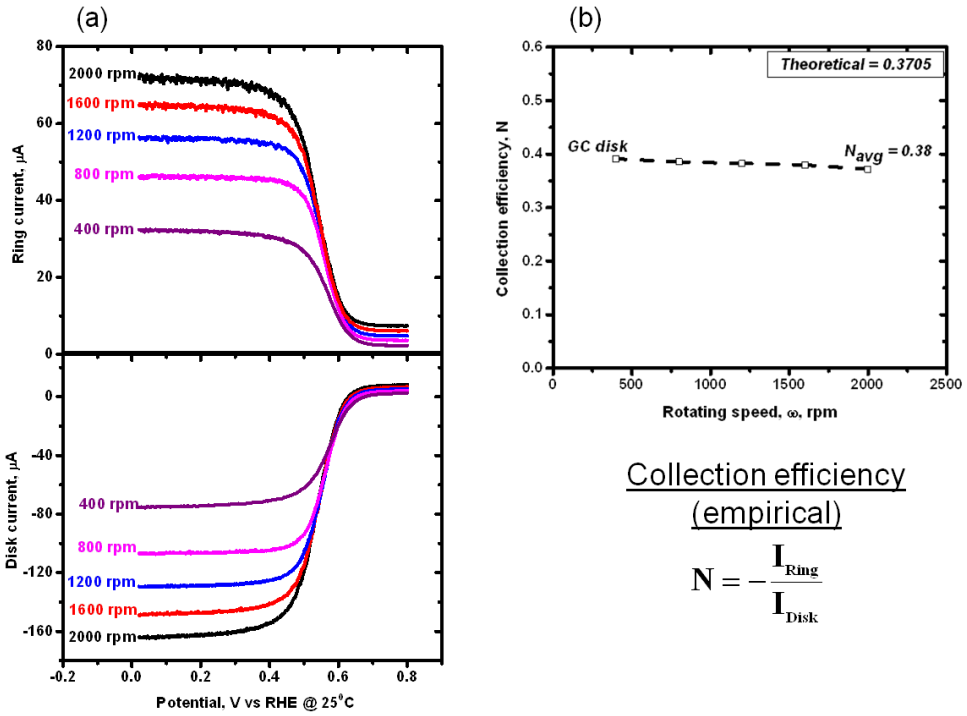

Figure 2.19: (a) Ring and disk currents for the determination of collection efficiency of a GC disk electrode with Pt ring in 1 mM $K_3Fe(CN)_6$ in 0.1M $NaNO_3$ soltuion with disk electrode scanned from 0.8 to 0.02 V vs RHE at 25 ^oC and 10 mV s^{-1}, and ring electrode held at 0.8 V vs RHE, and (b) collection efficiency (N-empirical and N-theoretical) of the GC disk electrode.

2.3.9. Electrochemical durability measurement

Accelerated degradation tests were carried out to simulate long-term behavior of the catalysts and to analyze the extent of dissolution under different operating conditions of fuel cells. The catalysts were cycled to different upper potentials and also as a function

of the number of potential cycles. The testing protocol is shown in Figure 2.20. Fresh electrolyte was used for each dissolution experiment. The specific testing conditions for different catalysts are mentioned in the respective chapters. It has been reported that cycling in the oxide formation-reduction region leads to higher dissolution rates [43]. This study also helps to understand the influence of the surface oxide on the dissolution rates as a function of potential.

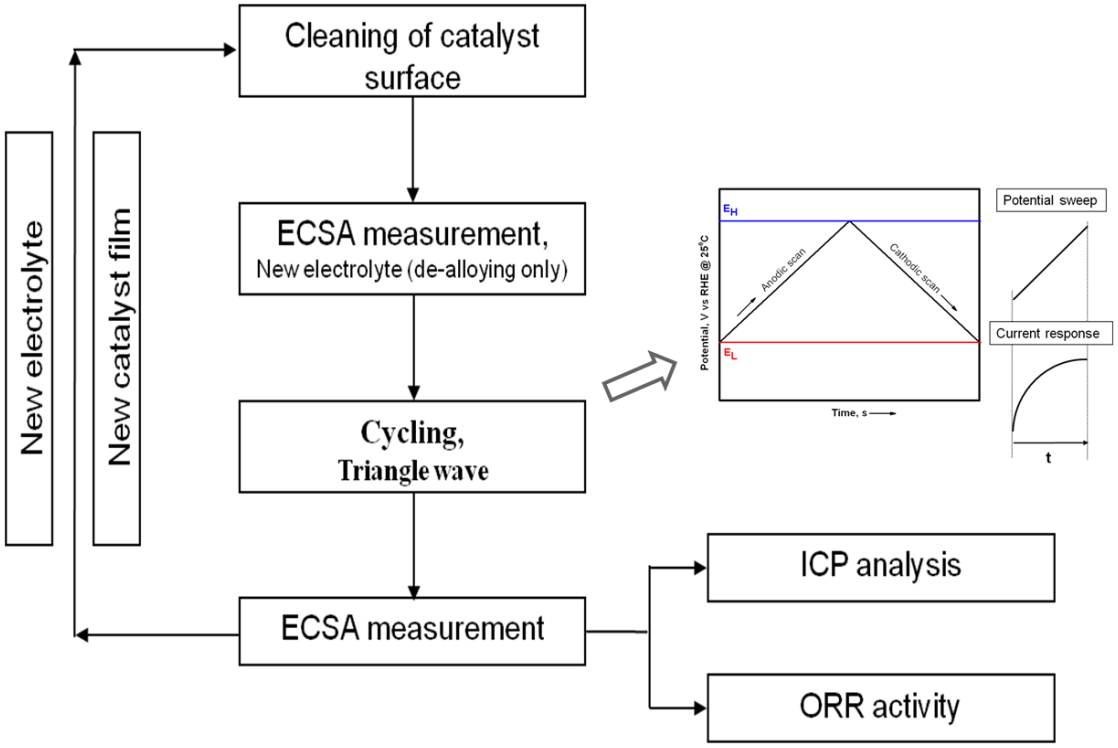

Figure 2.20: Testing protocol for long-term durability studies.

PLATINUM-BASED CATALYSTS

Polymer electrolyte fuel cells (PEFCs) are being pursued for transport, stationary, and portable applications owing to their inherent distinguishing features, which include low-temperature operation and a polymer electrolyte membrane. However, the critical technical challenges in the commercialization of the PEFCs are performance degradation, poor durability of the Pt catalyst material or long-term performance instability, a high overpotential for the oxygen-reduction reaction (ORR) at the cathode, and the high cost of the PEFC. The US Department of Energy (DOE) program for the development of the fuel cells is focused on PEFCs for use in vehicles with targets of at least 5000 hours durability with cycling and with a mass activity of 0.44 A/mg $_{Pt}$ at 0.9 $V_{IR\text{-}free}$ [4]. Platinum (Pt), in spite of its high cost, has been used since the first prototypes of the acid-electrolyte fuel cell [5] owing to its electrochemical stability over a wide potential range and comparatively good catalytic activity. Although Pt is a noble metal, it does not behave as a true inert material under the operating conditions of the PEFC. It interacts with the environment to form a thin layer of oxide on its surface [44]. Research is continuously being carried out to enhance the performance and reduce the cost of the PEFCs.

Some recent advances in the fuel-cell technology include the use of carbon-supported Pt and Pt alloy nanoparticles that reduce the Pt loading, thereby lowering the cost of the fuel cell. These developments have also led to an enhanced ORR activity and durability [45].

In this section, the results of the surface phenomena on the fuel cell catalysts such as polycrystalline platinum, unsupported platinum black nanoparticles, carbon-supported platinum and platinum binary-alloy nanoparticles are presented and discussed.

3. Surface oxide growth on polycrystalline platinum electrodes by EQCN analysis

3.1. INTRODUCTION

A Pt electrode interacts with the environment and forms various oxides. It has been reported that different crystal faces of the polycrystalline Pt catalyst have different preferences for the type of oxide being adsorbed on the surface [29] that form the multiple peaks observed during anodic oxidation of the Pt catalyst. It is apparent that multiple oxides exist on the surface of the Pt catalyst at different potentials, though only a few of them are reported to be stable, contributing to the actual faradaic current as seen in the cyclic voltammogram (CV) of the Pt catalyst. Most electrochemical investigations suggest surface oxides such as PtOH, Pt-O (PtO), PtO_2 or their admixtures as stable oxides [30, 44]. Definite experiments are yet to be carried out to determine conclusively the form in which the adsorbed oxide exists on the surface of the Pt catalyst and the effect of different operating conditions on the type of surface oxide.

The interaction of water molecules with a Pt surface studied by Surface-Enhanced Infrared Absorption Spectroscopy was shown to be dependent on the electrode potential [46]. It has been reported that above point-of-zero-charge (pzc) *i.e.*, at positive electrode potentials, the water molecules had a flat orientation and formed ice-like structure on the electrode. As the potential increases to the region of oxide formation, the deprotonation of the water molecules occurs forming different surface oxides [47]. It has also been reported that the initial sub-monolayer stage of adsorption of the O-containing species is influenced by the competitive chemisorption of the anions.

The objective of this study is to analyze the nature of surface oxides (or adsorbed intermediates) at different potentials and under the actual conditions of an oxygen reduction reaction (ORR). In this chapter, we present the results of the extent of surface

oxidation as a function of potential, and type of anions, dissolved gases, and pH of the electrolyte.

3.2. EXPERIMENTAL METHODS

3.2.1. Electrochemical characterization

The EQCN *in situ* mass measurements were performed by using a Pt EQCN sensor. A sensor with Pt coated on a titanium (Ti) underlayer on either side of the quartz crystal was used for electrochemical measurements. A batch-cell using a 5 MHz sensor was used for the measurements. The details of the EQCN measurement technique are given in Section 2.3.3.

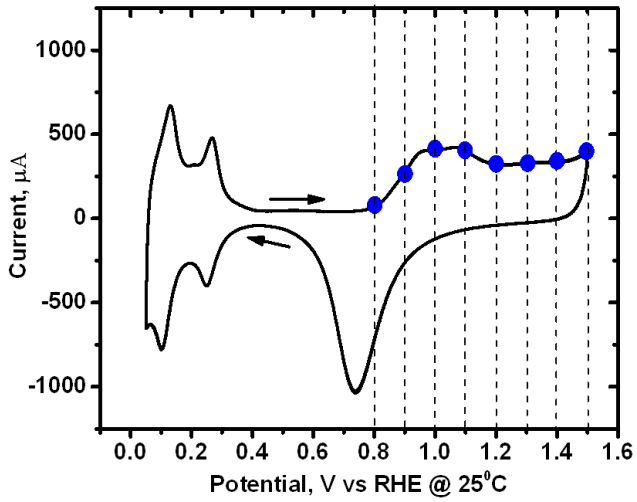

Figure 3.1: Cyclic voltammogram of a Pt electrode in 0.5 M H_2SO_4, at 50 mV s^{-1}. The dashed-vertical lines denote the upper potentials (E_H) to which the electrode is scanned.

Different sets of experiments were carried out to study the surface oxide on Pt. The first set of experiments involved the electrochemical characterization of the Pt electrode by a potential scan between 0.05 and E_H (Figure 3.1, E_H: upper potential), at 50 mV s^{-1}. This measurement was carried out in 0.01, 0.05, 0.1, and 0.5 M H_2SO_4, and 0.1

M $HClO_4$ solutions (deaerated). The upper potential was varied from 0.8 to 1.5 V in steps of 0.1 V. The resistance of the different sulfuric acid solutions is measured by impedance spectroscopy (Figures B.1 and B.2) and the details are given in Table 3.1. Measurements were also made in 0.1 M NaOH in the potential range of 0.05 to 1.2 V at 50 mV s^{-1}.

Table 3.1: Details of the sulfuric acid solution used for electrochemical measurements

Electrolyte, M, H_2SO_4	**pH**	**R, Ω**
0.01	1.80	205.090
0.05	1.30	51.304
0.1	1.08	26.958
0.5	0.30	5.789

The second set of experiments consisted of the potential scans from 0.05 V to 1.2 V at 50 mV s^{-1} in deaerated and oxygen-saturated 0.5 M H_2SO_4 solutions. The third set of experiments consisted of the potential scans between 0.05 and 1.2 V at 20 mV s^{-1} and a staircase voltammetry (SCV) (Figure 3.2) in deaerated 0.5 M H_2SO_4 solution. SCV was carried out between 0.05 and 1.2 V with a potential increment (ΔE) of 4 mV, a step period (t_p) of 0.2 s (equivalent to a scan rate of 20 mV s^{-1}), and a sampling width (t_s) of 100 ms. The chosen parameters sample the data at 50 % of the step, thereby minimizing the effect of double-layer capacitance.

Electrode cleaning was carried out as given in Section 2.3. The maximum electrochemical surface area ($ECSA_{Pt}$) was calculated from hydrogen desorption charge (H_{UPD}) as mentioned in Section 2.3.5.

The amount of adsorbed intermediates on the electrode surface was obtained from the combined CV and EQCN measurements for the potential cycling. The interfacial mass response is calculated as mentioned in Section 2.3.4.

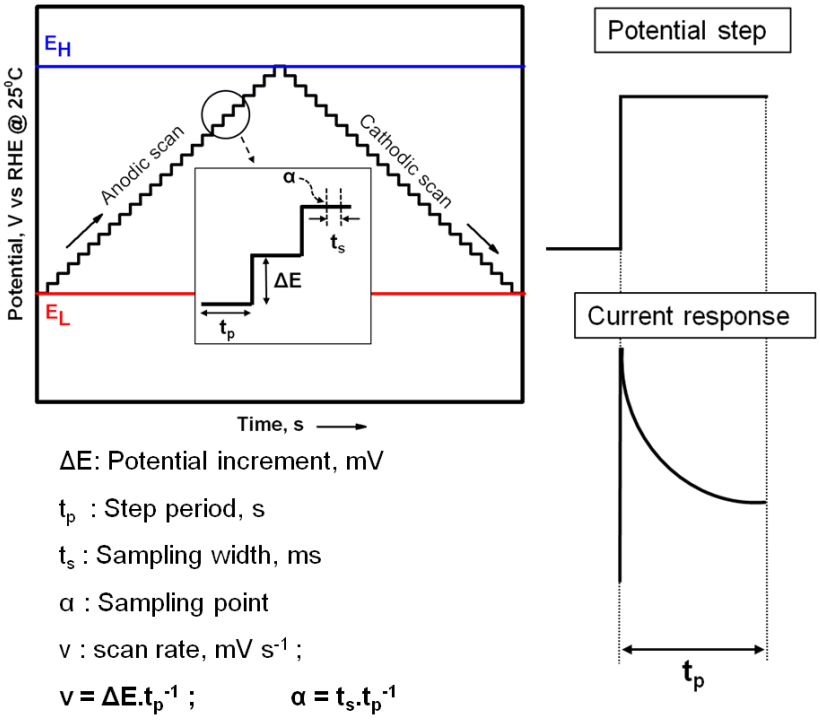

Figure 3.2: Potential-step sweep and current response for a potential step in staircase voltammetry (SCV).

3.3. RESULTS AND DISCUSSION

3.3.1. Electrochemical characterization

Potentiodynamic sweep experiments were carried out in solutions of anions that adsorb weakly ($HClO_4$) or strongly (H_2SO_4) and saturated with either O_2 or Ar to study the influence of various parameters on the extent of surface oxidation on polycrystalline Pt.

3.3.1.1. Effect of upper potential and the adsorbing ions

Measurements were carried out as a function of the upper potential to identify the different stages of oxide formation on the Pt electrode. The amount of surface oxide calculated with Equation (2.4) for different upper potentials and different electrolytes (0.5 M H_2SO_4 and 0.1 M $HClO_4$) are shown in Figure 3.3. The combined CV and EQCN

response of the polycrystalline Pt electrode is shown in Figure 3.4. A summary of the reactions on a Pt electrode with expected mass change is given in Table 3.2. From the integrated charge density and the associated change in mass during the anodic scan, an amount of 8 g mol^{-1} per electron passed is typically obtained indicating the formation of an anhydrous oxide film on the surface of Pt. The suggested reactions for the formation of the oxide film can be written as

$$Pt + H_2O \leftrightarrow PtO + 2H^+ + 2e^- \quad (3.1)$$

$$Pt + 2\,H_2O \leftrightarrow PtO_2 + 4H^+ + 4e^- \quad (3.2)$$

Increase in the upper potential results in increased addition of mass to the interface. The EQCN response does not distinguish between the different oxidation states of Pt. However, the results show that an anhydrous film is formed on the Pt surface. From Figure 3.3, it is seen that the amount of adsorbed oxide, M g mol^{-1}, is the same over the potential range of 1.0 to 1.5 V, indicating that the surface oxide is independent of the upper potential. At the onset of oxide formation, the nature of oxide is influenced by the type of anions in the solution as seen in Figures 3.3 and B.4.

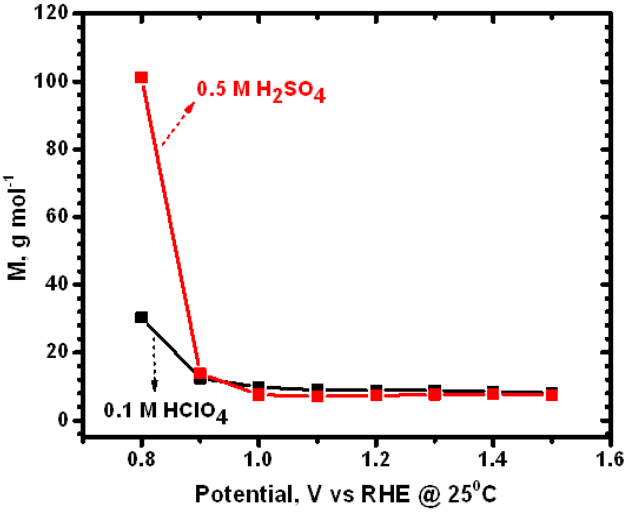

Figure 3.3: Amount of adsorbed species (M) on a Pt electrode in 0.5 M H_2SO_4 and 0.1 M $HClO_4$ in the potential range of 0.05 to E_H at 25 ^oC and 50 mV s^{-1}.

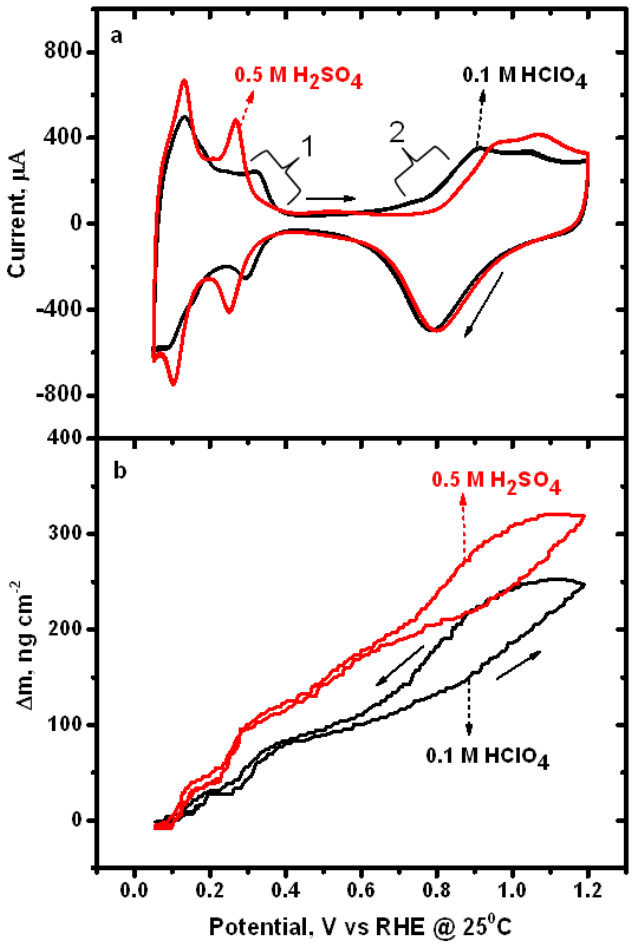

Figure 3.4: (a) CV (1 indicates the characteristic H_{UPD} peaks and 2 shows the shift in the onset of oxide formation to less positive potential due to the absence of anion adsorption) and (b) associated EQCN response of a Pt electrode in 0.5 M H_2SO_4 and 0.1 M $HClO_4$ in the range of 0.05 to 1.2 V at 25 ^oC and 50 mV s^{-1}.

The combined CV and EQCN response at different upper potentials are given in appendix B (Figure B.3). The electrochemical behavior of the Pt electrode under different conditions is given in Figures B.4 and B.5. The summary of the data is given in Tables B.1, B.2, and B.3.

3.3.1.2. Effect of double-layer capacitance

Measurements were carried out to study the effect of capacitance on the amount of surface oxide. The parameters for the SCV were chosen such that the double-layer contribution to the charging current is reduced, which results in data for only the faradaic process. SCV measurements suppress the H_{UPD} region because of the high reversibility of

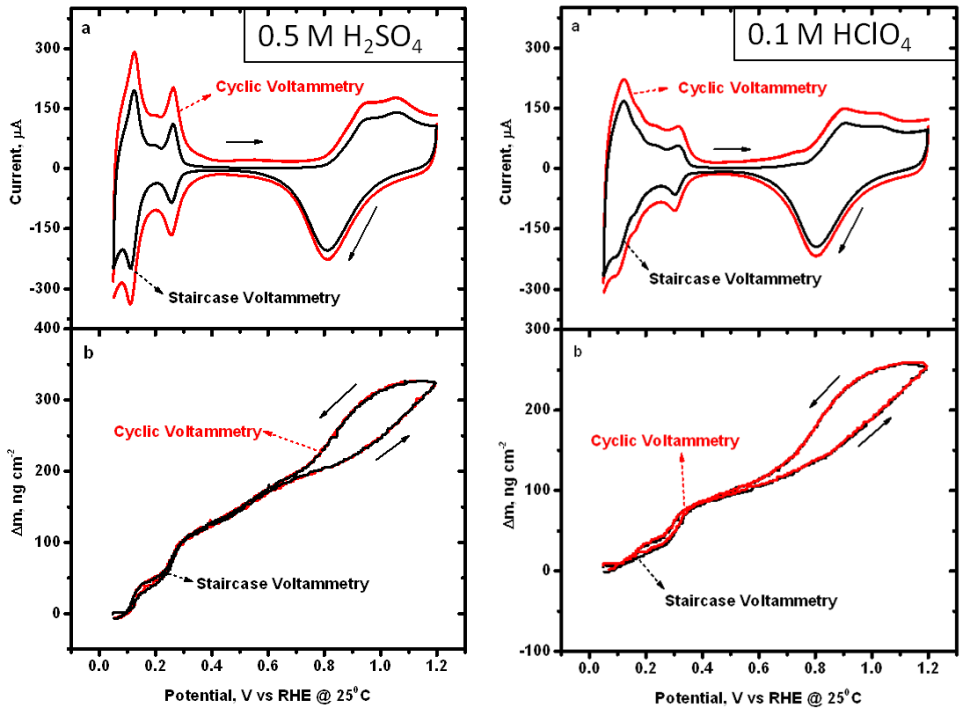

Figure 3.5: SCV and CV with associated EQCN response of a Pt electrode in 0.5 M H_2SO_4 and 0.1 M $HClO_4$ between 0.05 and 1.2 V at 25 ^oC and 20 mV s^{-1}.

the H adsorption/desorption kinetics, which occurs at the beginning of the step and decays when the current is being measured. The CV and EQCN response under CV and SCV are shown in Figure 3.5. The charging currents due to double-layer capacitance are minimized when the SCV method is used. The influence of the different techniques on the extent of surface oxidation on Pt is shown in Figure 3.6. It is seen that the amount of adsorbed oxide is independent of the scan rate and the measurement technique. A

Table 3.2: Summary of reactions occurring on the surface of a Pt electrode with expected mass response

Reaction	Mass change response		Mass change expected, g mole^{-1} (electron)	Mol. Wt of species, g mole^{-1}	Electrochemical Eqv. µg C^{-1} (ng mC^{-1})
	Oxide formation	Oxide reduction			
$Pt + H_2O \leftrightarrow PtO + 2H^+ + 2e^-$	Mass gain	Mass loss	8	Pt^{++} : 195.078	1094
$PtO + H_2O \leftrightarrow PtO_2 + 2H^+ + 2e^-$	Mass gain	Mass loss	8	Pt : 195.078	1177
$Pt^{++} + H_2O \leftrightarrow PtO + 2H^+$	*Mass loss*	Mass loss	-	PtO : 211.077	-
$Pt \leftrightarrow Pt^{++} + 2e^-$	*Mass loss*	*Mass gain*	97.539	PtO_2 : 227.077	1011
$Pt^{++} + 2H_2O \leftrightarrow PtO_2 + 4H^+ + 2e^-$	Mass gain	Mass loss	16*		1177
Mass response of interest	**Mass gain**	**Mass loss**			

* if Pt^{++} stays on the electrode surface in the specific-adsorbed region; those italicized are the EQCN responses that are not expected for the particular scan. (Reactions taken from the Pourbaix diagram) [48].

summary of the data is given in Table B.1. Subsequent electrochemical measurements were carried out at a scan rate of 50 mV s^{-1}.

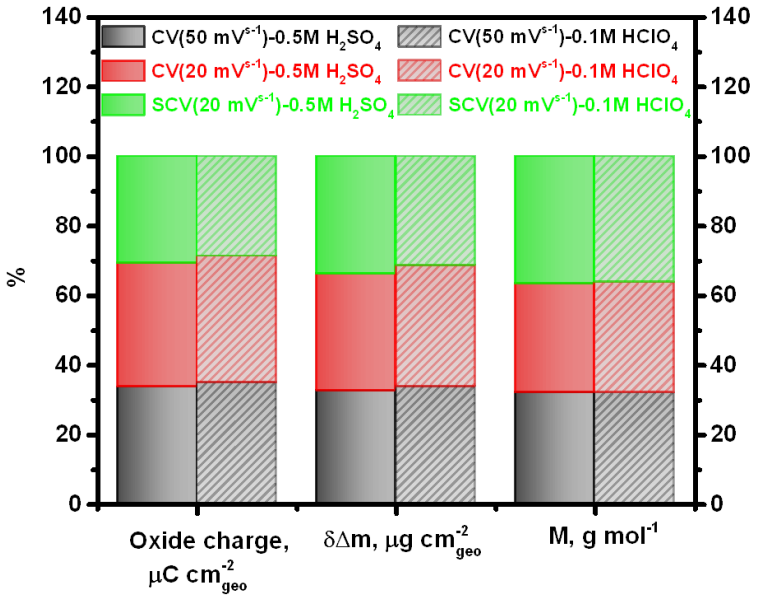

Figure 3.6: Electrochemical behavior of oxide formation on Pt electrode in 0.5 M H_2SO_4 and 0.1 M $HClO_4$: comparison of different techniques.

3.3.1.3. Influence of O_2-saturated solution

Measurements were carried out to evaluate the type and nature of surface oxide in the presence of dissolved O_2 by using a solution saturated with O_2. The combined CV and EQCN response of a Pt electrode in O_2-saturated solution is shown in Figure 3.7. It is seen that the H_{UPD} region is shifted lower relative to the CV in Ar-saturated solution, but the oxide region is comparable in both the cases. The electrochemical behavior in the oxide region of the Pt electrode is shown in Figure 3.8. The amount of adsorbed oxide, M, calculated with Equation (2.4) indicated that the extent of surface oxidation was independent of the partial pressure of O_2 in the solution. It also indicates that the surface oxidation is a function of only the surface characteristics of the electrode being studied. The data are summarized in Table B.1.

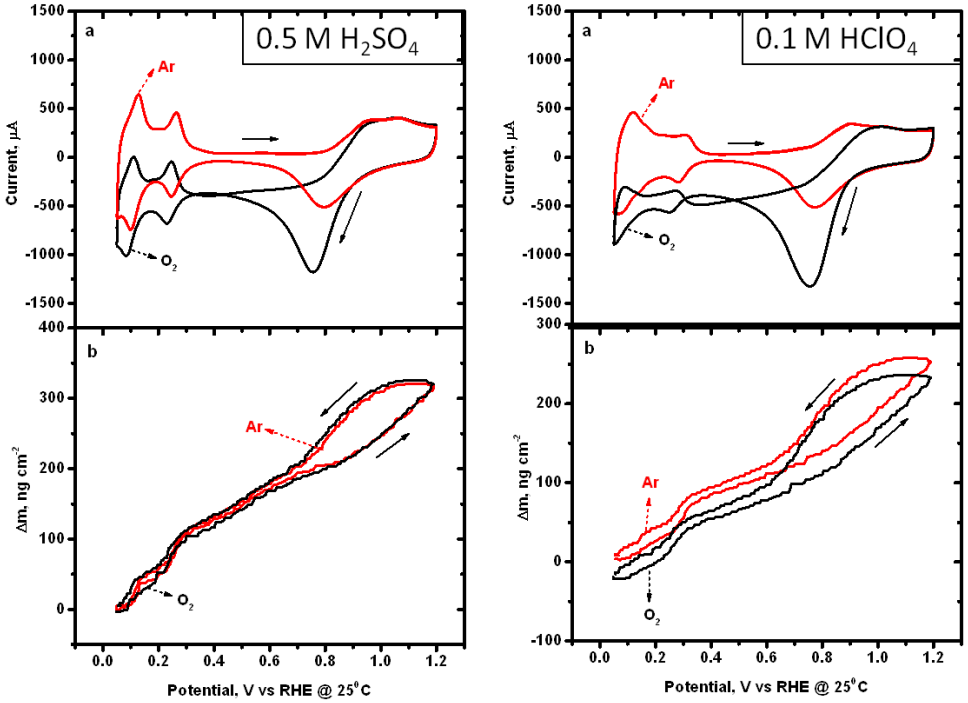

Figure 3.7: CV and EQCN response of Pt electrode in 0.5 M H_2SO_4 and 0.1 M $HClO_4$ between 0.05 and 1.2 V at 25 °C and 50 mV s^{-1} in O_2 - and Ar -saturated electrolytes.

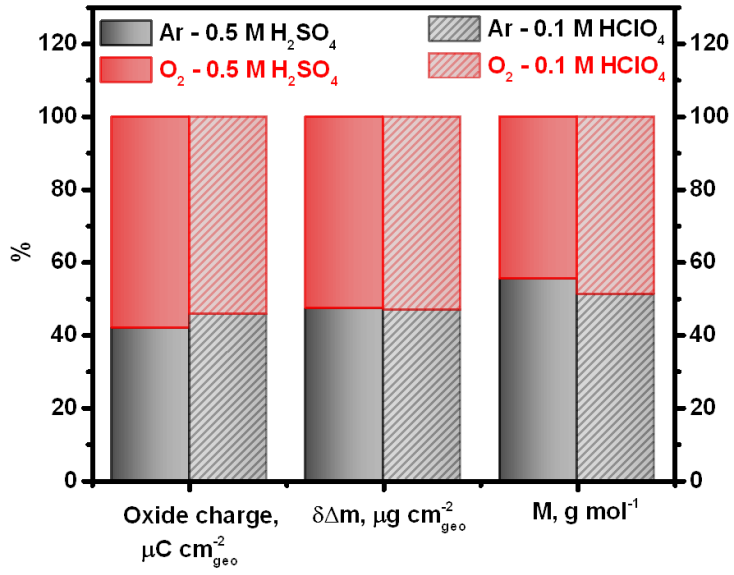

Figure 3.8: Electrochemical behavior of oxide formation on Pt electrode in 0.5 M H_2SO_4 and 0.1 M $HClO_4$: comparison O_2- and Ar- saturated solutions.

3.3.1.4. Effect of the pH of the solution

Measurements were carried out in different pH of the electrolyte to study the influence of the concentration of protons on the extent of surface oxidations. The amount of surface oxide, M, as a function of upper potential in different electrolytes are given in Figure 3.9 and the combined CV and EQCN response for an upper potential of 1.2 V shown in Figure 3.10. The results were also compared with the mass response in 0.1 M NaOH (Figure 3.11, M = 9.85 g mol^{-1}). It is seen that the extent of surface oxidation was independent of the pH of the electrolyte. The presence of H_2O and OH^- ions resulted in the formation of PtO as the surface oxide. The experiments indicate that the electrode surface interacts with the O-containing species (H_2O or OH^-) in the solution and forms an oxide lattice as the reaction progresses with the subsequent discharge of the protons and water molecules at high potentials. The combined CV and EQCN response at different upper potentials are given in appendix B, Figure B.6. The electrochemical behavior of the Pt electrode under different conditions is given in Figure B.7. The summary of the data is given in Tables B.4, B.5, and B.6.

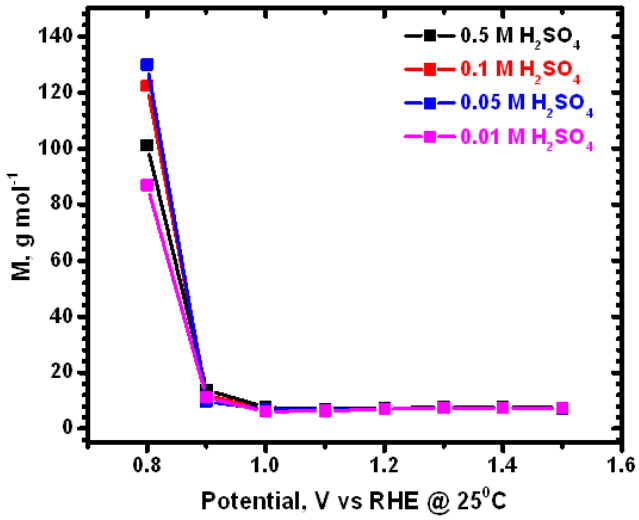

Figure 3.9: Amount of adsorbed species (M) on Pt electrode in different concentrations of H_2SO_4 in the potential range of 0.05 to E_H at 25 ^oC and 50 mV s^{-1}.

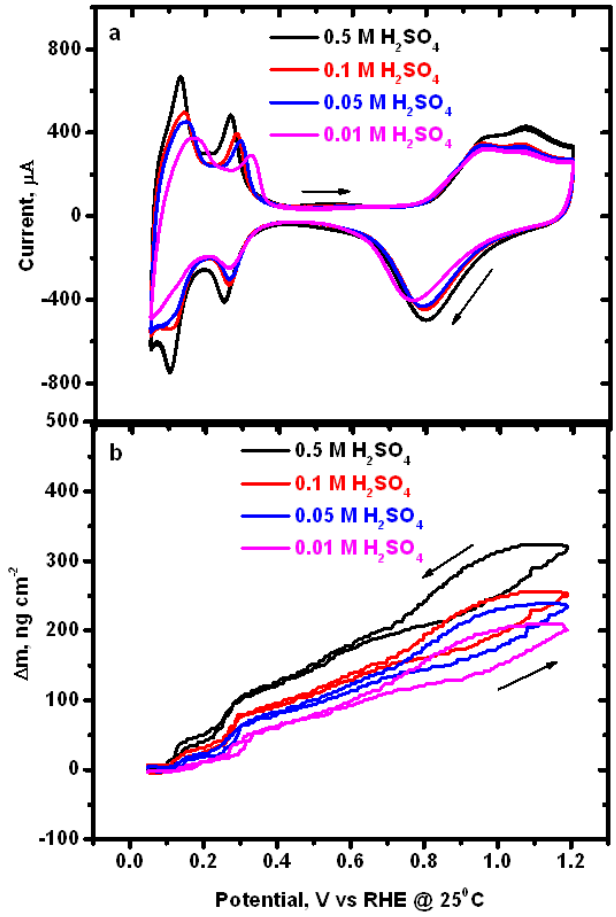

Figure 3.10: Combined CV and EQCN response of Pt electrode in 0.5, 0.1, 0.05, and 0.01 M H_2SO_4 between 0.05 and 1.2 V at 25 ^oC and 50 mV s^{-1}.

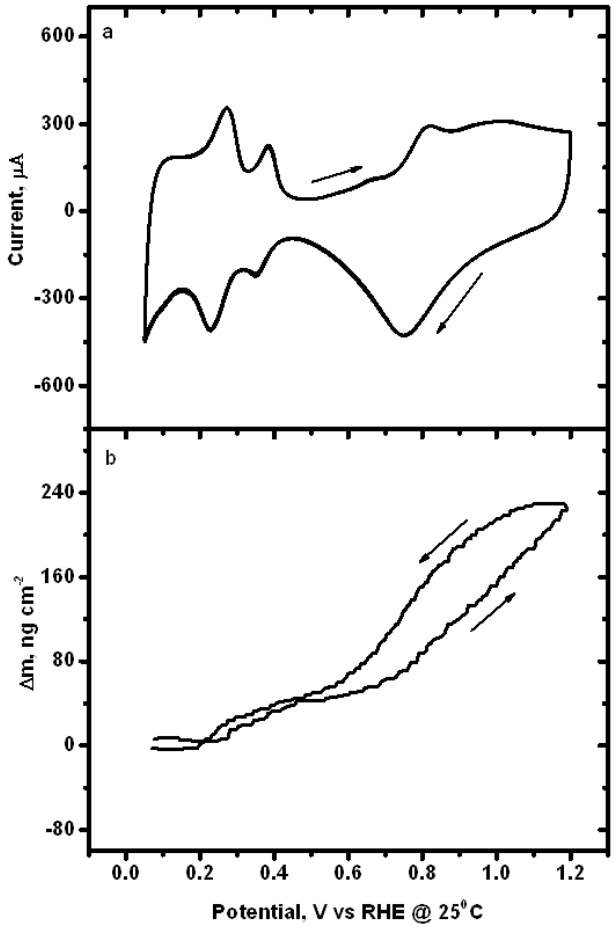

Figure 3.11: Combined CV and EQCN response of Pt electrode in 0.1 M NaOH between 0.05 and 1.2 V at 25 ^{o}C and 50 mV s^{-1}.

A change in frequency as a function of charge for a single potential cycle in 0.5 M H_2SO_4 is given in Figure 3.12. The linear relationship observed between the charge and frequency indicated the formation of the same anhydrous oxide. It is also seen that a step occurs at potentials greater than 1.15 V. This step may indicate the onset of a surface restructuring involving an interfacial place-exchange between the adsorbed oxide species and the surface Pt atoms. It has been reported that strong repulsive interactions between the adsorbed O atoms could lead to this place-exchange in the potential range of 1.1–1.2 V [49].

Also, the CV of Pt in 0.5 M H_2SO_4 showed two peaks (the transition of the first peak to the second peak occurs at ~1.0 V) during the anodic sweep with amplitudes for them being more or less the same, which suggests that one part could be the formation of OH and the other part could be O. This possibility was tested by doing a potential scan to 1.0 V. The anodic scan showed a two-electron transfer in the formation of the oxide whereas the reduction of the oxide showed a one-electron transfer corresponding to OH. A place exchange of surface oxide ions could stabilize surface OH on reducing the potential below 1.0 V.

Based on the results, the Equations (3.1) and (3.2) can be modified as

$$Pt + H_2O \leftrightarrow PtOH + H^+ + e^- \quad (3.1a)$$

$$PtOH \leftrightarrow PtO + H^+ + e^- \quad (3.1b)$$

$$PtO + H_2O \leftrightarrow PtOOH + H^+ + e^- \quad (3.2a)$$

$$PtOOH \leftrightarrow PtO_2 + H^+ + e^- \quad (3.2b)$$

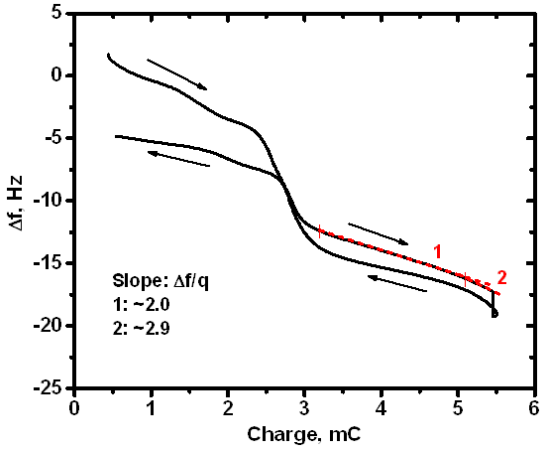

Sauerbrey equation: (Equation (2.3))

$$\Delta f = -C_f \Delta m$$

Faraday's law: (Equation (2.4))

$$\frac{\Delta m.n}{\Delta q} = \frac{M}{F}$$

Figure 3.12: Change in frequency (Δf) vs Charge (Q) for a single potential cycle of Pt electrode in 0.5 M H_2SO_4.

3.4. CONCLUSIONS

The extent of surface oxidation on polycrystalline Pt was studied by combined CV and EQCN measurements. The amount and type of the adsorbed species was analyzed as a function of upper potential, nature of anions, type of dissolved gas in the electrolyte, and electrolyte pH. From the experimental results, the following conclusions can be drawn:

- The type and nature of the adsorbed oxide is the same in the potential range of 1.0–1.5 V and is neither influenced by the anions nor the double-layer capacitance. The initial film formed on the electrode surface is an anhydrous PtO surface oxide.
- The extent of surface oxidation is only dependent on the O-containing species in the solution (H_2O) and is independent of the partial pressure of O_2 in the solution. The ORR on a Pt electrode involves the formation of a surface oxide intermediate from the aqueous electrolyte.
- The adsorption of the oxide species on the electrode is influenced only by the surface characteristics of the catalyst.

4. Analysis of surface oxidation and the extent of surface oxide growth on the durability of carbon-supported platinum and platinum binary-alloy catalysts

4.1. INTRODUCTION

In PEFCs, the ORR occurs in the potential range wherein the surface of the catalyst is oxidized; and the oxides could exist in several forms that are either weakly or strongly bonded [28]. Moreover, the ORR proceeds via the formation of adsorbed oxygen intermediates. The oxide film may also induce the dissolution and redeposition of Pt at high potentials [27]. The continuous formation and reduction of the surface oxide, a condition experienced by the PEFC under frequent start-stop of the device, may result in roughening and destabilization of the surface of the Pt catalyst, thus increasing the rate of dissolution of Pt [43]. Recent advances to enhance catalyst durability and activity have led to the development of Pt alloy catalysts that show a decrease in oxidation of the Pt surface [45]. However, accurate descriptions of the oxide and the surface phenomena on the catalysts are yet to be clearly understood. There is not enough reported work to quantify and establish the oxides as species-specific (*viz.*, OH^- or O^{2-}) on the carbon-supported nanoparticles. Also, knowledge of the mechanism of surface oxidation on Pt and the role of these oxides in Pt dissolution would help to understand the generation of the soluble/mobile Pt species in a PEFC.

In this work, we present results on the surface phenomena of carbon-supported core-shell platinum-copper (Pt-Cu), platinum-cobalt (Pt-Co), and platinum-scandium (Pt_3Sc) binary alloy catalysts. The results are compared with carbon-supported Pt (Pt/C) and unsupported Pt (Pt black) catalysts. Different catalysts are compared to understand the characteristics of the surface oxide and hence it's possible influence on the ORR activity and catalyst durability. The catalysts for this study, *viz.*, Pt black, Pt/C, and Pt-

Co/C were purchased from BASF, USA. The Pt-Cu/C (Cu_3Pt/C) precursor catalyst was synthesized by Strasser's research group at the University of Houston, TX. The Pt_3Sc/ C catalyst was obtained from Johnson Matthey plc.

4.2. EXPERIMENTAL METHODS

4.2.1. Structural/chemical characterization

Bulk metal compositions were determined with SEM-EDS scanning electron microscopy (Section 2.2.2) and ICP analysis (Section 2.2.5). The metal loading was determined by TGA (Section 2.2.3). The structural characterization of the catalysts was carried out with a Philips 3520 X-ray diffractometer (Section 2.2.1). Particle size distribution was determined with a JEOL 2010F TEM (Section 2.2.4).

4.2.2. Electrochemical characterization

4.2.2.1. Preparation of catalyst ink and electrode

The catalyst inks were prepared by the procedure described in Section 2.3.1. The drop-cast ink was allowed to dry at room temperature. The method of ink preparation was the same for all the catalyst materials being studied. The details of the cast electrodes are given in appendix C, Table C.1.

4.2.2.2. Cyclic voltammetry (CV)

The electrochemical characterization was carried out by cyclic voltammetry (CV) (Section 2.3). The $PtCu_3$/C precursor catalyst was subjected to electrochemical voltammetric dealloying in the potential range of 0.5–1.0 V at 0.1 V s^{-1} for 220 cycles. The dealloying results in Pt on the surface of Cu to give a core-shell catalyst. The core-shell electrode was electrochemically pretreated after the dealloying process by a potential scan between 0.05–1.2 V at 0.5 V s^{-1} for 120-220 cycles (the number of cycles

was dependent on the catalyst loading) in a fresh electrolyte to monitor the extent of dealloying and to obtain stabilized voltammograms. The electrochemical measurements of the core-shell electrode, after the pretreatment cycles, were carried out in a fresh electrolyte.

4.2.2.3. Electrochemical quartz crystal nanobalance measurements (EQCN)

The *in situ* mass measurements were performed with the EQCN setup (Section 2.3.3). A flow cell with a 7.9 MHz sensor and/or a batch cell with a 5 MHz sensor were used for the measurements as reported in Table C.1. The amount of adsorbed intermediate on the electrode surface was obtained from combined CV and EQCN measurements (Section 2.3.4).

4.2.2.4. Accelerated degradation tests

The catalysts were cycled under different test conditions as described in section 2.3.9. The tests as a function of the upper potentials were carried out at 0.5 V s^{-1} between 0.4 and E_H (E_H: 0.7 to 1.3 V) for 500 cycles. The potential cycling tests were carried out at 1.0 V s^{-1} between 0.4 and 1.3 V, for n cycles. (n: 500 to 15000 cycles). Sample solutions were collected at the end of each experiment, and the amount of dissolved metal species in solution was determined by ICP-MS (Section 2.2.5). ORR activity measurements (Section 2.3.7) were carried out before and after each degradation test to measure the change in catalyst performance with cycling.

Accelerated degradation tests were also carried out by combined CV and EQCN as a function of cycling potential to measure the amount of surface oxide as a function of potential. The amount of surface oxide was measured before and after each test.

4.2.2.5. Determination of H_2O_2 intermediates

The measurements were conducted in a three-compartment cell by using the RDE/RRDE electrode set-up with a potentiostat and rotation control (PINE instruments Inc.). The details are given in Sections 2.3.2 and 2.3.8.

4.3. RESULTS AND DISCUSSION

4.3.1. Structural/chemical characterization

4.3.1.1. EDS, ICP and TGA analyses

Bulk compositions determined by EDS and ICP analyses are reported in Table 4.1. The metal loading from TGA analysis was found to be 40 wt.%.

4.3.1.2. XRD analysis

Figure 4.1 compares the XRD patterns of the catalyst samples. All the peaks can be indexed with the f.c.c crystal structure except the XRD pattern of Pt_3Sc/C, which shows superlattice reflections. The sharp Cu peaks in the XRD pattern of the Pt-Cu/C precursor catalyst indicates the presence of a pure Cu phase with a large particle size, which also form oxides as seen from the oxide peaks. The lattice parameters obtained from the fitted XRD peaks are given in Table 4.1. The particle surface area in $m^2\ g^{-1}$ was calculated with the equation $S_A = 6000/d\rho$ assuming spherical particles, where d is the crystallite size in nm and ρ is the density of the alloy in g cm^{-3}. The Pt surface density (cm^{-2}) and the degree of dispersion were calculated with the Benfield approximation for a spherical particle [50]. The values are given in Table 4.1

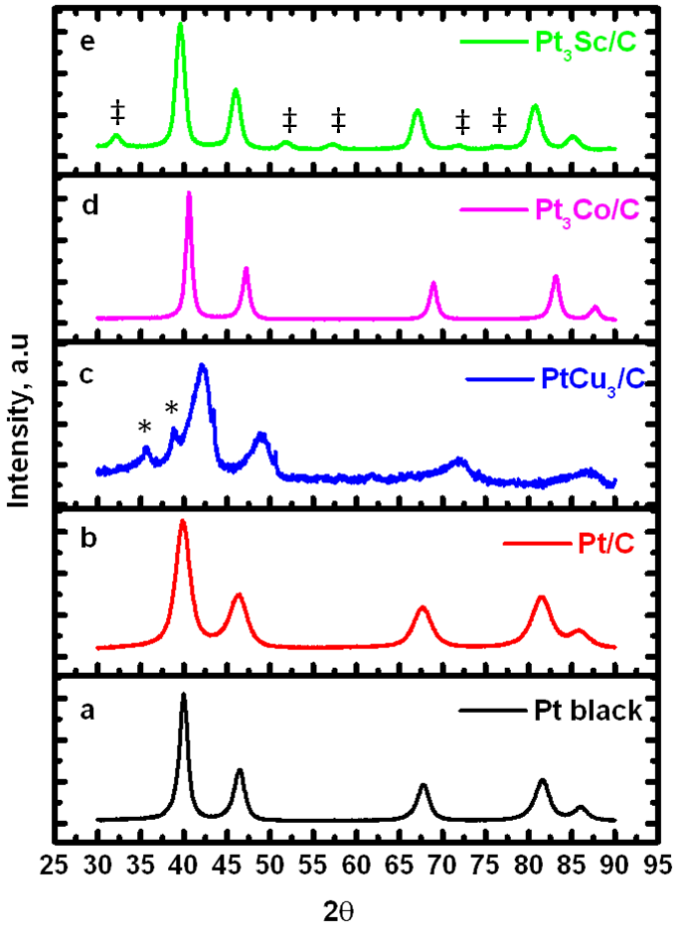

Figure 4.1: XRD patterns of the catalyst samples (* Copper oxide; ‡ superlattice reflections).

4.3.1.3. TEM analysis

The TEM images and the particle size distribution of the catalysts obtained from Gaussian models show that the catalyst nanoparticles have a spherical morphology (Figure 4.2). The average diameter of the catalyst nanoparticles calculated from an ensemble of 100 particles is given Table 4.1. It has been reported that there is no significant change in the particle size of the Pt-Cu/C catalyst before and after the dealloying process [51]. It has also been reported that size variations have negligible effect on the surface electronic properties of the Pt nanoparticles [52].

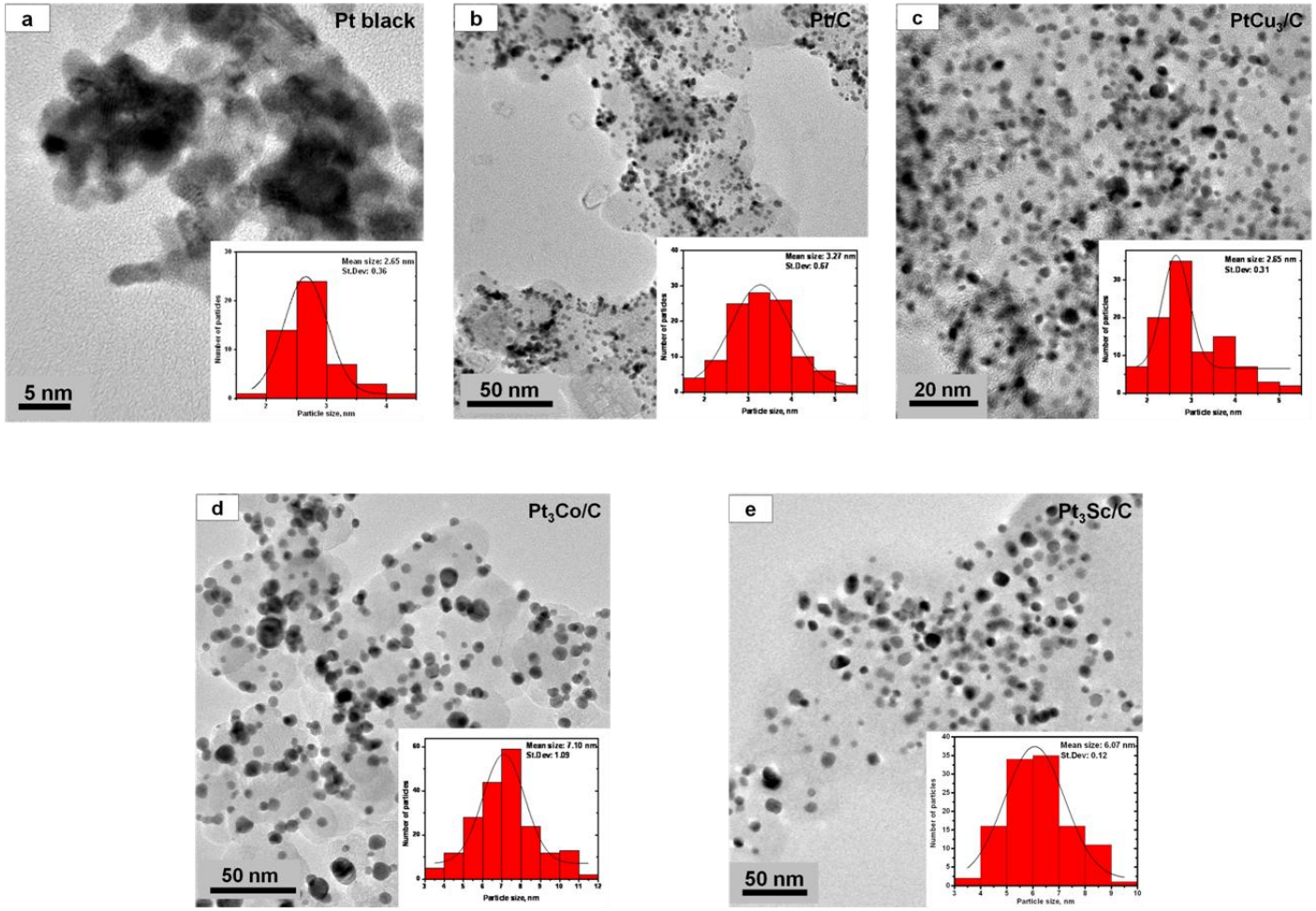

Figure 4.2: TEM images of the catalysts (inset-particle size distribution): (a) Pt black, (b) Pt/C, (c) $PtCu_3$/C, (d) Pt_3Co/C, and (e) Pt_3Sc/C.

Table 4.1: Characteristics of the catalyst nanoparticles studied

Catalyst	Metal, at.% (nominal)	Metal (bulk), at.% (EDS)	Particle size, nm (TEM)	Lattice parameter, Å (XRD)	Surface area, S_A, $m^2\ g^{-1}$ (metal)	Pt surface atom density, cm^{-2}	Degree of dispersion	
							Pt	X (=Cu, Co, Sc)
Pt black	-	-	2.65 ± 0.36	3.9081	107.4	1.05×10^{15}	46.2	-
Pt/C	-	-	3.27 ± 0.67	3.9146	87.0	1.01×10^{15}	40.2	-
Pt-Cu/C (precursor)	$Pt_{25}Cu_{75}$	$Pt_{25.0}\ Cu_{75.0}$	2.65 ± 0.31	3.7029	179.7	2.86×10^{14}	11.2	33.7
Pt_3Cu/C(†)	*$Pt_{75}Cu_{25}$*	-	*2.65 ± 0.31*	*3.8469(‡)*	*121.7*	*7.89×10^{14}*	*34.7*	*11.6*
Pt-Co/C	$Pt_{75}Co_{25}$	$Pt_{78.5}\ Co_{21.5}$	7.10 ± 1.09	3.8372	44.2	8.01×10^{14}	15.4	5.2
Pt_3Sc/C	$Pt_{75}Sc_{25}$	$Pt_{75.3}\ Sc_{24.7}$	6.07 ± 0.12	3.9436*	67.8	7.60×10^{14}	18.3	6.1

* considering the disordered phase; † assuming Pt_3Cu/C is the composition of the surface after dealloying [51]; ‡ calculated using Végard's law for solid solution.

4.3.2. Electrochemical characterization

4.3.2.1. Voltammetric dealloying of the precursor Pt-Cu/C catalyst

Figure 4.3b represents the cyclic voltammogram of the selective dealloying of the Cu rich Pt-Cu/C precursor. The catalyst is only cycled in the Cu-UPD region to avoid deposition of Cu back on the surface of the catalyst. Complete dissolution of the surface Cu atoms was confirmed by the stabilized voltammogram. The initial stage of the dealloying process shown in Figure 4.3a matches well with the reported theoretical plot [53]. The dissolution of pure Cu phases occurs near the Cu standard potential of 0.34 V. It has been reported that the dissolution at potentials close to 0.6-0.7 V is consistent with stripping Cu layers from pure Pt-Cu alloys [54, 55]. Dissolution of additional Cu atoms at potentials positive to the potential of oxygen reduction reaction may seem probable. However, the voltammogram of the dealloyed catalyst shown in Figure 4.5a closely resembles that of polycrystalline Pt, revealing the peaks of hydrogen adsorption/desorption and oxide formation/stripping regions, which is a key characteristic of the Pt surface electrochemistry. The schematic diagram of the core-shell structure is shown in Figure 4.3c.

4.3.2.2. Understanding the EQCN response of the carbon-supported nanoparticles

The combined CV and EQCN response for the carbon-supported Pt and Pt binary-alloy catalysts are shown in Figures 4.4 and 4.5, respectively. The results have been compared with the CV and EQCN response of Pt electroplated on a gold-coated quartz sensor (Figure 4.4a). In an ideal EQCN response, desorption of H from the surface should show a mass decrease. However, there is a net mass increase in the H desorption region on unsupported Pt (Figure 4.4b). This mass increase is due to the adsorption of water (H_2O) molecules on the Pt sites immediately following desorption of H from the sites

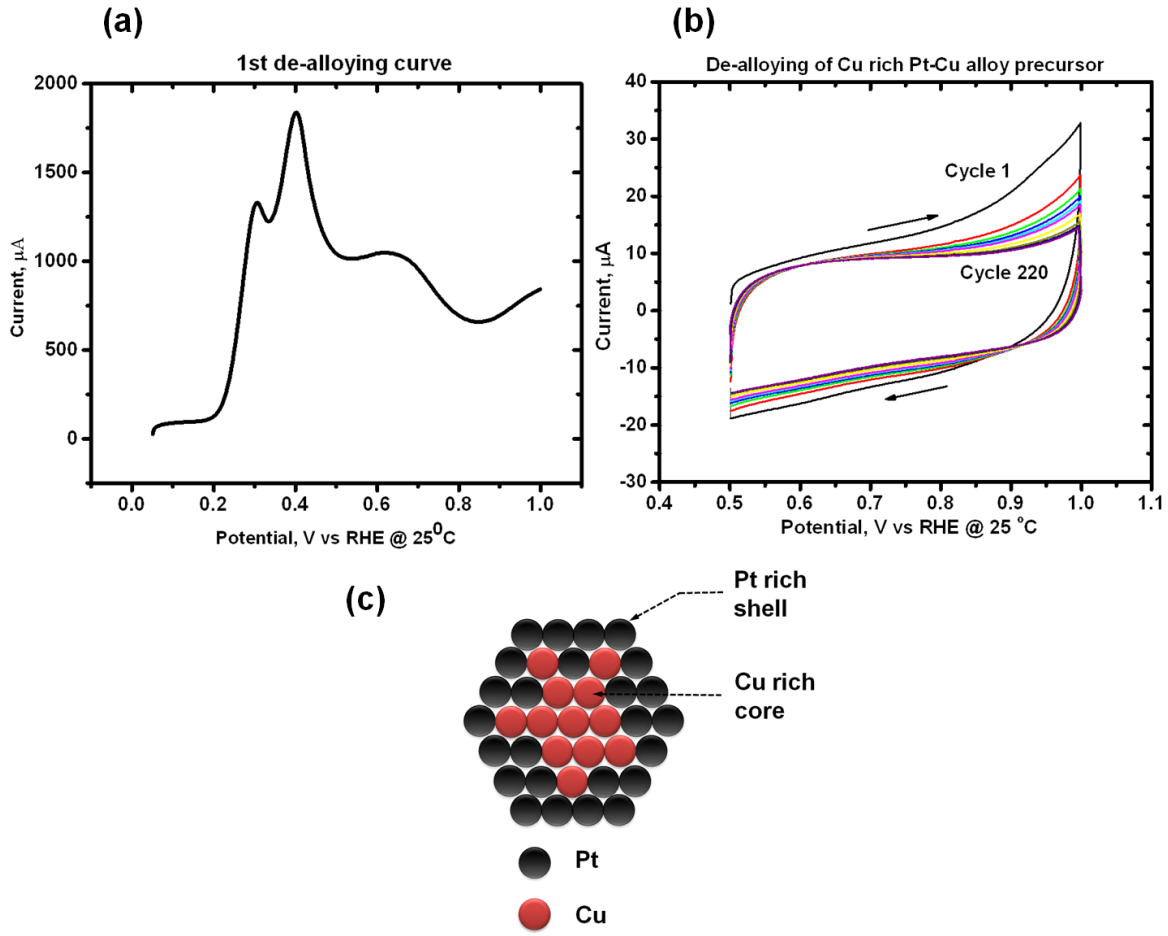

Figure 4.3: (a) Characteristic CV showing the initial stage of dealloying process, (b) voltammogram showing dealloying of the Pt-Cu precursor catalyst at 0.1 V s^{-1} between 0.5 and 1.0 V in 0.5 M H_2SO_4 at 25 ^oC, and (c) the schematic diagram of the core-shell catalyst.

[56]. For supported catalysts, the different wetting characteristics of the support and the metal catalysts results in a mass decrease in the H desorption region (Figure 4.4c). The reversibility of the H adsorption and desorption process is indicated by the uniform mass change in the H region. The adsorption of anions on the surface occurs in the double-layer region after all the H has been desorbed from the catalyst surface. When the physisorbed H_2O molecules are replaced by physisorption with sulfate or bisulfate ions in the double-layer region, the mass change will not be significant as seen for unsupported

Pt (Figure 4.4b). A continuous increasing trend in the EQCN response in the double-layer region occurs due to the specific adsorption of both anions and the H_2O molecules. A narrow double-layer region is observed in cases of optimum wetting of the catalyst material. The double-layer region separates the H_{UPD} and the oxide regions. Surface oxidation causes a further increase in mass in the oxide formation region. It has been reported that monolayer coverage of oxide species excludes further adsorption of anions and H_2O molecules [57]. Studies on polycrystalline Pt (Chapter 3) also showed that the amount of chemisorbed species in the oxide region was not influenced by the adsorption of anions. The coverage is calculated from the ratio of the charge for the formation of oxide to the charge for hydrogen desorption and is given by $Q_O/2Q_H$ when the surface species is oxide, and Q_{OH}/Q_H when hydroxyl species are adsorbed on the surface (Figure 4.7). In this work, the oxide content has been obtained from the change in EQCN mass response during the CV to 1.2 V. Measurements were made at different upper potentials, (E_H: 0.7 – 1.4 V). It was found that the mass-change obtained during the CV to 1.2 V was more reliable in terms of analyzing the amount of adsorbed intermediates on carbon-supported catalysts. The charge in the oxide formation region was assumed to be entirely due to the chemisorbed oxides on the catalyst surface.

4.3.2.3. Interfacial mass change

The change in the interfacial mass (Δm) was calculated by using Equation (2.3). A summary of the data for the combined CV and EQCN response is given in the appendix (Table C.1). The electrochemical area was calculated from the charge density for H desorption as described in Section 2.3.5. The amount of adsorbed species, M, was calculated from the integrated charge density and the associated mass change over the potential range of oxide formation by using Equation (2.4). The results are summarized in

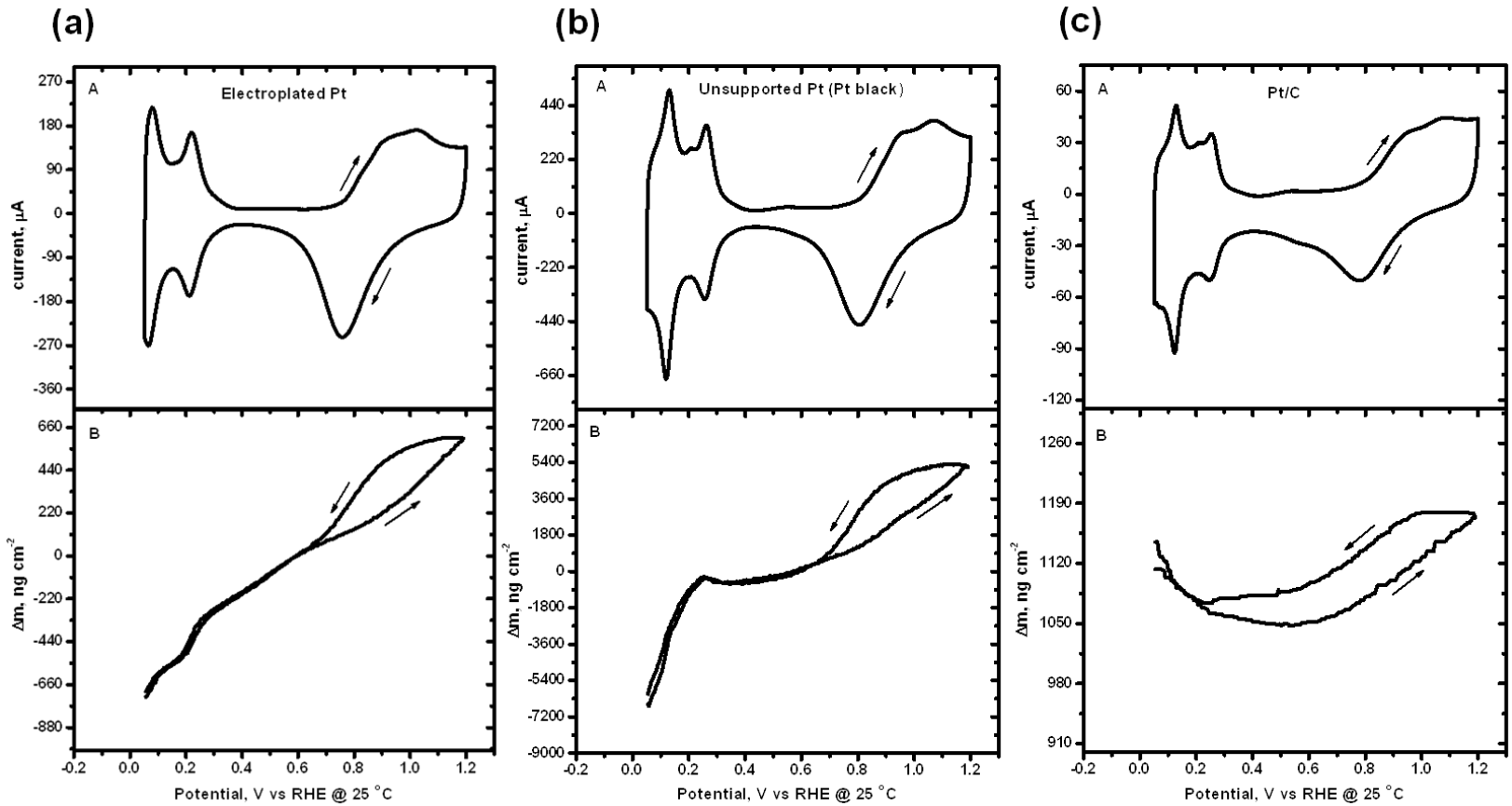

Figure 4.4: Combined CV and EQCN response of: (a) electrodeposited Pt, (b) unsupported Pt (Pt black), and (c) Pt/C in 0.5 M H_2SO_4 between 0.05 and 1.20 V at 50 mV s^{-1} and 25 ^oC.

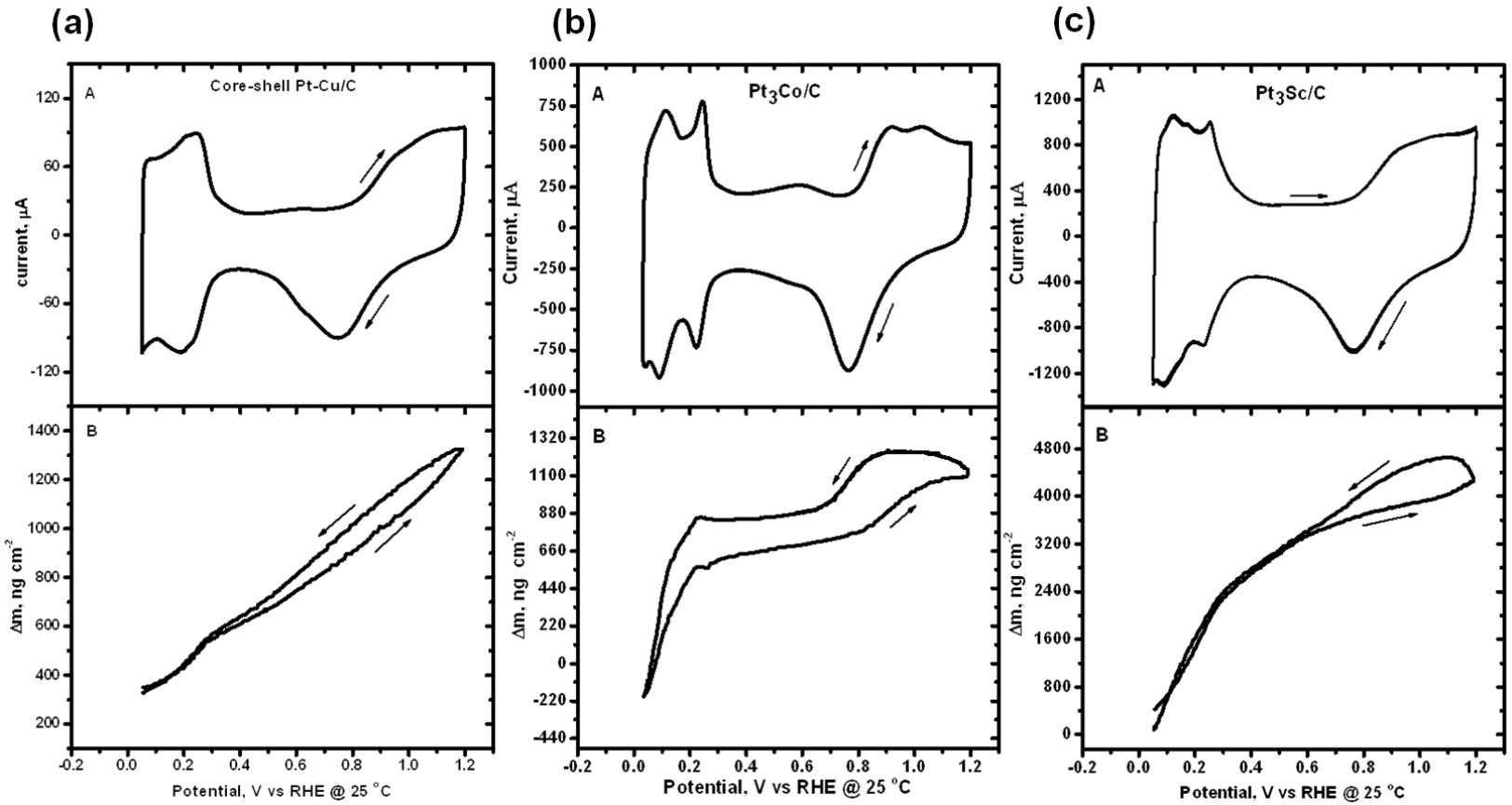

Figure 4.5: Combined CV and EQCN response of: (a) core-shell Pt-Cu/C, (b) Pt_3Co/C, and (c) Pt_3Sc/C in 0.5 M H_2SO_4 between 0.05 and 1.20 V at 50 mV s^{-1} and 25 ^oC.

Table 4.2. The amount of adsorbed species (M) in the oxide region was equivalent to approximately 8 g mol^{-1} of electrons passed for electroplated Pt and Pt/C catalyst. These results are in agreement with the work reported by Birss *et al* [58] and Jerkiewicz *et al* [49] for the formation of an anhydrous Pt oxide film. In the present work, the experiments were carried out on Pt nanoparticles whereas most of the reported work has been with metallic Pt or Pt sputtered onto the working electrode. These results indicate that the Sauerbrey equation considered was valid for the experiments in this work.

For the unsupported Pt, the change in mass in the oxide region was equivalent to a value of approximately 35 g mol^{-1} of electrons passed. This result indicates a mixture of PtO together with other species in Pt black [57, 58] on the surface of the catalyst. For example, Frelink *et al* [57] have indicated that occluded bisulfate with PtO would give 35 g mol^{-1}.

The results obtained for the binary alloys studied here show that the oxide formation on Pt binary-alloy catalysts occurs via the formation of an initial hydroxyl layer followed by a subsequent deprotonation (Equations (4.4) and (4.5)). The surface oxide formation on Pt_3Sc/C (M =25 g mol^{-1}) indicates the adsorption of OH species besides the oxygen atoms (Equation (4.6)). This competition for adsorption of other species may be due to the difference in size between Pt (atomic radius: 1.77 Å) and Sc (atomic radius: 1.84 Å) atoms and the difference in the electronic configuration (Sc: 21 $\{[Ar]4s^2\ 3d^1\}$ and Pt: 78 $\{[Xe]4f^{14}\ 5d^9\ 6s^1\}$). The bigger size of Sc introduces a tensile strain on Pt and electrons flow from Sc to Pt in an alloy. The strain argument was the result of calculations in which there was no change in the chemical composition by alloying. It was also seen from the XRD results that Pt_3Sc/C showed superlattice reflections representing an ordering of Pt and Sc. Based on the experimental results, the

mechanism of adsorption of oxygen on the surface of different catalysts can be summarized as shown in Figure 4.6.

Work function measurements (UV-PES measurements) of the catalysts were carried out to obtain a relation between the type of catalyst and the amount of surface oxide. The results are given in Figure C.1 (appendix C). The work-function values are seen to be dependent on the support and the size of the particle. No correlation could be obtained as the values were affected by the presence of the carbon support.

Table 4.2: Oxide formation on the catalysts

Type of catalyst	**M, g mol^{-1} (+1.5/-1.0)**	**Reaction**
Pt- electroplated	8	$Pt + H_2O \leftrightarrow PtO + 2H^+ + 2e^-$ (4.1)
Pt black	35	$Pt + H_2O \leftrightarrow PtO + 2H^+ + 2e^-$ (4.2)
Pt/C	8	$Pt + H_2O \leftrightarrow PtO + 2H^+ + 2e^-$ (4.3)
Pt-Cu/C – core-shell	17	$Pt + H_2O \leftrightarrow PtOH + H^+ + 1e^-$ (4.4)
Pt_3Co/C	17	$Pt + H_2O \leftrightarrow PtOH + H^+ + 1e^-$ (4.5)
Pt_3Sc/C	25	$*Pt + 3H_2O \leftrightarrow PtO.2H_2O + 2H^+ + 2e^-$ (4.6) (or PtO + PtOH)

* the reaction is written for 26 g mol^{-1}.

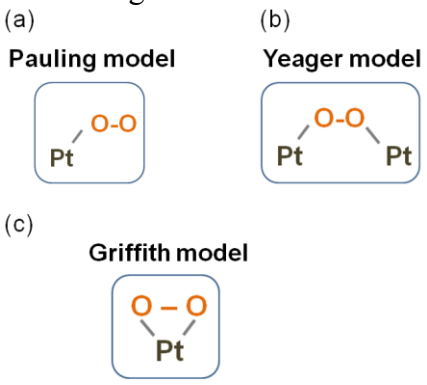

Figure 4.6: Schematic diagram of the surface oxidation on the catalysts: (a) and (b) Pt surface (high and low current densities, respectively) [7], and (c) Pt-alloy surface (Pt-Cu/C and Pt_3Co/C) [18].

4.3.2.4. Oxide coverage

From the EQCN response, it is seen that the nature of the oxide and the oxide growth on the alloy catalysts (for elements inducing compressive strain on Pt) is different from that on the Pt catalyst. The interfacial mass change on the binary alloy catalyst proceeds via the formation of a hydroxyl intermediate, which accounts for 1 electron per surface site whereas the oxide growth on the pure Pt catalyst accounts for 2 electrons per Pt site resulting in the formation of PtO for which the coverage is less than unity at 1.1 V as seen from Figure 4.7. This behavior is a result of a modification of the properties of the surface Pt layers by the underlying metal, the effect of which has been found to be operative up to approximately 5 surface layers [59]. It is also reported that the rate of the ORR on a catalyst surface is limited by the removal of the adsorbed oxide intermediates on the surface [60]. The formation of hydroxyl intermediates shows that hydroxyl rather than oxide intermediates increase the ORR rates as reported [61] for the core-shell and binary alloy catalysts.

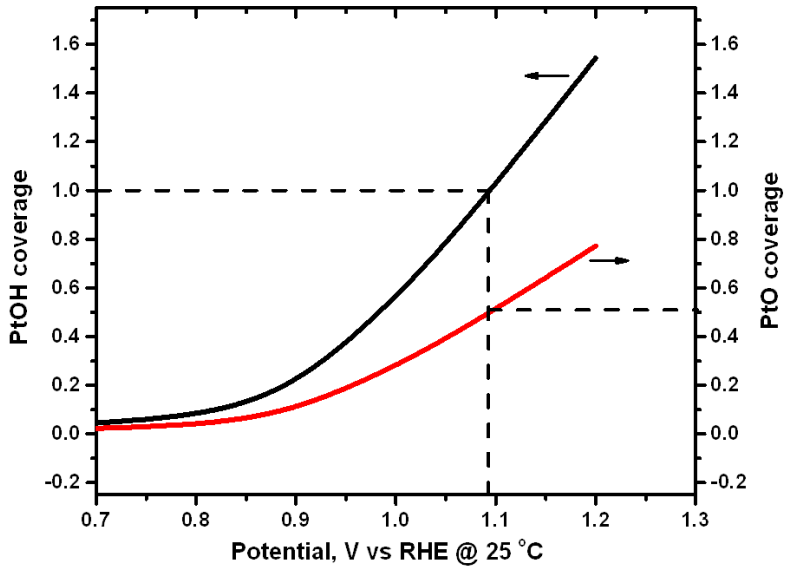

Figure 4.7: Surface oxide coverage on the catalysts.

4.3.2.5. Accelerated degradation tests

The durability tests were carried out to evaluate the performance of the catalysts under different operating conditions of the fuel cell. It has been reported that continuous cycling in the oxide formation-reduction region leads to higher degradation rates [43]. The various losses and their causes are given below:

- Loss in $ECSA_{Pt}$ (equivalent to loss of active Pt surface sites) due to Ostwald ripening, particle migration, sintering, recrystallization/redeposition of particles, all of which result in bigger particles and loss of metal into the solution;
- Mass loss in solution (Pt in solution) due to corrosion of carbon support and the metals, metal loss due to dissolution of surface oxide when the bond between the metal surface and the adsorbed oxide is stronger than the metal-metal interaction;
- Performance loss (mass-activity loss equivalent to loss of Pt surface sites) due to larger particles, and fewer active sites;
- Loss in half-wave potential (overpotential/voltage drop) due to resistance to the conduction of electrons and loss of carbon support.

Increase in $ECSA_{Pt}$ loss with lower concentration of dissolved Pt species indicates the increase in the particle size whereas a higher concentration of dissolved Pt species with a lower $ECSA_{Pt}$ loss indicates the corrosion of carbon support and metal exposing new surface active sites for reaction with minimum growth in particle size.

The degradation tests at different upper potentials provide information on the influence of the surface oxide on the dissolution rates as a function of potential (Figure 4.8). Accelerated cycling at 1.3 V shows the durability of the catalysts in the dynamic PEFC environment (Figure 4.9). Comparison of unsupported Pt and Pt/C shows that the loss of active area is higher for the unsupported Pt catalyst than that of Pt/C. This loss is due to the higher rate of agglomeration and growth of the unsupported Pt nanoparticles

forming larger particles, which also results in a higher loss of mass activity (Figure 4.9b). The higher loss in the half-wave potential (Figure 4.9c) and increase in dissolved species (Figure 4.8b) of Pt/C indicates the corrosion of the carbon support. It is seen that the carbon support increases degradation losses.

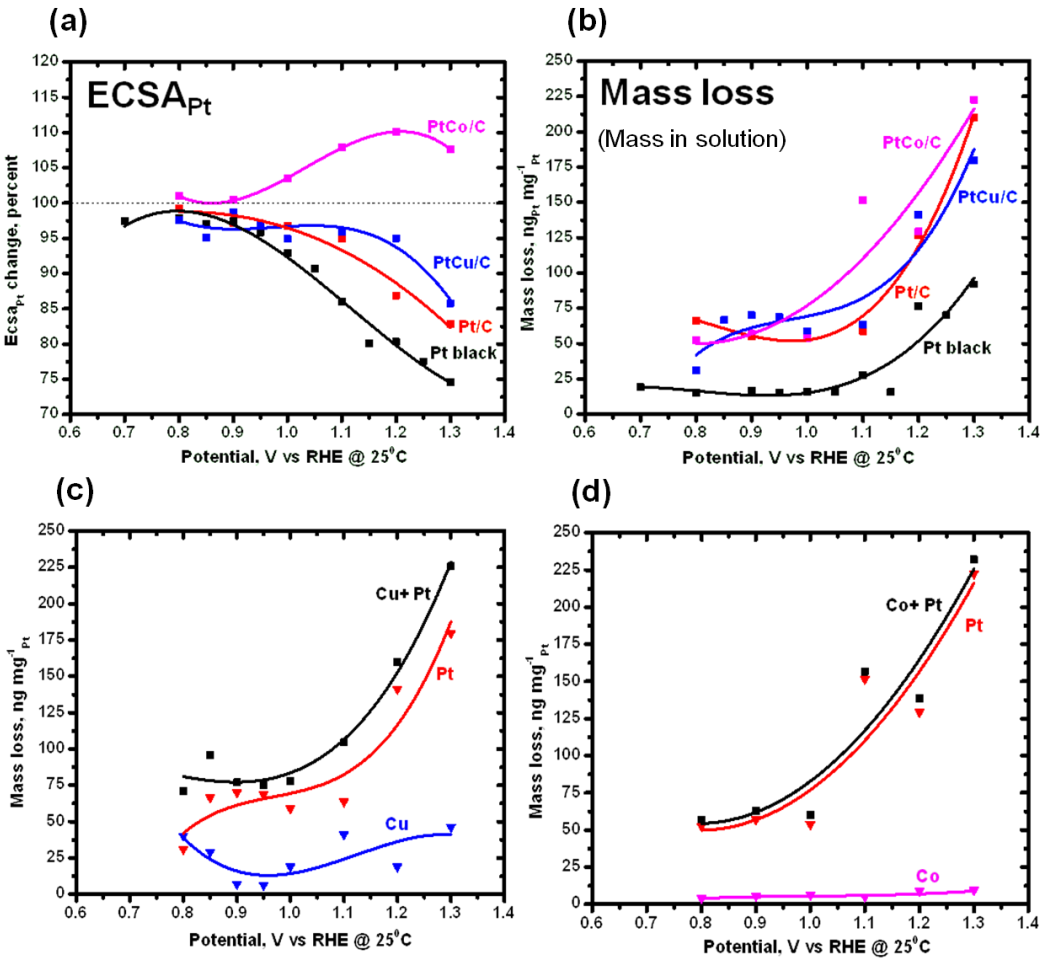

Figure 4.8: Change in the catalyst performance as a function of upper potential, E_H: (a) change in $ECSA_{Pt}$, (b) mass loss (amount of species in solution), (c) amount of Pt and Cu in solution (core-shell Pt-Cu/C), and (d) amount of Pt and Co in solution (Pt_3Co/C).

The unalloyed catalysts showed a continued degradation with potential cycling. In the case of the alloyed catalysts, dissolution of the base metal (Figures 4.8c and 4.8.d)

was observed even though the overall degradation rate is lower than that of Pt. The results showed that the core-shell Pt-Cu/C had a lower rate of carbon corrosion, which could be due to the type of support (high-surface-area carbon) used to synthesize the precursor. Though monolayer oxide coverage is formed at potentials > 1.1 V, there is an increased Pt dissolution in this region as seen from the results of Figure 4.8. This loss indicates increased corrosion of the carbon support, which is catalyzed by surface oxidation on the catalyst.

The Pt_3Co/C alloy catalyst had a higher performance loss than Pt/C in the first 500 cycles (Figure 4.9 b and c). The ECSAPt of Pt_3Co/C initially increased with cycling (Figures 4.8a and 4.9a), but the amount of dissolved Co in the solution (Figures 4.8d and C.2) did not increase significantly with cycling at different potentials. These results indicate that there is no correlation between Co loss and the decrease in performance in the first 500 cycles, Figure 4.9, or the increase in the electrochemical area of the catalyst and the dissolution of the base metal as has been reported [62]. Based on the experimental results, it can be concluded that the Pt_3Co/C catalyst undergoes corrosion of the carbon support and metal during the first 500 cycles. The increase in the electrochemical area with cycling indicates the resistance to sintering and growth in particle size for the Pt_3Co/C alloy catalyst. To understand better the degradation behavior of the alloy catalyst and Co dissolution, more insight into the microstructure of the catalyst is required. It has been reported that in the region of 75 at. % Pt, the alloy can show ordering with the ordered phase being ferromagnetic at room temperature [63]. Magnetic measurements on Pt_3Co/C showed a superparamagnetic behavior (1.56–1.57 Bohr magneton, appendix C: Figure C.3), which indicates ordering of Pt and Co in the catalyst. A lower concentration of Co ions in the solution (Figure 4.8d) indicates that the surface Co atoms migrate into the alloy particle forming a Pt-rich shell during

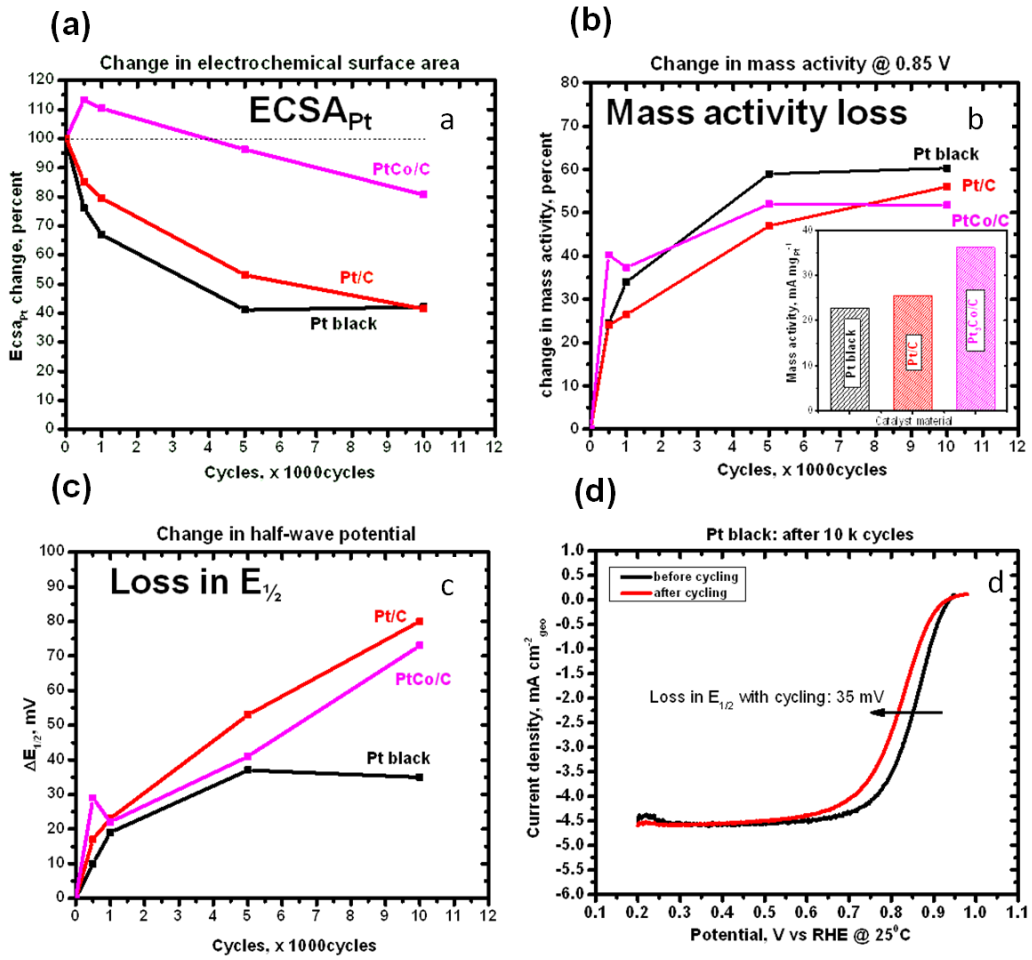

Figure 4.9: Change in the catalyst performance as a function of potential cycling: (a) change in $ECSA_{Pt}$, (b) loss in mass activity at 0.85 V (inset: initial mass activity of the catalysts), (c) loss in the half-wave potential, and (d) typical ORR curve showing the direction of change in half-wave potential with degradation.

electrochemical cycling. It has also been reported that the ordered structure forms a core-shell structure during electrochemical cycling in an acid medium [64]. The core-shell would be favored by loss of surface Co and retention of Co in the bulk by ordering of the Co as a result of the strong anti-segregation energy of Co in a Pt host [65]. The catalyst behavior as shown in the Figures (4.8 and 4.9) is due to this surface modification during cycling.

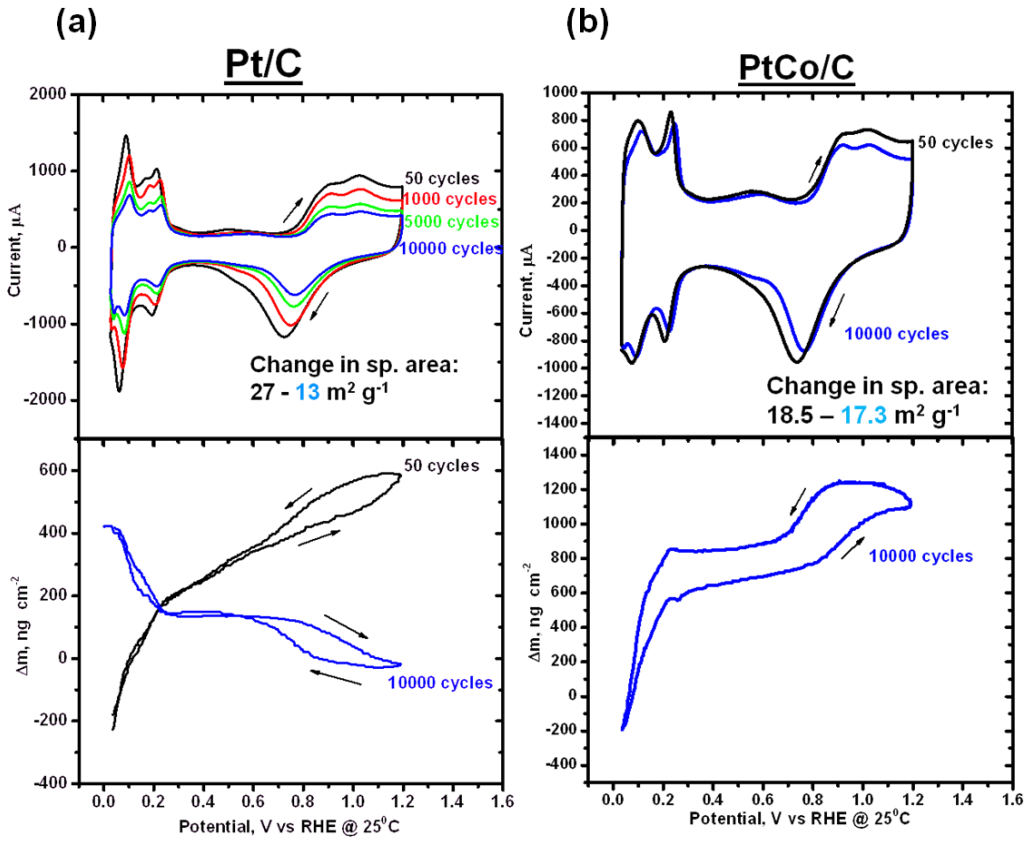

Figure 4.10: Combined CV and EQCN response of the catalysts as a function of potential cycling in 0.5 M H_2SO_4 between 0.4 and 1.3 at 50 mV s^{-1}: (a) Pt/C, and (b) Pt_3Co/C.

A study was carried out to evaluate the change in the coordination environment of the metal atoms with cycling and its influence on the type of surface oxide. The amount of adsorbed species (M) was monitored as a function of potential cycling. The combined CV and EQCN response for the accelerated degradation tests is shown in Figure 4.10. The EQCN response loop changes sign in the region of H adsorption on Pt and the loops are in the opposite direction in the region of oxide formation for the Pt/C catalyst after 10000 cycles (Figure 4.10a). The EQCN response of the Pt_3Co/C catalyst does not change sign even after 10000 cycles (Figure 4.10b). The change in sign is due to a

roughening of the catalyst surface with accelerated degradation. The EQCN response indicates that the binary alloy catalysts are more stable under the operating conditions of the PEFCs. The absolute value of the adsorbed species (M) was the same before and after 10000 cycles, *i.e.*, approximately 8 g mol^{-1} (O) and 17 g mol^{-1} (OH), respectively, for Pt/C and Pt_3Co/C catalysts. This value of M shows that the coordination environment of the catalysts does not change with cycling. The study also shows that the roughness of the electrode surface has a profound influence on the EQCN response. A rough surface retains electrolyte within the pores, which dissipates the vibration frequency causing a shift in frequency.

4.3.2.6. Determination of H_2O_2 intermediates

A study was carried out to identify the 4-electron vs. 2-electron mechanism for the ORR on the catalysts and to compare them with the amount of surface oxide. The results are shown in Figure 4.11. The efficiency for the collection-generation experiments was evaluated as described in Section 2.3.8 and the results are given in Figure 4.11a. The disk was scanned from 0.1 to 1.0 V at 10 mV s^{-1} while the ring was held at 1.2 V, the potential at which the oxidation of H_2O_2 was diffusion-limited on the surface. The results reported are for a rotation rate of 1600 rpm. The amount of H_2O_2 generated and the selectivity of the catalyst were determined by Equations (2.10) and (2.11), respectively. The results are dependent on the catalyst loading and electrode thickness, the values of which are given in Table 4.3.

There was no significant change in the peroxide formation for the different catalysts. The amount of peroxide decreased as the disk potential was increased as seen

Table 4.3: Details of catalyst film for H_2O_2 measurements

Type of catalyst	Catalyst loading, µg cm^{-2}_{geo}		Film thickness, µm
	Pt	C	
Pt black	225.76	0	0.435
Pt/C	72.70	109.05	0.769
Pt_3Co/C	69.22	114.29	0.815

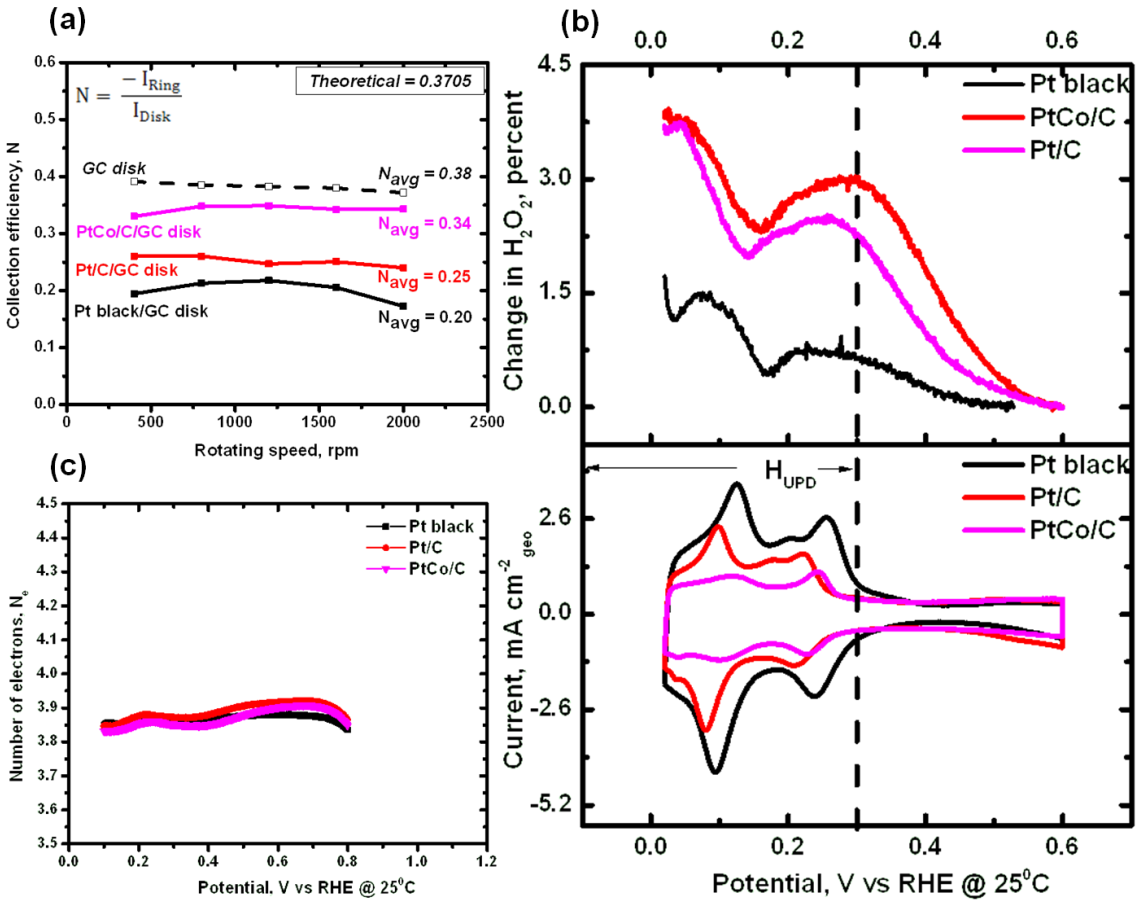

Figure 4.11: (a) Collection efficiency of the catalysts as a function of the rotating speed, (b) change in amount of H_2O_2 collected at the ring electrode and the corresponding voltammogram of the H-region (the disk electrode was scanned from 0.1 to 1.0 V at 10 mV s^{-1} and the ring electrode was held at 1.2 V in 0.5 M H_2SO_4), and (c) selectivity of the catalysts.

from Figure 4.11b. The highest value of the peroxide was seen in the H_{UPD} region where the under-potential-deposited H makes it difficult to dissociate the adsorbed O_2 molecule on the electrode. The mechanism for the ORR is close to the direct 4-electron-transfer reaction on the catalysts. It has been reported that the peroxide content decreases as the catalyst loading and film thickness increases [66].

4.4. CONCLUSIONS

The type and nature of the adsorbed oxide on the Pt catalyst and Pt alloy catalyst has been identified, respectively, as O and OH species. Although, this study correlates the nature of the adsorbed intermediates on the catalyst surface with the stress/strain introduced on the host metal (Pt) by the alloying elements (Cu, Co and Sc), it also correlates with the average strength of the Pt bonding with near-neighbor atoms; the competition of the catalyst M-M versus M-O bonding appears to be the more critical factor. In this study, we have shown that understanding the preformed surface oxides on the catalyst surface is important for predicting the mechanism of the ORR on the catalyst surface. The description of the surface oxide on a binary alloy can show the influence of the adsorbates on the durability of the catalyst surface as the extent of catalyst dissolution depends on the formation of Pt oxide (*viz*., O or OH) as seen from the results presented in this work. Also confirmed by the experiments is that the type of oxide remains unchanged with accelerated cycling.

PALLADIUM-BASED CATALYSTS

Palladium (Pd) and Pd alloys are being explored as an alternative to the platinum-based catalysts for use in low-temperature fuel cells (polymer electrolyte fuel cells – PEFCs, direct methanol fuel cells – DMFCs and direct formic acid fuel cells – DFAFCs). Pd alloys are considerably less expensive than platinum. Pd-based catalysts also have high methanol tolerance as cathode catalysts for DMFCs in which the methanol crossover to the cathode significantly decreases the efficiency of the fuel cell.

Pd forms compact surface oxides on anodic polarization as seen from the Pourbaix diagram [67]. These affect the electrode stability and limit the electron transfer kinetics of fuel-cell reactions. Several approaches have been attempted to resolve this problem and increase the activity of the catalysts towards oxygen reduction reactions (ORR). These include alloying Pd with other metals, thereby increasing the catalytic activity while maintaining a high tolerance to methanol crossover.

In this section, Pd-based fuel-cell catalysts such as carbon-supported Pd nanoparticles and Pd binary-alloy nanoparticles synthesized by the polyol method are studied. The surface analysis by EQCN on the carbon-supported palladium-based nanoparticles is reported for the first time. Pd-alloy catalysts are compared against the as-prepared Pd/C catalysts.

5. Investigation of the surface phenomena on carbon-supported palladium-gold binary-alloy catalysts

5.1. INTRODUCTION

Palladium-gold (Pd-Au) alloys are often used as catalysts in a number of chemical and electrochemical reactions [68-70]. The catalytic properties of these alloys for different reactions, e.g., oxygen reduction [71] and oxidation of carbon monoxide [72] and methanol [73], and the electrochemistry of hydrogen absorption [74, 75] and surface oxidation [76, 77] on these alloys have been a subject of investigation for a long time. Recently, Pd-Au catalyst particles on different supports have found much use in low-temperature fuel cells [78, 79]. Not much has been reported on the interfacial changes on these catalysts during the different electrochemical reactions, especially in the potential range of surface oxidation of these catalysts. Using different experimental techniques to study the oxide formation on Pd-based catalysts, several authors have suggested the formation of PdOH as the first step of the oxidation of Pd in both acidic and basic medium [80-82] based on the mechanism of oxidation of platinum (Pt) proposed by Conway [28]. However, detailed investigation of the Pt surface by nanogravimetry measurements proved this mechanism is invalid on Pt [58, 49].

Palladium (Pd) alloyed with other metals exhibits unique physical and chemical properties that are different from those of the pure metals. Several types of synergistic effects have been reported for these Pd alloys [83, 84]. Gold, by itself, is not a good catalyst. However, when alloyed with Pd, it changes the activity and selectivity of Pd catalysts [85]. Au has a high electronegativity, high work function [22], and a larger lattice constant than Pd. It also has negative segregation energy (moderate) when used as a solute in a Pd host [65].

The primary objective of this study is to understand the effect of alloying Pd with the noble metal Au on the surface phenomena (surface oxidation) of the binary alloy catalyst nanoparticles. Electrons flow from Pd to Au when they form an alloy as the work function of Pd is lower than that of gold. The resultant work function of the alloy is higher than that of pure Pd. The electronic structure may also be affected by the differences in the atomic sizes of these atoms in the alloy and the surface compositions (due to difference in segregation energy). In this study, we determine the influence of the ligand effect (electronic modification) in the alloy on the type and amount of adsorbed species during the surface oxidation of the alloy catalyst by using a surface-sensitive technique to measure the interfacial mass changes. Further, study is carried out to analyze the durability of the catalyst nanoparticles as a function of the adsorbed oxide.

In this work, we present results on the surface phenomena of carbon-supported Pd_3Au binary alloy catalysts. The catalysts for this study were synthesized by the easily scalable polyol reduction and were characterized by different techniques described in Chapter 2. The results of this investigation help us to understand the effect of the degree of alloying on the surface oxidation and the stability of the alloy catalysts.

5.2. EXPERIMENTAL METHODS

5.2.1. Catalyst synthesis

Carbon-supported Pd_3Au catalysts with a 40 wt. % metal loading were synthesized by the polyol method. In a typical experiment, 125 mg of carbon black was dispersed in 48 mL of ethylene glycol by ultrasonication and magnetic stirring. The pH of the solution was adjusted by drop-wise addition of 16 mL of 1 M NaOH (in ethylene glycol) to obtain a final concentration of 0.12 M NaOH. Palladium (Pd) and gold (Au) metal precursor solutions were prepared by dissolving the metal salts separately in

ethylene glycol to obtain 0.012 M Pd and 0.006 M Au salt solutions, respectively. Sodium tetrachloropalladate (Na_2PdCl_4, Pd precursor) and auric chloride ($HAuCl_4.3H_2O$, Alfa Aesar) were used as the metal precursor salts. The EG to precursor ratio was maintained at 0.7 (approx.). The precursor salt solutions were added drop wise to the carbon-ethylene glycol dispersion and heated to 150 ^oC for 2 hours under continuous stirring. The synthesis was carried out under an inert atmosphere by continuous purging of the solution with ultrapure nitrogen gas (N_2). After cooling the polyol solution, the supported catalysts were filtered, washed with ultrapure water ($\geq$ 18.2 MΩ.cm), and dried overnight in a vacuum oven. The as-prepared catalyst nanoparticles are hereafter referred to as Pd_3Au/C-as. The catalyst samples were further heated in a tube furnace under a reducing atmosphere (10% H_2/ 90% Ar gas) and at a ramp rate of 5 $^oC\ min^{-1}$ to 200 ^oC and 300 ^oC, respectively, for 2 hours. The heat treated samples are, hereafter designated as Pd_3Au/C-200 and Pd_3Au/C-300, respectively. For a comparison, a Pd/C catalyst was also prepared by a similar procedure and is denoted as Pd/C-as. The details of the polyol method are given in Section 2.1.

5.2.2. Structural/chemical characterization

Bulk metal compositions were determined with an SEM-EDS (JEOL-JSM5610) scanning electron microscope as described in Section 2.2.2. The metal loading in the carbon-supported catalysts was determined by TGA as described in Section 2.2.3. The near-surface composition was determined by X-ray photoelectron spectroscopy measurements as given in Section 2.2.6. The structural characterization of the catalysts was carried out with a Philips 3520 X-ray diffractometer as described in Section 2.2.1. Particle size distribution was determined with a JEOL 2010F TEM as described in Section 2.2.4.

5.2.3. Electrochemical characterization

5.2.3.1. Preparation of catalyst ink and electrode

The catalyst inks were prepared by mixing a known amount of the catalyst powder in 5 wt. % Nafion solution and 2-propanol-water mixture as described in Section 2.3.1. 60 µL of the homogeneous ink was drop-cast onto the gold-coated quartz crystal sensor (5 MHz) with a geometric area of 1.37 cm^2 and allowed to dry at room temperature. The method of ink preparation was the same for all the catalyst materials being studied. The thickness of the dry-cast film was maintained less than 0.5 µm. The details of the cast electrodes are given in Table 5.1.

Table 5.1: Ink loading for different catalysts

Catalyst	Loading level, µg cm^{-2}			Thickness of dry film, µm	Nafion, wt. % (dry film)
	C	PGM	Metal		
Pd/C – as	50	34	34	0.37	21.45
Pd_3Au/C – as	60	26	40	0.43	21.45
Pd_3Au/C – 200	56	24	37	0.41	22.83
Pd_3Au/C – 300	58	25	39	0.42	22.12

5.2.3.2. Cyclic voltammetry (CV)

The electrochemical characterization was carried out by cyclic voltammetry (CV) as described in Section 2.3.

5.2.3.3. Electrochemical quartz crystal nanobalance measurements (EQCN)

The *in situ* mass measurements were performed with an EQCN setup as described in Section 2.3.3. A batch cell with a 5 MHz sensor was used for the measurements. The capacitance cancellation adjustment was performed with the crystal (electrode) in the

actual solution used for electrochemical measurements and under a potential hold condition.

The amount of adsorbed intermediate on the electrode surface was obtained from the combined CV and EQCN measurements for the potential cycling. The details are given in Section 2.3.4.

Accelerated degradation tests were carried out by cycling the electrodes between 0.4 and 1.24 V at 100 mV s^{-1} for 150 cycles. The amount of surface oxide was measured before and after cycling by the combined CV and EQCN measurements for a potential cycling of 0.4 to 1.24 V at 50 mV s^{-1}.

5.3. RESULTS AND DISCUSSION

5.3.1. Structural/chemical characterization

5.3.1.1. EDS and TGA analysis

Bulk compositions determined by EDS and TGA are reported in Table 5.2 and are comparable with the nominal composition based on the stoichiometric amount of precursor salts taken for synthesis. The extent of alloying can be seen from the EDS line scans and the TGA curves given in the appendix (Figure D.1). The alloy density (ρ_{alloy}) in g cm^{-3} was calculated as given by Equation (2.2).

Table 5.2: Compositional data analysis of the Pd_3Au/C and Pd/C catalysts (EDS and TGA)

Catalyst	Metal, at.% (nominal)	Metal (bulk), at.%, (EDS)	Metal loading, wt.% (TGA)	Average, density, g cm^{-3}
Pd/C	-	-	39.4	12.023
Pd_3Au/C	$Pd_{75}Au_{25}$	$Pd_{77.7}$ $Au_{22.3}$	35.5	13.836

5.3.1.2. XPS analysis

The XPS spectra to determine the near-surface characteristics of the catalysts are shown in Figure 5.1 and the fitted spectra of the different catalysts are shown in Figure 5.2. The elemental quantification is obtained from the peak intensities (peak area). The peak with the largest peak area is chosen for the elemental quantification. The most intense peak for Pd was the Pd $3d_{5/2}$ signal. However, this had an interference with the Au 4d signal. The most intense peaks of Pd (Pd $3d_{3/2}$) and Au (Au $4f_{7/2}$) without interferences were chosen to quantify the surface composition of the alloy catalysts. The relative sensitivity factors (R.S.F) were adjusted accordingly to include one peak of the doublet pair for elemental quantification (Au $4f_{7/2}$, 3.5714; Pd $3d_{3/2}$, 2.1424).

The Au 4f XPS spectra, as shown in Figure 5.1a, indicated the presence of Au^o species (doublet pair). It is seen that the Au 4f BE shifted to lower values as the temperature increases. The standard peak for the pure Au metal is 84 eV (Au $4f_{7/2}$) [36]. This decrease in the Au binding energy for the Pd_3Au/C alloy suggests electron transfer from Pd to Au, which is related to the electronic interaction (due to the difference in the work function of the pure metals) and the alloy formation. The XPS spectra of Pd, as shown in Figures 5.1b, indicates the doublet pair of elemental Pd (Pd^o) and different chemical states (from shape of the spectra). It is seen that the Pd 3d binding energy values do not shift significantly for the different catalysts (BE of Pure Pd: 340.36 eV (Pd $3d_{3/2}$)) [36]. However, there is a change observed in the shape of the spectra as the heat treatment temperature is increased, suggesting changes in near-neighbor composition of the different chemical states of Pd. The ratio of Au-to-Pd peak intensities (Figure 5.1c) as a function of the heat-treatment temperature suggests a mixing of Au with Pd at higher temperature. The binding energy values of the Au and Pd peaks as a function of temperature are shown in Figure 5.1d.

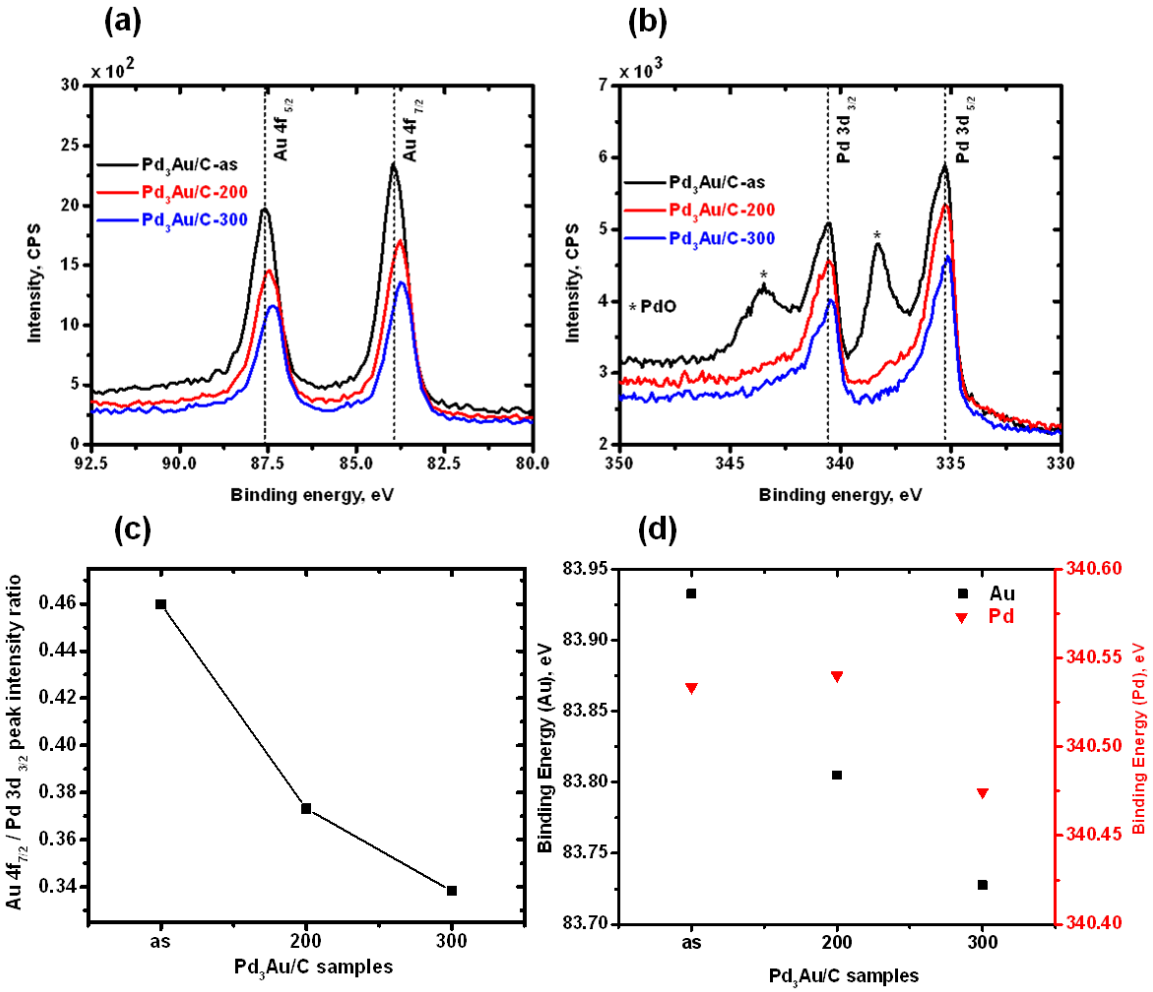

Figure 5.1: (a) XPS spectra of Au 4f, (b) XPS spectra of Pd 3d, and (c) ratio of peak intensity of Au $4f_{7/2}$ and Pd $3d_{3/2}$.

Table 5.3: Near-surface compositional data analysis from XPS spectra of the Pd_3Au/C catalysts

Catalyst	**Au, ($4f_{7/2}$), at. %**	**Pd, ($3d_{3/2}$), relative at. %**		
		Pd^0	**Pd-O_{ads}**	**PdO (Pd^{2+})**
Pd_3Au/C – as	16.90	39.45	10.35	33.3
Pd_3Au/C – 200	21.62	51.4	19.5	7.48
Pd_3Au/C – 300	22.41	47.57	24.74	5.28

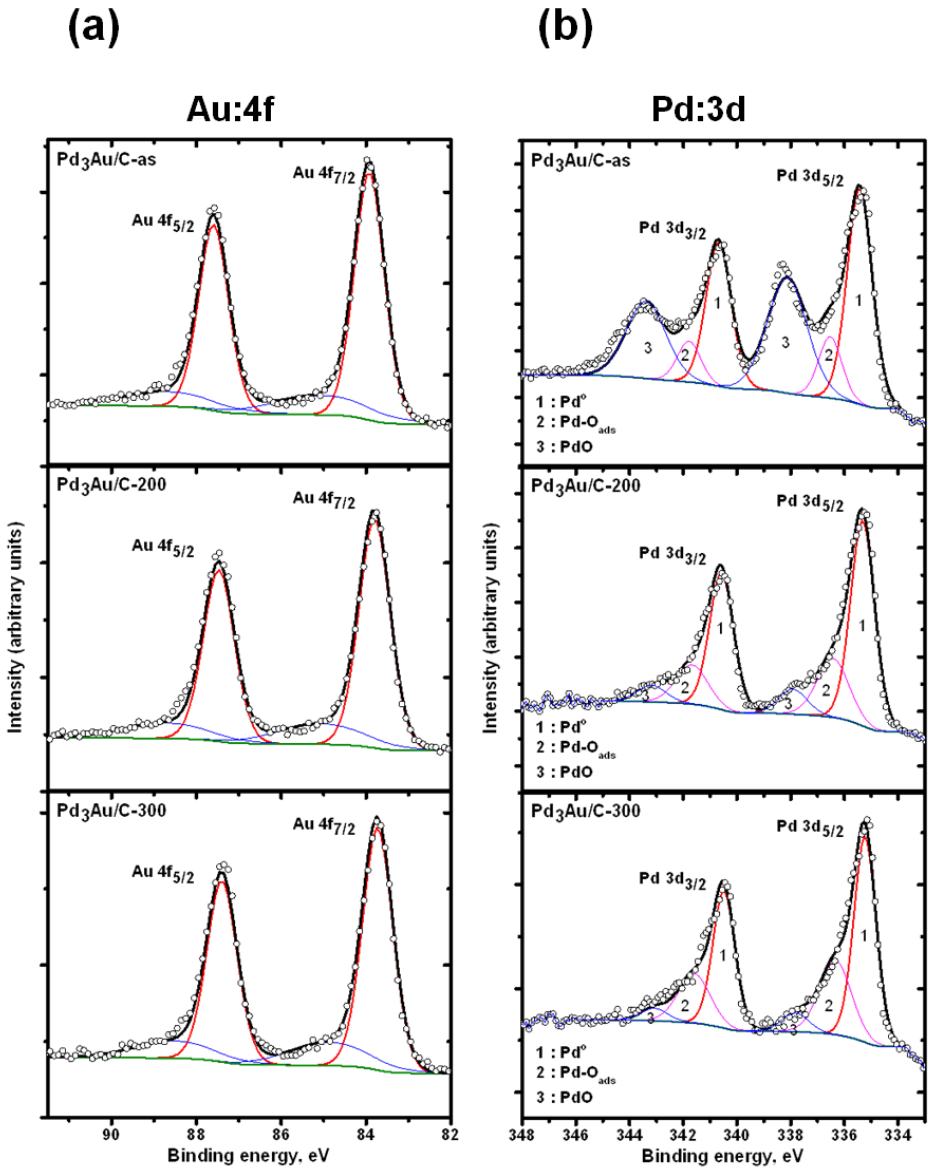

Figure 5.2: Core-level XPS spectra with the deconvolution fits: (a) Au 4f region, and (b) Pd 3d region, the open circles indicate experimental data.

The chemical states of the components can be identified from the deconvoluted core-level (Figure 5.2) XPS spectra of Au 4f and Pd 3d. In Figure 5.2a (Au 4f), the peaks correspond to Au^{o} (elemental Au) and Au-$2O_3$ [86]. The three peaks in the Pd spectra (Figure 5.2b) correspond to Pd^{o} (elemental Pd), Pd-O_{ads}, and Pd^{++} (PdO), respectively

[86]. From XPS analysis, it can be seen that all the oxidized Pd atoms in the as-prepared sample were reduced in H_2 at 300 ^oC. Also, the difference in the state of Pd atoms before and after high temperature treatment shows that the Pd atoms were located on the surface, probably in ensembles, in the as-prepared catalysts. The relative compositions are summarized in Table 5.3. The survey scans are shown in Figure D.2 (appendix D).

5.3.1.3. XRD analysis

Figure 5.3 compares the XRD patterns of the Pd_3Au/C and Pd/C samples prepared by the polyol method before and after heat treatment at various temperatures under a reducing atmosphere. All the peaks can be indexed with the f.c.c crystal structure. The absence of impurity peaks indicates the formation of a pure single-phase disordered Pd-Au binary alloy. This observation confirms the miscibility of Pd and Au as seen in the binary phase diagram [87] for the atomic ratio considered in this paper. As the heat-treatment temperature increased, the peaks were located closer to the Pd Bragg lines.

From the Williamson-Hall analysis for the Pd_3Au/C samples, as prepared and heat treated at 200 ^oC and 300 ^oC, the microstrain involving local lattice distortions was found to be, respectively, 0.034, 0.049 and 0.013. The average crystallite size, calculated from the Scherrer's formula increased with increasing temperature. The d-spacing, as obtained for the (220) peaks, decreased with increasing temperature, which corresponds to a reduction of the lattice parameter indicative of the progressive replacement of the larger Au atoms (atomic radius: 1.74 Å) in the f.c.c crystal structure by the smaller Pd atoms (atomic radius: 1.69 Å). The increased alloying with increasing temperature is confirmed by the negligible difference between the observed (a = 3.9277 Å, Pd_3Au/C-300) and calculated (a = 3.9326 Å, Végard's law for a continuous substitutional solid solution) values of the lattice parameter for the alloy catalyst. The fraction of Au (x) in the lattice

was calculated with Equation (2.1). A uniform metal loading (40 wt.%) was maintained for all catalysts to ensure a uniform effect of the carbon support on alloying. The particle surface area in m^2 g^{-1}, was calculated with the equation, $S_A = 6000/d\rho$, assuming spherical particles, where d is the crystallite size in nm and ρ is the density of the Pd-Au alloy in g cm^{-3}. The Pd surface density (cm^{-2}), number of surface atoms and total number of atoms in a particle, were calculated with the Benfield approximation for a spherical particle [50]. It has been reported that icosahedral and cuboctahedral particles can be approximated as quasispherical particles. The particle surface area decreased and the Pd surface-atom density increased with increasing temperature owing to an increase in the crystallite size. The degree of dispersion of Pd was essentially complete in the Pd_3Au/C-300 catalyst. All the values are given in Table 5.4.

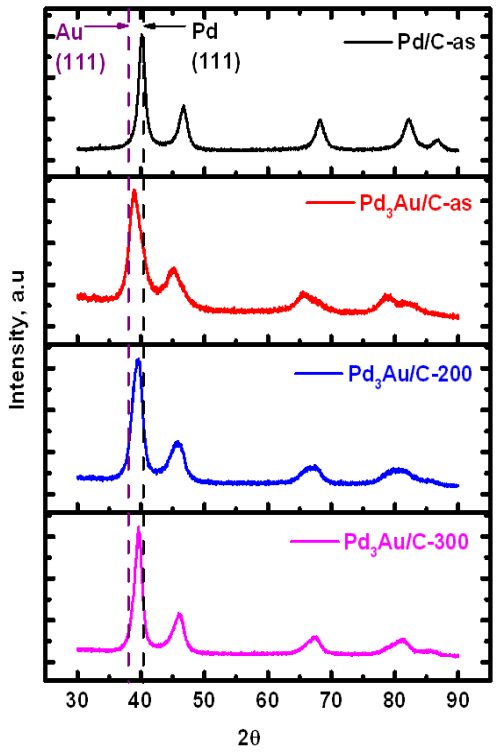

Figure 5.3: XRD patterns of the catalyst samples with the expected positions of Pd (111) and Au (111) peaks.

Based on the analysis of XPS and XRD, the catalysts could be categorized as having a surface with blocks of Pd in the Pd_3Au/C-as and Pd randomly distributed in the Pd_3Au/C-300 samples as shown in Figure 5.4.

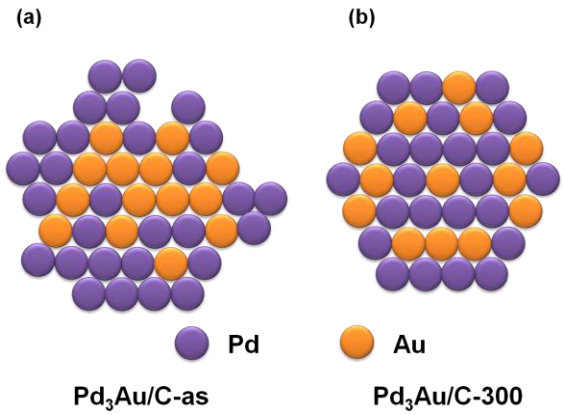

Figure 5.4: Schematic diagram illustrating the elemental distribution in the (a) Pd_3Au/C-as and (b) Pd_3Au/C-300 samples.

5.3.1.4. TEM analysis

The TEM images and the particle size distribution of the catalysts obtained from Gaussian models are shown in Figure 5.5. As seen, the synthesized particles have predominantly a spherical morphology. The evaluation of the diameter of the catalyst nanoparticles from an ensemble of 100 particles indicate an average particle size value of 3.90 and 4.25 nm, respectively, for the Pd_3Au/C-as and Pd_3Au/C-300 samples with a wide size distribution for both catalysts. The size distribution between the as-prepared and heated samples is comparable with that obtained from XRD (Table 5.4).

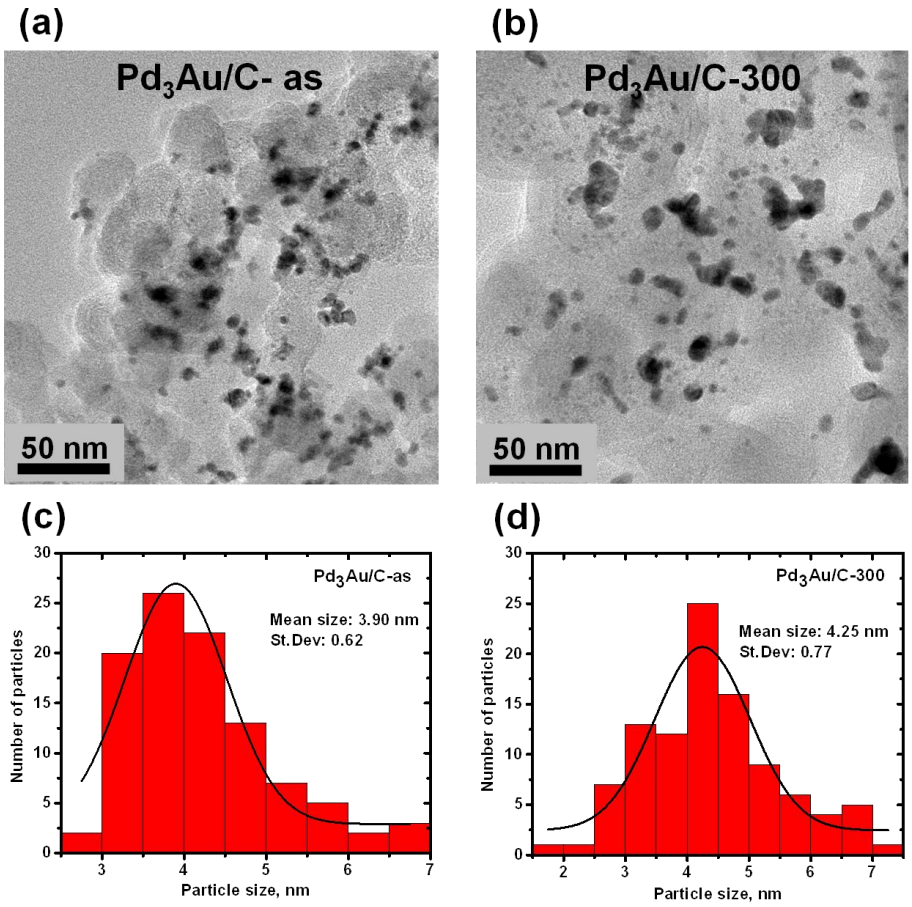

Figure 5.5: (a) and (b) TEM images, and (c) and (d) particle size distributions of Pd_3Au/C-as and Pd_3Au/C-300 samples, respectively.

Table 5.4: Data obtained from XRD and TEM analysis of the Pd_3Au/C and Pd/C catalysts

Catalyst	Crystallite size (avg.), nm (XRD)	Particle size, nm (TEM)	Lattice parameter, Å (XRD)	d-spacing (220), Å (XRD)	Fraction of Au in the lattice	Surface area, S_A, $m^2\ g^{-1}$ (metal)	Pd surface atom density, cm^{-2}	Degree of dispersion	
								Pd	Au
Pd/C – as	6 ± 1	-	3.8914	1.3744	-	99.81	1.03×10^{15}	28.3	-
Pd_3Au/C – as	3 ± 1	3.90 (0.62)	4.0310	1.4247	0.76	144.55	6.68×10^{14}	33.7	11.2
Pd_3Au/C – 200	3.5 ± 1	-	3.9524	1.3964	0.33	123.90	7.07×10^{14}	29.5	9.9
Pd_3Au/C – 300	4 ± 1	4.25 (0.77)	3.9277	1.3881	0.20	108.41	7.34×10^{14}	26.0	8.7

Surface atom density and the degree of dispersion were calculated assuming the composition on the surface to be the same as that in the bulk.

5.3.2. Electrochemical characterization

5.3.2.1. Electrochemical behavior of Pd-based electrodes

A typical voltammogram for the Pd_3Au/C electrode cycled between 0.05 and 1.24 V at 50 mV s^{-1} in 0.5 M H_2SO_4 (pH = 0.3) is shown in Figure 5.6a. In the hydrogen region, H absorption/adsorption and subsequent desorption take place; and in the oxide region, surface oxide formation and reduction occur. The different reactions in the hydrogen and oxide regions of a palladium electrode as given in the Pourbaix diagram [67] are summarized in Figure 5.6b. It is seen from the Pourbaix diagram [67] and Figure 5.6b that hydrogen dissolves into Pd forming α (solid solution of H in Pd) and β (non-stoichiometric metal hydrides) phases [88]. In such cases, it becomes difficult to differentiate between H_{UPD} and $H_{absorbed}$. Therefore, the determination of the real surface area of Pd is not as straightforward as that of Pt, which involves the determination of the charge associated with monolayer coverage of hydrogen on the Pt surface (H_{UPD}). It also becomes important that the Pd electrode is not cycled into the hydrogen region to avoid bonding changes being introduced into the electrode due to hydrogen absorption. The Pd catalysts in this study were cycled in the range of 0.4 to 1.24 V. The voltammograms were recorded within the potential limits of Pd and not extended into the region of Au. It is also seen that several competing reactions (*viz*., surface oxidation, dissolution of metal, dissolution of surface oxide) occur in the oxide region on Pd (Figure 5.6b) [67]. A mass loss was seen between consecutive cycles during the CV of the alloy catalyst as shown in Figure 5.7 though no noticeable changes were seen in the corresponding voltammograms. This observation indicates that the catalyst surface undergoes dissolution during electrochemical cycling. A typical EQCN response of a Pd-based electrode with regions of mass-change is shown in Figure 5.8. It is seen that during the anodic scan there is a

loss of mass after the onset of oxide formation on the surface. The mass loss represents the presence of surface oxide that undergoes chemical dissolution when in contact with the protons in the acidic solution, leading to a mass decrease in the potential range of 0.88 to 1.0 V as reported in the Pourbaix diagram [67]. Surface oxidation continues during the anodic scan. Reduction of the surface oxide occurs during the potential reversal. A mass gain is seen in the potential range of ~ 0.67 to 0.4 V during the reduction of the surface oxide. The mass gain is due to the partial redeposition of metal ions from the electrolyte (reactions given in Figure 5.6b). It is also seen from the Pourbaix diagram that the deposition of the ions is a function of the concentration of the ions in the solution.

(a)

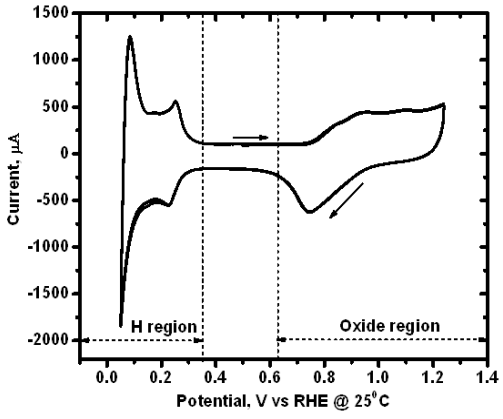

(b)

Reactions in H region	Reactions in oxide region
$Pd_2H = 2\,Pd + H^+ + e^-$	$Pd + H_2O = PdO + 2H^+ + 2e^-$
α & β phases formed	$Pd = Pd^{++} + 2e^-$
	$Pd^{++} + H_2O = PdO + 2H^+$
	$Pd^{++} + 2H_2O = PdO_2 + 4H^+ + 2e^-$

Figure 5.6: (a) Typical cyclic voltammogram of Pd_3Au/C-300 catalyst in 0.5 M H_2SO_4, between 0.4 and 1.24 V at 50 mV s^{-1} and 25 ^oC, and (b) different reactions occurring on the surface of Pd as given in the Pourbaix diagram [67].

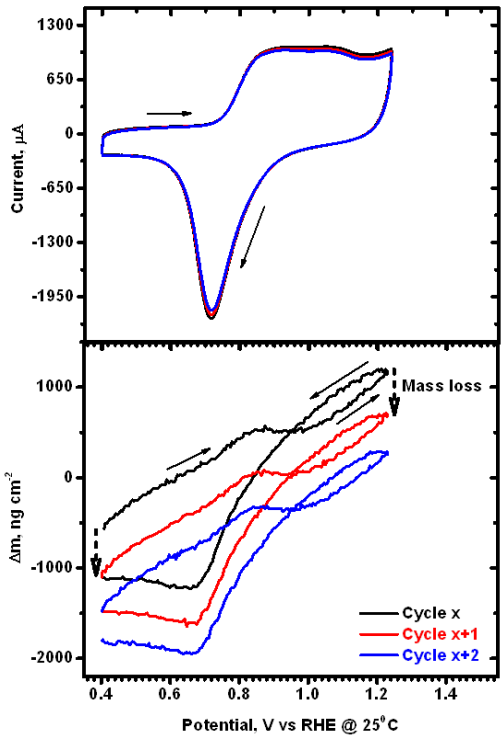

Figure 5.7: (a) Typical CV and EQCN response of Pd-based catalyst (Pd_3Au/C-as) in 0.5 M H_2SO_4 between 0.4 and 1.24 V at 50 mV s^{-1} and 25 ^{o}C.

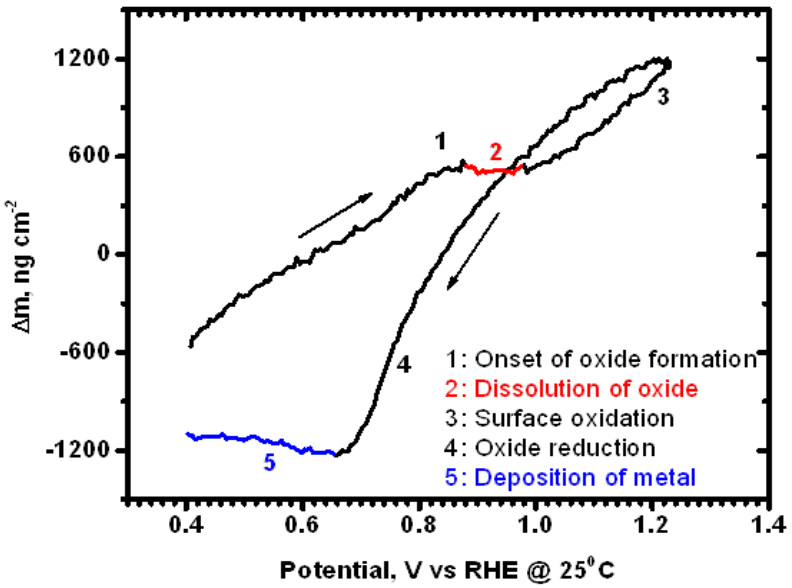

Figure 5.8: (a) Typical EQCN response showing different regions in the interfacial mass change on Pd-based catalyst (Pd_3Au/C-as) in 0.5 M H_2SO_4.

5.3.2.2. Determination of real surface area

The common method of measurement of the real surface area of a Pd electrode involves a measurement of the charge density associated with the reduction of a monolayer of palladium oxide. The voltammograms for the samples being studied are shown in Figure 5.9a. The theoretical charge density of the reduction of the monolayer of oxide was considered to be 420 μC cm^{-2}. However, dissolution of Pd (Figure 5.6b) occurs in the region of stripping of a monolayer of PdO. Hence, these measurements are an approximate measure of the real surface area of the electrode. The electrochemical active area ($ECSA_{Pd}$) of the catalyst samples is shown in Figure 5.9b. The active area decreased with an increase in the heat-treatment temperature. The trend was similar to that analyzed by XRD (Table 5.4, surface area and degree of dispersion). The real area of the Pd_3Au/C-as samples was comparable to that of Pd/C-as samples.

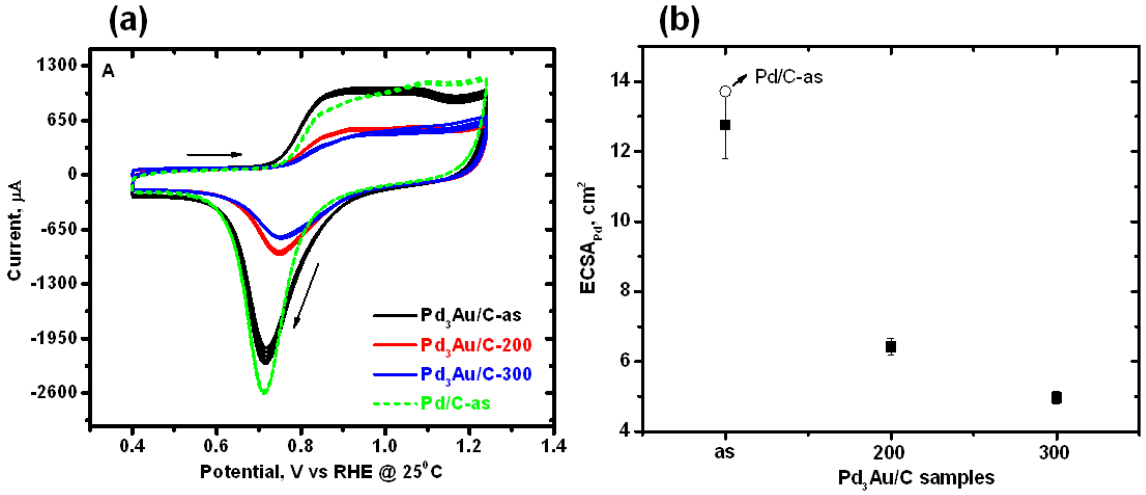

Figure 5.9: (a) CVs of Pd_3Au/C-as, Pd_3Au/C-200 and Pd_3Au/C-300 compared with Pd/C-as in 0.5 M H_2SO_4 between 0.4 and 1.24 V at 50 mV s^{-1} and 25 ^oC, and (b) electrochemical active surface area ($ECSA_{Pd}$) of the different catalysts measured from the oxide reduction area.

5.3.2.3. EQCN response of the Pd_3Au/C alloy catalysts

The combined CV and EQCN response for the Pd_3Au/C and Pd/C samples are shown in Figure 5.10. In the anodic scan, the mass increased with potential. The initial increase in mass in the double-layer region is due to the physisorption of anions and/or water molecules (H_2O) on the carbon-supported catalysts as has been reported [51]. Adsorption of electrolyte together with surface oxidation causes a further increase in mass in the oxide-formation region. Studies carried out on polycrystalline platinum and previously reported work [51] on carbon-supported platinum-based catalysts under similar conditions have shown that the effect of adsorption of anions and water is insignificant at an upper potential ≥ 1.2 V. In this work, the amount of oxide formed has been obtained from the change in EQCN mass response during CV to 1.24 V. The coulomb charge and mass change in the oxide formation were assumed to be entirely due to chemisorbed surface oxides on the catalysts. A decrease in mass during the anodic scan in the potential range of 0.88 to 1.0 V was observed for the Pd_3Au/C-as catalyst due to the presence of excess surface adsorbates. Detailed analysis of the sample showed a mass loss of approximately 40–50 ng cm^{-2} (Figure 5.11). In the cathodic scan, the mass decreased in the oxide region as the surface oxides were reduced. However, a mass gain was seen for the Pd_3Au/C-as catalyst at the end of reduction of surface oxide in the potential range of ~ 0.67 to 0.4 V. The chemical dissolution of the initial excess surface adsorbates on the Pd_3Au/C-as catalyst during the anodic scan increased the concentration of soluble ions, which contributed to the redeposition of the metal ions on the surface. The mass gain for the Pd_3Au/C-as samples was observed to be approximately 90 ng cm^{-2} (Figure 5.11). The mass loss between the consecutive cycles (Figure 5.12) was the least for the Pd_3Au/C-300 alloy catalyst, which indicates the increased stability of the Pd-Au

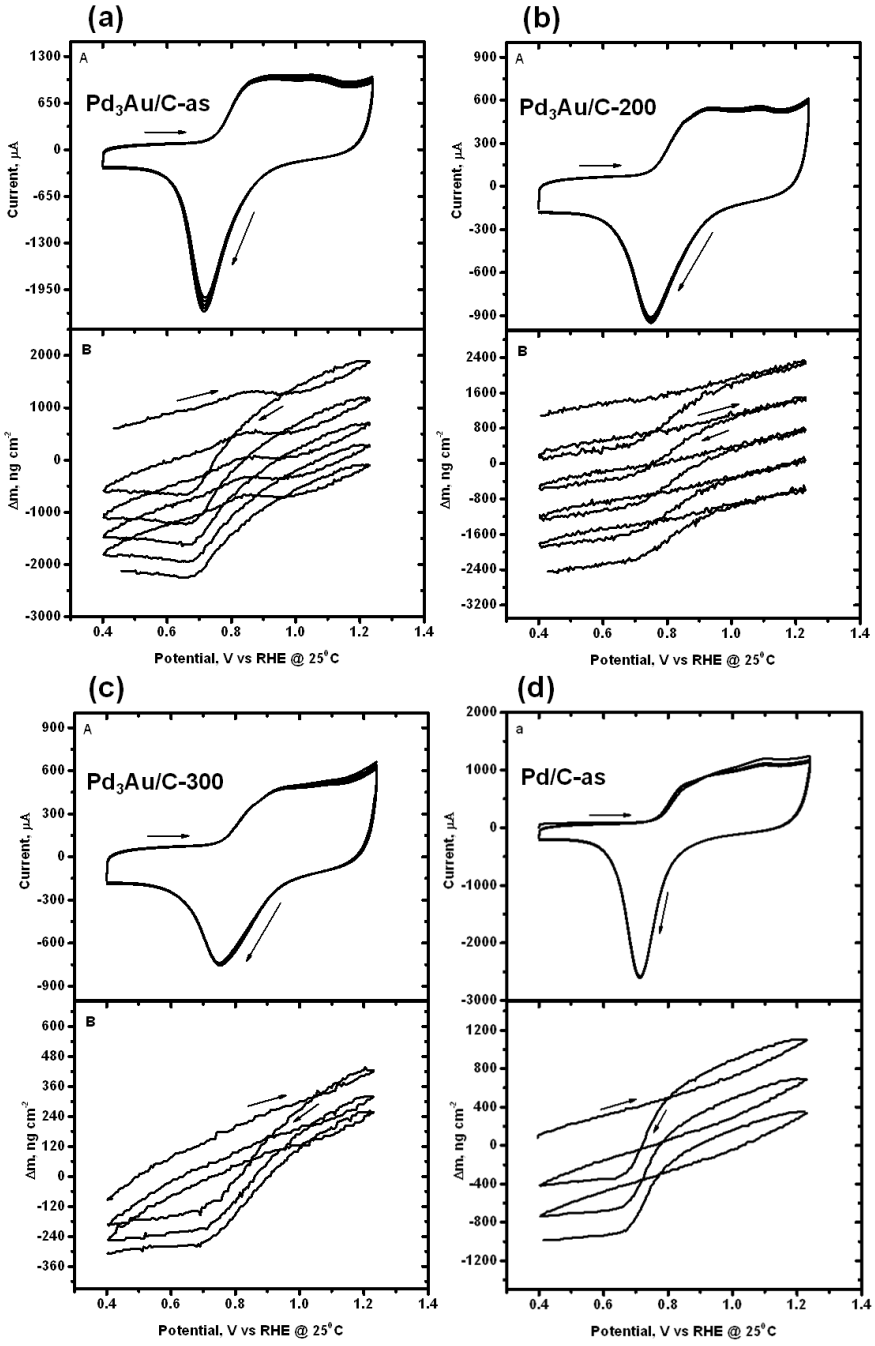

Figure 5.10: Combined CV and EQCN response in 0.5 M H_2SO_4 between 0.4 and 1.24 V at 50 mV s^{-1} and 25 ^{o}C: (a) Pd_3Au/C-as, (b) Pd_3Au/C-200, (c) Pd_3Au/C-300, and (d) Pd/C-as.

binary alloy on higher degree of alloying with increasing temperature. This measurement also shows the sensitivity of the EQCN measurement.

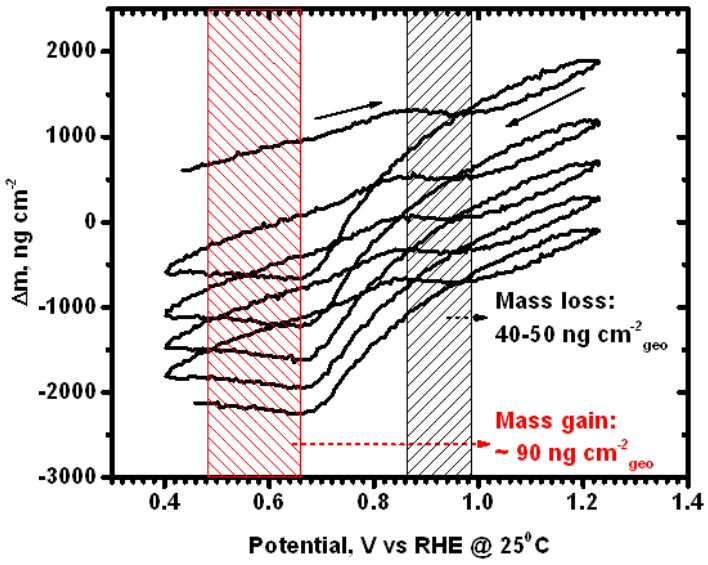

Figure 5.11: EQCN response of Pd_3Au/C-as in 0.5 M H_2SO_4, showing the regions of mass loss during anodic surface oxidation and mass gain during the reduction of the surface oxide.

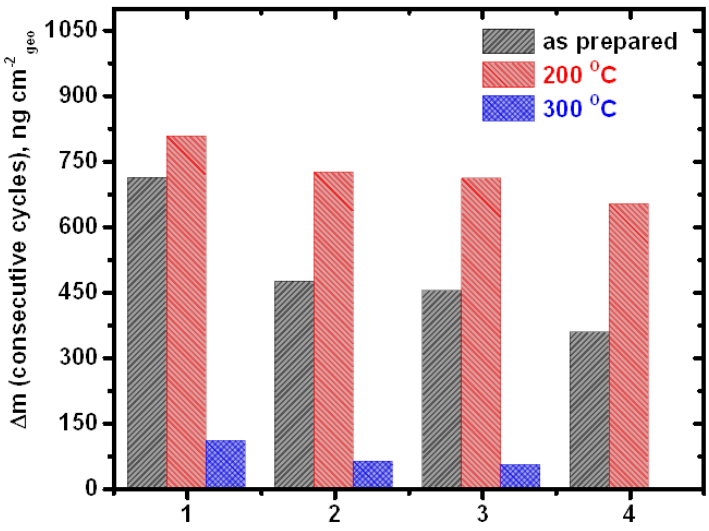

Figure 5.12: Change in mass between consecutive CV cycles for Pd_3Au/C-as, Pd_3Au/C-200, and Pd_3Au/C-300 samples.

5.3.2.4. Interfacial mass change

The change in the interfacial mass was calculated with Equation (2.3). The summary of the data for the combined CV and EQCN response is given in the appendix (Table D.1). The comparison of the values observed during oxide formation and reduction are given in the appendix (Figures D.3 and D.4). The change in mass ($\delta\Delta m$) is a direct measure of the surface characteristics of the catalysts. The difference between mass-change during oxide formation and reduction of the oxide indicates the extent of surface modification. This mass-change decreases from 670 ng cm^{-2} for Pd_3Au/C-as to 170 ng cm^{-2} for Pd_3Au/C-300 (Table 5.5). This decrease shows that the dissolution of the surface is reduced and the catalyst becomes more stable as the temperature of heat treatment increases.

The amount of adsorbed oxide, M, on the samples (Table 5.5) was calculated with Equation (2.4). The values were 11.23 (Pd/C-as), 15.84 (Pd_3Au/C-as), 25.81 (Pd_3Au/C-200) and 10.28 (Pd_3Au/C-300) g mol^{-1} of electrons. The molar mass for an oxide layer (O) adsorbed on the surface is 8 g mol^{-1} per electron (Table A.4). From the values reported above, it is seen that the surface oxidation on the Pd/C-as and Pd_3Au/C-300 catalysts is via the formation of O involving a 2-electron transfer. The surface oxidation on the Pd_3Au/C-300 sample is written, primarily, as:

$$Pd + H_2O \leftrightarrow PdO + 2H^{+} + 2e^{-} \qquad (5.1)$$

A similar equation can be written for the Pd/C-as sample (the different possible reactions for surface oxidation of Pd/C are given in Chapter 6). The experimental results in this work support the density function theory (DFT) calculations by Chen *et al* [89]. They showed that Pd-O is the energetically favorable oxide on a Pd-Au alloy and reported that the shortest bond length for Pd-O was observed when the fraction of Au in

the alloy was 0.25. Their results suggest that Pd-O was the strongest bond formed with largest hybridization between Pd and O energy states.

It has been reported that the highest oxidation state of a metal is formed in the potential region of anodic evolution of oxygen (E^{o}_{OER}) [90]. In this work, a CV was carried out over a potential range well below E^{o}_{OER} and the formation of Pd (IV) oxides is not considered.

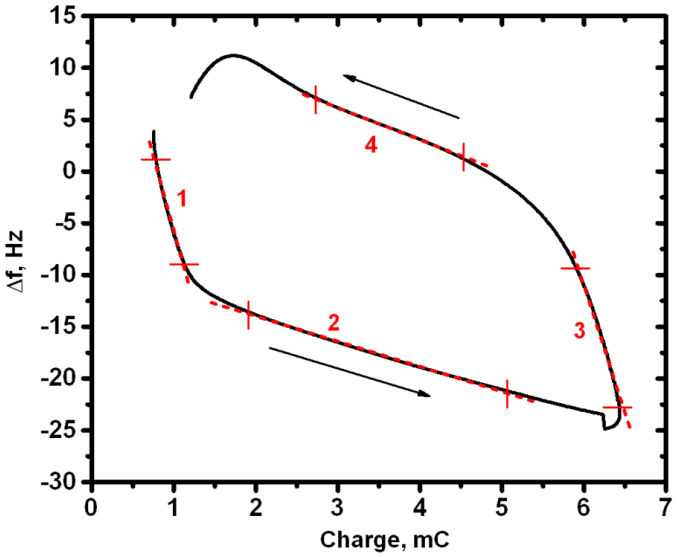

Region	Potential range, V	Δm/Q, ng cm^{-2} mC^{-1}
1	0.4 – 0.8	518
2	0.87 – 1.18	43
3	1.16 – 0.97	443
4	0.82 – 0.69	57

Figure 5.13: Change in frequency (Δf) vs Charge (Q) for a single potential cycle of Pd_3Au/C-300, and the corresponding potential range and electrochemical equivalents for each of the linear segments marked as regions 1, 2, 3, and 4.

Figure 5.13 shows the frequency–charge relationship for the Pd_3Au/C-300 sample. Different linear segments are marked on the plot and the corresponding electrochemical equivalent (ng cm^{-2} mC^{-1}) for each of the linear segment is shown in the

figure. The electrochemical equivalent was calculated with Equation (2.4). Comparison of these values against the calculated values for the expected reactions (Table 5.6) shows that a combination of reactions occurs on the surface of the electrode in the potential range considered in this study.

It is also seen from Figure 5.14 that the hydrogen region is modified by alloying Pd with Au. Further study is needed to understand the stress induced into the alloy surface by the adsorption and absorption of hydrogen into the lattice.

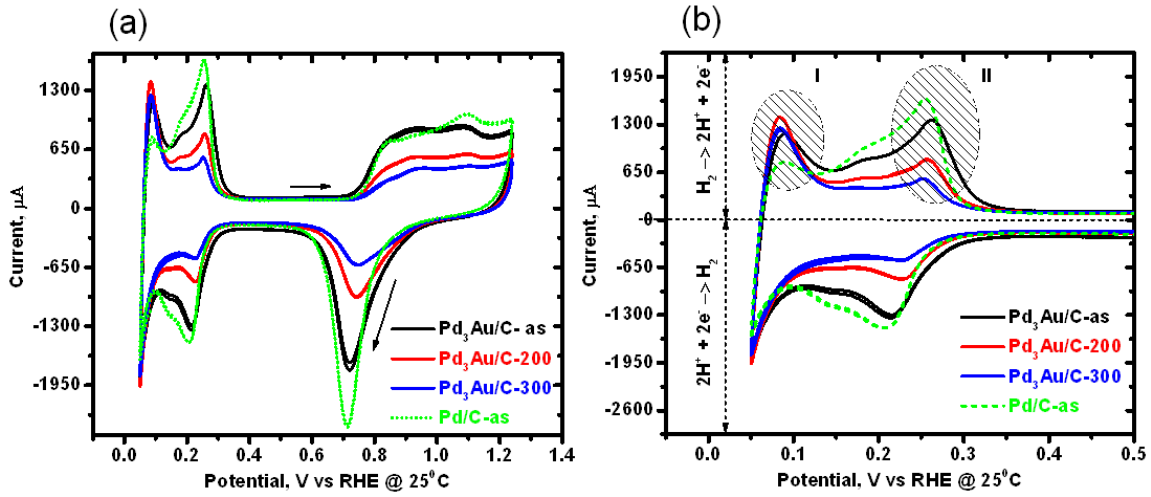

Figure 5.14: (a) CV of Pd_3Au/C-as, Pd_3Au/C-200 and Pd_3Au/C-300, compared with Pd/C-as in 0.5 M H_2SO_4 between 0.05 and 1.24 V at 50 mV s^{-1} and 25 ^oC, and (b) enlarged view of the hydrogen region of the CVs.

Experiments were also carried out at 20 mV s^{-1} for the Pd_3Au/C-300 catalyst samples (appendix D: Figure D.5a). The results were comparable to that reported for a scan rate of 50 mV s^{-1}.

The experiments carried out in a solution saturated with oxygen also showed results comparable with those carried out in an argon purged solution for Pd_3Au/C-300 catalyst (appendix D: Figure D.5b). The results are given in the appendix (Table D.1). These experiments confirm that the surface of the catalyst interacts with O-containing

Table 5.5: Amount of adsorbed species on the Pd_3Au/C electrodes (italicized values: amount in excess of 8 g mol^{-1})

Catalyst	Oxide formation		Oxide reduction		M_{red}/M_{ox}	$\delta\Delta m_{red}/\delta\Delta m_{ox}$	$(\delta\Delta m_{red} - \delta\Delta m_{ox})$ ng cm^{-2}_{geo}
	M_{ox}, g mol^{-1}	*M_{ox} (excess of O), g mol^{-1}*	M_{red}, g mol^{-1}	*M_{red} (excess of O), g mol^{-1}*			
Pd/C – as	11.23	*3.23*	25.96	*17.96*	2.31	1.64	472
Pd_3Au/C – as	15.84	*7.84*	39.16	*31.16*	2.47	1.73	670
Pd_3Au/C – 200	25.81	*17.81*	66.61	*58.61*	2.58	1.67	545
Pd_3Au/C – 300	10.28	*2.28*	27.82	*19.82*	2.71	1.61	167

Table 5.6: Summary of reactions occurring on the surface of the Pd_3Au/C electrodes with expected mass response

Reaction	Mass change response		Mass change expected, g $mole^{-1}$ (electron)	Mol. Wt of species, g $mole^{-1}$	Electrochemical Eqv. µg C^{-1} (ng mC^{-1})
	Oxide formation	Oxide reduction			
$Pd + H_2O \leftrightarrow PdO + 2H^+ + 2e^-$	Mass gain	Mass loss	8	Pd^{++} : 106.42	634
$Pd^{++} + H_2O \leftrightarrow PdO + 2H^+$	*Mass loss*	Mass loss	-	Pd : 106.42	-
$Pd \leftrightarrow Pd^{++} + 2e^-$	*Mass loss*	*Mass gain*	53.21	PdO : 122.42	551
$Pd^{++} + 2H_2O \leftrightarrow PdO_2 + 4H^+ + 2e^-$	Mass gain	Mass loss	16*	PdO_2 : 138.42	717
Mass response of interest	**Mass gain**	**Mass loss**			

* if Pd^{++} stays on the electrode surface in the specific-adsorbed region; those italicized are the EQCN responses that are not expected for the particular scan. (Reactions taken from Pourbaix diagram) [67].

species (H_2O) present in the solution and forms an oxide layer as the reaction progresses irrespective of the partial pressure of oxygen in the solution. Similar behavior was observed during the surface oxidation of polycrystalline Pt in different electrolytes and Ar/O_2 saturated solutions (Chapter 3).

5.3.2.5. Accelerated degradation tests

The combined CV and EQCN response before and after the accelerated degradation tests for Pd_3Au/C-as and Pd_3Au/C-300 catalysts are shown in Figure 5.14. The comparisons of the results are shown in Figure 5.15. The data are summarized in Tables 5.7 and D.2. From the results (Table 5.7), it is seen that there is a decrease in the charge density (equivalent to the surface density of Pd atoms) of the catalysts after the tests, which indicate the loss of active Pd sites on the catalyst surface. The charge density of the Pd_3Au/C-as catalyst decreased by 80 % whereas that of the Pd_3Au/C-300 catalyst decreased by only 56 % after the tests. The degradation tests show that the extent of alloying and mixing of Au with Pd is important in the stabilization of the surface atoms. The EQCN response of the Pd_3Au/C-as catalyst after the degradation showed a continuous increase in the mass during the anodic scan. The accelerated degradation also resulted in the dissolution of the different chemical states of Pd_3Au/C-as, which removed the initial surface oxide. The EQCN response shows that the amount of active Pd sites decreased with the degradation test, thereby reducing the amount of surface oxide. The interfacial mass change (M, g mol^{-1}, Table D.2) calculated for the catalysts after the degradation tests indicate the mass contribution due to different competing reactions.

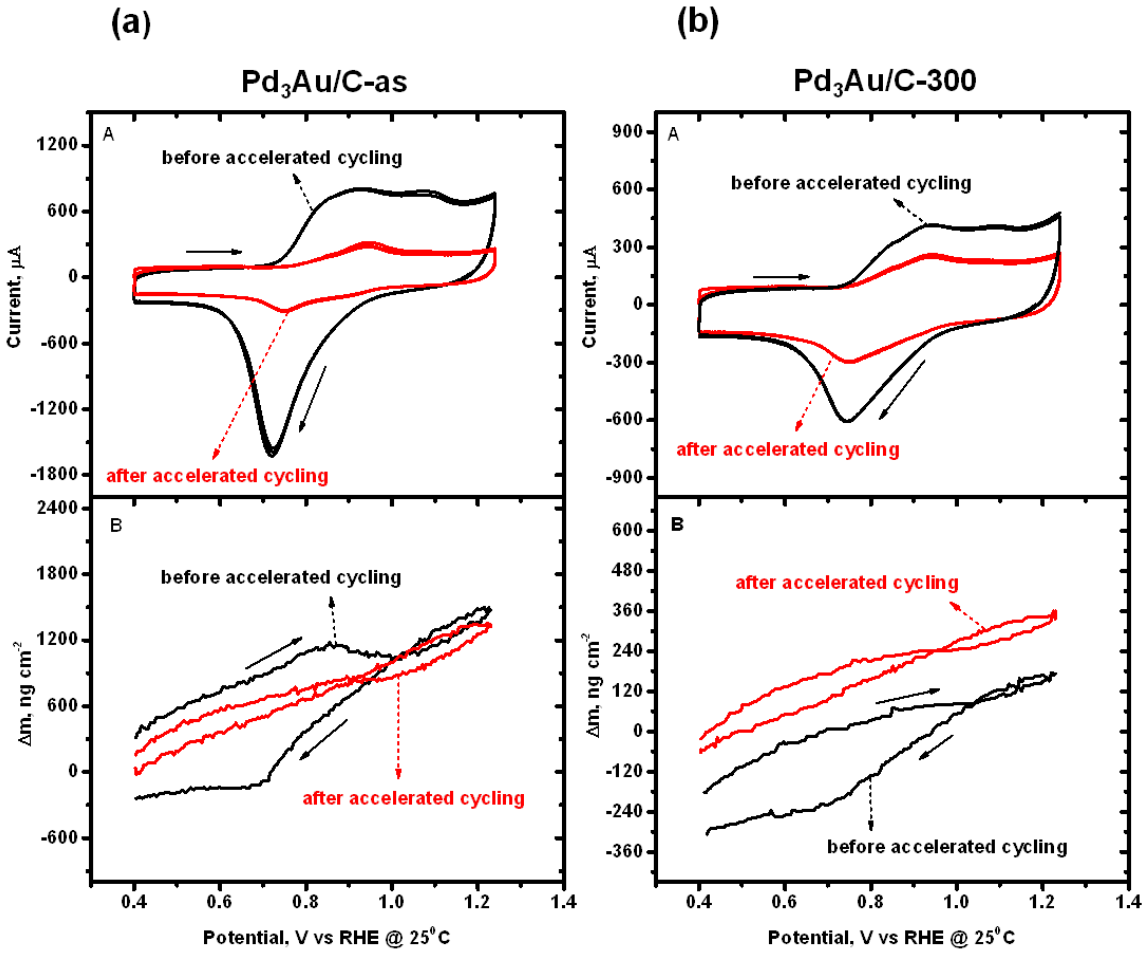

Figure 5.15: Combined CV and EQCN response of Pd_3Au/C-as and Pd_3Au/C-300 before and after accelerated degradation tests in 0.5 M H_2SO_4 between 0.4 and 1.24 at 25 ^oC and 50 mV s^{-1}.

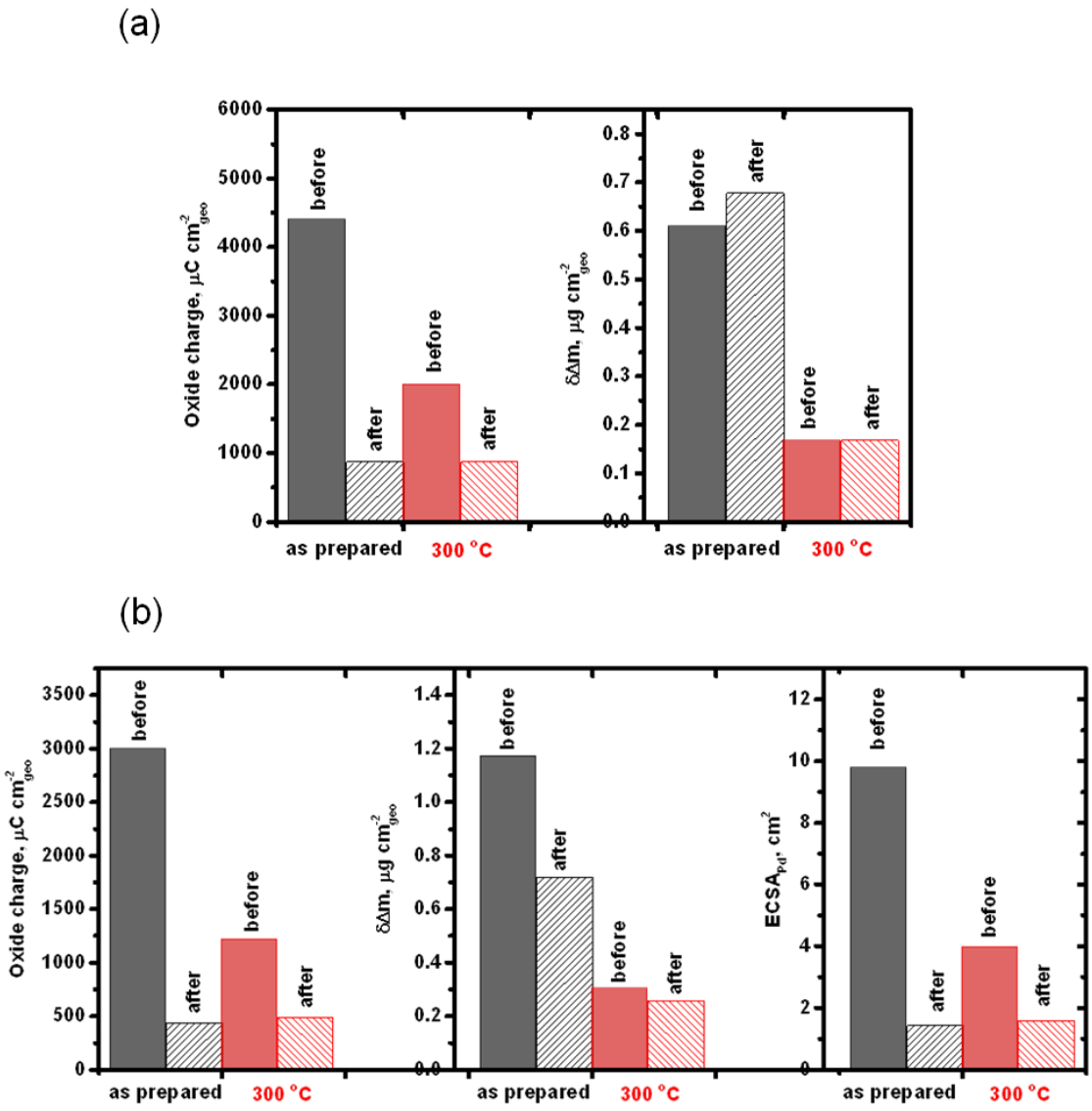

Figure 5.16: Comparison of electrochemical behavior before and after accelerated degradation tests: (a) Change in charge density and amount of adsorbed mass on Pd_3Au/C-as and Pd_3Au/C-300 during oxide formation, and (b) change in charge density, amount of adsorbed mass, molar mass of the adsorbed species on Pd_3Au/C-as and Pd_3Au/C-300 during oxide reduction.

Table 5.7: Change in the surface characteristics (%) after accelerated degradation tests

Catalyst	Oxide formation		Oxide reduction	
	Charge, $\mu C\ cm^{-2}_{geo}$ (loss)	M_{ox}, g mol^{-1} (gain)	Charge, $\mu C\ cm^{-2}_{geo}$ (loss)	M_{red}, g mol^{-1} (gain)
Pd_3Au/C – as	80.28	83.88	84.96	77.64
Pd_3Au/C – 300	56.13	54.35	59.28	52.59

5.4. CONCLUSIONS

The electrochemical behavior of the surface of carbon-supported Pd and Pd_3Au alloy nanoparticles synthesized by the polyol method followed by heat treatment at different temperatures has been analyzed by combined CV and EQCN measurements. In this study, we have shown that heat treatment of the alloy to a minimum of 300 ^oC is essential to form a randomly distributed alloy composition with increased durability. The type and nature of the principal adsorbed oxide on the alloyed catalyst (Pd_3Au/C-300) has been identified as O. The study showed that formation of a surface oxide does not affect the durability of the heat treated Pd-Au binary alloy. The charge transfer between Pd and Au atoms in the randomly distributed composition of the alloy increases the durability, showing that the Au atoms have an ability to stabilize the surface Pd atoms. The amount of adsorbed species on the surface of the catalyst was independent of the partial pressure of oxygen.

6. Electrochemical behavior of carbon-supported palladium-platinum binary-alloy catalysts in low-temperature fuel cells

6.1. INTRODUCTION

The platinum group metals (PGM) are considered good candidates for use as cathode catalysts from the viewpoint of the ORR catalytic activity and stability in low-temperature fuel cells. Among the PGM, it has been reported that both Pd and Pt have a four-electron pathway for the oxygen reduction reaction [91, 92]. It has also been reported that Pd has no catalytic activity for methanol oxidation in an acid medium [93, 94], which makes it a good ORR selective catalyst for low-temperature fuel cells operating on a liquid fuel such as methanol (e.g., Direct methanol fuel cells, DMFCs). Although, Pd has a high tolerance to methanol oxidation, its activity for the ORR in a methanol-free electrolyte is significantly lower than that of a Pt catalyst. Methanol crossover from the anode to a Pt cathode is a major problem in the DMFCs; the reaction of methanol with Pt blocks the ORR. Much work has been carried out to enhance the ORR activity of the catalysts in the presence of methanol to improve the overall performance of the DMFCs. The recent developments include the synthesis of Pd-based binary alloy catalysts and catalysts with a Pt/Pd-monolayer [15, 95]. However, the electrochemical behavior of these novel catalysts is yet to be clearly understood.

In this study, we analyze the effect of alloying Pd with Pt on the extent of metal-metal interaction, metal-adsorbate interaction, methanol tolerance, and surface oxidation of the binary-alloy catalyst nanoparticles. Palladium and platinum are elements in the same group, and each has distinct chemical properties. Pd and Pt mostly show comparable electrochemical behavior under similar experimental conditions [48, 67]. It is also known that both Pd and Pt adsorb hydrogen on their surface, from both the gas phase and electrochemically. However, under the same conditions of pressure and temperature,

the bulk absorption of hydrogen in Pt is negligible. Both metals also form strong surface oxides in the same potential range of oxidation. Pd has a lower work function than Pt [22] and is also smaller in size than Pt. Alloying Pd with Pt will result in the flow of electrons from Pd to Pt, which raises the Fermi level and the energy of the d-states in Pt while lowering the same in Pd. Thus, the resultant work function of the binary alloy catalysts will be higher than that of Pd, but lower than the work function of Pt.

In this work, we present the results of the electrochemical behavior of the Pd-Pt binary alloy catalysts. The catalysts are analyzed for the ORR activity and methanol tolerance. The alloy catalysts, *viz.*, Pd_3Pt/C and Pt_3Pd/C, for this study were synthesized by polyol reduction and are characterized by different techniques described in Chapter 2. The performance of the alloy catalysts is compared to Pd/C and Pt/C catalysts. We also present the results of surface phenomena on the Pd-Pt binary alloy in an oxidizing and acidic environment measured with the EQCN technique. From a comparison of the Pd/C and Pt/C catalysts, it will be argued that Pd is more tolerant to methanol crossover than Pt because of a stronger Pt-Pt versus Pd-Pd bond. This is demonstrated by also investigating the alloys of Pd_3Pt and Pt_3Pd on a carbon substrate.

6.2. EXPERIMENTAL METHODS

6.2.1. Catalyst synthesis

Carbon-supported Pd-Pt catalysts with a 40 wt. % metal loading were synthesized by the polyol method as described in Section 2.1. In a typical experiment, 125 mg of carbon black was dispersed in 48 mL of ethylene glycol by ultrasonication and magnetic stirring. The pH of the solution was adjusted by drop-wise addition of 30 mL of 1 M NaOH (in ethylene glycol) to obtain a final concentration of 0.20 M NaOH. Palladium (Pd) and platinum (Pt) metal precursor solutions were prepared by dissolving the metal

salts separately in ethylene glycol. Sodium tetrachloropalladate (Na_2PdCl_4) and potassium chloroplatinate (K_2PtCl_4) were used as the metal precursor salts. The precursor salt solutions were added drop wise to the carbon-ethylene glycol dispersion and heated to temperature, T, for 2.5 hours under continuous stirring. The synthesis was carried out under an inert atmosphere by continuous purging of the solution with ultrapure nitrogen gas (N_2). After cooling the polyol solution, the supported catalysts were filtered, washed with ultrapure water and dried overnight in a vacuum oven. The Pd-Pt catalyst samples were further heated in a tube furnace under a reducing atmosphere (10% H_2/ 90% Ar gas) and at a ramp rate of 5 $^oC\ min^{-1}$ to 200 ^oC for 2 hours. For a comparison, a Pd/C catalyst was also prepared by a similar procedure. The details of the synthesis process are given in Table 6.1.

Table 6.1: Details of synthesis process

Catalyst	Pd salt, M	Pt salt, M	EG/precursor	Synthesis T, ^oC
Pd/C	0.025	-	0.4	140 (2 hours)
Pd_3Pt/C	0.015	0.008	0.6	165
Pt_3Pd/C	0.007	0.017	0.5	175

6.2.2. Structural/chemical characterization

Bulk metal compositions were determined with an SEM-EDS scanning electron microscope as described in Section 2.2.2. The metal loading in the carbon-supported catalysts was determined by TGA as described in Section 2.2.3. The near-surface composition was determined by X-ray photoelectron spectroscopy measurements as given in Section 2.2.6. The structural characterization of the catalysts was carried out with a Philips 3520 X-ray diffractometer as described in Section 2.2.1.

6.2.3. Electrochemical characterization

6.2.3.1. Preparation of catalyst ink and electrode

The catalyst inks were prepared by mixing a known amount of the catalyst powder in 5 wt. % Nafion solution and 2-propanol-water mixture as described in Section 2.3.1. 60 μL of the homogeneous ink was drop-cast onto the gold-coated quartz crystal sensor (5 MHz) with a geometric area of 1.37 cm^2 and allowed to dry at room temperature. For the RDE measurements, 10 μL of the homogeneous ink was drop-cast onto a glassy-carbon electrode with a geometric area of 0.19634 cm^2. For the RRDE measurements, 12 μL of the homogeneous ink was drop-cast onto a glassy-carbon electrode with a geometric area of 0.2472 cm^2. The method of ink preparation was the same for all the catalyst materials being studied. The details of the cast electrodes are given in Table E.1.

6.2.3.2. Cyclic voltammetry (CV)

The electrochemical characterization was carried out by cyclic voltammetry (CV) as described in Section 2.3. CO-stripping voltammetry was carried out on the electrodes as described in Section 2.3.6 for the Pd-based catalysts. Methanol oxidation was carried out by a potential scan in the range of 0.4 to 1.24 V at 50 mV s^{-1} in 0.1 M $HClO_4$ containing 0.1 M CH_3OH (deaerated electrolyte). Hydrodynamic voltammetry (oxygen reduction reaction measurements, ORR) with a rotating disk electrode (Section 2.3.2) was carried out in an O_2-saturated solution (0.1 M $HClO_4$) as described in Section 2.3.4 and the methanol tolerance study was carried out by the same procedure in an O_2-saturated 0.1 M $HClO_4$ electrolyte containing 0.1 M CH_3OH. Measurements were also carried out to determine the H_2O_2 intermediates as described in Sections 2.3.2 and 2.3.8.

6.2.3.3. Electrochemical quartz crystal nanobalance measurements (EQCN)

The *in situ* mass measurements were performed with an EQCN setup as described in Section 2.3.3. A batch cell with a 5 MHz sensor was used for the measurements. The amount of adsorbed intermediate on the electrode surface was obtained from the combined CV and EQCN measurements for the potential cycling. The details are given in Section 2.3.4.

The various characterization measurements were also carried out for a commercial Pt/C (BASF).

6.3. RESULTS AND DISCUSSION

6.3.1. Structural/chemical characterization

Bulk compositions determined by EDS and TGA are reported in Table 6.2. The TGA profiles are shown in the appendix (Figure E.1).

The XPS spectra to determine the near-surface characteristics of the catalysts are shown in Figure 6.1, and the compositions are given in Table 6.2. Figure 6.1 a and b exhibits the core level spectra of Pt 4f and Pd 3d, respectively. The different chemical states of the samples are shown in Figure 6.1c-f. The two peaks shown in Figure 6.1b can be assigned to Pd $3d_{5/2}$ and $3d_{3/2}$ of elemental Pd (Pd^o). The binding energies (BE) of Pd $3d_{5/2}$ for Pd_3Pt/C and Pt_3Pd/C are 335.37 and 335.54 eV, respectively, which are higher than that of pure Pd (335.1 eV [36], dashed vertical line) indicating the stronger Pd bonds in the binary alloy catalysts. The observed BE values of Pd^o shift to larger values with a decrease in the Pd/Pt ratios, which indicates that the Pd-Pt bonding is stronger than the Pd-Pd bonding. The standard BE of pure Pt is 71.2 eV [36] (dashed vertical line in Figure 6.1a). The BE values of Pt $4f_{7/2}$ for Pd_3Pt/C and Pt_3Pd/C are 71.02 and 71.19 eV, respectively. The BE values of Pd and Pt of the catalysts reflect the larger radial

extension of the 5d orbitals. The Pd $3d_{5/2}$ and $3d_{3/2}$ peaks and the Pt $4f_{7/2}$ and $4f_{5/2}$ peaks were used to quantify the Pd_3Pt/C sample (Figure 6.1 d and c). The Pd $3d_{5/2}$ had an interference with the Pt 4d signal of the Pt_3Pd/C sample. Hence, Pd $3d_{3/2}$ and Pt $4f_{7/2}$ peaks without interferences were chosen to quantify the surface composition of the Pt_3Pd/C sample (Figure 6.1 f and e). The relative sensitivity factors (R.S.F) were adjusted accordingly to include one peak of the doublet pair for elemental quantification (Pt $4f_{7/2}$, 3.1857; Pd $3d_{3/2}$, 2.1424). The negligible deviations between the near-surface composition (XPS) and the bulk composition (EDS) indicate an insignificant surface segregation in the binary alloy catalysts. The two deconvoluted peaks of Pt in Figure 6.1 c and e correspond to Pt^o (elemental Pt) and PtO_2 (peak position of Pt^o + 0.77 eV, [10]). The 3 peaks of Pd in Figure 6.1d correspond to Pd^o (elemental Pd), Pd-O_{ads}, and PdO (Pd^{++}) with peak positions consistent with those given in the literature [86]. The peak corresponding to PdO was not significant in the Pt_3Pd/C sample as shown in Figure 6.1f.

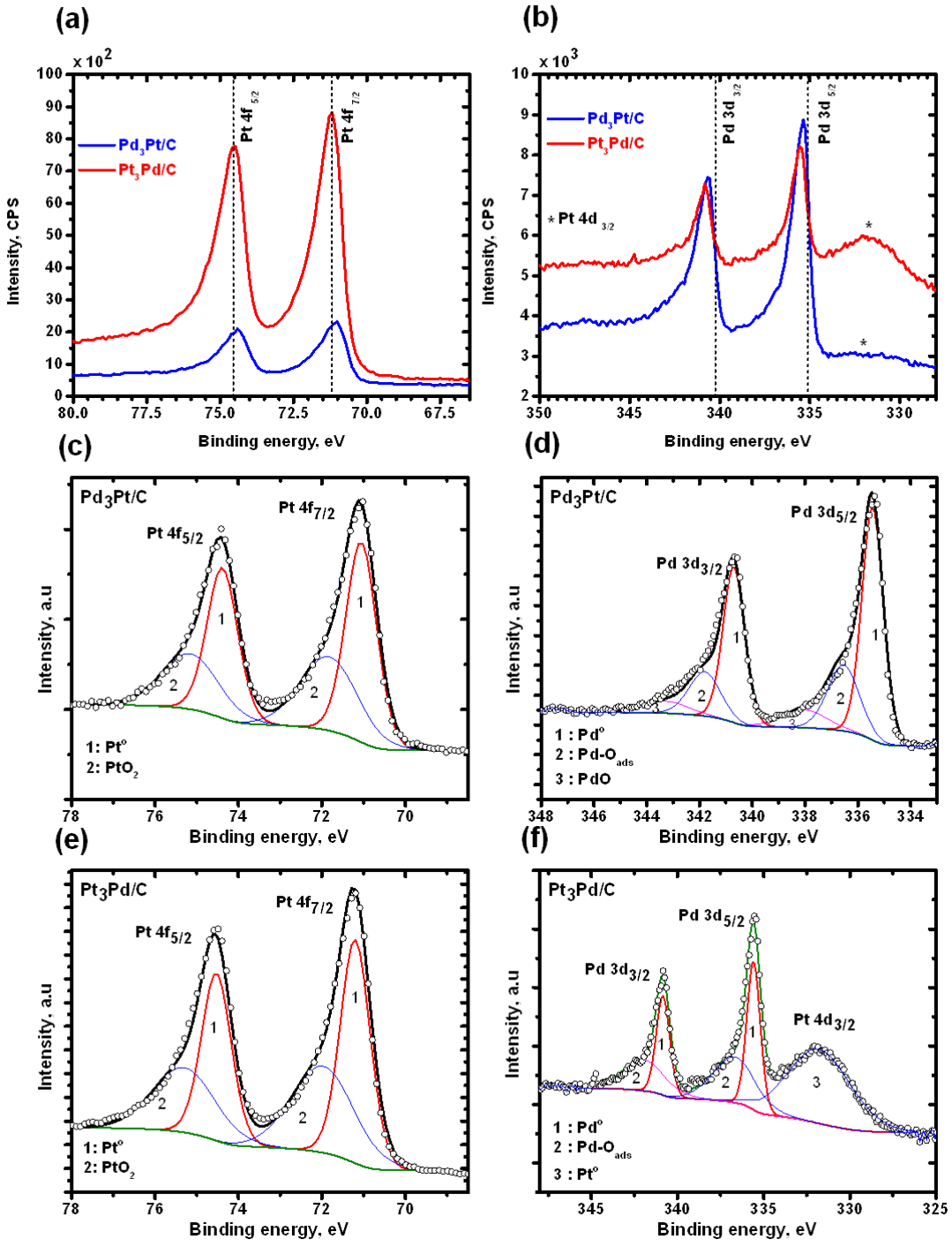

Figure 6.1: Core-level XPS spectra of (a) Pt 4f and (b) Pd 3d. XPS spectra with the deconvolution fit for the Pt 4f region ((c) and (e)) and the Pd 3d region ((d) and (f)). The open circles indicate the experimental data.

Figure 6.2 compares the XRD patterns of the samples. All the peaks can be indexed in the f.c.c crystal structure. The absence of superlattice reflections corresponding to atomic ordering indicates the formation of a pure single-phase disordered binary alloy, which is consistent with the complete miscibility of Pd and Pt as seen in the binary phase diagram [96].

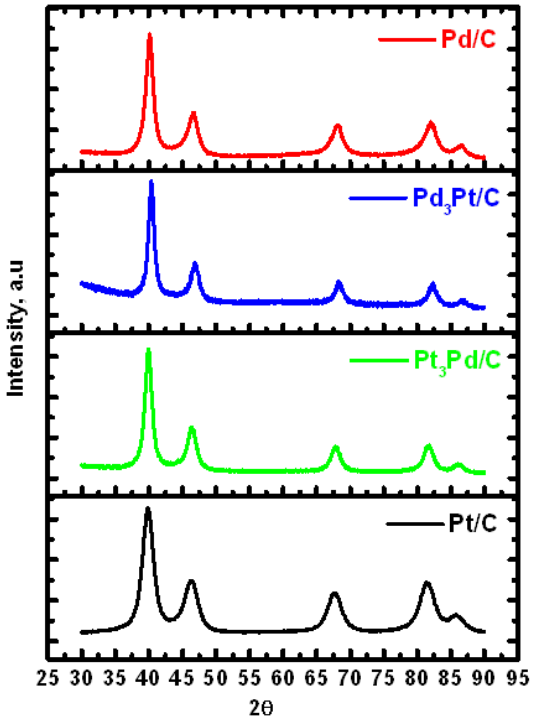

Figure 6.2: XRD patterns of the catalyst samples.

Table 6.2: Summary of structural/chemical characterization of the catalysts

Catalyst	Metal, at.% (nominal)	Metal (bulk), at.%, (EDS)	Metal loading, wt.% (TGA)	Near-surface composition, (XPS) at.%	Crystallite size (avg.), nm (XRD)
Pd/C	-	-	39.4	-	6.0 ± 1.0
Pd_3Pt/C	$Pd_{75}Pt_{25}$	$Pd_{77.9}$ $Pt_{22.1}$	42.8	$Pd_{76.9}$ $Pt_{23.1}$	6.5 ± 0.5
Pt_3Pd/C	$Pt_{75}Pd_{25}$	$Pt_{70.9}$ $Pd_{29.1}$	47.4	$Pt_{70.2}$ $Pd_{29.8}$*	5.5 ± 0.5
Pt/C	-	-	40.0	-	3.5 ± 0.5

*From the analysis of $Pt4f_{7/2}$ and $Pd3d_{3/2}$ (combination of elemental and the oxide forms).

6.3.2. Electrochemical characterization

6.3.2.1. Understanding methanol tolerance and CO oxidation

In DMFCs, the primary loss of efficiency of the cathodic reaction is the competitive reactions of the ORR and the oxidation of methanol (MOR, methanol oxidation reaction). Methanol crosses over from the anode through the proton exchange membrane to the cathode side of the fuel cell. Figure 6.3a shows the ORR and MOR reactions occurring on carbon-supported Pt and Pd catalysts. A peak is seen for the MOR on the Pt catalyst in the region of the ORR when the O_2-saturated electrolyte contains methanol (CH_3OH). Thus, in the presence of methanol, the ORR activity is considerably reduced on the Pt/C electrode (black-colored curve). However, no MOR peaks are seen for the Pd/C catalyst (red-colored curve). The behavior of Pd/C in the presence of CH_3OH indicates the high tolerance of the catalyst toward the MOR.

The MOR is given by Equation (6.1). The primary intermediate of the MOR is the carbon monoxide adsorbed (CO) on the metal surface. The reaction for the formation of CO is given by Equation (6.2).

$$CH_3OH + H_2O \leftrightarrow CO_2 + 6H^+ + 6e^- \quad (6.1)$$

$$CH_3OH \leftrightarrow CO + 4H^+ + 4e^- \quad (6.2)$$

The MOR is completed by the oxidation of CO to carbon dioxide, which can occur by different mechanisms, as given below:

$$CO + H_2O \leftrightarrow CO_2 + 2H^+ + 2e^- \quad (6.3)$$

$$CO + M(Pt)O \leftrightarrow CO_2 + M(Pt) \quad (6.4a)$$

$$M(Pt) + H_2O \leftrightarrow M(Pt)O + 2H^+ + 2e^- \quad (6.4b)$$

The oxidation of CO as given in Equation (6.3) involves the O-containing species in the solution, *i.e.*, H_2O, whereas the oxidation as given in Equation (6.4) involves the O-species on the catalyst surface, M(Pt) (Equation (6.4a)). The surface oxidation continues on the catalyst surface, as given by Equation 6.4b, after the complete removal of the adsorbed CO (CO-stripping). The CO-stripping voltammograms for Pt/C and Pd/C are shown in Figure 6.3b. It is seen that the oxidation of CO on Pt/C occurs at a lower potential than on Pd/C and in the potential range of onset of surface oxidation on Pt/C. This behavior indicates that the oxidation of CO on Pt/C occurs via the mechanism given by Equation (6.4a). Although a Pt-O bond is stronger than a Pd-O bond, the stronger Pt-Pt bonding relative to the Pt-O bonding in the catalyst makes it easier to strip the CO by Equation (6.4a) than by Equation (6.3). It is also seen that oxidation of CO occurs at higher positive potentials on Pd/C, above the region of surface oxidation of Pd. The onset of surface oxidation on Pd is at lower potentials than on Pt, indicating that although a Pd-O bond is weaker than a Pt-O bond, weaker Pd-Pd interactions in the Pd catalyst make the formation of surface PdO occur at a lower anodic potential. The strength of the surface oxide bond and the CO oxidation potentials on Pd/C indicate that the CO oxidation occurs via the reaction given by Equation (6.3) on Pd/C. This study shows that the high tolerance of catalysts to the MOR is related to a high oxidation potential of CO on the catalyst surface.

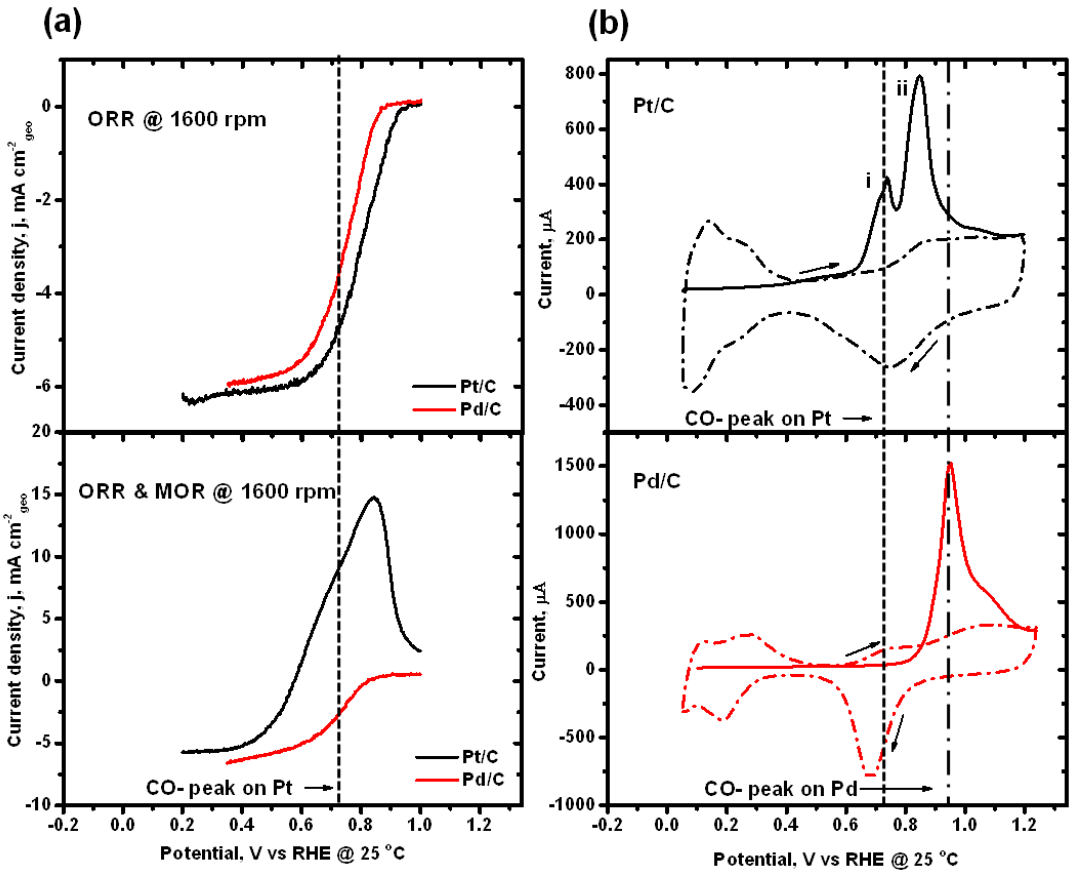

Figure 6.3: (a) Typical hydrodynamic voltammograms without (0.1 M $HClO_4$) and with CH_3OH (0.1 M $HClO_4$ + 0.1 M CH_3OH), and (b) typical CV and CO-stripping voltammograms (comparison of Pt/C and Pd/C).

6.3.2.2. CO-stripping voltammetry (CO oxidation) and methanol oxidation

The CO-stripping and the MOR voltammograms for the different catalysts are compared in Figure 6.4. The peak potential and current values for the CO-stripping are given in Table 6.3. The two dashed vertical lines in Figure 6.4 represent the CO oxidation peaks for Pt/C and Pd/C, respectively. The shift in the peak potentials of the alloys to lower values than that of Pd/C indicates a relative weakening of the metal-O bond with a decrease in methanol tolerance as discussed in Section 6.3.2.1. This shift also indicates that the Pd-Pt bond is stronger than the Pd-Pd bond in the binary-alloy catalysts, which is

consistent with the XPS results as seen in Section 6.3.1. The results show that a competition exists between the metal (M)-metal (M) and the metal-O bond; a stronger M-M bond indicates a weaker M-O bond relative to the M-M bond. Dilution of Pd with Pt strengthens the M-M bond and it weakens the relative strength of the M-O bond, favoring Equation 6.4 vs Equation 6.3. CO oxidation on Pt/C showed two peaks at 0.737 V (peak i) and 0.847 V (peak ii). Different explanations are presented in the literature for the presence of two peaks on Pt/C; they include: variation in particle size [97, 98], distribution of different adsorption sites [99], orientation of the crystallographic planes [100, 101], difference in the number of nucleating sites for O-containing species on the surface [102], difference in the mobility of the surface species [103], and differences in the type of adsorption (end-on vs bridged) [42, 104]. In the present study, the particle size distribution of the catalysts on carbon was uniform (unimodal distribution) (Section 4.3.1.3). In this study, CO adsorption on Pt/C was carried out at a lower potential hold, which favors a direct metal-CO adsorption (Section 2.3.6). A lower potential hold for CO adsorption also forms maximum CO coverage on the surface. It has been reported that a maximum coverage of CO on the surface leads to two peaks [105]. It was also seen that the surface of Pt/C reaches monolayer coverage of oxide at potentials greater than 1.0 V (Section 4.3.2.4), which indicates an increase in the number of adsorbed O with increasing potential. The two peaks for CO oxidation on Pt/C are attributed to the difference in the number of O-containing species on the catalyst surface.

The MOR studies were carried out to study the behavior and the voltammograms of the catalysts in the presence of methanol (Figure 6.4). The Pd/C catalyst showed no peak for methanol oxidation whereas Pt/C and Pd-Pt binary-alloy catalysts exhibited distinct peaks for methanol oxidation. For Pd/C, the CV with and without methanol were similar, indicating the tolerance of the catalysts to methanol. The Pd_3Pt/C catalyst showed

no peaks for MOR during the initial CVs; however, continuous potential cycling in methanol showed the appearance of peaks for the MOR with an increase in the peak height with cycling. This behavior in Pd_3Pt/C shows that the catalyst becomes less tolerant to the MOR with potential cycling, which signals the formation of a Pt-enriched surface. Figure 6.4 also shows that the surface oxide formation peaks on Pt/C and Pt_3Pd/C are suppressed by the large MOR current. The ratio of the forward to the reverse current for the MOR is given in Figure 6.4.

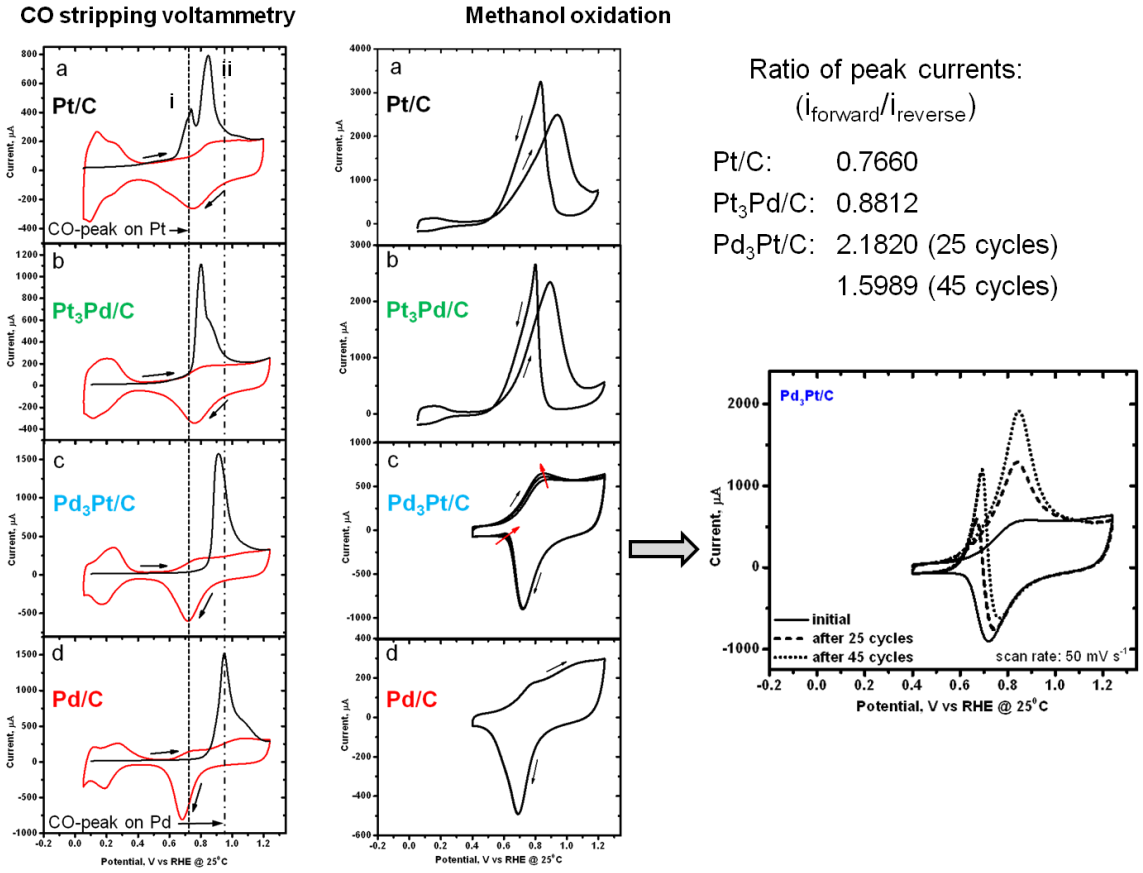

Figure 6.4: CO-stripping and methanol oxidation reaction (MOR) voltammograms of the catalysts.

Table 6.3: Peak potential and peak current of CO-stripping voltammograms

Catalyst	Peak potential, V	Peak current, µA
Pd/C	0.947	1522
Pd_3Pt/C	0.912	1575
Pt_3Pd/C	0.801	1111
Pt/C, Peak i:	0.737	426
Pt/C, Peak ii:	0.847	792.6

6.3.2.3. ORR and methanol tolerance

The hydrodynamic voltammograms with and without methanol are shown in Figure 6.5. The limiting currents obtained for all the catalysts during the ORR measurements without alcohol were comparable to the expected theoretical limiting current density for the ORR in 0.1 M $HClO_4$. The half-wave potentials for Pt/C, Pt_3Pd/C, Pd_3Pt/C and Pd/C were 0.796, 0.794, 0.757 and 0.749 V, respectively (Pt/C > Pt_3Pd/C > Pd_3Pt/C > Pd/C). The higher half-wave potentials of the Pt/C and Pt_3Pd/C catalysts indicate the low overpotential loss of these catalysts. The mass activities for the different catalysts measured at 0.82 V are shown in Figure 6.6. The activities, calculated per unit mass of Pt and per unit mass of PGM (platinum group metals, (Pt+Pd)), reveal the rate of catalytic activity per amount of the catalyst. The order of decrease of activity per unit mass of Pt was: Pd_3Pt/C > Pt_3Pd/C > Pt/C and per unit mass of PGM was: Pt/C > Pt_3Pd/C > Pd_3Pt/C > Pd/C. The ORR activity of the catalysts were also measured in the presence of methanol (O_2-saturated 0.1 M $HClO_4$ containing 0.1 M CH_3OH) (Figure 6.5b). The Pt/C and Pt_3Pd/C catalysts showed strong MOR peaks in the potential range of the ORR, indicating a low tolerance to methanol oxidation consistent with the discussion in Section 6.3.2.2. The strong Pd-oxide bond blocks the surface and prevents the oxidation of

methanol. In the case of Pt, Equation (6.4a) strips both the CO and the oxygen from the Pt to leave a bare Pt surface for further adsorption of methanol.

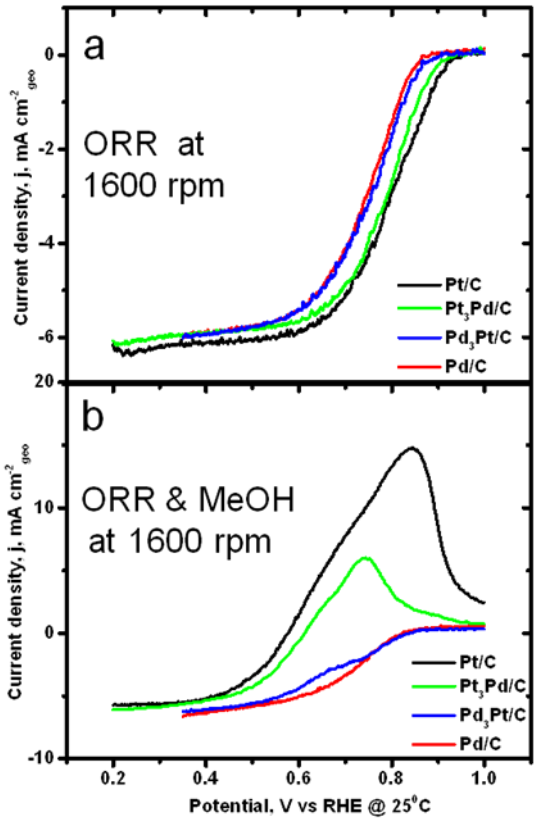

Figure 6.5: Hydrodynamic voltammograms (ORR curves) at 10 mV s^{-1} in O_2-saturated electrolyte: (a) 0.1 M $HClO_4$ and (b) 0.1 M $HClO_4$ + 0.1 M CH_3OH.

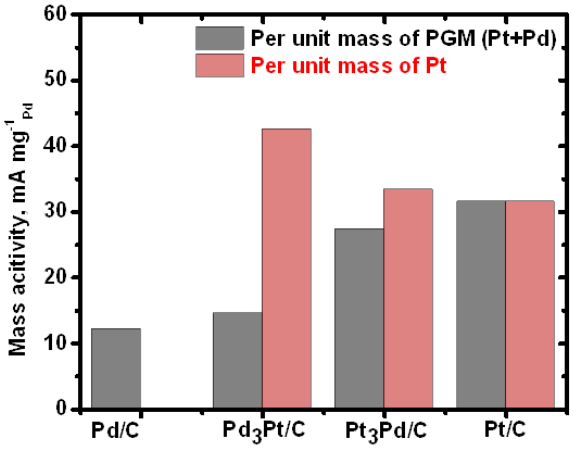

Figure 6.6: Mass activity of the catalysts at 0.82 V in the absence of methanol.

6.3.2.4. Determination of ORR intermediates

The amount of H_2O_2 formed during the ORR was evaluated with the R(RDE) measurements to identify the electron transfer mechanism (4-electron vs. 2-electron) for the ORR on the catalysts. The change in the amount of H_2O_2 during the ORR, calculated with Equation (2.10), and the selectivity of the catalysts calculated with Equation (2.11), is shown in Figure 6.7. The disk electrode was scanned from 0.2 to 1.0 V for Pt/C and Pt_3Pd/C catalysts, and from 0.35 to 1.0 V for Pd/C and Pd_3Pt/C catalysts at 10 mV s^{-1}, while the ring electrode was held at 1.4 V. The efficiency of the collection-generation experiments were determined as mentioned in Section 2.3.8 and was found to be 0.23, 0.24, and 0.28 for Pt/C, Pt_3Pd/C and Pd_3Pt/C catalysts, respectively. The amount of H_2O_2 generated was less than 5 %. This study shows that a negligible amount of H_2O_2 is generated even in the region of the largest peroxide formation (potential < 0.5 V, Section 4.3.2.6) and the mechanism of the ORR is close to a 4-electron reaction for the different catalysts.

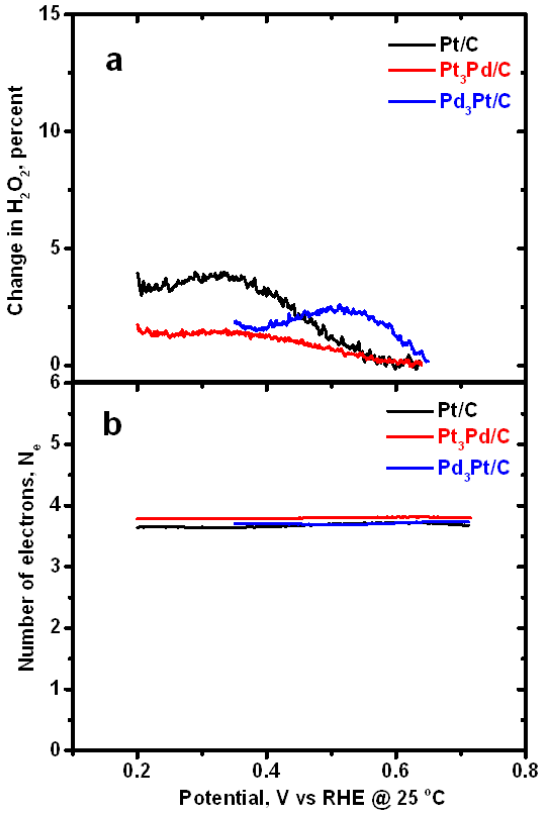

Figure 6.7: (a) Change in the amount of H_2O_2 collected at the ring electrode, (b) selectivity of the catalysts (The disk electrode was scanned from 0.2 to 1.0 V (Pt/C and Pt_3Pd/C) and 0.35 to 1.0 V (Pd/C and Pd_3Pt/C) at 10 mV s^{-1} in 0.1 M $HClO_4$ for different catalysts and the ring electrode was held at 1.4 V).

6.3.2.5. Analysis of surface phenomena on the catalysts

Surface oxidation of Pt/C and Pd/C occurs in the same potential range as seen in Chapters 4 and 5. However, the onset potential for surface oxidation on Pd/C is lower than that of Pt/C, indicating that Pd forms stronger surface oxide bonds compared to the Pt-O bond relative to the catalyst M-M bonding. A study was carried out to understand the behavior of the Pd-Pt binary-alloy catalysts under oxidizing potentials in an acidic environment. The catalyst inks for these measurements simulated the long-term exposure of the catalysts to acidic environment. The combined CV and EQCN response of the

catalysts are shown in Figures 6.8, 6.9 and 6.10 for Pd/C, Pd_3Pt/C and Pt_3Pd/C, respectively. A summary of the data is given in Table 6.4. The data for Pt/C catalyst is given in Chapter 4. The charge during the oxide formation corresponds to the Faradaic reactions on the surface and the interfacial mass-change ($\delta\Delta m$) on the catalyst surface.

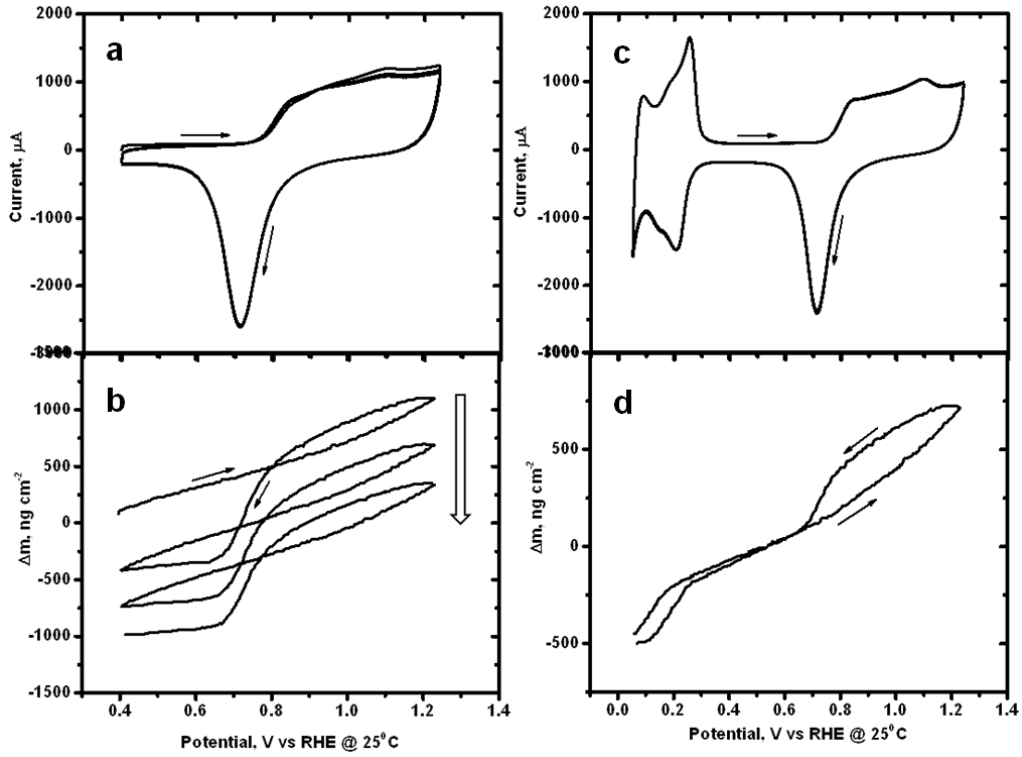

Figure 6.8: (a) and (b) Combined CV and EQCN response of Pd/C between 0.4 and 1.24 V, and (c) and (d) combined CV and EQCN response of Pd/C between 0.4 and 1.24 V in 0.5 M H_2SO_4 at 50 mV s^{-1} and 25 ^oC (The down-arrow in (b) indicates the loss of mass).

Table 6.4: Data summary of CV and EQCN response of the catalysts

Parameter	**Pd/C**	**Pd_3Pt/C**	**Pt_3Pd/C**
Charge, µC cm^{-2}_{geo}	5680	3933	3131
$\delta\Delta m$, µg cm^{-2}_{geo}	0.673	0.110	0.129
M_{ox}, g mol^{-1}	11.43 (0.4-1.24 V) 10.8 (0.05-1.24 V)	2.69	3.97

Figure 6.8 a and b shows the CV and the EQCN response of Pd/C in the potential range of surface oxidation and Figure 6.8 c and d shows the response in the potential range that includes both the H_{UPD} and oxide regions. A mass loss (~ 370 ng cm^{-2}_{geo}) was seen between consecutive cycles (Figure 6.8b). The anodic scan showed a continuous increase in mass as result of binding O. The amount of species adsorbed (Table 6.4) calculated with Equation (2.4) changed little during the potentials sweeps of the catalyst in the potential range of 0.4-1.24 V and 0.05-1.24 V. The surface oxidation of Pd can be written as shown in Equations (6.5 a-c) for different values of M, g mol^{-1}. Equation (6.5c) involves the formation of 11 g mol^{-1}. This shows that a strong surface oxide is formed on the surface of Pd/C catalyst.

$$Pd + H_2O \leftrightarrow PdO + 2H^+ + 2e^- \quad (6.5a)$$

$$PdO + H_2O \leftrightarrow PdOOH + H^+ + e^- \quad (6.5b)$$

$$\text{or} \quad Pd + 2H_2O \leftrightarrow PdOOH + 3H^+ + 3e^- \quad (6.5c)$$

It can be seen from Figure 6.9 a and b (Pd_3Pt/C) that there is a mass increase (~ 100 ng cm^{-2}_{geo}) between the consecutive cycles as indicated by the up-arrow in Figure 6.9b. The data in Table 6.4 shows that the total change in mass ($\delta\Delta m$) during the surface oxidation of the catalyst was considerably lower than that on Pd/C. The interfacial mass change during a scan reflects the competitive reactions occurring on the surface. It was seen in Section 5.3.2.1 that surface chemisorption and dissolution of oxide species occurs in the oxide region on a Pd/C catalyst. The summary of the reactions on a Pd/C catalyst as given in Table 5.6 also showed the contribution due to each reaction on the expected mass response during each potential scan. The surface oxidation of both Pd and Pt in the Pd_3Pt/C catalyst should show an increase in mass similar to that for Pd/C and Pt/C during the anodic scan. A lower mass change indicates that both addition and dissolution of surface oxygen occurs during the anodic potential scan. It was also seen that there was a

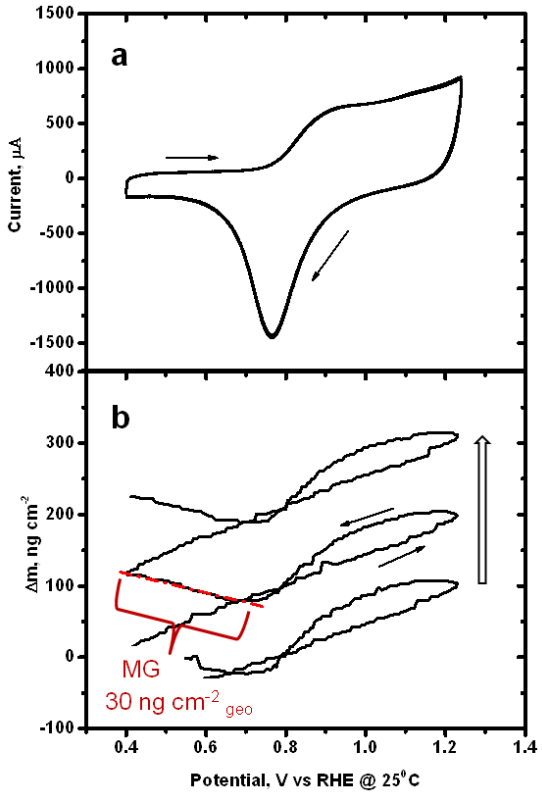

Figure 6.9: (a) CV and (b) associated EQCN response of Pd_3Pt/C between 0.4 and 1.24 V in 0.5 M H_2SO_4 at 50 mV s^{-1} and 25 ^oC (The up-arrow in (b) indicates the gain in mass).

mass gain (~ 30 ng cm^{-2}_{geo}) in the potential range of ~ 0.7-0.4 V during the cathodic scan (*i.e.*, reduction of surface oxide). This mass gain was due to the partial redeposition of the Pd metal ions from the solution onto the catalyst surface, as described in Section 5.3.2.1. In Section 5.3.2.3, it was seen that the dissolution of the initial excess surface adsorbate on the catalyst raised the concentration of Pd^{2+} ions in the solution layer adjacent to the electrode. These metal ions were deposited back onto the electrode during the cathodic scan. The presence of initial adsorbate was confirmed from the XPS analysis of the alloy catalysts. A detailed analysis of the different chemical states of the metals on the surface of the catalysts (Table 6.5) showed that the Pd_3Pt/C catalyst had a relatively higher

amount of PdO compared to Pt_3Pd/C. This species dissolved during the anodic scan and resulted in the mass gain seen in Figure 6.9b. This study shows a clear correlation between the adsorbate in the form of PdO (Pd^{2+}) and the electrochemical behavior of the catalysts.

The EQCN response of Pt_3Pd/C catalyst (Figure 6.10b) was similar to the response of a Pt surface (Chapters 3 and 4). However, the interfacial mass-change ($\delta\Delta m$) was lower than that seen on a Pt/C or a Pd/C surface. This behavior again shows the competitive surface oxidation and selective dissolution occurring on the catalyst surface. The mass gain between consecutive cycles as shown by the up-arrow in Figure 6.10b was ~ 50 ng cm^{-2}_{geo}.

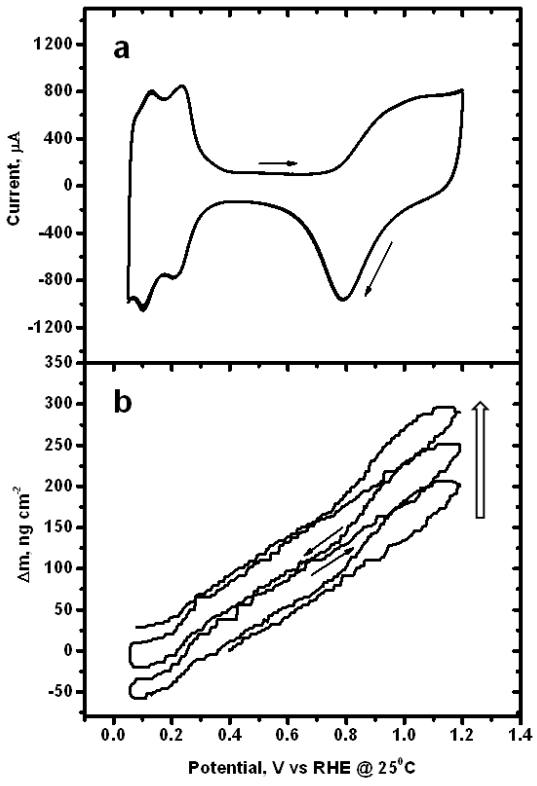

Figure 6.10: (a) CV and (b) associated EQCN response of Pt_3Pd/C between 0.4 and 1.24 V in 0.5 M H_2SO_4 at 50 mV s^{-1} and 25 ^oC (The up-arrow in (b) indicates the gain in mass).

Table 6.5: Relative near-surface composition of the different chemical states of the metals in the binary alloy catalysts

Catalyst	Pt, ($4f_{7/2}$), relative at. %		Pd, ($3d_{3/2}$), relative at. %		
	Pt^{o}	PtO_2 (Pt^{2+})	Pd^{o}	Pd-O_{ads}	PdO (Pd^{2+})
Pd_3Pt/C	13.73	9.33	48.69	7.95	20.3
Pt_3Pd/C	38.8	31.37	15.13	14.7	-

6.4. CONCLUSIONS

Carbon-supported Pd-Pt binary alloy catalysts in the atomic ratio of 3:1 and 1:3, respectively, were synthesized by the polyol reduction method, followed by heat treatment at 200 ^{o}C in a reducing atmosphere. XRD analysis showed the formation of single-phase disordered alloys. Compositional ratios of the metals obtained from EDS and XPS showed negligible surface segregation in the binary alloy catalysts. The origin of methanol tolerance and its relation to CO oxidation was investigated and compared by studying the behavior of the most tolerant (Pd/C) and the least tolerant (Pt/C) catalysts and their alloys, *viz*., Pd_3Pt/C and Pt_3Pd/C. The results show that the relative Pd-O bond is stronger than the relative Pt-O bond, which is due to the weaker Pd-Pd than Pt-Pt bonding. The study showed that the strong Pt-Pt interaction in Pt/C favored the stripping of CO via the reaction involving the adsorbed oxide on Pt, whereas the stronger relative Pd-O bond in Pd/C resulted in the oxidation of CO with a reaction with the water molecules in the solution. The alloy with a higher Pd content showed an increased tolerance to methanol oxidation reaction under similar experimental conditions. Continued potential cycling in the presence of methanol also showed that the Pd_3Pt/C binary alloy formed a more Pt-rich surface during electrochemical cycling. The reaction kinetics showed that the Pd-Pt binary alloy catalysts were very active for the ORR. The amount of peroxide intermediates during the ORR was found to be negligible, which

showed that the kinetics of the ORR predominantly involved a four-electron transfer reaction. The interfacial surface phenomena on the catalysts were studied by combined CV and EQCN measurements. The EQCN measurements revealed different competing reactions occurring on the surface of Pd and Pt in the alloy catalysts, which were not clearly resolved in the cyclic voltammograms of the alloy. This study exhibited the sensitivity of the EQCN technique. Analysis of the EQCN mass response of the catalysts showed a distinct correlation existed between the initial surface oxide (PdO, determined by XPS) on the Pd-based catalysts and their electrochemical behavior. This relation demonstrates the use of EQCN as a tool for accurate analysis of the surface.

7. Carbon-supported palladium ternary-alloy nanoparticles as a methanol-tolerant oxygen reduction reaction catalyst for fuel cells

7.1. INTRODUCTION

The direct methanol fuel cell (DMFC) is a promising power source with a high theoretical energy density operating on an easy-to-handle liquid fuel. However, the performance of the DMFC is below its theoretical value because of the low efficiency and instability of catalysts. The cathode catalysts are easily poisoned by methanol crossover from the anode through the proton-exchange membrane to the cathode. Pt-based nanoparticles are the most studied catalysts for the ORR, but their performance is degraded in the presence of methanol. Pd is a promising catalyst to replace Pt in a DMFC as it has a high methanol tolerance. However, pure Pd is a poor catalyst for the ORR and modifications have been carried out on Pd by alloying with other metals to increase the ORR activity of Pd-based catalysts. Recent developments have been toward synthesizing carbon-supported Pd-based binary alloy nanoparticles as potential cathode catalysts for low-temperature fuel cells [95, 106-109].

The primary objective of this study is to evaluate the performance of Pd when alloyed with two different base metals, Co and Ni. The work functions of Cobalt (Co) and Nickel (Ni) are lower than that of Pd, which introduces a ligand effect on Pd in an alloy of Pd-Co or Pd-Ni. The resultant work function of the ternary alloy is smaller (lies in between that of Co/Ni and Pd) than that of pure Pd. In this study, we analyze the performance of the ternary catalysts toward the ORR activity and its methanol tolerance. We also determine the nature of the surface oxide formed on the ternary-alloy catalysts by monitoring the interfacial mass-change with a surface-sensitive technique.

A carbon-supported Pd ternary-alloy catalyst (Pd_3CoNi/C) was also synthesized by the polyol method and was characterized by the different techniques described in

Chapter 2. The performance of the catalyst is compared to that of a binary alloy (Pd_3Co/C) and Pd/C catalysts synthesized by a similar procedure.

7.2. EXPERIMENTAL METHODS

7.2.1. Catalyst synthesis

Carbon-supported Pd_3CoNi and Pd_3Co catalysts with a 40 wt. % metal loading were synthesized by the polyol reduction method. In a typical experiment, 125 mg of carbon black was dispersed in 48 mL of ethylene glycol by ultrasonication and magnetic stirring. 5-15 mL of water was added to the dispersion to obtain an azeotropic mixture. The pH of the solution was adjusted by drop-wise addition of 1 M NaOH (in ethylene glycol). Palladium (Pd), cobalt (Co) and nickel (Ni) metal precursor solutions were prepared by dissolving the metal salts separately in ethylene glycol. Sodium tetrachloropalladate (Na_2PdCl_4), cobalt (II) chloride ($CoCl_2.6H_2O$) and nickel (II) chloride ($NiCl_2.6H_2O$) were used as the metal precursor salts. The Co and Ni salts with similar reduction potentials in EG were chosen for the synthesis (Section 2.1). The precursor salt solutions were added drop wise to the carbon-ethylene glycol dispersion and heated to 185 ^oC for 3.5 and 4 hours, respectively, for Pd_3Co/C and Pd_3CoNi/C, under continuous stirring. The synthesis was carried out under an inert atmosphere by continuous purging of the solution with ultrapure nitrogen gas (N_2). After cooling the polyol solution, the supported catalysts were filtered, washed with ultrapure water and dried overnight in a vacuum oven. The catalyst samples were further heated in a tube furnace under a reducing atmosphere (10% H_2/ 90% Ar gas) and at a ramp rate of 5 ^oC min^{-1} to 350 ^oC for 2 hours. The details of the polyol method are given in Section 2.1 and the compositions of the salts are given in Table 7.1. For a comparison, a PdCoNi/C and Pd/C catalysts were prepared by a similar procedure.

Table 7.1: Details of synthesis process

Catalyst	Pd salt, M	Co salt, M	Ni salt, M	EG/precursor	NaOH, M
Pd_3Co/C	0.012	0.003	-	1.14	0.19
Pd_3CoNi/C	0.025	0.008	0.008	0.64	0.21
PdCoNi/C	0.016	0.016	0.016	0.58	0.21
Pd/C	0.025	-	-	0.4	0.20

7.2.2. Structural/chemical characterization

Bulk metal compositions were determined with an SEM-EDS scanning electron microscope as described in Section 2.2.2. The metal loading in the carbon-supported catalysts was determined by TGA as described in Section 2.2.3. The structural characterization of the catalysts was carried out with a Philips 3520 X-ray diffractometer as described in Section 2.2.1. The morphology of the samples was analyzed with a JEOL 2010F TEM as described in Section 2.2.4.

7.2.3. Electrochemical characterization

7.2.3.1. Preparation of catalyst ink and electrode

The catalyst inks were prepared by mixing a known amount of the catalyst powder in 5 wt. % Nafion solution and 2-propanol-water mixture as described in Section 2.3.1. 60 μL of the homogeneous ink was drop-cast onto the gold-coated quartz crystal sensor (5 MHz) with a geometric area of 1.37 cm^2 and allowed to dry at room temperature. For the RDE measurements, 10 μL of the homogeneous ink was drop-cast onto a glassy-carbon electrode with a geometric area of 0.19634 cm^2. The method of ink preparation was the same for all the catalyst materials being studied. The details of the cast electrodes are given in Table 7.2.

Table 7.2: Ink loading for different catalysts

Catalyst	Loading level, µg cm^{-2}			Thickness of dry film, µm	Nafion, wt. % (dry film)
	C	PGM	Metal		
Pd_3CoNi/C-EQCN	62	32	41	0.45	21.8
Pd_3CoNi/C-ORR	124.1	65.0	82.7	0.90	21.4
PdCoNi/C-ORR	119.3	40.0	79.6	0.89	22.1
Pd_3Co/C-ORR	122.2	73.2	81.5	0.88	21.1
Pd/C-ORR	108.0	72.0	72.0	0.79	22.1

7.2.3.2. Cyclic voltammetry (CV)

The electrochemical characterization was carried out by cyclic voltammetry (CV) as described in Section 2.3. CO-stripping voltammetry was carried out on the electrodes as described in Section 2.3.6 for the Pd-based catalysts. Methanol oxidation was carried out by a potential scan in the range of 0.4 to 1.24 V at 50 mV s^{-1} in 0.1 M $HClO_4$ containing 0.1 CH_3OH (deaerated electrolyte). Hydrodynamic voltammetry (oxygen reduction reaction measurements, ORR) with a rotating disk electrode (Section 2.3.2) was carried out in an O_2-saturated solution (0.1 M $HClO_4$) as described in Section 2.3.4 and the methanol tolerance study was carried out by the same procedure in an O_2-saturated 0.1 M $HClO_4$ electrolyte containing 0.1 M CH_3OH.

7.2.3.3. Electrochemical quartz crystal nanobalance measurements (EQCN)

The *in situ* mass measurements were performed with an EQCN setup as described in Section 2.3.3. A batch cell with a 5 MHz sensor was used for the measurements. The amount of adsorbed intermediate on the electrode surface was obtained from the combined CV and EQCN measurements for the potential cycling, and steady-state values are reported. The details are given in Section 2.3.4.

7.3. RESULTS AND DISCUSSION

7.3.1. Structural/chemical characterization

7.3.1.1. Chemical characterization

Bulk compositions determined by EDS are reported in Table 7.3 and are comparable with the nominal composition based on the stoichiometric amount of precursor salts taken for synthesis. Images of the EDS maps of the catalysts are given in Figure 7.1c. It is seen that the metals are uniformly distributed on the catalysts. The metal loading was found to be approximately 40 wt.%.

7.3.1.2. Structural characterization

Figure 7.1 compares the XRD patterns of the different catalyst samples. The pattern was also compared with a CoNi/C sample prepared by a similar procedure. All the peaks can be indexed with the f.c.c crystal structure. The narrow peaks observed for CoNi/C indicate the high degree of crystallinity of the synthesized nanoparticles. Pd has a smaller surface energy, and addition of Pd to the Co-Ni mixture helps form nanoparticles. Broad peaks with a shoulder in the first peak at locations close to the (111) peaks of Co and Ni are seen for the PdCoNi/C sample. This shoulder indicates that Co and Ni tend to form a separate phase. At large concentrations of Pd in solution, the Pd-Co/Ni particles are homogeneous, but at low concentrations they are not homogeneous. Polyol synthesis under high synthesis temperature and under reflux conditions formed PdCoNi/C nanoparticles with a similar shoulder/peak. The average crystallite size calculated from the Scherrrer's formula and the lattice parameter of the samples as obtained from the XRD patterns are given in Table 7.3.

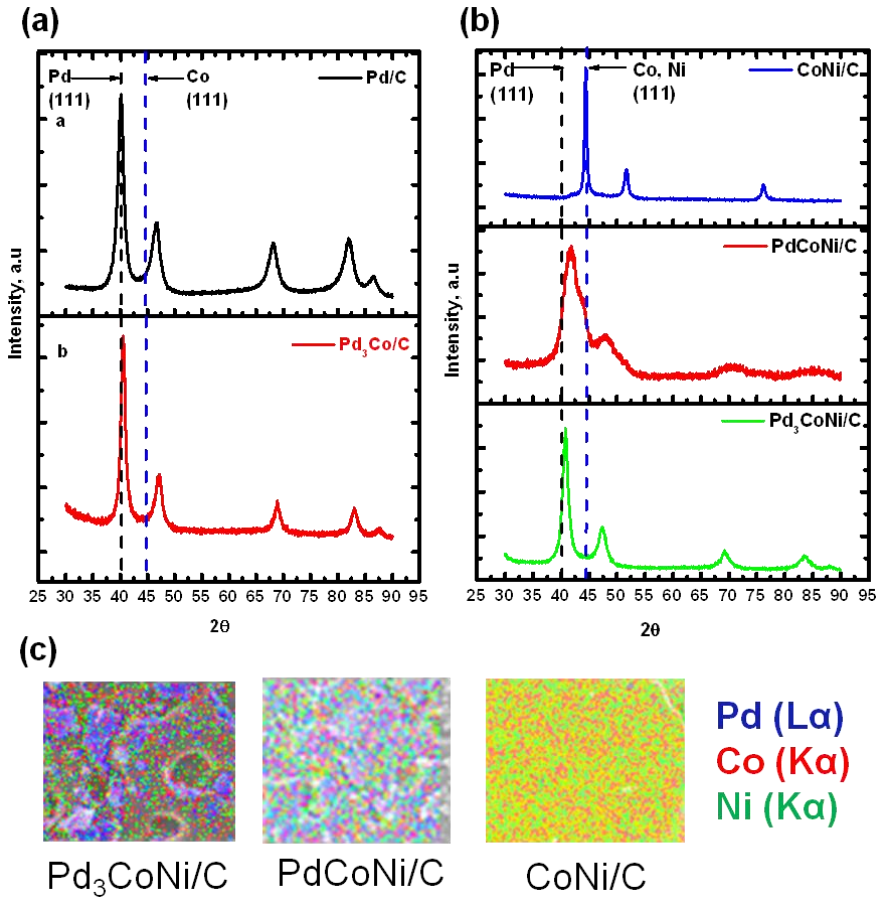

Figure 7.1: (a) XRD patterns of Pd/C and Pd_3Co/C, (b) XRD patterns of CoNi/C, PdCoNi/C and Pd_3CoNi/C with the expected positions of Pd (111) and Co, Ni (111) peaks, and (c) Images of the EDS maps of the catalysts.

The TEM images and the particle size distribution of the catalysts are shown in Figure 7.2. It is seen that the synthesized particles have predominantly a spherical morphology. The size of the nanoparticles (averaged over 70 particles) was found to be 6.02 and 5.52 nm, respectively, for the Pd_3Co/C and Pd_3CoNi/C samples. A wide distribution was seen for the Pd_3CoNi/C samples. The observed distribution is due to differences in the surface energies of the constituent atoms (Pd_{SE} < $(Co, Ni)_{SE}$, SE-surface energy) and its influence on the rate of formation of the ternary alloy nanoparticles as mentioned above.

Table 7.3: Summary of structural/chemical characterization of the catalysts

Catalyst	**Metal, at.% (nominal)**	**Metal (bulk), at.%, (EDS)**	**Crystallite size (avg.), nm (XRD)**	**Lattice parameter, Å (XRD)**	**d-spacing (220), Å (XRD)**	**Lattice mismatch (compressive strain), %**
Pd_3Co/C	$Pd_{75}Co_{25}$	$Pd_{83}Co_{17}$	6.5 ± 0.5	3.8556	1.3628	0.84
Pd_3CoNi/C	$Pd_{60}Co_{20}\ Ni_{20}$	$Pd_{67}Co_{18.3}\ Ni_{14.7}$	5.5 ± 0.5	3.8346	1.3561	1.33
PdCoNi/C	$Pd_{33.4}Co_{33.3}\ Ni_{33.3}$	$Pd_{35.9}Co_{33.3}\ Ni_{30.8}$	-	3.8306	-	-
CoNi/C	$Co_{50}\ Ni_{50}$	$Co_{49.8}\ Ni_{50.2}$	13.5 ± 1.5	3.5326	-	-
Pd/C	-	-	6.0 ± 1.0	3.8914	1.3744	-

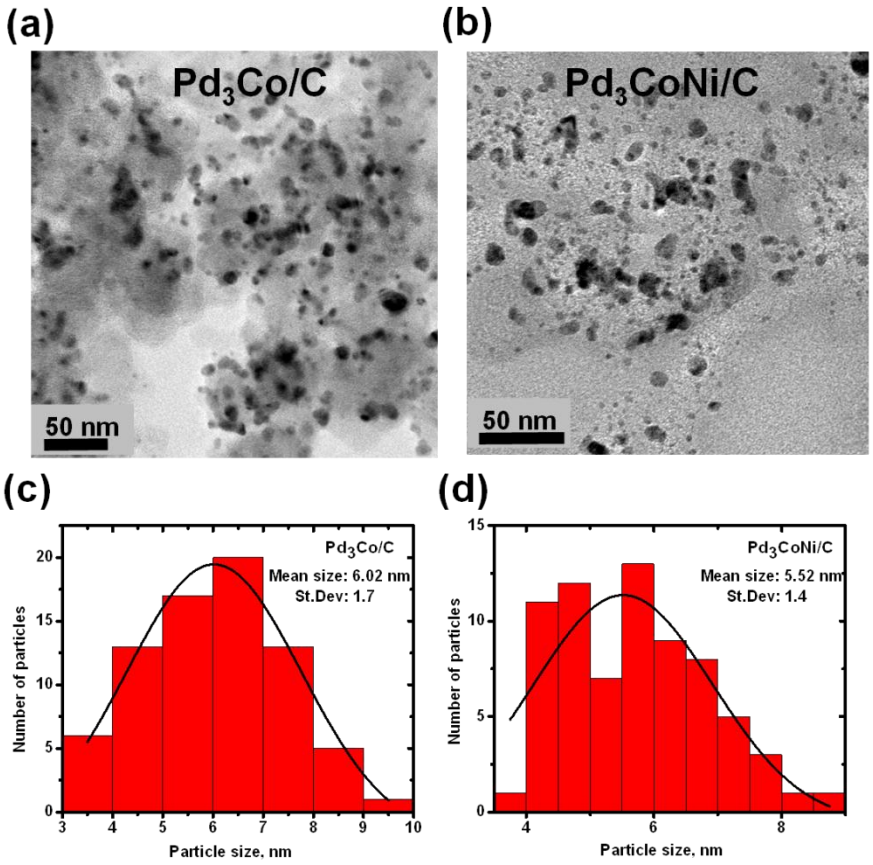

Figure 7.2: (a) and (b) TEM images, and (c) and (d) particle size distributions of Pd_3Co/C and Pd_3CoNi/C samples.

7.3.2. Electrochemical characterization

7.3.2.1. CO-stripping voltammetry and methanol oxidation

CO is the primary intermediate in the methanol oxidation reaction. The study of oxidation of CO helps to understand the behavior of the catalysts with regard to the methanol oxidation reaction (MOR) and the ORR in the presence of methanol. The CO-stripping voltammograms and the MOR voltammograms for the different catalysts are shown in Figure 7.3. The peak potential and current values (indicator of the binding strength of CO to the active metal site and reaction rate) are given in Table 7.4. The dashed vertical line in Figure 7.3 represents the CO oxidation peak for Pd/C. The CO

oxidation peak potential is shifted to negative values for the alloy catalysts compared to that for Pd/C, indicating a decrease in methanol tolerance. This shift indicates a weakening of the CO-metal binding energy. The current values of the alloy catalysts span a lower voltage range relative to Pd/C, which is due to a change in the strength of the CO adsorption by the alloying effect. Details of the analysis of oxidation of CO and methanol tolerance on Pt/C and Pd/C catalysts are given in Section 6.3.2.1. A weaker metal-metal interaction was shown to increase the metal-adsorbate interaction. The MOR studies were carried out to understand the origin of methanol tolerance; potential scans were carried out both in the presence and absence of methanol (Figure 7.3). There were no peaks for methanol oxidation and a similar behavior was observed in the absence of methanol indicating the tolerance of these Pd-based catalysts to the MOR. This study is consistent with the observation of a tolerance to the MOR where there is a weakening of the strength of the catalyst M-M interaction compared to the Pt-Pt interaction in a Pt catalyst.

Table 7.4: Peak potential and peak current of CO-stripping voltammograms

Catalyst	**Peak potential, V**	**Peak current, µA**
Pd_3Co/C	0.937	1056
Pd_3CoNi/C	0.935	738
PdCoNi/C	0.922	606
Pd/C	0.949	1518

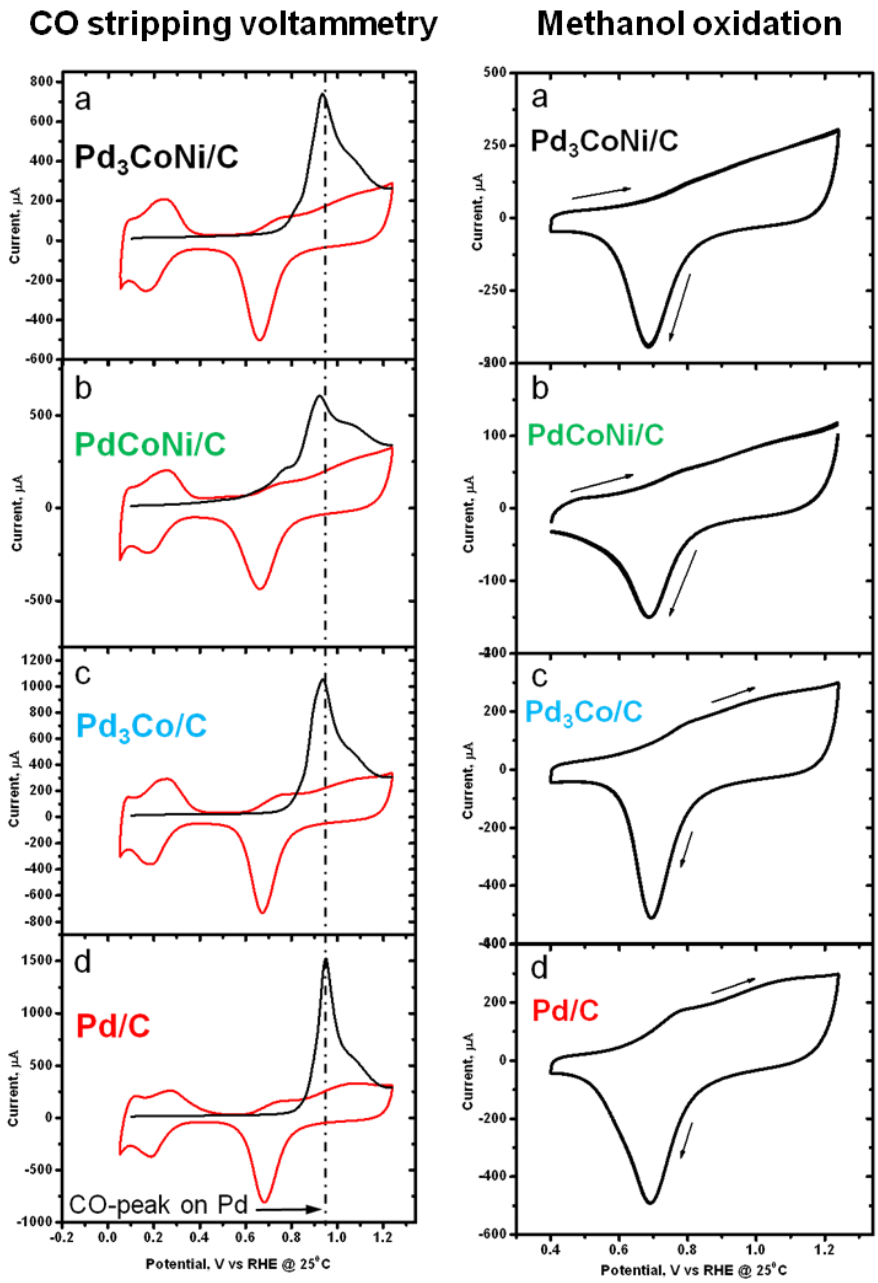

Figure 7.3: CO-stripping and methanol oxidation reaction (MOR) voltammograms of the catalysts.

7.3.2.2. ORR and methanol tolerance

Figure 7.4 shows the response of the hydrodynamic measurements with the RDE technique carried out to evaluate the ORR activity in the presence and absence of methanol. As seen from Figure 7.4a, a clear limiting current is obtained for all the catalysts and the values were comparable to the expected theoretical limiting current density for the ORR in 0.1 M $HClO_4$. It is also seen that the polarization curves shift toward higher potentials with increasing Pd content in the catalyst. A comparison of the activities of the catalysts per unit mass of Pd is shown in Figure 7.5. Among the catalysts with high Pd content (Pd_3Co/C and Pd_3CoNi/C), the Pd_3CoNi/C ternary alloy catalyst showed a higher mass activity. In DMFCs, a decrease in the ORR activity occurs when methanol from the anode compartment permeates through the proton-exchange membrane and reaches the cathode compartment. To investigate the activity of the catalysts under methanol crossover, experiments similar to the ORR measurements were carried out in an O_2-saturated 0.1 M $HClO_4$ containing 0.1 M CH_3OH (Figure 7.4b). A decrease in the half-wave potential for the ORR is seen for the catalysts in the presence of methanol though no peaks were seen for the methanol oxidation in the potential range of the ORR measurements. The decrease in half-wave potential indicates the blocking of some active Pd sites for ORR by the adsorbed methanol. The details are explained in Chapter 6. The data are summarized in Table 7.5.

The CV (Figure 7.3) and hydrodynamic (Figure 7.4) measurements indicate the tolerance of the ternary catalyst to methanol oxidation and suggests its potential use as a good catalyst to alleviate the problem of methanol crossover in DMFCs.

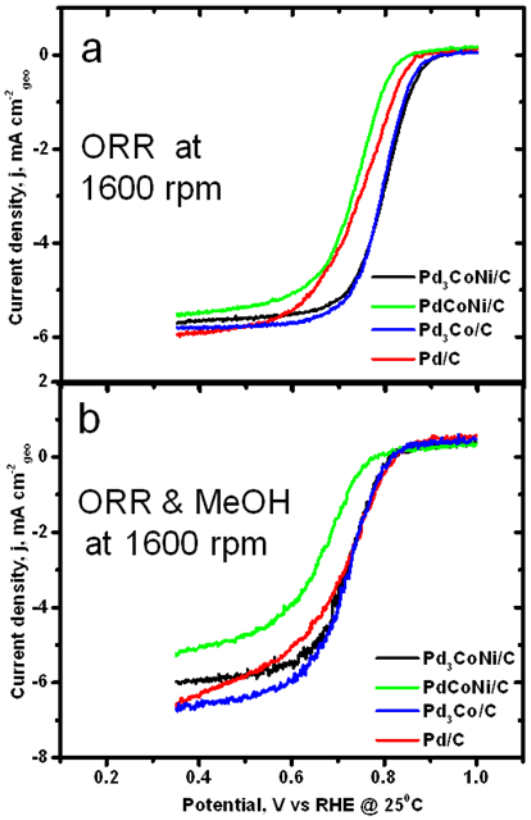

Figure 7.4: Hydrodynamic voltammograms (ORR curves) at 10 mV s^{-1} in O_2-saturated electrolyte: (a) 0.1 M $HClO_4$ and (b) 0.1 M $HClO_4$ + 0.1 M CH_3OH.

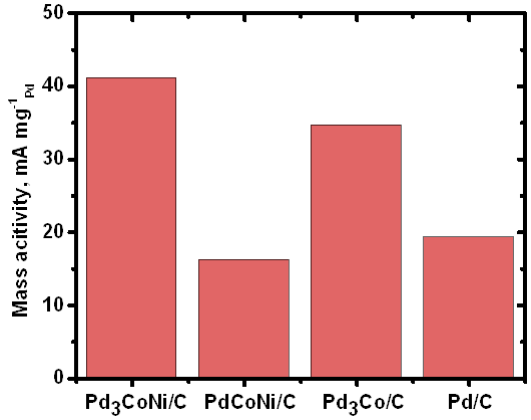

Figure 7.5: Mass activity of the catalysts at 0.8 V in the absence of methanol.

Table 7.5: Mass activity and half-wave potential of the catalysts

Catalyst	Half-wave potential, V			Mass activity, $mA\ mg_{Pd}^{-1}$
	without CH_3OH	with CH_3OH	ΔV	
Pd_3CoNi/C	0.797	0.725	72	41.1
PdCoNi/C	0.738	0.658	80	16.2
Pd_3Co/C	0.793	0.729	64	34.6
Pd/C	0.749	0.718	31	19.3

7.3.2.3. Interfacial mass change

The combined CV and EQCN response of the Pd_3CoNi/C ternary alloy catalyst is shown in Figure 7.6. In the anodic scan, there was a continuous mass increase with potential. This confirms the absence of initial surface adsorbates on the catalyst as described in Section 5.3.2.1. During the cathodic scan, the mass decreased in the oxide region as the surface oxides were reduced. Details of the analysis of the EQCN response of a Pd-based catalyst are given in Sections 5.3.2.1 and 5.3.2.3. The change in the interfacial mass (Δm) was calculated with Equation (2.3) and the amount of the adsorbed species was calculated with Equation (2.4). From the integrated charge density and the associated mass change in the potential range of surface oxidation of Pd, a ratio of 19 g mol^{-1} (approx.) of electrons passed was obtained, which indicates the formation of a hydrated form of surface oxide on the ternary alloy catalyst. The formation of a hydroxyl intermediate would account for a mass change of 17 g $mole^{-1}$ of electrons passed. A higher mass change for the ternary alloy catalyst may signal the incomplete deprotonation of the water molecules that were initially adsorbed on the surface of the catalyst at the onset of surface oxidation. Assuming a hydroxyl species is adsorbed on the ternary alloy catalyst, the surface oxidation can be written as,

$$Pd + H_2O \leftrightarrow PdOH + H^+ + e^- \quad (7.1)$$

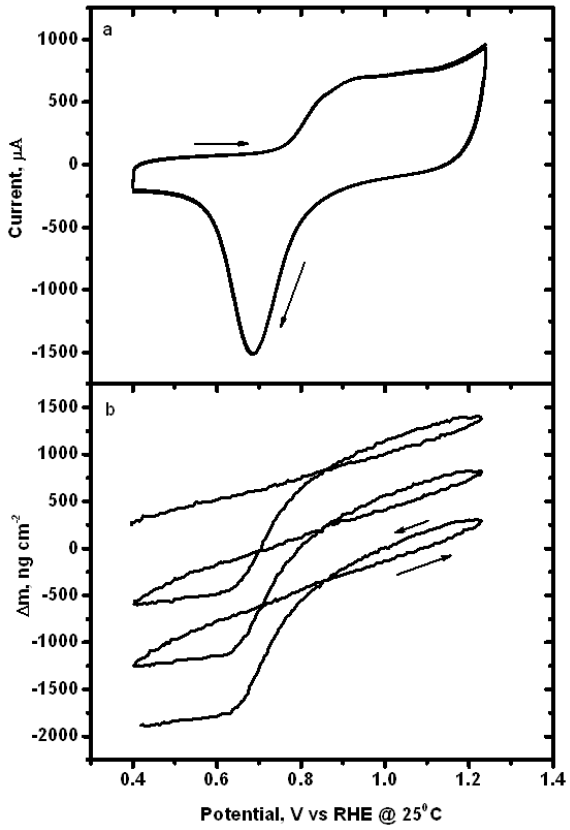

Figure 7.6: Combined CV and EQCN response of Pd_3CoNi/C in 0.5 M H_2SO_4 between 0.4 and 1.24 V at 50 mV s^{-1} and 25 ^oC.

The coulomb charge and mass change in the oxide formation were assumed to be entirely due to adsorbed surface oxides on the catalysts. It was seen that an anhydrous oxide film (PdO) was formed on the Pd/C as given in Chapters 5 and 6. The formation of the hydroxyl intermediate indicates a weakening of the adsorbate-metal interaction in the case of the ternary alloy catalyst. It has been reported that Co and Ni in a Pd host experience a moderate anti-segregation energy [65]. High-temperature heating results in the migration of Pd atoms to the surface of the alloy nanoparticles because a stronger Pd-Pd bonding reduces the surface energy. Thus, a Pd-rich shell should be formed on the nanoparticles. However, the change in work function should also play a role. Due to the

differences in the work function of the individual atoms (the work function of Co/Ni is lower than that of Pd) electrons flow from Co/Ni to Pd. This transfer of electrons raises the Fermi level of Pd in the ternary alloy.

Combined CV and EQCN response of Pd_3Co/C binary-alloy catalyst is shown in appendix F (Figure F.1). The measurements were carried out for a CV in the potential range of 0.05 to 1.20 V at 50 mV s^{-1} in 0.5 M H_2SO_4. The amount of adsorbed oxide (M) calculated with Equation (2.4), was found to be 17 ± 1 g mol^{-1} of electrons passed indicating the formation of an hydroxyl intermediate as given by Equation (7.1).

7.4. CONCLUSIONS

A carbon-supported Pd_3CoNi was synthesized by the polyol reduction method. The ORR activity and methanol tolerance of the ternary catalyst was measured with a rotating disk electrode. The performance of the catalyst was compared to that of the Pd_3Co/C binary-alloy and Pd/C catalysts. The ternary-alloy catalyst showed a higher mass activity for the ORR compared to the binary-alloy catalyst (Pd_3Co/C). A weakening was observed for both the atomic (O) and molecular (CO) adsorbates. The ternary alloy catalyst showed good tolerance to methanol oxidation and thus retained the high catalytic activity of the ORR in the presence of methanol. The surface oxide on the ternary alloy catalyst has been analyzed by combined CV and EQCN measurements. The type of adsorbate on Pd_3CoNi/C has been identified as OH. Subject to the long-term stability, the Pd_3CoNi/C ternary alloy catalyst is an excellent economical candidate that can be considered as a cathode fuel-cell catalyst in DMFCs.

8. Summary and perspectives

The primary objective of this dissertation was to analyze the surface phenomena on platinum-based and palladium-based catalysts for the oxygen reduction reaction in low-temperature fuel cells and to gain an understanding of the role of surface adsorbates on the catalyst activity and durability. In this regard, an *in situ* surface sensitive technique was used to monitor the electrode-electrolyte interface to determine the origin and nature of the adsorbates. The results of this dissertation are briefly summarized below.

The surface oxidation on polycrystalline platinum at different cathodic potentials, electrolytes, and dissolved gases was studied by combined CV and EQCN measurements. The results show that over an anodic sweep, an anhydrous oxide layer (O) is formed on a Pt surface over a wide potential range. It was found that the type of anion in the electrolyte does not influence the surface oxidation at high positive potentials. It was also found that the O_2 gas in the electrolyte does not influence the extent of surface oxidation. It was concluded that the surface chemisorbed species came from the water of the electrolyte at a particular potential.

The validity of the EQCN technique for catalyst nanoparticles was established for the first time by measuring the *in situ* mass change and dissipation energy of the catalyst film. The extent of surface oxidation on the carbon-supported platinum and platinum binary-alloy catalysts was evaluated with EQCN and rigid model analysis. The surface analysis showed that O is first formed on the carbon-supported Pt catalysts whereas a hydroxyl (OH) intermediate is adsorbed on the surface of the Pt when alloyed with Co and Cu. The catalysts with a strong metal-O bond show a greater degradation loss when compared to an alloy. It was concluded that the type of surface oxide on the catalyst influenced the activity and durability of the catalysts for the ORR.

A series of carbon-supported palladium-based catalysts were synthesized by the polyol method. Structural characterization showed the formation of single-phase disordered alloys. The surface analysis with combined CV and EQCN measurements showed the influence of the initial surface oxide on the stability of the palladium surface. It was found that the oxide on the synthesized catalysts undergoes chemical dissolution at higher anodic potentials when in contact with the acidic electrolyte. It was also found that an oxide (O) was formed on Pd and Pt and if Pd was alloyed with Au whereas a hydroxyl (OH) was formed when Pd was alloyed with Co and Ni as a result of a weaker M-O bond. However, the M-O bond strength relative to the M-M bonding in the catalyst was weaker.

Studies on the carbon-supported palladium-gold binary alloy catalysts (Pd_3Au/C) were carried out as a function of heat-treatment temperature. The results show that heating the catalysts to a minimum temperature of 300 ^{o}C is required to form an alloy with random distribution of metals. The EQCN analysis shows the formation of O on the catalyst surface. It was found that the durability of the catalysts increased with the heat treatment temperature.

The electrochemical behavior of platinum and palladium was analyzed for the individual metal catalysts (Pt/C and Pd/C) and the binary-alloy catalysts (Pd_3Pt/C and Pt_3Pd/C). A competition between the metal-metal interaction and the metal-adsorbate interaction was observed. A stronger metal-metal bond weakened the relative metal-oxygen bond. The EQCN analysis of Pt/C and Pd/C showed the formation of a surface oxide (O) on the anodic sweep. The ORR activity and methanol tolerance measurements showed that the Pd-O bonding was stronger than the Pt-O bonding relative to the catalyst M-M bondng. The studies also show strengthening of the Pd-metal bonding by alloying

Pd with Pt, which weakens the relative metal-O bond thereby decreasing the tolerance of the catalysts to methanol oxidation.

Analysis of the carbon-supported Pd_3CoNi/C ternary-alloy catalyst showed enhanced ORR mass activity compared to Pd_3Co/C. EQCN analysis of the Pd-base metal alloy catalysts showed the formation of hydroxyl adsorbed species as the surface oxide on both catalysts as a result of a weaker M-O bond strength. The results show that the high tolerance of the catalysts to methanol oxidation is consistent with a weaker catalyst M-M bonding than that of Pt.

In summary, this dissertation focused on the synthesis and analysis of the surface phenomena of catalysts for the oxygen reduction reaction. A combination of physical and electrochemical characterizations techniques were used to characterize the catalysts and to explain the observed catalytic performances. The results in this work show that surface oxidation on the catalyst in an acidic electrolyte results from interactions with the electrolyte and not with O_2. The activity of the oxygen reduction reaction, which depends on interaction of O_2 with the catalyst surface, appears to be stronger in the presence of surface OH than surface O.

These studies leave open the question regarding the steps of the ORR by reaction of the O_2 molecule with a catalyst having oxide species on the surface.

Appendices

APPENDIX A (*CHAPTER 2)*

ACS grade chemicals and reagents were used, as received, for the studies.

Table A.1: List of Consumables.

S.No.	Material	Supplier	Details
1	Carbon black (Vulcan XC 72R)	CABOT, Fuel cell store	CAS # 1333-86-4
2	Unsupported Pt black	BASF	
3	40 wt.% Pt/Vulcan XC 72R	BASF	
4	40 wt.% Pt_3Co/Vulcan XC 72R	BASF	
5	$PtCu_3$/HSC	Strasser research group-Univ. of Houston	GM 0103 S182/1
6	2-propanol	Fisher Scientific (certified ACS plus)	CAS # 67-63-0
7	Amyl acetate ($C_7H_{14}O_2$)	Fisher Scientific	Laboratory grade, CAS # 628-63-7
8	Auric (III) chloride	Alfa Aesar	CAS # 27988-77-3, 99.9% (metals basis), Au 49 % (min)
9	Cobalt (II) chloride hexahydrate	Alfa Aesar	CAS # 7791-13-1, 99.9% (metals basis)
10	Copper (II) sulfate pentahydrate	Fisher Scientific (certified ACS)	CAS # 7758-99-8, 100.0% (assay)
11	Ethylene Glycol	Fisher Scientific (certified)	CAS # 107-21-1
12	Hydrochloric acid	Fisher Scientific (certified)	CAS # 7647-01-0
13	Methanol	Optima ® 0.2 μ filtered, Fisher scientific	Methanol A454-1, CAS # 67-56-1

Table A.1 continued.

S.No.	Material	Supplier	Details
14	Nafion 5wt.% solution	Ion power, Inc	Dupont DE521 Nafion® solution
15	Nickel (II) chloride hexahydrate	Fisher Scientific (certified)	CAS # 7791-20-0, 100.4% (assay)
16	Nitric acid	Fisher Scientific (certified)	CAS # 7697-37-2
17	Nylon membrane filter	Whatman	0.8 μm, diameter 47 mm, Cat no 7408-004
18	Perchloric acid	Optima grade, Fisher scientific	A 469-250, CAS # 7601-90-3, 65-71% (assay)
19	Potassium chloride, KCl	Fisher Scientific (certified ACS)	CAS # 7447-40-7, 99.4% (assay)
20	Potassium chloroplatinate (II)	Alfa Aesar	CAS # 10025-99-7, 99.9% (metals basis), Pt 46 % (min)
21	Potassium Ferricyanide, $K_3Fe(CN)_6$	Fisher Scientific (certified ACS)	CAS # 13746-66-2, 99.8% (assay)
22	Potassium nitrate, KNO_3	Fisher Scientific (certified)	CAS # 7757-79-1
23	Silver (II) nitrate	Alfa Aesar	CAS # 7761-88-8, 99.9% (metals basis)
24	Sodium tetra chloropalladate (II)	Alfa-aesar, Acros ogranics	CAS # 13820-53-6, 99.9% (metals basis)
25	Sulfuric acid	Fisher Scientific (certified ACS plus)	A 300 s-212, CAS # 7664-93-9
26	Water	Millipore	>18 MΩ.cm at room temperature

Table A.2: List of Compressed gases.

S.No.	Compressed gas	Company	CAS #	Details
1	Air	Airgas	7782-44-7	Air Zero Grade Size 300
2	Argon	Airgas	7440-37-1	UHP size 300, grade 5.0
3	Carbon monoxide	Airgas	630-08-0	5 % Carbon monoxide, balance Argon
4	Hydrogen	Airgas	1333-74-0	10 % Hydrogen, balance Argon 300
5	Nitrogen	Airgas	7727-37-9	UHP size 300, grade 5.0
6	Oxygen	Airgas	7782-44-7	UHP size 300, grade 4.4

Table A.3: List of Equipments.

S.No.	Equipment	Company
1	Air oven (Gravity convection)	Precision®
2	CH 760 C Electrochemical work station	CH instruments
3	Glassy carbon electrodes	Pine instruments
4	Hot stirring plate	Corning® PC-420D, Isotemp-Fisher scientific
5	Hydrogen electrode	Gaskatel, Edaq
6	Impedance phase analyzer (S1 1260) with electrochemical interface (S 1287)	Solartron
7	Maxtek-RQCM	Maxtek, Inficon
8	Milli Q integral water purification system	Millipore
9	R(R)DE set-up	Pine instruments
10	Sonicator (batch type, 2510)	Branson
11	Vacuum oven	VWR scientific products
12	Weighing balance (d=0.1 mg)	Mettler Toledo; Ohaus

Table A.4: Surface oxygenated species.

Species	M_{ox}, g mol^{-1} (per electron)	No. of electrons
O	8	2
OO	8/16	4 / 2
$O(OH)_2$	12.5	4
OH	17	1
$(OH)_2$	17	2
$(OH)_4$	17	4
$O_2.H_2O$	12.5	4
OH_2	18	1 / 2
$O_2.3H_2O$	21.5	4
$(OH)_6^{2-}$	25.5	4
$O.2H_2O$	26	2
$O_2.4H_2O$	26	4
OOH	11	3
$(OH)_3SO_4$	37	4

Note: The reactions involving higher number of electrons may form thicker oxides. The values were calculated from the different possible reaction occurring on Pt surface.

APPENDIX B (*CHAPTER 3)*

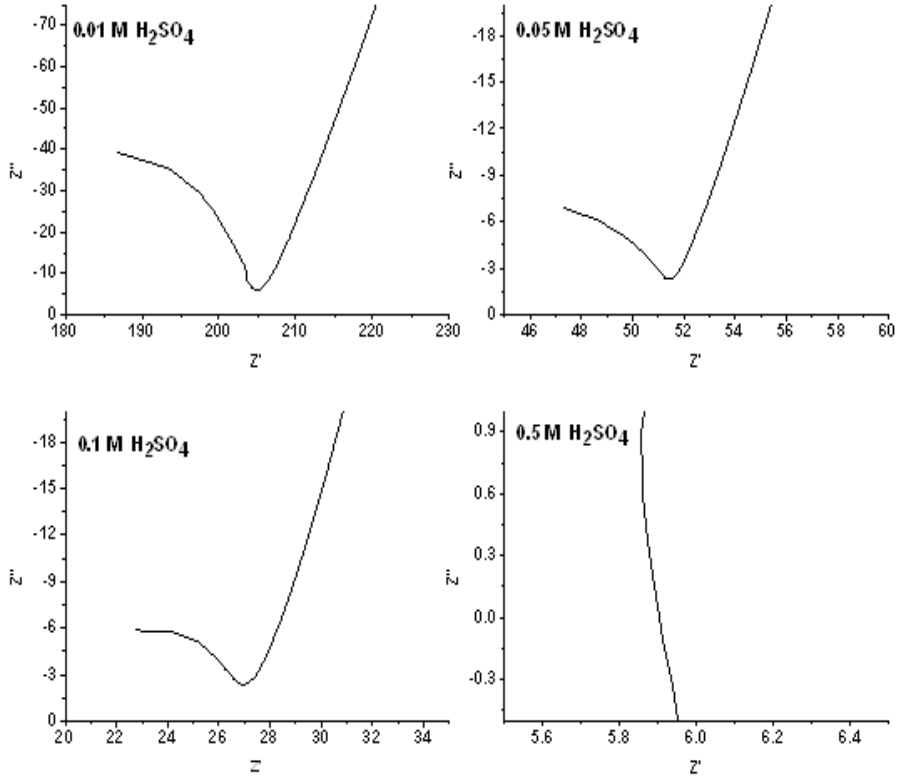

Figure B.1: Nyquist plots for measurement of solution resistance (Electrochemical impedance spectroscopy).

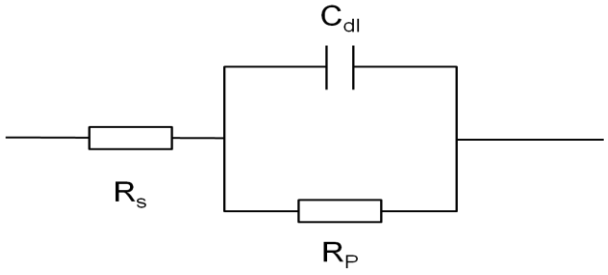

Figure B.2: Schematic of simplified Randles circuit.

The minimum value of Z' (at Z" = 0) is taken as the solution resistance (R_s), assuming a simplified Randles circuit.

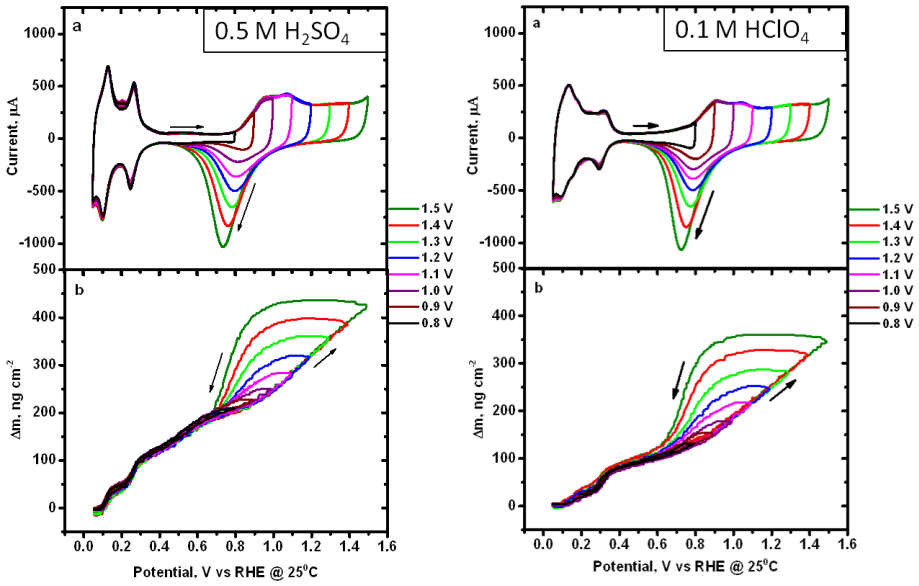

Figure B.3: Combined CV and EQCN response of Pt electrode in 0.5 M H_2SO_4 and 0.1 M $HClO_4$ in the potential range of 0.05 and E_H at 25 °C and 50 mV s^{-1}.

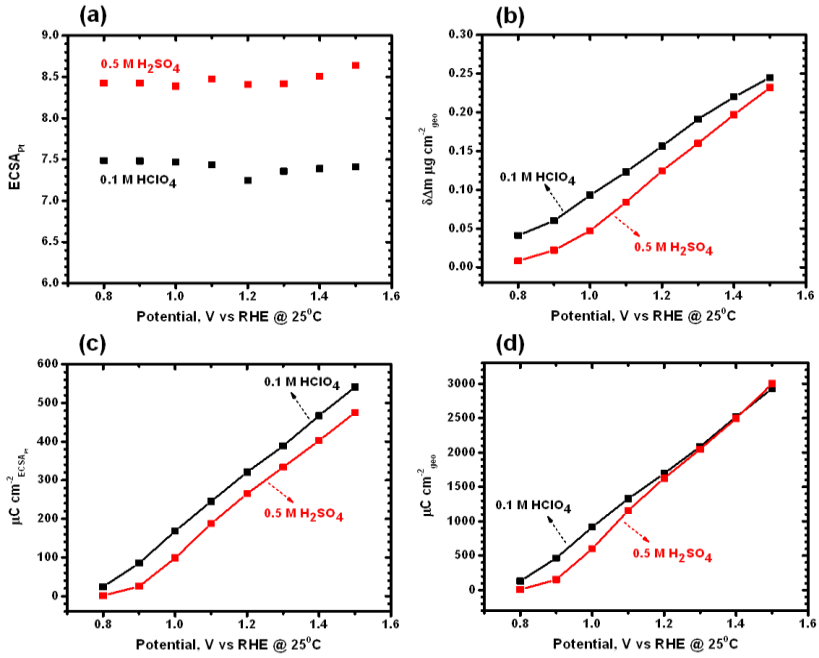

Figure B.4: Electrochemical behavior of Pt electrode in 0.5 M H_2SO_4 and 0.1 M $HClO_4$: (a) $ECSA_{Pt}$, (b) interfacial mass-change, (c) charge density of oxide formation normalized per electrochemical area, and (d) charge density of oxide formation normalized per geometric area.

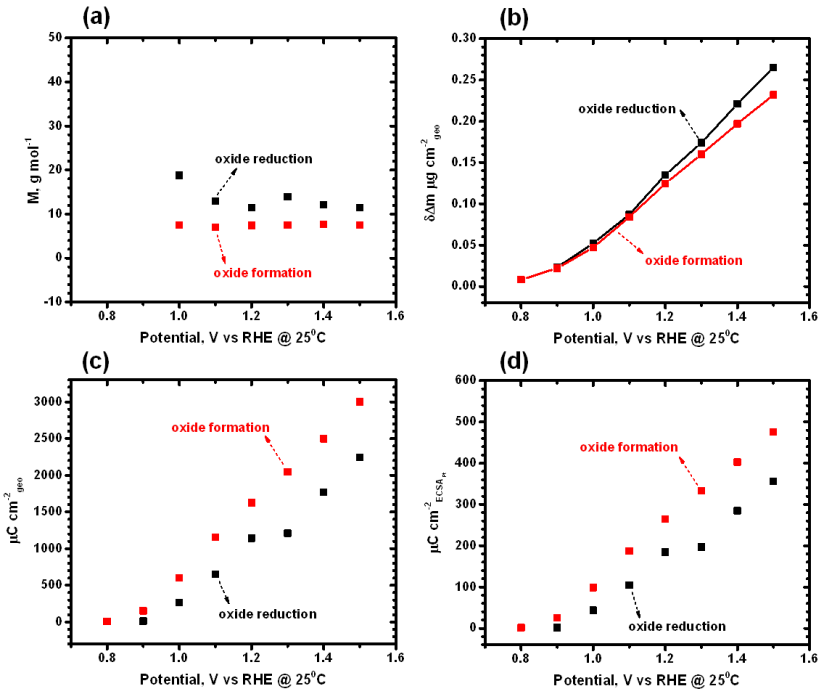

Figure B.5: Electrochemical behavior of Pt electrode in 0.5 M H_2SO_4 during oxide formation and oxide reduction: (a) amount of adsorbed species, M, g mol^{-1}, (b) interfacial mass-change, (c) charge density of oxide normalized per geometric area, and (d) charge density of oxide normalized per electrochemical area.

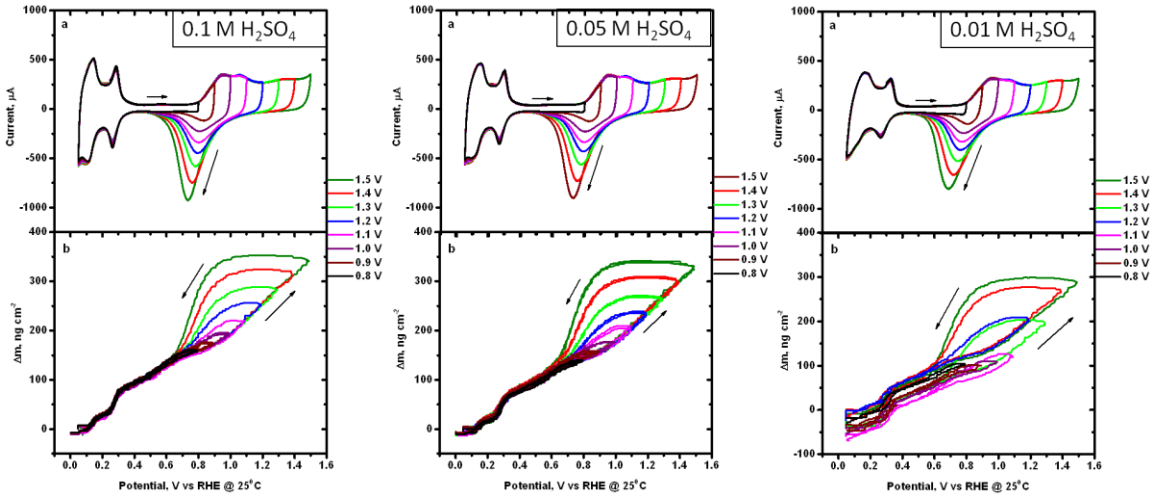

Figure B.6: Combined CV and EQCN response of Pt electrode in 0.1 M H_2SO_4, 0.05 M H_2SO_4, and 0.01 M H_2SO_4, in the potential range of 0.05 and E_H at 25 ^oC and 50 mV s^{-1}.

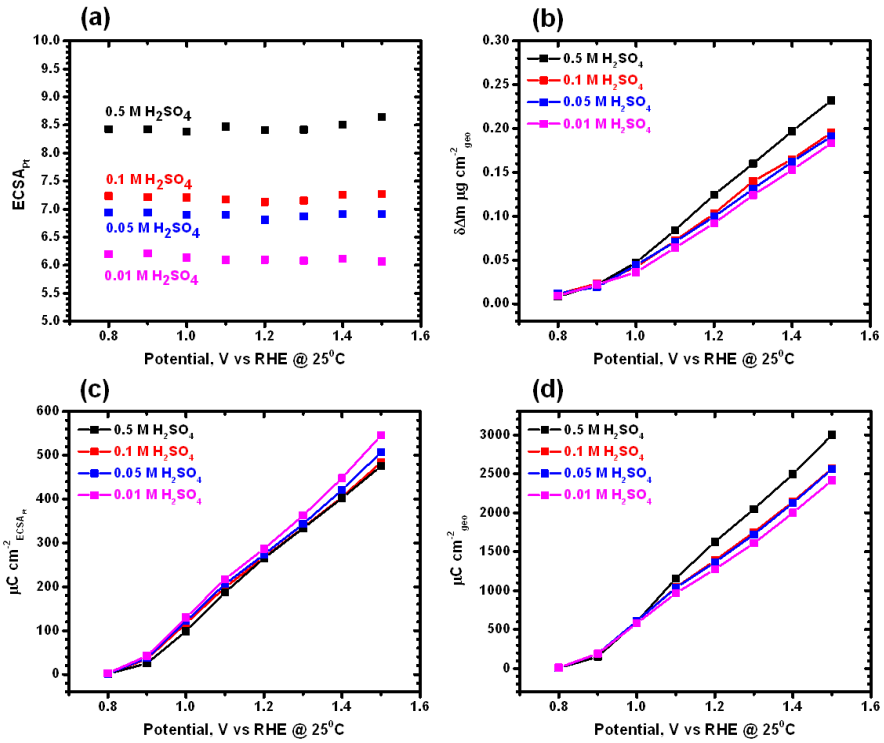

Figure B.7: Electrochemical behavior of Pt electrode in 0.5, 0.1, 0.05, and 0.01 M H_2SO_4: (a) $ECSA_{Pt}$, (b) interfacial mass-change, (c) charge density of oxide formation normalized per electrochemical area, and (d) charge density of oxide formation normalized per geometric area.

Table B.1: Data summary- Oxide formation on Pt electrode in 0.5 M H_2SO_4

Test Condition in 0.5 M H_2SO_4	**$ECSA_{Pt}$, cm^2**	**Roughness factor, RF**	**Oxide formation**			
			Charge, $\mu C\ cm^{-2}_{geo}$	**Charge, $\mu C\ cm^{-2}_{ECSA}$**	**$\delta\Delta m$, $\mu g\ cm^{-2}_{geo}$**	**M, g mol^{-1}**
E_H: 0.8 V	8.43	6.15	7.63	1.24	0.008	101.16
E_H: 0.9 V	8.42	6.15	152.97	24.88	0.022	13.88
E_H: 1.0 V	8.39	6.12	601.86	98.32	0.047	7.53
E_H: 1.1 V	8.47	6.18	1158.14	187.29	0.084	7.00
E_H: 1.2 V	8.41	6.10	1625.18	264.96	0.125	7.39
E_H: 1.3 V	8.42	6.14	2048.05	333.41	0.160	7.54
E_H: 1.4 V	8.50	6.21	2496.88	402.23	0.197	7.61
E_H: 1.5 V	8.64	6.31	2998.87	475.50	0.232	7.46
O_2	-	-	2249.03	-	0.144	6.18
Ar	8.12	5.93	1621.85	273.69	0.129	7.67
20 mV s^{-1}	9.01	6.58	1718.93	261.29	0.128	7.18
SCV	-	-	1478.07	-	0.129	8.42

Table B.2: Data summary- Oxide reduction on Pt electrode in 0.5 M H_2SO_4

Test Condition in 0.5 M H_2SO_4	**Oxide reduction**			
	Charge, $\mu C\ cm^{-2}_{geo}$	**Charge, $\mu C\ cm^{-2}_{ECSA}$**	**$\delta\Delta m$, $\mu g\ cm^{-2}_{geo}$**	**M, g mol^{-1}**
E_H: 0.9 V	9.939699	1.616373	0.023	223.2664
E_H: 1.0 V	267.0118	43.61872	0.052	18.79064

Table B.2 continued.

Test Condition in 0.5 M H_2SO_4	Oxide reduction			
	Charge, $\mu C\ cm^{-2}_{geo}$	Charge, $\mu C\ cm^{-2}_{ECSA}$	$\delta\Delta m$, $\mu g\ cm^{-2}_{geo}$	M, $g\ mol^{-1}$
E_H: 1.1 V	648.4172	104.8616	0.087	12.94594
E_H: 1.2 V	1142.564	184.1649	0.135	11.40291
E_H: 1.3 V	1208.093	196.6692	0.174	13.89689
E_H: 1.4 V	1768.454	284.8881	0.221	12.05778
E_H: 1.5 V	2243.427	355.7186	0.265	11.39732

Table B.3: Data summary- Oxide formation on Pt electrode in 0.1 M $HClO_4$

Test Condition in 0.1 M $HClO_4$	$ECSA_{Pt}$, cm^2	Roughness factor, RF	Oxide formation			
			Charge, $\mu C\ cm^{-2}_{geo}$	Charge, $\mu C\ cm^{-2}_{ECSA}$	$\delta\Delta m$, $\mu g\ cm^{-2}_{geo}$	M, $g\ mol^{-1}$
E_H: 0.8 V	7.49	5.47	130.48	23.87	0.041	30.32
E_H: 0.9 V	7.48	5.46	465.16	85.17	0.060	12.45
E_H: 1.0 V	7.47	5.45	916.37	168.13	0.093	9.79
E_H: 1.1 V	7.43	5.43	1328.57	244.87	0.123	8.93
E_H: 1.2 V	7.25	5.37	1694.60	320.92	0.156	8.89
E_H: 1.3 V	7.36	5.37	2086.06	388.43	0.191	8.83
E_H: 1.4 V	7.39	5.39	2519.56	467.16	0.220	8.42
E_H: 1.5 V	7.41	5.41	2927.54	541.38	0.245	8.07
O_2	-	-	2054.66	-	0.182	8.55
Ar	6.80	4.97	1728.01	347.90	0.161	8.99

Table B.3 continued.

Test Condition in 0.1 M $HClO_4$	$ECSA_{Pt}$, cm^2	Roughness factor, RF	Oxide formation			
			Charge, $\mu C\ cm^{-2}_{geo}$	Charge, $\mu C\ cm^{-2}_{ECSA}$	$\delta\Delta m$, $\mu g\ cm^{-2}_{geo}$	M, g mol^{-1}
20 mV s^{-1}	8.01	5.85	1762.98	301.44	0.161	8.81
SCV	-	-	1391.43	-	0.145	10.05

Table B.4: Data summary- Oxide formation on Pt electrode in 0.1 M H_2SO_4

Test Condition	$ECSA_{Pt}$, cm^2	Roughness factor, RF	Oxide formation			
			Charge, $\mu C\ cm^{-2}_{geo}$	Charge, $\mu C\ cm^{-2}_{ECSA}$	$\delta\Delta m$, $\mu g\ cm^{-2}_{geo}$	M, g mol^{-1}
E_H: 0.8 V	7.23	5.28	8.68	1.64	0.011	122.29
E_H: 0.9 V	7.22	5.27	184.78	35.08	0.023	12.01
E_H: 1.0 V	7.21	5.26	611.24	116.22	0.042	6.63
E_H: 1.1 V	7.17	5.23	1039.99	198.67	0.072	6.68
E_H: 1.2 V	7.12	5.19	1388.50	267.17	0.103	7.15
E_H: 1.3 V	7.15	5.22	1749.41	335.05	0.140	7.72
E_H: 1.4 V	7.26	5.30	2144.25	404.90	0.165	7.42
E_H: 1.5 V	7.27	5.31	2568.84	484.10	0.195	7.32

Table B.5: Data summary- Oxide formation on Pt electrode in 0.05 M H_2SO_4

Test Condition	$ECSA_{Pt}$, cm^2	Roughness factor, RF	Oxide formation			
			Charge, $\mu C\ cm^{-2}_{geo}$	Charge, $\mu C\ cm^{-2}_{ECSA}$	$\delta\Delta m$, $\mu g\ cm^{-2}_{geo}$	M, g mol^{-1}
E_H: 0.8 V	6.94	5.06	8.91	1.76	0.012	129.88

Table B.5 continued.

E_H: 0.9 V	6.94	5.07	190.04	37.52	0.019	9.65
E_H: 1.0 V	6.89	5.03	611.57	121.54	0.044	6.94
E_H: 1.1 V	6.90	5.03	1036.53	205.91	0.071	6.61
E_H: 1.2 V	6.81	4.97	1364.60	273.88	0.100	7.05
E_H: 1.3 V	6.87	5.01	1722.22	343.42	0.131	7.34
E_H: 1.4 V	6.92	5.05	2124.83	420.90	0.162	7.36
E_H: 1.5 V	6.91	5.05	2559.84	507.18	0.191	7.20

Table B.6: Data summary- Oxide formation on Pt electrode in 0.01 M H_2SO_4

Test Condition	**$ECSA_{Pt}$, cm^2**	**Roughness factor, RF**	**Oxide formation**			
			Charge, $\mu C\ cm^{-2}_{geo}$	**Charge, $\mu C\ cm^{-2}_{ECSA}$**	**$\delta\Delta m$, $\mu g\ cm^{-2}_{geo}$**	**M, g mol^{-1}**
E_H: 0.8 V	6.20	4.53	10.00	2.21	0.009	86.87
E_H: 0.9 V	6.21	4.53	191.60	42.25	0.022	11.08
E_H: 1.0 V	6.14	4.48	580.64	129.62	0.036	5.98
E_H: 1.1 V	6.10	4.45	967.43	217.45	0.064	6.38
E_H: 1.2 V	6.09	4.41	1275.92	286.81	0.092	6.96
E_H: 1.3 V	6.08	4.44	1608.04	362.38	0.124	7.44
E_H: 1.4 V	6.12	4.46	2000.46	448.12	0.153	7.38
E_H: 1.5 V	6.07	4.43	2417.63	545.87	0.183	7.30

APPENDIX C ***(CHAPTER 4)***

Table C.1: Data summary- Oxide formation on Pt and Pt alloy catalysts in 0.5 M H_2SO_4

Sample	Type of EQCN sensor, MHz	Catalyst loading, μg_{Pt} cm^{-2}	Thickness of film, µm	Specific area, m^2 g^{-1}	Roughness factor, RF	Oxide formation		
						Charge, $\mu C\ cm^{-2}_{ECSA}$	Onset potential, V	M, $g\ mol^{-1}$
Pt black	7.9	191.7	0.36	19.1	36.6	299.00	0.701	33–38
Pt/C	7.9	9.3	0.12	41.1	3.82	367.80	0.717	7.5–9
Pt-Cu/C	7.9	9.3	0.17	76.3	7.00	318.80	0.722	17–20
Pt-Co/C	5	38.9	0.46	17.4	6.76	301.36	0.721	16–18
Pt-Sc/C	5	26.7	0.31	36.5	11.4	260.50	0.696	24–26

EQCN measurements were also carried out with 5 MHz sensor for Pt/C. Results were comparable with that obtained with 7.9 MHz.

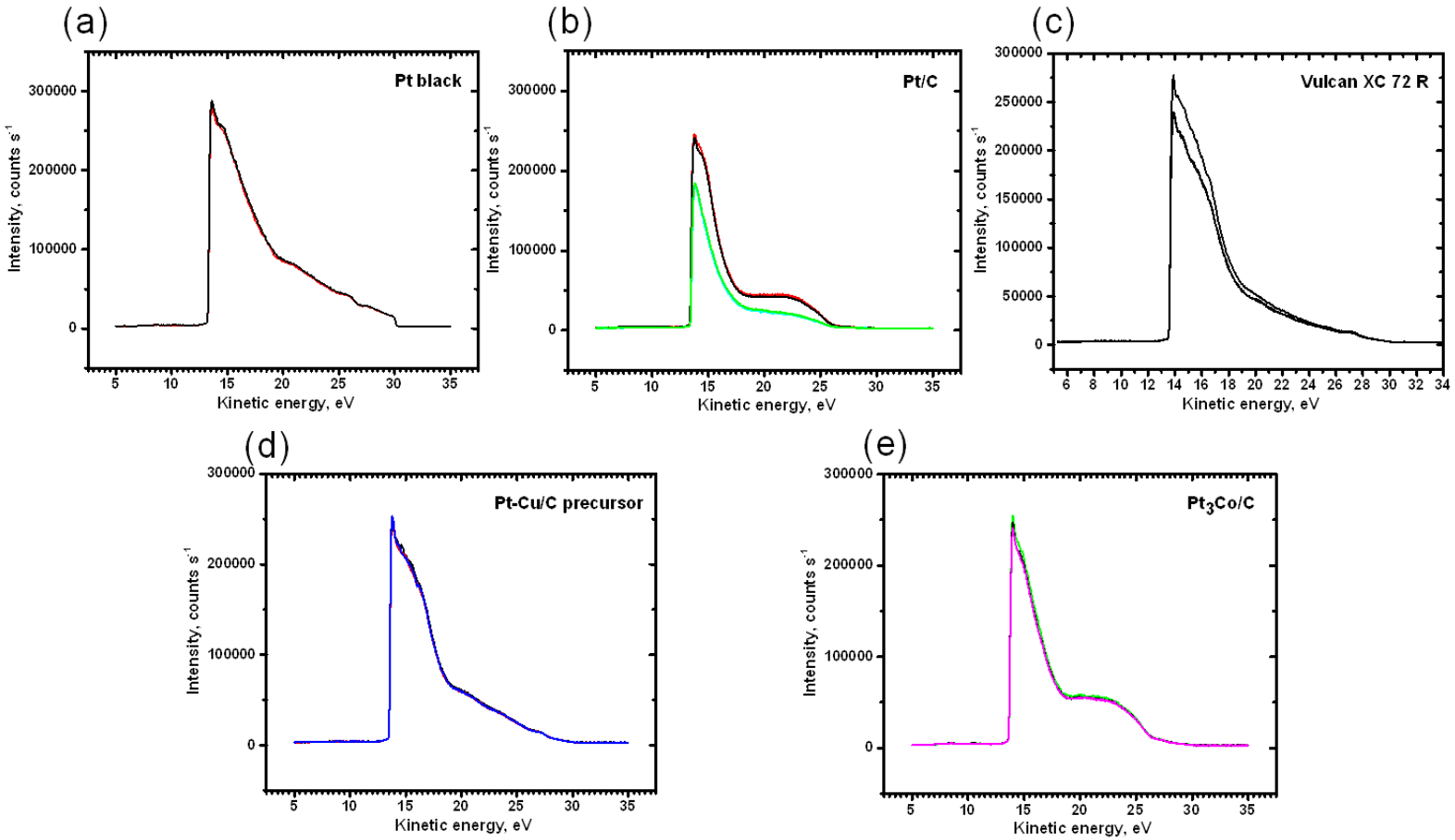

Figure C.1: Work function of the materials: (a) Vulcan XC 72 R (4.8298 eV), (b) Pt black (4.483 eV), (c) Pt/C (4.7654 eV), (d) Pt-Cu precursor (4.7388 eV), and (e) Pt_3Co/C (4.8356 eV).

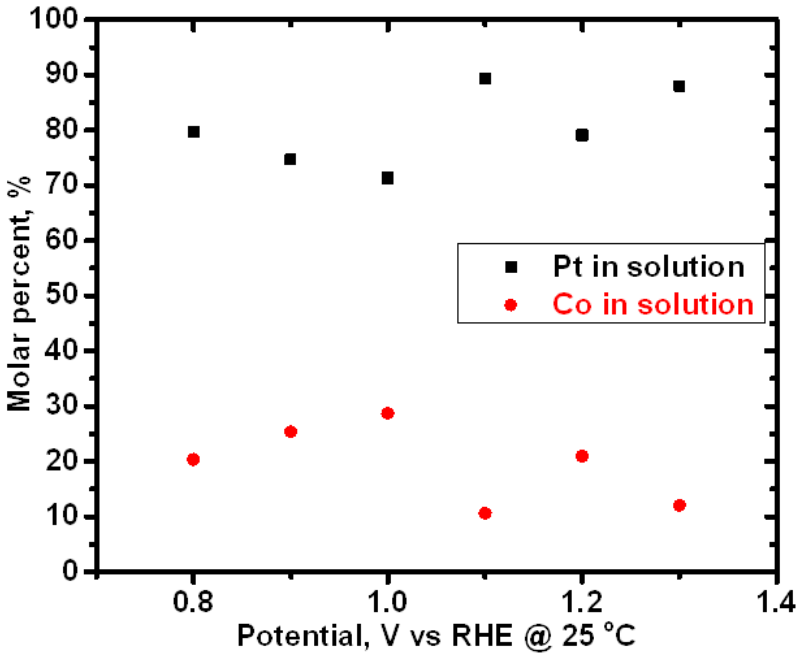

Figure C.2: Molar percent of dissolved Pt and Co (Pt_3Co/C) as a function of upper potential.

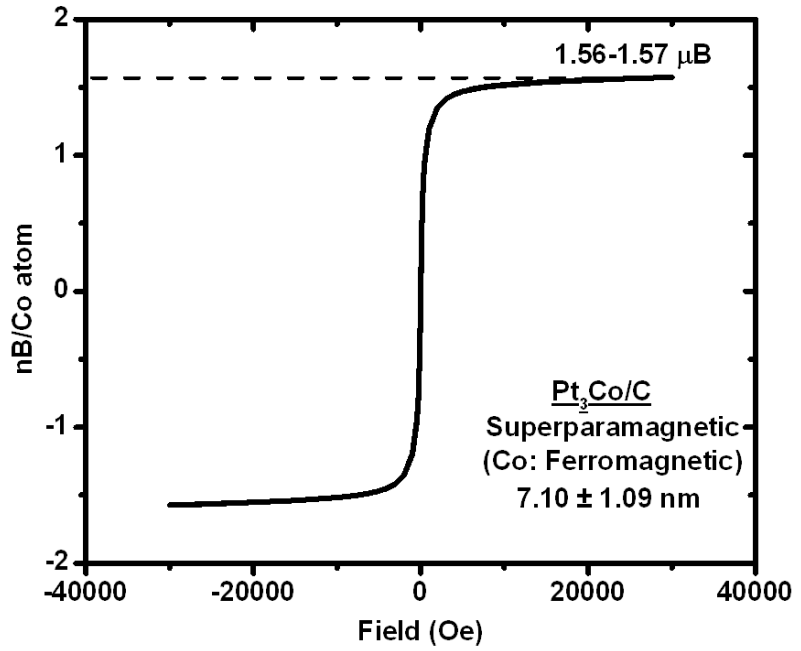

Figure C.3: The magnetic property of Pt_3Co/C catalyst (Co metal, HCP: 1.73 μB, Bohr magneton at 0 K).

APPENDIX D *(CHAPTER 5)*

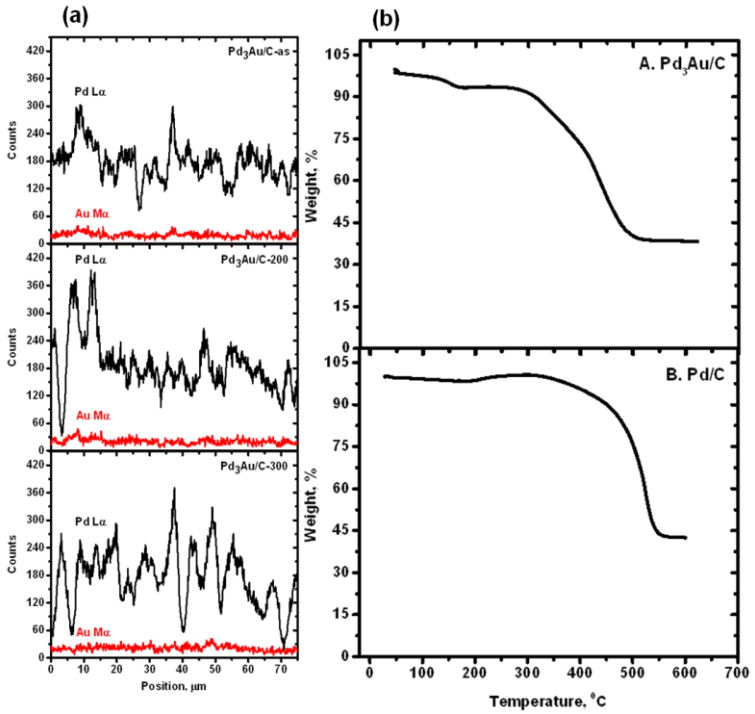

Figure D.1: (a) EDS line scans and (b) Thermogravimetric profiles of the samples.

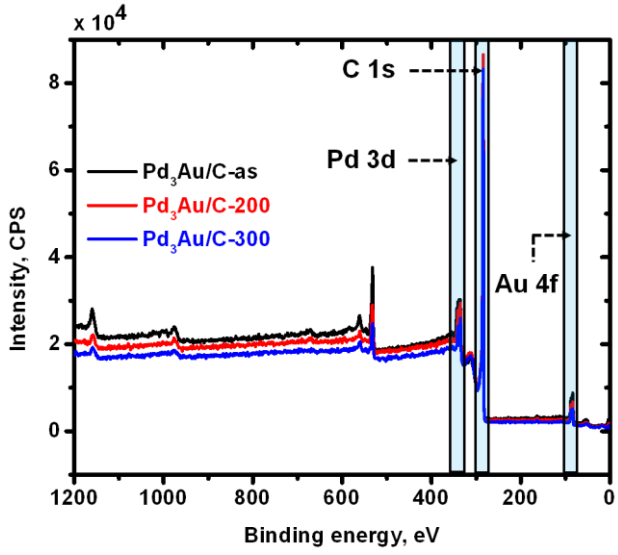

Figure D.2: XPS survey scans of the samples.

Table D.1: Data summary: Oxide formation and Oxide reduction on Pd_3Au/C electrodes in 0.5 M H_2SO_4

Catalyst	Oxide formation			Oxide reduction				M_{red}/M_{ox}
	Charge, $\mu C\ cm^{-2}_{geo}$	$\delta\Delta m$, $\mu g\ cm^{-2}_{geo}$	M_{ox}, g mol^{-1}	Charge, $\mu C\ cm^{-2}_{geo}$	$ECSA_{Pd}$, cm^2	$\delta\Delta m$, $\mu g\ cm^{-2}_{geo}$	M_{red}, g mol^{-1}	
Pd/C – as	5916.27	0.6885	11.23	4203.77	13.71	1.131	25.96	2.31
Pd_3Au/C – as	5593.20	0.9195	15.84	3910.57	12.76	1.5908	39.16	2.47
Pd_3Au/C – 200	3054.26	0.8168	25.81	1967.61	6.42	1.3614	66.61	2.58
Pd_3Au/C – 300	2553.69	0.2718	10.28	1523.90	4.97	0.4385	27.82	2.71
Pd_3Au/C – 300 (O_2)	2164.60	0.1680	7.49	1849.73	6.03	0.2740	14.29	1.91
Pd_3Au/C – 300 (20 mV s^{-1})	2626.42	0.2225	8.18	1420.06	4.63	0.3838	26.07	3.19

Table D.2: Summary of data: Accelerated degradation tests of Pd_3Au/C electrodes in 0.5 M H_2SO_4

Catalyst	Oxide formation			Oxide reduction				M_{red}/M_{ox}
	Charge, $\mu C\ cm^{-2}_{geo}$	$\delta\Delta m$, $\mu g\ cm^{-2}_{geo}$	M_{ox}, g mol^{-1}	Charge, $\mu C\ cm^{-2}_{geo}$	$ECSA_{Pd}$, cm^2	$\delta\Delta m$, $\mu g\ cm^{-2}_{geo}$	M_{red}, g mol^{-1}	
Pd_3Au/C – as - before	4286.75	0.557	12.54	2927.75	9.55	1.04	34.11	2.72
Pd_3Au/C – as - after	840.93	0.755	86.63	452.33	1.48	0.765	163.18	1.88
Pd_3Au/C – 300 - before	1952.12	0.177	8.75	1199.08	3.91	0.301	24.22	2.77
Pd_3Au/C – 300 - after	857.56	0.162	18.23	494.88	1.61	0.262	51.08	2.8

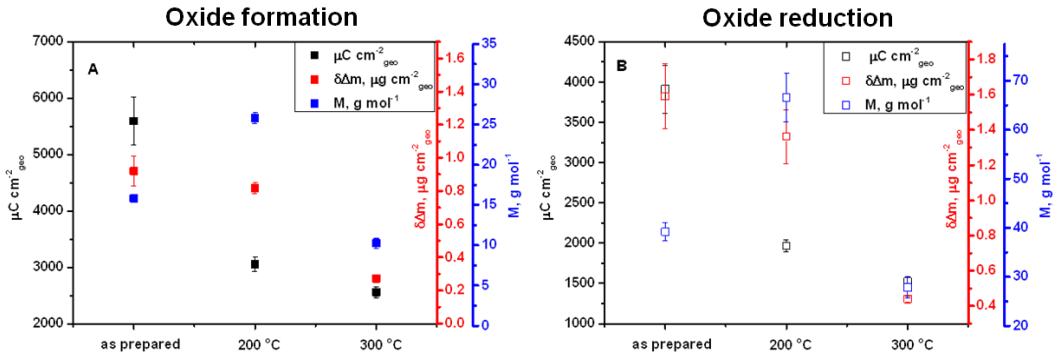

Figure D.3: Charge density, amount of mass adsorbed and Molar mass of the adsorbed species on the samples during oxide formation and oxide reduction.

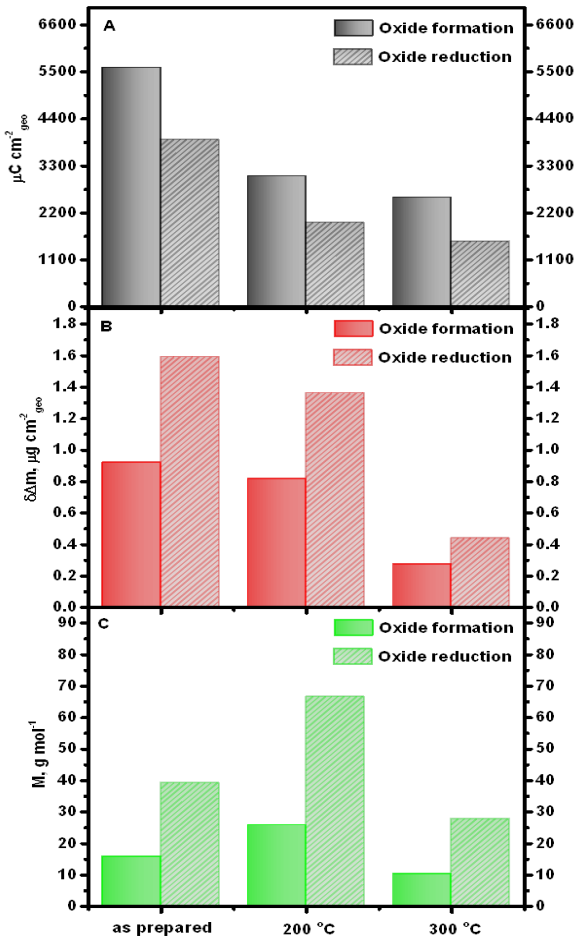

Figure D.4: Comparison of the EQCN data obtained during oxide formation and oxide reduction of the samples.

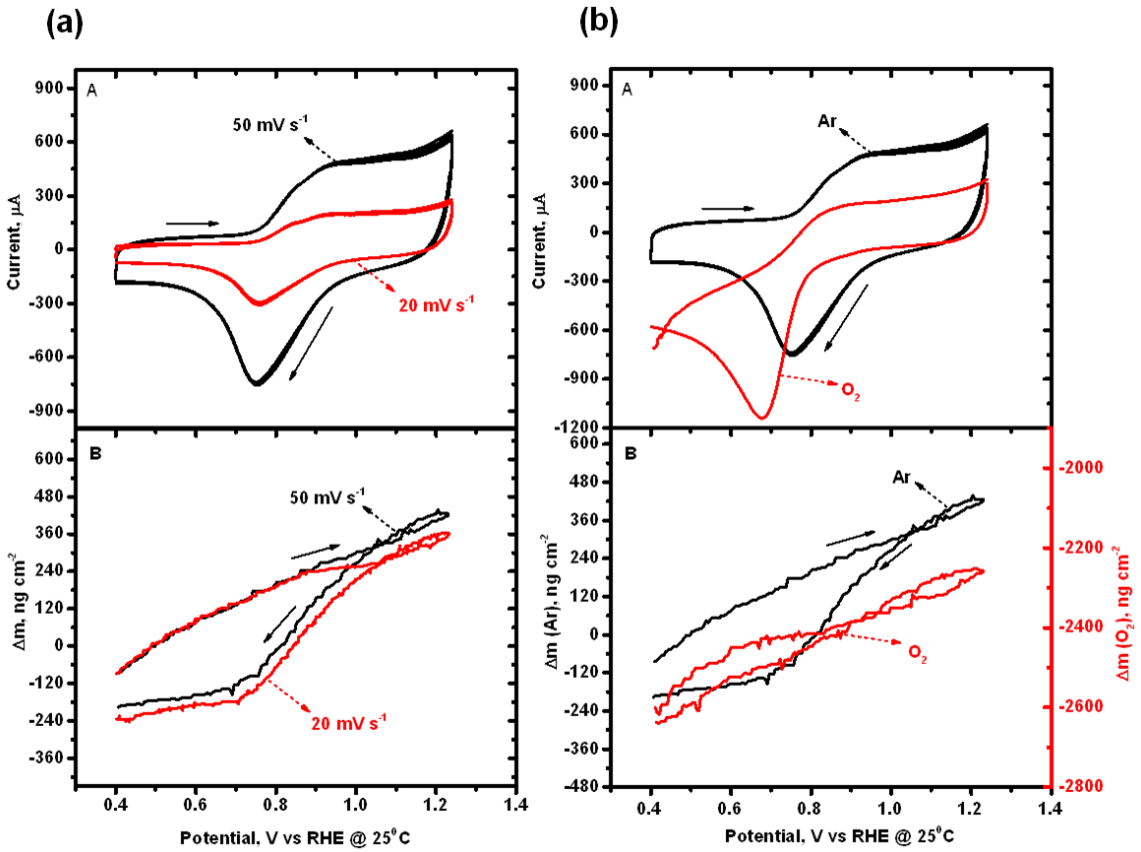

Figure D.5: Combined CV and EQCN response of Pd_3Au/C-300 in 0.5 M H_2SO_4 between 0.4 and 1.24 V at 25 ^{o}C as a function of: (a) scan rate (50 mV s^{-1} and 20 mV s^{-1}), and (b) purge gas (Ar and O_2).

APPENDIX E *(CHAPTER 6)*

Table E.1: Ink loading for different catalysts

Catalyst	Loading level, µg cm^{-2}			Thickness of dry film, µm	Nafion, wt. % (dry film)
	C	Pt	PGM		
Pd/C-EQCN	50	-	34	0.37	21.5
Pd/C-ORR	108	-	72	0.79	22.1
Pd/C-H_2O_2	103	-	69	0.75	22.1
Pd_3Pt/C-EQCN	49	11	32	0.35	22.1
Pd_3Pt/C-ORR	110	25	73	0.80	21.8
Pd_3Pt/C-H_2O_2	105	24	70	0.76	21.8
Pt_3Pd/C-EQCN	49	26	32	0.35	22.1
Pt_3Pd/C-ORR	108	59	72	0.77	21.1
Pt_3Pd/C-H_2O_2	103	56	66	0.74	22.1
Pt/C-EQCN	62	42	42	0.47	25.1
Pt/C-ORR	112	75	75	0.79	21.5
Pt/C-H_2O_2	107	71	71	0.75	21.5

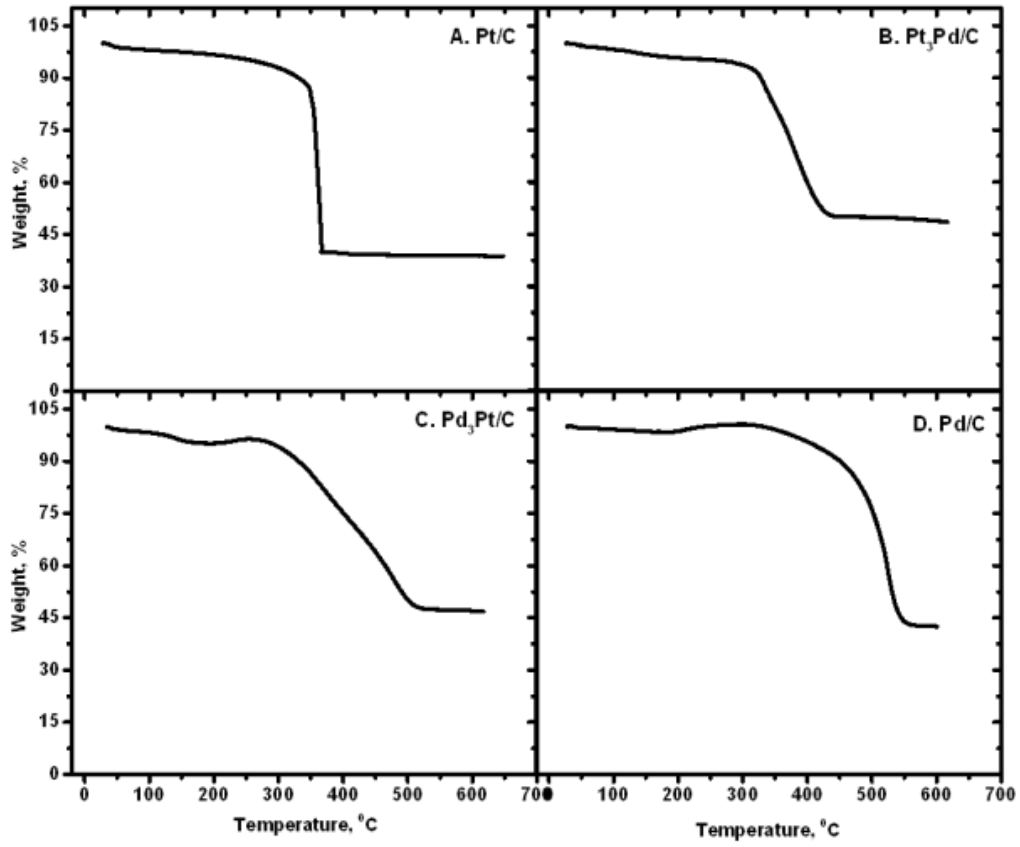

Figure E.1: Thermogravimetric profiles of the samples.

APPENDIX F *(CHAPTER 7)*

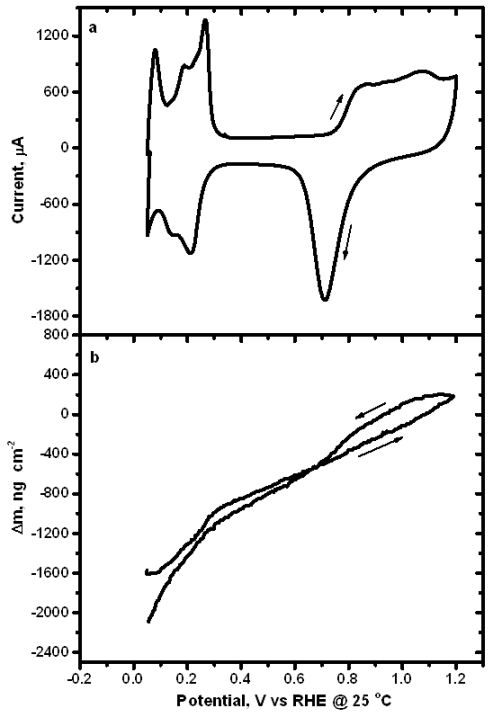

Figure F.1: Combined CV and EQCN response of Pd_3Co/C in 0.5 M H_2SO_4 between 0.05 and 1.20 V at 50 mV s^{-1} and 25 ^{o}C.

References

[1] A. Kirubakaran, S. Jain, and R. K. Nema, "A review on fuel cell technologies and power electronic interface," *Renew. and Sust. Energy Rev.,* **13,** 2430-2440 (2009).

[2] M. Mathias, H. Gasteiger, R. Makharia, and S. Kocha, "T. fuller, J. Pisco," *Abstr. Pap, Am. Chem. Soc*., **228**, U653 (2004).

[3] P. Costamagna, and S. Srinivasan, "Quantum jumps in the PEMFC science and technology from the 1960s to the year 2000: Part I. Fundamental scientific aspects," *J. Power Sources,* **102**, 242-252 (2001).

[4] Technical Plan: Fuel Cells, *Hydrogen, Fuel Cells & Infrastructure Technologies Program: Multi-Year Research, Development and Demonstration Plan*, U.S. Department of Energy, Washington D. C. (2011).

[5] T.J. Schmidt, H.A. Gasteiger, G.D. Stäb, P.M. Urban, D.M. Kolb, and R.J. Behm, "Characterization of high-surface-area electrocatalysts using a rotating disk electrode configuration," *J. Electrochem. Soc.,* **145**, 2354-2358 (1998).

[6] J.O'M. Bockris, and S.Srinivasan, "Fuel cells-their electrochemistry," McGraw-Hill, New York (1969).

[7] J.K. Nørskov, J. Rossmeisl, A.Logadottir, L. Lindqvist, J.R. Kitchin, T. Bligaard, and H. Jonsson, "Origin of the overpotential for oxygen reduction at a fuel-cell cathode," *J. Phy. Chem. B,* **108**, 17886-17892 (2004).

[8] S.-Y. Ahn, S.-J. Shin, H.Y. Ha, S.-A. Hong, Y.-C. Lee, T.W. Lim, and I.-H. Oh, "Performance and lifetime analysis of the kW-class PEMFC stack," *J. Power Sources,* **106**, 295-303 (2002).

[9] E. Guilminot, A. Corcella, F. Charlot, F. Maillard, and M. Chatnet, "Detection of Pt z+ ions and Pt nanoparticles inside the membrane of a used PEMFC," *J. Electrochem. Soc.,* **154**, B96-B105 (2007).

[10] Y. Shao-Horn, W.C. Sheng, S. Chen, P.J. Ferreira, E.F. Holby, and D. Morgan, "Instability of supported platinum nanoparticles in low-temperature fuel cells," *Top. in Catal.,* **46**, 285-305 (2007).

[11] T. Bligaard, J.K. Nørskov, S. Dahl, J. Matthiesen, C.H. Christensen, and J. Sehested, "The Brønsted–Evans–Polanyi relation and the volcano curve in heterogeneous catalysis," *J. Catal.,* **224**, 206-217 (2004).

[12] J.K. Nørskov, T. Bligaard, A. Logadottir, S. Bahn, L.B. Hansen, M. Bollinger, H. Bengaard, B. Hammer, Z. Sljivancanin, M.Mavrikakis, Y. Xu, S. Dahl, and C.J.H. Jacobsen, "Universality in heterogeneous catalysis," *J. Catal.,* **209**, 275-278 (2002).

[13] James *et al*., DTI, Inc., 2010 DOE Hydrogen Program Review, Washington, DC, June 9 (2010).

[14] H.S. Wroblowa, Yen-Chi-Pan, and G. Razumney, "Electroreduction of Oxygen: A new mechanistic criterion," *J. Electroanal. Chem.*, **69**, 195-201 (1976).

[15] J. Zhang, Y. Mo, M.B. Vukmirovic, R. Klie, K. Sasaki, R.R. Adzic, "Platinum monolayer electrocatalysts for O2 reduction: Pt monolayer on Pd (111) and on carbon-supported Pd nanoparticles," *J. Phy. Chem. B.*, **108**, 10955-10964 (2004).

[16] K. Sasaki , H. Naohara, Y. Cai, Y.M. Choi, P. Liu, M.B. Vukmirovic, J.X. Wang, and R.R. Adzic, "Core-Protected Platinum Monolayer Shell High-Stability Electrocatalysts for Fuel-Cell Cathodes," *Ange. Chemie Intl. Ed.*, **49**, 8602-8607 (2010).

[17] V. Stamenkovic, B.S. Mun, K.J.J. Mayrhofer, P.N. Ross, and N.M. Markovic, "Effect of surface composition on electronic structure, stability, and electrocatalytic properties of Pt-transition metal alloys: Pt-skin versus Pt-skeleton surfaces," *J. Am. Chem. Soc.*, **128**, 8813-8819 (2006).

[18] T. Toda, H. Igarashi, H. Uchida, and M. Watanabe, "Enhancement of the electroreduction of oxygen on Pt alloys with Fe, Ni, and Co," *J. Electrochem. Soc.,* **146**, 3750-3756 (1999).

[19] H.A. Gasteiger, and N.M. Markovic, "Just a dream—or future reality?," *Sci.,* **324**, 48-49 (2009).

[20] P. Strasser, "Dealloyed core-shell fuel cell electrocatalysts," *Reviews in Chem. Engg.,* **25**, 255-295 (2009).

[21] B. Gurau, R. Viswanathan, R. Liu, T.J. Lafrenz, K.L. Ley, E.S. Smotkin, E. Reddington, A. Sapienza, B.C. Chan, and T.E. Mallouk, "Structural and electrochemical characterization of binary, ternary, and quaternary platinum alloy catalysts for methanol electro-oxidation," *J. Phy. Chem. B,* **102**, 9997-10003 (1998).

[22] CRC Handbook of Chemistry and Physics, 12-124, 93rd edition, Boca Raton, FL: CRC Press, (2012).

[23] C.R.A. Catlow, Z.X. Guo, M. Miskufova, S.A. Shevlin, A.G.H. Smith, A.A. Sokol, A. Walsh, D.J. Wilson, and S.M. Woodley, "Advances in computational studies of energy materials," *Phil. Trans. Roy. Soc. A: Mathematical, Physical and Engineering Sciences*, **368**, 3379-3456 (2010).

[24] C.A. Reiser, L. Bregoli, T.W. Patterson, J.S. Yi, J.D. Yang, M.L. Perry, and T.D. Jarvi, "A reverse-current decay mechanism for fuel cells," *Electrochem. and Solid-State Lett,* **8** (6), A273-A276 (2005).

[25] M. Matsumoto, T. Miyazaki, and H. Imai, "Oxygen-enhanced dissolution of platinum in acidic electrochemical environments," *J. Phy. Chem.C,* **115**, 11163-11169 (2011).

[26] G. Jerkiewicz, G. Vatankah, A. Zolfaghari, and J. Lessard, "Analysis of the mass response of the electrochemical quartz-crystal nanobalance in horizontal and vertical geometry," *Electrochem. Comm.*, **1**, 419-424 (1999).

[27] Y. Tamura, K. Taneda, M. Ueda, and T. Ohtsuka, "Effect of oxide film on oxygen reduction current for the platinum–cobalt alloy electrodes in PEFC," *Corr. Sci.*, **51**, 1560-1564 (2009).

[28] B.E. Conway, "Electrochemical oxide film formation at noble metals as a surface-chemical process," *Prog. Surf. Sci.,* **49**, 331-452 (1995).

[29] K. Tamamoto, D.M. Kolbe, R. Kötz, and G. Lehmpfuhl, "Hydrogen adsorption and oxide formation on platinum single crystal electrodes," *J. Electroanal. Chem. and Interfac. Electrochem.*, **96**, 233-239 (1979).

[30] J.S. Mayell, and S.H. Langer, "A study of surface oxides on platinum electrodes," *J. Electrochem. Soc.*, **111**, 438-446 (1964).

[31] H.A. Laitinen, and C.G. Enke, "The electrolytic formation and dissolution of oxide films on platinum," *J. Electrochem. Soc.*, **107**, 773-781 (1960).

[32] S. Shibata, "Conductance measurement of thin oxide films on a platinum anode," *Electrochim. Acta,* **22**, 175-179 (1977).

[33] D.A. Buttry, and M.D. Ward, "Measurement of interfacial processes at electrode surfaces with the electrochemical quartz crystal microbalance," *Chem. Rev.*, **92**, 1355-1379 (1992).

[34] K.J. Vetter, and J.W. Schultze, "The kinetics of the electrochemical formation and reduction of monomolecular oxide layers on platinum in 0.5< i> M</i> H< sub> 2</sub> SO< sub> 4</sub>: Part II. Galvanostatic pulse measurements and the model of oxide growth," *J. Electroanal. Chem. and Interfac. Electrochem.,* **34**, 141-158 (1972).

[35] F. Colmati, E. Antolini, and E.R. Gonzalez, "Preparation, structural characterization and activity for ethanol oxidation of carbon supported ternary Pt–Sn–Rh catalysts," *J. Alloys and Compds.*, **456,** 264-270 (2008).

[36] J.F. Moulder, W.F. Stickle, P.E. Sobol and K.D. Bomben, in: *Handbook of X-ray Photoelectron Spectroscopy*, MN: Perkin-Elmer Corp., J. Chastian and R.C. King (Jr), (Eds) (1992)

[37] A.C. Riddiford, "The rotating disk system," *Adv. Electrochem. Electrochem. Engg.*, **4**, 47-116 (1966).

[38] C. Song, and J. Zhang, in: *PEM Fuel Cell Electrocatalysts and Catalyst Layers: Fundamentals and Applications*, London: Springer, J. Zhang, (Ed), chapter 2 (2008).

[39] Y. Sugawara, A.P. Yadav, A. Nishikata, and T. Tsuru, "EQCM study on dissolution of ruthenium in sulfuric acid," *J. Electrochem. Soc.,* **155**, B897-B902 (2008).

[40] T. Biegler, D.A.J. Rand, and R. Woods, "Limiting oxygen coverage on platinized platinum; relevance to determination of real platinum area by hydrogen adsorption," *J. Electroanal. Chem. and Interfac. Electrochem.,* **29**, 269-277 (1971).

[41] S. Trasatti, and O.A. Petril, Real surface area measurements in electrochemistry," *Pure and Appl. Chem.,* **63**, 711-734 (1991).

[42] A. López-Cudero, A. Cuesta, C. Gutiérrez, "Potential dependence of the saturation CO coverage of Pt electrodes: The origin of the pre-peak in CO-stripping voltammograms. Part 1: Pt (111)," *J. Electroanal. Chem.,* **579**, 1-12 (2005).

[43] X. Wang, R. Kumar, and D.J. Myers, "Effect of voltage on platinum dissolution relevance to polymer electrolyte fuel cells," *Electrochem. and Solid-State Lett*, **9**, A225-A227 (2006).

[44] J.P. Hoare, *The electrochemistry of Oxygen,* New York: Interscience Publishers, 1968.

[45] R.R. Adzic, J. Zhang, K. Sasaki, M.B. Vukmirovic, M. Shao, J.X. Wang, A.U. Nilekar, M. Mavrikakis, J.A. Valerio, and F. Uribe, "Platinum monolayer fuel cell electrocatalysts," *Top. Catal.,* **46**, 249-262 (2007).

[46] M. Osawa, M. Tsushima, H. Mogami, G. Samjeské, and A. Yamakata, "Structure of water at the electrified platinum-water interface: A study by surface-enhanced infrared absorption spectroscopy," *J. Phy. Chem. C,* **112**, 4248-4256 (2008).

[47] B.V. Tilak, B.E. Conway, and H. Angerstein-Kozlowska, "The real condition of oxidized pt electrodes: Part III. Kinetic theory of formation and reduction of surface oxides," *J. Electroanal. Chem. and Interfac. Electrochem.,* **48**, 1-23 (1973).

[48] M. Pourbaix, *Atlas of Electrochem. Equilibria in Aq. Sol.*, Oxford: Pergamon Press Ltd., pgs 378-383 (1966).

[49] G. Jerkiewicz, G. Vatankah, J. Lessard, M.P. Soriaga, and Y. Park, "Surface-oxide growth at platinum electrodes in aqueous H< sub> 2</sub> SO< sub> 4</sub>: Reexamination of its mechanism through combined cyclic-voltammetry, electrochemical quartz-crystal nanobalance, and Auger electron spectroscopy measurements," *Electrochim Acta***, 49**, 1451-1459 (2004).

[50] R.E. Benfield, "Mean coordination numbers and the non-metal–metal transition in clusters," *J. Chem. Soc., Faraday Trans*., **88**, 1107–1110 (1992).

[51] P. Mathew, J.P. Meyers, R.S rivastava, and P. Strasser, "Analysis of Surface Oxidation on Pt and Pt Core-Shell Electrocatalysts for PEFCs," *J. Electrochem. Soc.*, **159**, B554-B563 (2012).

[52] H. Yano, J. Inukai, H. Uchida, M. Watnabe, P.K. Babu, T. Kobayashi, J.H. Chung, E. Oldfield, and A. Wieckowski, "Particle-size effect of nanoscale platinum catalysts in oxygen reduction reaction: an electrochemical and 195Pt EC-NMR study," *Phys. Chem. Chem. Phys.*, **8**, 4932-4939 (2006).

[53] P. Strasser, S. Koh, and J. Greeley, "Voltammetric surface dealloying of Pt bimetallic nanoparticles: an experimental and DFT computational analysis," *Phys. Chem. Chem. Phys.*, **10**, 3670-3683 (2008).

[54] J. Erlebacher, M.J. Aziz, A. Karma, N. Dimitrov, and K. Sieradzki, "Evolution of nanoporosity in dealloying," *Nat.*, **410**, 450-453 (2001).

[55] S. Koh, and P. Strasser, "Electrocatalysis on bimetallic surfaces: modifying catalytic reactivity for oxygen reduction by voltammetric surface dealloying," *J. Am. Chem. Soc*., **129**, 12624-12625 (2007).

[56] H. Angerstein-Kozlowska, B.E. Conway, and W.B.A. Sharp, "The real condition of electrochemically oxidized platinum surfaces: Part I. Resolution of component processes," *J. Electroanal. Chem. and Interfac. Electrochem.,* **43**, 9-36 (1973).

[57] T. Frelink, W. Visscher, and J.A.R. Van Veen, "Measurement of the Ru surface content of electrocodeposited PtRu electrodes with the electrochemical quartz crystal microbalance: implications for methanol and CO electrooxidation," *Langmuir*, **12**, 3702-3708 (1996).

[58] V.I. Birss, M. Chang, and J. Segal., "Platinum oxide film formation—reduction: an in-situ mass measurement study," *J Electroanal Chem*., **355**, 181-191 (1993).

[59] S. Papadimitriou, A. Tegou, E. Pavlidoc, S. Armyanov, E. Valova, G. Kokkinidis, and S.Sotiropoulos, "Preparation and characterisation of platinum-and gold-coated copper, iron, cobalt and nickel deposits on glassy carbon substrates," *Electrochim. Acta*, **53**, 6559-6567 (2008).

[60] V. Stamenkovic, B.S. Mun, K.J.J. Mayrhofer, P.N. Ross, N.M. Markovic, J. Rossmeisl, J. Greeley, and J.K. Nørskov, "Changing the activity of electrocatalysts for oxygen reduction by tuning the surface electronic structure," *Angew. Chem.*, **118**, 2963-2967 (2006).

[61] V. Stamenkovic, T.J. Schmidt, P.N. Ross, N.M. Markovic, "Surface composition effects in electrocatalysis: Kinetics of oxygen reduction on well-defined Pt3Ni and Pt3Co alloy surfaces," *J.Phys.Chem. B*, **106**, 11970-11979 (2002).

[62] P. Yu, M. Pemberton, and P. Plasse, "PtCo/C cathode catalyst for improved durability in PEMFCs," *J. Power Sources*, **144**, 11-20 (2005).

[63] M.A. Vasiliev, "Surface effects of ordering in binary alloys," *J. Phys. D: Appl. Phys.,* **30**, 3037 (1997).

[64] S. Chen, W. Sheng, N. Yabuuchi, P.J. Ferreira, L.F. Allard, and Y. Shao-Horn, "Origin of oxygen reduction reaction activity on "Pt3Co" nanoparticles: atomically resolved chemical compositions and structures," *J.Phys.Chem. C*, **113**, 1109-1125 (2008).

[65] B. Hammer, and J.K. Nørskov, "Theoretical surface science and catalysis—calculations and concepts," *Adv.in Catal.,* **45**, 71-129 (2000).

[66] A. Bonakdarpour, M. Lefevre, R. Yang, F. Jaouen, T. Dahn, J-P Dodelet, and J.R. Dahn, "Impact of loading in RRDE experiments on Fe–N–C catalysts: two-or four-electron oxygen reduction?," *Electrochem. and Solid-State Lett*, **11**, B105-B108 (2008).

[67] M. Pourbaix, *Atlas of Electrochem. Equilibria in Aq. Sol.*, Oxford: Pergamon Press Ltd., pgs 358-363 (1966)

[68] F. Gao, Y.L. Wang, and D.W. Goodman, "CO oxidation over AuPd (100) from ultrahigh vacuum to near-atmospheric pressures: the critical role of contiguous Pd atoms," *J. Am. Chem. Soc.,* **131**, 5734-5735 (2009).

[69] J.K. Edwards, B.E. Solsona, P. Landon, A.F. Carley, A. Herzing, C.J. Kiely, and G.J. Hutchings, "Direct synthesis of hydrogen peroxide from H< sub> 2</sub> and O< sub> 2</sub> using TiO< sub> 2</sub>-supported Au–Pd catalysts," *J. Catal.,* **236**, 69-79 (2005).

[70] F. Gao, and D.W. Goodman, "Pd–Au bimetallic catalysts: understanding alloy effects from planar models and (supported) nanoparticles," *Chem. Soc. Reviews,* **41**, 8009-8020 (2012).

[71] A. Damjanovic, and V. Brusic, "Pretreatment of Pt-Au and Pd-Au alloy electrodes in the study of oxygen reduction," *J. Electroanal. Chem. and Interfac. Electrochem.,* **15**, 29-33 (1967).

[72] K. Gossner, and E. Mizera, "Investigations on the adsorption and electrocatalytic oxidation of carbon monoxide on gold+ palladium alloys," *J. Electroanal. Chem. and Interfac. Electrochem.,* **140**, 35-45 (1982).

[73] K. Nishimura, K. Machida, and M. Enyo, "Electrocatalysis on Pd+ Au alloy electrodes: Part III. IR spectroscopic studies on the surface species derived from CO and CH3OH in NaOH solution," *J. Electroanal. Chem. and Interfac. Electrochem.,* **260**, 167-179 (1989).

[74] J.P. Hoare, G.W. Castellan, and S. Schuldiner, "Potentials of noble metal and palladium alloy hydrogen electrodes," *J. Phy. Chem.,* **62**, 1141-1142 (1958).

[75] K. Machida, and M. Enyo, "In Situ X-Ray diffraction study of hydrogen entry into Pd and Pd-Au alloy electrodes during anodic HCHO oxidation," *J. Electrochem. Soc.,* **134**, 1472-1474 (1987).

[76] K. Gossner, and E. Mizera, "The anodic oxidation of gold+ palladium alloys," *J. Electroanal. Chem. and Interfac. Electrochem.,* **140**, 47-56 (1982).

[77] R. Woods, "Electrolytic co-deposited palladium-gold electrodes: Effect of potential cycles on surface properties," *Electrochim. Acta,* **14**, 632-635 (1969).

[78] Y. Liu, L. Wang, G. Wang, C. Deng, B. Wu, and Y. Gao, "High Active Carbon Supported PdAu Catalyst for Formic Acid Electrooxidation and Study of the Kinetics," *J. Phy. Chem. C,* **114**, 21417-21422 (2010).

[79] S. Zhang, M. Qing, H. Zhang, and Y. Tian, "Electrocatalytic oxidation of formic acid on functional MWCNTs supported nanostructured Pd–Au catalyst," *Electrochem. Comm.,* **11**, 2249-2252 (2009).

[80] M. Seo, and M. Aomi, "Piezoelectric Response to Surface Stress Change of a Palladium Electrode in Sulfate Aqueous Solutions," *J. Electrochem. Soc.,* **139**, 1087-1090 (1992).

[81] J.A. Harrison, and T.A. Whitfield, "The dissolution of palladium in various electrolytes," *Electrochim Acta***, 28**, 1229-1236 (1983).

[82] C.C. Hu, and T.C. Wen, "Voltammetric investigation of palladium oxides—II. Their formation/reduction behaviour during glucose oxidation in NaOH," *Electrochim Acta***, 39**, 2763-2771 (1994).

[83] C.-W. Yi, K. Luo, T. Wei, and D.W. Goodman, "The composition and structure of Pd-Au surfaces," *J. Phys.Chem B,* **109**, 18535-18540 (2005).

[84] J.H. Sinfelt in, *Bimetallic catalysts: discoveries, concepts and applications*, New York: Wiley (1983).

[85] P. Landon, P.J. Collier, A.J. Papworth, C.J. Kiely, G.J. Hutchings, "Direct formation of hydrogen peroxide from H2/O2 using a gold catalyst," *Chem. Commun,* 2058-2059 (2002).

[86] B. Vincent Crist in, *Handbook of Monochromatic XPS Spectra, Vol 1: The elements and native oxides*, Iowa: XPS International, Inc. (1999)

[87] H. Okamoto, *1990 Au-Pd Phase Diagram, ASM Alloy Phase Diagrams Center*, P. Villars, editor-in-chief; H. Okamoto and K. Cenzual, section editors; ASM international, Materials Park, OH (2006).

[88] N. Ibl, G. Gut, and M. Weber, "Electrodeposition and catalytic activity of palladium powders," *Electrochim. Acta*, **18**, 307–314 (1973).

[89] L.Y. Chen, N. Chen, Y. Hou, Z.C. Wang, S.H. Lv, T. Fujita, J.H. Jiang, A. Hirata, and M.W. Chen, "Geometrically Controlled Nanoporous PdAu Bimetallic

Catalysts with Tunable Pd/Au Ratio for Direct Ethanol Fuel Cells," *ACS Catal,* **3**, 1220–1230 (2013).

[90] M. Grdeń, M. Lukaszewski, G. Jerkiewicz, and A. Czerwiński, "Electrochemical behaviour of palladium electrode: oxidation, electrodissolution and ionic adsorption," *Electrochim. Acta*, **53**, 7583–7598 (2008).

[91] K. Kinoshita, *Electrochemical oxygen technology the electrochemical society series*, New York: John Wiley and Sons (1992).

[92] Lj.M. Vracar, D.B. Sepa, and A. Damjanovic, "Palladium Electrode in Oxygen-Saturated Aqueous Solutions Reduction of Oxygen in the Activation-Controlled Region," *J. Electrochem. Soc.,* **133**, 1835-1839 (1986).

[93] A. Capon, and R. Parsons, "The oxidation of formic acid on noble metal electrodes: II. A comparison of the behaviour of pure electrodes," *J. Electroanal. Chem. and Interfac. Electrochem.,* **44**, 239-254 (1973).

[94] C. Lamy, "Electrocatalytic oxidation of organic compounds on noble metals in aqueous solution," *Electrochim. Acta,* **29**, 1581-1588 (1984).

[95] M.H. Shao, T. Huang, P. Liu, J. Zhang, K. Sasaki, M.B. Vukmirovic, and R.R. Adzic, "Palladium monolayer and palladium alloy electrocatalysts for oxygen reduction," *Langmuir* **22**, 10409-10415 (2006).

[96] H. Okamoto, *1990 Pd-Pt Phase Diagram, ASM Alloy Phase Diagrams Center*, P. Villars, editor-in-chief; H. Okamoto and K. Cenzual, section editors; ASM International, Materials Park, OH (2006).

[97] F. Maillard, E.R. Savinova, P.A. Simonov, V.I. Zaikovskii, and U. Stimming, "Infrared spectroscopic study of CO adsorption and electro-oxidation on carbon-supported Pt nanoparticles: Interparticle versus intraparticle heterogeneity," *J. Phy. Chem. B,* **108**, 17893-17904 (2004).

[98] O.V. Cherstiouk, P.A. Simonov, and E.R. Savinova, "Model approach to evaluate particle size effects in electrocatalysis: preparation and properties of Pt nanoparticles supported on GC and HOPG," *Electrochim. Acta,* **48**, 3851-3860 (2003).

[99] S. Guerin, B.E. Hayden, C.E. Lee, C. Mormiche, J.R. Owen, A.E. Russell, B. Theobald, and D. Thompsett, "Combinatorial electrochemical screening of fuel cell electrocatalysts," *J. Combinatorial Chem.,* **6**, 149-158 (2004).

[100] J. Solla-Gullon, F.J. Vidal-Iglesias, E. Herrero, J.M. Feliu, and A. Aldaz, "CO monolayer oxidation on semi-spherical and preferentially oriented (100) and (111) platinum nanoparticles," *Electrochem. Comm,* **8**, 189-194 (2006).

[101] K.J.J. Mayrhofer, M. Arenz, B.B. Blizanac, V. Stamenkovic, P.N. Ross, and N.M. Markovic, "CO surface electrochemistry on Pt-nanoparticles: A selective review," *Electrochim. Acta,* **50**, 5144-5154 (2005).

[102] F. Maillard, M. Eikerling, O.V. Cherstiouk, S. Schreier, E. Savinova, and U. Stimming, "Size effects on reactivity of Pt nanoparticles in CO monolayer oxidation: The role of surface mobility," *Faraday Discussions,* **125**, 357-377 (2004).

[103] V.P. Zhdanov, and B. Kasemo, "Simulation of CO electrooxidation on nm-sized supported Pt particles: stripping voltammetry," *Chem. Phy. Lett.,* **376**, 220-225 (2003).

[104] S. Gilman, "A study of the mechanism of carbon monoxide adsorption on platinum by a new electrochemical procedure," *J. Phy. Chem.,* **67**, 78-84 (1963).

[105] R. Dalbeck, H.W. Buschmann, and W. Vielstich, "Ex-situ TDS investigation of carbon monoxide electrosorbed on polycrystalline platinum," *J. Electroanal. Chem.,* **372**, 251-259 (1994).

[106] J.L. Fernandez, V. Raghuveer, A. Manthiram, and A.J. Bard, "Pd-Ti and Pd-Co-Au electrocatalysts as a replacement for platinum for oxygen reduction in proton exchange membrane fuel cells," *J. Am. Chem. Soc.*, **127**, 13100-13101 (2005).

[107] V. Raghuveer, A. Manthiram, and A.J. Bard, "Pd-Co-Mo electrocatalyst for the oxygen reduction reaction in proton exchange membrane fuel cells," *J. Phy. Chem. B*, **109**, 22909-22912 (2005).

[108] V. Raghuveer, P.J. Ferreira, and A. Manthiram, "Comparison of Pd–Co–Au electrocatalysts prepared by conventional borohydride and microemulsion methods for oxygen reduction in fuel cells," *Electrochem. Commun.*, **8**, 807-814 (2006).

[109] H. Liu, and A. Manthiram, "Controlled synthesis and characterization of carbon-supported Pd4Co nanoalloy electrocatalysts for oxygen reduction reaction in fuel cells," *Energy and Environ. Sci.*, **2**, 124-132 (2009).

Vita

Preethi Mathew was born in Kerala, India. She earned her B.Tech. degree in Electrochemical Engineering and Technology from Central Electrochemical Research Institute, Karaikudi, Tamil Nadu, India and M.Tech. in Energy Engineering from National Institute of Technology (formerly known as REC), Tiruchirappalli, Tamil Nadu, India. She worked as a Scientist/Engineer with Vikram Sarabhai Space Center (VSSC), a unit of Indian Space Research Organization (ISRO), India for seven years. She entered the Materials Science and Engineering Graduate Program at the University of Texas at Austin, U.S.A in August 2008.

Permanent email: preethimathew@utexas.edu

This dissertation was typed by the author.